UNIVERSITY OF OKLAHOMA

GRADUATE COLLEGE

MOBILE, PHASED-ARRAY, DOPPLER RADAR OBSERVATIONS OF TORNADOES AT X BAND

A DISSERTATION

SUBMITTED TO THE GRADUATE FACULTY

in partial fulfillment of the requirements for the

Degree of

DOCTOR OF PHILOSOPHY

By

MICHAEL MILES FRENCH
Norman, Oklahoma
2012

MOBILE, PHASED-ARRAY, DOPPLER RADAR OBSERVATIONS OF TORNADOES AT X BAND

A DISSERTATION APPROVED FOR THE
SCHOOL OF METEOROLOGY

BY

_____
Dr. Howard Bluestein, Chair

_____
Dr. Phillip Chilson

_____
Dr. Richard Doviak

_____
Dr. Nikola Petrov

_____
Dr. Alan Shapiro

Acknowledgements

I am indebted to several people for their help on this project. First and foremost, thanks go to my advisor, Dr. Howard Bluestein, for his continued support, frequent conversations, and challenging questions about my research. My work has benefitted substantially from help provided by the additional members of my committee, Dr. Phillip Chilson, Dr. Richard Doviak, Dr. Nikola Petrov, and Dr. Alan Shapiro. Thanks also to Jeff Snyder, Mike Buban, Matt Kumjian, Alex Schenkman, Dr. Curtis Alexander, Dr. Dan Dawson, Dr. Karen Kosiba, and Dr. Lance Leslie for useful discussions regarding the results of this research.

Ivan PopStefanija of ProSensing, Inc. and Bob Bluth from the Naval Postgraduate School provided important information about the radar system. Chad Baldi of ProSensing, Inc. was instrumental in running, trouble-shooting, and driving the MWR-05XP from 2007-2010. Ryan May, Jeremy Gibbs, Eric Bruning, Patrick Marsh, and Patrick Skinner all provided much-needed help in computing. Bethany Seeger was extremely helpful in processing data and answering all of my questions while she was at ProSensing, Inc. Thanks also to Jana Houser, Robin Tanamachi, and the dozens of colleagues I worked with on VORTEX2 in 2009-2010. This work was generously funded by NSF grants ATM-0241037, ATM-0637148, and ATM-0934307.

Finally, I'd like to thank my wife, Jennifer French, who somehow allowed for her career, our marriage, and my dissertation to envelop the best time of my life.

Table of Contents

List of Tables

List of Figures

Abstract

Previous studies of tornadoes have utilized high-spatial-resolution data obtained by mobile Doppler radars to better understand phenomena that occur on small spatial scales. There has not been a similar focus on using high-temporal-resolution radar data to investigate short-time-scale volumetric processes that occur in tornadoes. The Mobile Weather Radar, 2005 X-band, Phased-Array (MWR-05XP) is a hybrid phased-array Doppler radar that obtains volumetric data of weather phenomena in ~10 seconds, an order of magnitude faster than that of other mobile Doppler radars. Data obtained by the MWR-05XP from 2008-2010 are used to examine (i) short-time-scale processes that occur in tornadoes, and (ii) the volumetric evolution of tornadoes in supercells.

Tornadic supercell datasets from three dates are studied in-depth to learn more about the tornadogenesis process and volumetric characteristics of tornadoes. It is found that tornadic vortex signatures (TVSs) form upward with time at tornadogenesis for two cases. These results are consistent with mobile, Doppler radar observations of tornadogenesis from the past ~10 years, but counter to studies prior to that, in which a descending TVS was observed in roughly half of tornado cases utilizing WSR-88D data. Possible explanations for this apparent discrepancy in the literature are discussed using a comparative example. Also, it is found that tornadoes can undergo short-time-scale fluctuations in intensity likely not the result of multiple vortices. These fluctuations are shown to have strong height dependence. In one case, the intensity fluctuations are strong enough that the TVS aloft cannot be detected for a short time before it strengthens again. The lack of TVS detection at certain times may be evidence of height-dependent tornado decay and subsequent secondary genesis.

Finally, volumetric characteristics of TVSs up through storm midlevels are discussed. Vertical ΔV profiles and tornado orientation are examined during multiple phases of tornado lifecycles to determine their general trends in time and whether they hold promise in the future as real-time predictors of tornado behavior. TVS vertical ΔV profiles are found to have a distinct signal during the dissipation phases of two tornadoes, though TVS tilt is found to be highly variable at all times. The volumetric evolution of tornado dissipation also is studied. TVSs are found to dissipate first at 2-3 km and then quickly upward and slowly downward from there. Concurrently, TVSs are observed to move in radically different directions at different height levels. Possible explanations for disparate tornado motion and the resulting dissipation are provided.

Chapter 1

Introduction

Recent observational research of supercell thunderstorms using mobile Doppler radars has focused on detecting small-spatial-scale features within supercells not sufficiently resolved by the network of Weather Surveillance Radar-1988 Doppler (WSR-88D). Tornadoes, in particular, occur on spatial scales ($\Delta x = \Delta y = \sim 100$ m) often much smaller than that which can be resolved by WSR-88D radars, even at close ranges (e.g., Wurman and Gill 2000; Bluestein et al. 2003b). The increased spatial resolution of mobile, Doppler radar systems such as the Doppler on Wheels (DOW; Wurman et al. 1997) ~3-cm wavelength (X-band) systems and the University of Massachusetts ~3-mm wavelength (W-band) system (Bluestein et al. 1995) have allowed for unique observations of supercells and tornadoes to be obtained. Examples include observations in tornadoes of multiple vortices (Wurman 2002) and very narrow pendants of reflectivity in hook echoes (e.g., Bluestein and Pazmany 2000), among other observations.

Tornadoes are thought to evolve over very short time scales, as short as < 10 sec. (e.g., Bluestein et al. 2003b), in addition to the small spatial scales over which they occur. For example, the advective time scale of a tornado, T_s, is estimated by:

$$T_s = \frac{2\pi r_c}{V} \tag{1.1}$$

where r_c is the tornado's core radius and V is the velocity scale. Based on a recent climatology of Doppler radar observations of tornadoes by Alexander (2010), the

median tornado core radius is ~50 m when the core radius is defined as the radius of maximum axisymmetric vertical vorticity (AVV):

$$AVV = \frac{2*\Delta V}{\Delta x} \tag{1.2}$$

where ΔV is the radial velocity difference between flow toward the radar origin (hereafter inbounds) and flow away from the radar (hereafter outbounds) and Δx is the distance between the inbound and outbound extrema. If defining the core radius as the distance from the vortex center to the radius of maximum winds, the median value is ~150 m. Averaging these two calculations gives a median core radius estimate of ~100 m. The median tornado ground-relative wind speed was found to be 65 m s^{-1}. The resulting advective time scale of a common tornado is ~9.5 sec. Further, volumetric sampling by conventional mobile Doppler radars relies either on steady state assumptions or on the fidelity of advection correction to retrieve an accurate snapshot of a feature at one time. Using typical values of volumetric update time (90 sec.) and assuming even relatively small errors in storm speed (±5 m s^{-1}) and direction (±25°), errors in feature positions between the lowest and highest elevation angle scans can be estimated as ±600 m. There has not been a focus on *volumetrically* sampling tornadoes commensurate with the small time scales over which they evolve.

This dissertation work uses several datasets obtained in the springs of 2008-2010 by the first mobile, ground-based, phased-array, Doppler radar used in severe storms research, the Mobile Weather Radar, 2005 X-band, phased-array (MWR-05XP; Bluestein et al. 2010), to investigate the short-time-scale evolution and time-height evolution of tornadoes in supercell thunderstorms. Dozens of supercell datasets were obtained and tornadoes can be identified in many of them. Volume scans from 1-20°

and to as high as 40° in elevation angle were obtained in as little as 6 sec. for these datasets. As a result, the data can be used to investigate rapid changes in the radial velocity field that may occur in tornadoes. In addition, the manner in which the MWR-05XP obtains data allows for the height evolution of tornadoes to be investigated without the need for steady state assumptions over the time it takes for a volume scan to be completed. Analysis of the time-height evolution will focus on the single-Doppler radial velocity field in tornadoes.

Topics of interest as they relate to tornado observations include: the tornadogenesis process, rapid fluctuations in radial winds, vertical variations in the horizontal radial wind field, the vertical orientation of tornadoes, and the volumetric evolution of tornado dissipation. Study of these topics was undertaken through a thorough examination of rapidly-updating, volumetric reflectivity and single-Doppler radial velocity data. In addition, using a mobile, phased-array radar (PAR) system for the first time in convective storms research has presented significant challenges. A large part of this work has been the process of obtaining data in a manner that is optimal in matching research objectives with the strengths of the radar system. As a result, significant discussions about the radar system and the data collection process through the spring of 2011 are provided.

Chapter 2 presents a literature review of the major topics, summarized above, that this dissertation discusses. In Chapter 3, the literature review is used to motivate why the observations presented herein are necessary to address outstanding research questions about tornadoes. The research questions are then provided and discussed in detail. Chapter 4 is focused on the data used in this study. The main observing tool, the

MWR-05XP, is discussed, including background information, radar parameters, and system strengths and weaknesses. More specific information about the data collection process also is provided, including strategy, logistics, and the impact that system strength and weakness have on resulting datasets. Chapter 4 ends with a description of analysis tools and any accompanying assumptions and shortcomings. Chapter 5 includes unique, detailed observations made in four supercell tornadoes with general discussion. In Chapter 6, the observations are put in the context of previous work and are used to develop hypotheses to explain the underlying processes driving the observations. Chapter 7 summarizes and concludes the research presented and briefly discusses future work.

Chapter 2

Literature Review

2.1 Tornadogenesis

It has been surmised that tornadogenesis results when near-surface convergence acts on existing vertical vorticity, amplifying it to tornadic levels (e.g., Ward 1972). However, less understood is the initial development and source of vorticity close to the surface at the scale and strength observed in tornadoes (e.g., Davies-Jones 1982; Davies-Jones et al. 2001). Several theories of mechanisms that would allow for tornadic-strength vertical vorticity to reach the surface have been suggested. A dynamic pipe effect (DPE) acting on strong rotation above the surface is one proposed mechanism. In a DPE, rotationally-induced rising air at the lower end of a pipe-like vortex in cyclostrophic balance is associated with radial convergence, which acts to enhance vertical vorticity until a new level of cyclostrophic balance is reached at the bottom end of the vortex (Leslie 1971). The process may continue until a vortex reaches the surface (Smith and Leslie 1978).

Circumstantial observational evidence of a DPE was presented in the case of the 24 May 1973 Union City tornado, in which 25 min. prior to tornadogenesis, strong radial wind shear was identified in adjacent azimuths, a feature that was named a tornadic vortex signature (TVS; Burgess et al. 1975). Subsequent observations confirmed that the TVS is a spatially-aliased representation of a tornado (e.g., Brown and Lemon 1976; Wilson et al. 1980; Dunn 1990; Burgess et al. 1993). In the Union

City tornado, the TVS was identified first at midlevels; it built downward with time, reaching close to the surface approximately coincident with the time of tornadogenesis (Fig. 2.1; Brown et al. 1978). Observations from Vasiloff (1993) and numerical simulations from Trapp and Fiedler (1995) showed that TVSs also could form uniformly over a large depth of the atmosphere or ascend, rather than descend, with time. Trapp et al. (1999) found that tornadoes were not preceded by the descending TVS signature in nearly half of their sample of 52 tornadoes (Fig. 2.2). Instead, the TVSs were detected near the surface first and built upward with time or azimuthal shear increased in the lowest levels (or even the whole depth of the storm) "almost simultaneously." WSR-88D observations of tornadogenesis in the Oklahoma City tornado on 3 May 1999, for example, showed ΔV values strengthening at the same time in the lowest ~6 km (Burgess et al. 2002). Terminal Doppler Weather Radar (TDWR) data obtained on a tornado in Salt Lake City included a TVS that built upward and intensified at the time of tornadogenesis (Dunn and Vasiloff 2001). More recent work by Alexander and Wurman (2008) and Alexander (2010) using a DOW climatology of high-resolution mobile, Doppler radar data of tornadoes found vortex signatures that formed nearly simultaneously in the lowest 2-3 km.

Trapp and Davies-Jones (1997) used numerical and analytical models to propose two different modes of tornadogenesis (Fig. 2.3). Mode I tornadogenesis involves the formation of an incipient tornado 3-4 km aloft that slowly descends to the surface, while in mode II tornadogenesis, the incipient tornado forms in the lowest levels rapidly. In addition, it was proposed that the tornadogenesis mode was dependent on the distribution of ambient vertical vorticity and radial inflow with height. The well-

established notion that mesocyclone detection is not a credible indicator of tornado formation (e.g., Burgess and Lemon 1990) coupled with the lack of a TVS prior to mode II tornadogenesis inherently makes tornado warning issuance prior to mode II tornadogenesis extremely difficult.

A number of theories have been proposed that would account for strong rotation developing very suddenly at or close to the surface, consistent with mode II tornadogenesis as described above. Nearly all of the hypothesized mechanisms require a downdraft because, in the absence of a downdraft, vertical vorticity is advected upward away from the surface (Davies-Jones 1982), and both radar observations and visual manifestations (i.e., clear slots) of downdrafts are ubiquitous in tornadic supercells (e.g., Lemon and Doswell 1979). In many early analytical and numerical models, low-level rotation was derived from baroclinically-generated horizontal vorticity in storm downdrafts that was acted on by convergence and tilted and stretched into vertical vorticity (e.g., Klemp and Rotunno 1983; Rotunno and Klemp 1985; Davies-Jones and Brooks 1993). A tornado simulated by Wicker and Wilhelmson (1995) occurred after strengthening of the low-level mesocyclone, which resulted in an upward-directed vertical pressure gradient force (VPGF) that enhanced surface convergence leading to the vortex. The main source of rotation was tilting and then stretching of baroclinic and barotropic vorticity associated with the forward flank downdraft. Grasso and Cotton (1995) simulated a strong, tornado-like vortex that formed at low levels and then built downward to the surface as it ingested vertical vorticity, possibly from downdraft air, which continually lowered the pressure in the vortex.

Markowski et al. (2003) simulated a tornado that resulted when convergence acted on high circulation air brought to the surface through a downdraft; vortex longevity and strength depended on the thermodynamic properties of the downdraft air. The results were used as a possible explanation for observations by Markowski et al. (2002) of relatively warm and buoyant rear-flank downdraft (RFD) regions in strongly tornadic supercells. Gaudet and Cotton (2006) simulated a sub-mesocyclone-scale vortex in which vorticity generation came from local horizontal vorticity advection. Conversely, in most other vortex simulations, axisymmetric horizontal convergence is necessary to increase vorticity to tornadic levels. Straka et al. (2007) reviewed several tornadic supercell cases and ran an idealized simulation to explain observations of arching vortex lines in supercells. The arching lines are proposed to form after downdraft-induced (i.e., baroclinically-generated) vortex rings are advected downward and then elongated horizontally until the front edge of the lines are advected upward by the storm updraft. The arching process produces a cyclonic-anticyclonic pair of low-level vortices in which the cyclonic vortex is hypothesized to be the tornado cyclone (Fig 2.4).

Experiments by Walko (1993) produced a vortex barotropically, rather than baroclinically, once an RFD was established using a heat source and sink. Davies-Jones (2008) proposed a method in which vorticity was generated at low levels barotropically through descending rain curtains in a supercell hook echo. Using an analytical model and large eddy simulations, Lewellen and Lewellen (2007a) argued that a process they call corner flow collapse (CFC) can explain very strong intensification in tornadoes relative to the flow aloft. They also contended that CFC may play a role in

tornadogenesis. An important parameter in CFC and many other proposed processes related to vortex development is the swirl ratio, *S*:

$$S = \frac{v}{u} \tag{2.1}$$

where u is the radial velocity, or inflow, in the vortex and v is the tangential velocity of the vortex. Similarly, S can be thought of as the ratio of vortex circulation to low-level inflow or the ratio of tangential velocity to vertical velocity. CFC generally occurs in simulations with nested scales of motion: a larger-scale vortex with high swirl ratio and a simultaneous low swirl ratio at the corner flow (the corner flow is the location where the surface or near-surface inflow of a vortex turns into a vertical jet of rising air). Once the low-level, low-swirl inflow is impeded (e.g., from RFD outflow wrapping around the primary storm updraft), rapid vortex intensification takes place. It was suggested CFC can lead to tornadogenesis with a high-swirl midlevel mesocyclone and low-swirl corner flow when a wrapping RFD cuts off low-level inflow. It was found, based on additional simulations, that the CFC process is extremely sensitive to several parameters, including analogs to the location and strength of the mesocyclone and RFD as well as the timing and completeness of RFD wrapping (Lewellen and Lewellen 2007b).

Up until the mid-1990s, most observational studies of the tornadogenesis process used data collected by the stationary 10-cm wavelength (S-band) Doppler radar network. Several studies investigated tornadogenesis using dual-Doppler analyses (DDA) from data obtained when tornadic supercells passed through a stationary network of S-band radars located in Norman and Cimarron, Oklahoma and used by the National Severe Storms Laboratory (e.g., Brandes 1977b; 1978; 1981; 1984a;

Heymsfield 1978; Ray et al. 1981). The above observational studies identified strengthening low-level mesocyclones, RFD development, increased low-level convergence, and strong vorticity stretching at low levels prior to and at the time of tornadogenesis. Brandes (1984b) performed thermodynamic retrievals using the same datasets and found, at the time of tornadogenesis, that pressure in the low-level mesocyclone increased. The weakening mesocyclone may have decreased the upward VPGF and possibly caused the observed RFD and, ultimately, the demise of the mesocyclone. Dowell and Bluestein (1997) studied tornadogenesis using DDA with similar results to previous tornadogenesis cases, but coupled the analyses with data from an instrumented tower that sampled the storm environment. Preceding the tornado, RFD development coincided with increased convergence and strengthening of the low-level mesocyclone. Data from the tower were used to calculate low-level vertical wind shear, horizontal streamwise vorticity (Davies-Jones 1984), and updraft speeds, all of which were larger than that indicated by the DDA. In general, the mean spatial and temporal resolutions of the DDA described above were ~1 km and ~5 min., respectively, thus precluding a diagnosis of processes occurring on the tornado scale.

Pseudo-dual-Doppler analyses synthesized from airborne Doppler radar data were used in several studies of tornadogenesis, many of them collected during the Verification of the Origins of Rotation in Tornadoes Experiment (VORTEX; Rasmussen et al. 1994). In examining a tornadogenesis case, Wakimoto and Liu (1998) proposed that tornadogenesis occurred within one of several vorticity centers that resulted when the storm's low-level mesocyclone underwent a vortex-breakdown-like process following the formation of a central downdraft. Trapp (2000) later challenged

the idea that the conditions necessary for vortex breakdown could occur in mesocyclones, though Lewellen and Lewellen (2007a) argued that a high-swirl mesocyclone in which the high-swirl air had not yet reached the surface could undergo a vortex breakdown. In observations of a tornado near Dimmitt, Texas, an increase in ΔV could be seen after the storm crossed a boundary. The increase occurred first at ~2-3 km AGL and then progressed upward and downward from there near the time of tornadogenesis (Rasmussen et al. 2000).

Dowell and Bluestein (2002a,b) used pseudo-dual-Doppler data from another VORTEX case to study tornadogenesis, though the primary focus was on the cycling process within a family of observed tornadoes. Once a tornado formed, tilting of cyclonic vertical vorticity (on a spatial scale larger than that of a tornado) occurred along gust front bulges; vorticity generation then increased through vorticity stretching. Advection by storm-relative inflow winds brought the vortex to the upstream side of the updraft, an area favorable for vorticity production, where it intensified to tornado strength. The focus of work by Ziegler et al. (2001) was not on the tornadogenesis process, but rather the development of rotation on the mesocyclone scale. Regardless, it was found that tornadogenesis occurred after a notable increase in vertical vorticity stretching. Wakimoto and Atkins (1996) looked at the same case as Ziegler et al. (2001), but used photogrammetric analysis and single-Doppler WSR-88D data. They argued that the tornadogenesis process resulted when a low-level shear feature became collocated with a flanking line updraft. Spatial resolutions for airborne Doppler radar studies were typically ~300-500 m with variable time resolutions of ~5-6 min. between

volumes; data below ~500 m above ground level (AGL) usually were contaminated by ground clutter and not usable.

The increased spatial and temporal resolution data provided by ground-based, mobile observing platforms provided an opportunity for more detailed observations of the tornadogenesis process to be obtained. Using the aforementioned W-band radar (with spatial resolution as fine as 15 m), tornadogenesis data were obtained near Bassett, Nebraska on 5 June 1999 (Bluestein and Pazmany 2000). Bluestein et al. (2003a) detailed the process, noting observations of several small-scale (~100 m) cyclonic vortices along the rear-flank gust front (RFGF), one of which interacted with a larger-scale (~500 m) vortex as tornadogenesis occurred. It also was suggested that a small, bowing reflectivity echo identified prior to tornadogenesis may have been associated with tornado formation through CFC if low-level inflow was impeded. Wurman et al. (2007a) used DDA performed at one level from two DOWs to study tornadoes in several merging supercells. Single-Doppler radar data from one level were used to show that two scale contractions took place during tornadogenesis while ΔVs were mostly steady and AVV increased at the one level sampled, ~3 km AGL (Fig. 2.5, left). Single-Doppler data of tornadogenesis briefly was discussed in Wurman et al. (2007b). Notable increases in AVV developed suddenly in the lowest 1 km and also in the 4-5 km layer (Fig. 2.5, right), at the time of tornadogenesis. The authors opined that the update time of the single-Doppler radar data (~60 sec.) was not sufficient to properly analyze the tornadogenesis process.

2.2 Fluctuations of Tornado Horizontal Wind Speeds

Analytical models, numerical models, and select observations have long shown evidence that the wind speeds in tornadoes can change rapidly. Observations of suction vortices from damage paths (e.g., Fujita et al. 1967, Fujita 1970) and visual sightings (e.g., Agee et al. 1975) provided circumstantial evidence of a main tornado vortex breaking down into smaller-scale sub-vortices with locally stronger wind speeds than that in the parent vortex. These multiple vortex structures in tornadoes also have been predicted by laboratory models (e.g., Ward 1972; Church et al. 1979) and computer simulations (e.g., Rotunno 1977; Lewellen et al. 1997; Fiedler 1998). As the swirl ratio increases, the structure of a vortex changes from a single-celled vortex with a central updraft to a two-celled vortex with a central downdraft; the interface between the two is where the flow goes from supercritical to subcritical, the cause of vortex breakdown (Benjamin 1962). As the swirl ratio increases more, the main vortex becomes unstable (e.g., Gall 1983; Walko and Gall 1984) and multiple vortices, which can significantly modulate the flow over short time scales, also are observed (Fig. 2.6). Visual observations of vortex breakdown in tornadoes exist (e.g., Hoecker 1960; Pauley and Snow 1988) but are rare, while visual observations of tornado multiple vortices are common (e.g., Zrnic 1985; Bluestein and Pazmany 2000). Otherwise, the results of simulations and analytical models often use time-averaged variables to study vortex dynamics, so that investigations of short-time-scale changes in the wind field are not a focus of the analyses.

Prior to the use of ground-based, mobile Doppler radar systems, very few observing platforms afforded the spatial and temporal resolutions necessary not only to observe radial wind speeds in tornadoes, but also to track short-time-scale (~10 sec.)

changes in tornadic wind speeds. Recently, a stationary S-band, agile-beam, phased-array radar, the National Weather Radar Testbed Phased Array Radar (NWRT PAR; Zrnic et al. 2007) has been used to scan tornadoes using volumetric update times as fast as ~30 sec., though no in-depth analyses of tornado data yet exist. A rapidly-updating mobile, X-band Doppler radar (Rapid DOW; Wurman and Randall 2001) uses a multiple frequency approach to scan several elevation angles simultaneously as the radar scans mechanically in azimuth. Thus far, only preliminary results have been presented (e.g., Wurman et al. 2008). If conventional-scanning, mobile Doppler radar systems are to achieve update times of ~10 sec., data collection must occur only at a limited number of elevation angles. Mobile systems use update times of ~100 sec. when scanning volumetrically, so smaller-scale temporal changes in tornado intensity can *begin* to be resolved. Most of the observations of short-time-scale fluctuations in tornado wind speeds have come from the DOW radars; their contributions are summarized below.

In one of the first tornadoes observed by a DOW radar, the Dimmitt tornado was revealed to have ΔVs and AVV that slowly dropped off with time as the tornado dissipated, particularly at ~1 km AGL (Wurman and Gill 2000). DDA were synthesized every ~13 sec. at one height level for ~40 sec. for a tornado near Kiefer, Oklahoma. The short amount of time covered in the DDA prevented a detailed look at the evolution of the wind field, but the lack of change in the wind field during this time period was used as evidence that the DDA were qualitatively correct. Single-Doppler data of a subsequent tornado again were obtained only at one level with update times of ~18 sec. Radial velocities were relatively steady during tornadogenesis, though they increased

notably at the time a tornado became apparent. As the tornado dissipated, radial velocities dropped off sharply and ΔVs dropped from 40 m s^{-1} to 20 m s^{-1} in less than one min. (Wurman et al. 2007a). In a climatology of tornadoes observed by DOW radars, typical (maximum) accelerations/decelerations of ground-relative velocity were ± 1 (4) m s^{-2}; typical and maximum changes in ΔV were nearly identical to that of ground-relative velocity (Alexander 2010).

Examination of several additional studies found small-time-scale changes in wind speeds likely caused by multiple vortices. DOW-observed radial velocities were compared to F-scale classifications from a damage survey of the 3 May 1999 Oklahoma City tornado and the two sets of data were found to be well correlated. However, there were several times when relatively large changes in ΔV (~20 m s^{-1}) occurred over the time it took to complete a volume scan (~80 sec.), though these changes were not resolved in the WSR-88D data (Burgess et al. 2002). On that same day, a violent tornado that passed near Mulhall, Oklahoma also was sampled by a DOW radar. The radar's high spatial resolution combined with the unusually large diameter of the core flow (as large as 1.75 km) allowed for low-level, multiple vortices in the flow to be resolved. The multiple vortices often were intense with radial velocities surpassing 100 m s^{-1} and ΔVs of 100 m s^{-1} over short distances (< 100 m), implying AVVs of 5 s^{-1} or greater. The multiple vortices rotated cyclonically around the main circulation and were strong enough to alter the winds in the main tornadic circulation. Different parts of the tornado had significantly different velocities between the 6 sec. scans, though successive observations were taken at different heights (Wurman 2002). A more thorough examination of the tornado was undertaken using ground-based velocity track

display (GBVTD; Lee et al. 1999) analysis, in which unobserved winds are inferred in an assumed axisymmetric vortex through Fourier decomposition. It was found that tornado intensity varied with a seven minute period over the ~13 min. the tornado was analyzed (Lee and Wurman 2005).

In a violent tornado that passed through Spencer, South Dakota, modulations in low-level ΔVs of 20-30 m s^{-1} were observed with ~2 min. periods (Fig. 2.7). Though multiple vortices were not directly observed, they were inferred from the sudden changes in ΔV and corresponding reflectivity minima (Alexander and Wurman 2005). It was suggested the much stronger wind speeds inferred close to the surface might have resulted from vortex interaction with the surface (Wurman and Alexander 2005). In a GBVTD analysis of the same Spencer tornado, calculated swirl ratios greater than 1 and axisymmetric tangential velocities less than the observed radial velocities provided further circumstantial evidence of the importance of multiple vortices and other asymmetries in modulating the tornadic flow (Kosiba and Wurman 2010). Evidence of multiple vortices also has been presented in other DOW analyses (e.g., Marquis et al. 2008).

In addition, there are a few W-band radar datasets with high-temporal-resolution data that were obtained by scanning only at one elevation angle. In the Bassett, Nebraska tornado, ΔV fluctuations as high as 10-15 m s^{-1} were observed over a ~15 sec. period (Bluestein et al. 2003b). Multiple vortices also have been observed with the W-band radar (e.g., Bluestein and Pazmany 2000).

2.3 Vertical Profile of Tornado Horizontal Wind Speeds

Conceptual and computer models have shown that peak tornado wind speeds should occur in the surface layer of a tornado (the lowest ~50 m AGL), where there is strong radial inflow, and decrease upward from there (e.g., Lewellen 1997). The vertical distribution of horizontal wind speeds also is affected by the vortex structure (one-celled vs. two-celled), especially at and near the location of any vortex breakdown, where wind speeds are thought to be locally higher (e.g., Fiedler and Rotunno 1986).

Outside a few studies that obtained data in tornadoes viewable in a range-height indicator (RHI) display, observations of the vertical structure of tornadoes are analyzed by comparing data obtained at different elevation angles at slightly different times and/or by constructing vertical cross sections of data employing a steady state assumption. In the Dimmitt tornado, Wurman and Gill (2000) found that AVV and ΔV typically decreased with height, maximum ΔVs were consistently in the lowest 250 m AGL, and ΔV decreased at all levels but was greatest closer to 1 km as the tornado dissipated. In one of the 3 May 1999 tornadoes, ΔV dropped off significantly with height above 1.5 km and changes in ΔV tended to occur at all levels at similar times (Burgess et al. 2002). In the Mulhall tornado from the same day, ΔVs in multiple vortices decreased with height and increased in radii in the lowest 1.5 km (Wurman 2002). As mentioned previously, Wurman et al. (2007b) found AVV that was strong at the surface and above 4 km (due to a tighter circulation) with lower values in between after tornadogenesis (Fig. 2.5, right). Circulation also was calculated at around the same time and was found to decrease with height between ~50 m and 2 km AGL; the magnitude and vertical evolution were in agreement with numerical simulations of circulation around a tornado (e.g., Wicker and Wilhelmson 1995). A tornado also has

been observed to have different scales of rotation with height in the lowest 2 km AGL (Marquis et al. 2008). In a large sample of observations from DOW tornadoes, a statistically significant decrease in ΔV in the lowest 10 km was observed. However, little to no change in ΔV with height was discovered in observations from the lowest 500 m, 100 m, 50 m, 20 m, and 10 m. In addition, ΔVs were ~70% of the value of the maximum ΔV for each tornado with little change in height (Alexander 2010).

Only occasionally have RHIs through a tornado been taken to gain a look at radial velocity variations with height at one time. In the Spencer tornado, both RHIs and PPIs were obtained from as far away as 12 km, so volumetric scanning sampled as high as 5 km AGL. Both ΔV and AVV were found to be most intense and most variable in the lowest 200 m AGL (Fig. 2.7). As the tornado passed through Spencer, the strongest wind speeds decreased dramatically above the lowest observed level (~50 m AGL) and then stayed approximately constant up to ~1 km. In addition, during a tornado that occurred prior to the Spencer tornado, ΔV increased in the lowest 5 km at roughly the same time at multiple heights (Alexander and Wurman 2005). In RHIs made by the W-band radar through a tornado in Happy, Texas, an area of enhanced radial velocities could be identified ~300 m AGL just outside of the tornado (Bluestein et al. 2004b). RHIs with the W-band radar also were taken in a tornado in Attica, Kansas. Increases in Doppler radial wind speeds as large as 25 (15) m s^{-1} in the lowest ~20 (25) m AGL outside (inside) of the tornado core flow were observed (Bluestein et al. 2007a).

2.4 Vertical Orientation of Tornadoes

Visual observations of tornado tilting in the sub-cloud layer are ubiquitous, particularly as a tornado nears the end of its life cycle, in the "rope" stage (e.g., Golden and Purcell 1977,1978; Moller 1978; Wakimoto and Martner 1992). Occasionally, photogrammetric analysis has been used to estimate the wind field coincident with a tilting tornado. For example, Golden and Purcell (1977) used photogrammetric analysis to speculate that varying tornado tilt with height caused unsteady results in retrieved vertical velocities during a tornado's decay phase. By combining single- and dual-Doppler radar data with photographs of a tornado, Wakimoto and Martner (1992) observed a tornado that tilted increasingly northeastward with height in the sub-cloud layer as it dissipated, presumably from surface outflow that was pushing it in a direction different to that of the parent mesocyclone (Fig. 2.8). Naturally, determining the tilt of a vortex above the cloud layer requires additional information from remote sensing platforms.

Wurman and Gill (2000) found disparate motion of the Dimmitt tornado with height, which led to time-varying tornado tilt. Close to the surface, tornado motion deviated from northward to northwestward for one scan, while vortex motion at ~1 km was consistently northward; tornado tilt was toward the west (with increasing height) until the vortex's northwest jog near the surface, after which the tilt became northeast, implying faster tornado motion at 1 km. In a GBVTD analysis of the Mulhall tornado, it was found that the tornado varied from having almost no tilt to tilting 25° toward the north-northwest. The observed tornado tilt was equivalent to horizontal displacements of close to 500 m between 50 m and ~1 km AGL (Lee and Wurman 2005). All of the above studies had to account for the time passed between successive PPI scans and

corrected the scans to a central time by estimating vortex motion over the course of a volume scan.

In RHIs taken through the Spencer tornado over a 3 min. period, a tornado incline of ~20° toward the north was observed; surging RFD outflow was suggested as a possible reason for vortex tilting (Alexander and Wurman 2005). RHIs through tornadoes by Bluestein et al. (2004b; 2007a) were taken from an unleveled truck through a tornado moving with a component normal to the radar. As a result, tornado tilt in the sub-cloud layer could not be determined accurately. Alexander (2010) found that DOW-observed tornadoes generally had inclination angles (i.e., tilt from the vertical) of 20-60° (< 10°) in the lowest 10 km (500 m) AGL. A directional tendency of tilt was not provided.

2.5 Tornado Dissipation

Observational and numerical modeling studies of tornado occlusion and dissipation have found that tornado decay occurs after cool, relatively stable RFD air wraps around the tornado, cutting off the moist, buoyant inflow air and vertical vorticity source necessary to maintain the vortex (e.g., Lemon and Doswell 1979; Brandes 1981; Wicker and Wilhelmson 1995; Wurman et al. 2007a; Wurman et al. 2010). Other processes, such as potentially cool RFDs (Markowski et al. 2002) and increasing tornado displacement from beneath the main storm updraft (Dowell and Bluestein 2002a) also have been hypothesized as leading to tornado demise. Marquis et al. (2012) examined four DOW tornado cases to determine predominant tornado maintenance

mechanisms. They hypothesized that changes in the magnitude of storm rear-flank downdrafts (strengthening or weakening) and increasing tornado proximity from areas of convergence along RFGFs (primary or secondary) are the factors most responsible for ending tornado maintenance.

Most radar observations lack the temporal resolution to capture the time-height evolution of vortex decay. Early analysis of TVSs associated with tornadoes found TVSs that dissipated at all heights at roughly the same time (Fig. 2.1; Brown et al. 1978; Vasiloff 1993). Burgess et al. (2002) show a WSR-88D time-height ΔV plot of the tornado cyclone associated with one of the 3 May 1999 tornadoes. The TVS weakens first at ~2.5 km AGL prior to dissipation, however the authors do not discuss this observed evolution. Wurman and Gill (2000) did not have DOW observations of the dissipation process in the Dimmitt tornado, but noted weakening ΔV just prior to dissipation that was more pronounced at ~1 km than that observed near the surface. In many other radar analyses of tornadoes, data collection either ended before tornado dissipation (e.g., Dowell and Bluestein 2002b; Wurman 2002) or there was insufficient radar vertical-temporal sampling to assess how the tornado dissipated in height (e.g., Dunn and Vasiloff 2001; Alexander and Wurman 2005, Bluestein et al. 2007; Wurman et al. 2010).

Chapter 3

Research Objectives

3.1 Motivation

A review of past research of observations of mesocyclone tornadoes provides evidence of some shortcomings. Tornadoes have significant vertical variations in space and they can evolve over short time scales. Tornadoes form quickly, have been observed throughout the depth of storms, and can undergo rapid changes in strength. Observations of the gross 3-D structure of tornadoes *or* rapid changes that occur in tornadoes are plentiful in the literature. However, virtually all studies of tornadoes utilize platforms that cannot obtain volumetric data with update times that are commensurate with the short-time scales over which they are known to evolve.

The focus of most recent studies is on better identification of tornadoes or features within tornadoes using high-spatial-resolution observations. However, if one is interested in tornado processes or tornado evolution, then increased temporal resolution is necessary. Volumetric updates from the WSR-88D network occur every ~250-300 sec. and most ground-based (airborne), mobile Doppler radar systems have volumetric update times of ~100 (300) sec. In addition, the methods usually employed to study the volumetric evolution of tornadoes, vertical cross sections and RHIs constructed from PPIs at different times, necessitate use of space-to-time conversions to correct the time-height calculations. As a result, not only are the volumetric update times not sufficient for observing small-time-scale processes in tornadoes, but the assumptions in even

creating a volumetric picture of tornadoes likely are dubious in many situations. In other words, *a lack of volumetric observations of tornadoes with update times sufficiently small enough to examine short-time-scale processes represents a major shortcoming in severe storms observational research.*

The main research objective of this doctoral work is to investigate tornadoes for *short-time-scale, volumetric processes* that are occurring. The objectives are reached by using data obtained by a unique, ground-based, observing platform: the first storm-scale, mobile, PAR used in severe storms research. This system, discussed at length in Chapter 4.1, obtained volumetric datasets of tornadoes utilizing volumetric update times of ~10 sec. As a result, *in situations where TVSs are sufficiently spatially resolved*, processes affecting the volumetric evolution of tornadoes can be investigated. Below, specific research questions that this doctoral work is aiming to address are motivated.

3.2 Research Questions

3.2.1 Question 1: Tornadogenesis

What is the vertical evolution of vertical vorticity (or vertical vorticity proxies) prior to, at, and after tornadogenesis? What can be said about the tornadogenesis process?

A review of the literature regarding observations of tornadogenesis shows that very little work has been done in determining the vertical evolution of vertical vorticity in mode II tornadogenesis cases over time scales in which tornadogenesis is thought to occur (~10 sec.). The vertical development of rotation in the mode II paradigm is not

well understood. As a result, any volumetric observations of the development of shear at the tornadogenesis time-scale in the mode II paradigm may significantly increase our knowledge of the development of rotation in tornadoes. In addition, it is suggested here that frequent observations of rotation development "simultaneously" in the low levels or through the depth of a storm in some mode II tornadogenesis cases do not result from physical processes that produce vertical vorticity over such depths simultaneously. Rather, the observing platforms used in the above studies cannot temporally resolve the volumetric evolution of vertical vorticity production inherent in the tornadogenesis process.

As the spatial and temporal resolutions of radar platforms have increased, the frequency of observations of mode I tornadogenesis has decreased (e.g., Alexander 2010). The decrease may be the result of a relatively low sample of tornadogenesis cases, insufficient storm sampling at storm mid and upper levels, or an indication that observations of mode I tornadogenesis are the result of shortcomings in previous observing platforms used to sample the tornadogenesis process. Observational data utilizing volumetric, ~10 sec. updates of mode I tornadogenesis or vertically-simultaneous low-level rotation development in mode II tornadogenesis would establish with more credibility that these observations are the result of real processes and not artifacts of insufficient storm sampling. However, considering that this work is not a climatology (see Chapter 6), the inability to make such observations does not necessarily imply that mode I tornadogenesis or vertically-simultaneous low-level rotation development in mode II tornadogenesis are not occurring.

The summary in Chapter 2.1 of several proposed sources of vertical vorticity production close to the surface illustrates well that the origin of low-level rotation is a topic worthy of study. Data from the MWR-05XP cannot be used to test the specific tornadogenesis hypotheses discussed in Chapter 2.1, such as CFC, because the radar cannot spatially resolve details of tornado-scale rotation. Rather, the focus here is on slightly larger spatial scales, including that of the tornado cyclone and bulk features of TVSs.

As mentioned above, volumetric observations of the evolution of radial velocities and quantities derived from radial velocity (ΔV) every ~10 sec. can be used to assess the development of rotation on multiple scales. Of particular interest is the interplay between both the low- and midlevel mesocyclone and the tornado just prior to and at the time of mode II tornadogenesis. Sudden changes in the strength of the mesocyclone have been shown to be important in numerical modeling studies of tornadogenesis (e.g., Wicker and Wilhelmson 1995). Data obtained by the WSR-88D network and airborne, mobile Doppler radars do not have the temporal resolution to investigate changes in mesocyclone strength commensurate with the time scale of the tornadogenesis process. High resolution, mobile, Doppler radar data also have shown a link between short-time-scale changes in the strength of the mesocyclone, scale contractions, and tornado formation, but only at one level (Wurman et al. 2007a). Wurman et al. (2008), using Rapid-DOW data, observed a scale contraction that occurred simultaneously at 6 elevation angles during the formation of a tornado near Jayton, Texas. In a DOW climatology of tornado observations, five cases were identified in which data were obtained both prior to tornadogenesis and above 2 km. All

five cases were found to undergo a scale contraction within a few minutes in the lowest 2 km almost simultaneously (Alexander 2010). A high-temporal resolution, volumetric survey of the mesocyclone and scale contractions during the tornadogenesis process has not yet been undertaken, but is necessary to establish the relative importance of the relationship between the mesocyclone and the developing tornado.

3.2.2 Question 2: Tornado Horizontal Wind Speeds

Are rapid fluctuations in tornado wind speeds common? If so, a. what is the frequency and magnitude of the fluctuations, b. are they well correlated in height, and c. what is causing them?

Almost all previous observations of rapid fluctuations in tornado wind speeds point to multiple vortices as the cause. The observed fluctuations tended to occur in very large tornadoes over relatively long time scales (as long as 120 sec.). Outside of tornadoes containing multiple vortices, observations of short-time-scale fluctuations of tornado wind speeds in the literature are relatively rare. The lack of observations of rapid fluctuations in tornado wind speeds may result from having very few studies that focused on ~10 sec. updates (those studies that did only examined one level). Another possibility is that multiple vortices are the main cause of small-time-scale changes in tornado wind speeds. Therefore, tornadoes with larger core flows, which are more likely to have multiple vortices, also are more likely to have observed rapid fluctuations in wind speeds. In other words, *tornadoes with smaller core flows and without multiple vortices reach periods in which their wind speeds are approximately steady state during their mature phase.* In this proposed scenario, external factors such as changes in the

tornado's environmental inflow air or tornado occlusion lead to wind speed fluctuations, but the fluctuations are not sudden and instead are relatively slow and linear. The increased temporal resolution of the data used in this study will provide an opportunity to examine the short-time-scale changes in tornado wind speeds over relatively long periods of time and at more than one height.

In the case that rapid fluctuations in tornado wind speeds are observed, whether from multiple vortices or not, of deep interest is the vertical extent of the fluctuations. Previous observations of wind speeds in tornadoes either examined a few select levels using PPIs or used single RHIs that could not characterize the entire quasi-horizontal radial wind field. As a result, it is unknown whether fluctuations in tornado wind speeds are correlated in height or not, and if so, if the fluctuations with height can be tracked. If rapid changes in tornado wind speeds can be tracked vertically, their evolution may be used to deduce something about their cause. For instance, a tornado that is ingesting environmental air that is suddenly less conducive to tornado-scale rotation would first weaken at low levels where the air is ingested and then upward with time from there. If fluctuations only occur at midlevels or occur first higher up in the tornado and proceed upward or downward with time from there, the fluctuations are more likely to result from dynamical changes internal to the tornado (e.g., vortex breakdown). Naturally, there are exceptions to these general ideas, as, for example, dynamical changes in tornadoes certainly can occur and impact wind speeds in the low levels. Regardless, through high-temporal resolution, volumetric sampling, it may be possible not only to sample rapid fluctuations in tornado wind speeds at multiple heights, but also to gain an understanding of how fluctuations progress in time and height. Neither of these

potentially important subjects are well represented in the body of current scientific tornado research.

3.2.3 Question 3: Volumetric Tornado Observations

What is the vertical distribution of quasi-horizontal wind speeds in tornadoes? What is the vertical orientation of tornadoes? Is there vertical directionality to the tornado decay process?

Mobile, Doppler radar observations of tornadoes have focused almost exclusively on wind speeds and tornado orientation in the lowest 2 km AGL. The focus on low levels likely is driven by the fact that a tornado's greatest impact is at the surface where it is doing damage and often undergoing important dynamical changes, particularly during tornadogenesis and periods of intensification. However, other than consistent observations of wind speeds decreasing above the surface layer in tornadoes, very little is known about the vertical profile of wind speeds in tornadoes. Of interest is the possibility that there are consistent anomalies of time-averaged wind speeds at different levels in tornadoes. Another possibility is that wind speeds in tornadoes tend to vary smoothly with height above the surface, to the point where firm relationships can be established between wind speeds at different heights up through and including midlevels. The distribution of wind speeds with height also may change predictably at different periods in a tornado's life cycle. In turn, these changes eventually may be used as short-time-scale predictors of tornado evolution. It is hoped that rapid-scan, volumetric data of tornadoes can be used to learn about and establish typical profiles of the height evolution of horizontal winds in tornadoes.

Tornado orientation, particularly in the cloud layer, is a subject that has received very little attention in the literature. In general, there are two things known about tornado orientation: tornadoes tend to become more tilted in the sub-cloud layer as they enter their decay phase and observations have shown a general tornado tilt in the Northern Hemisphere toward the north with height in the lowest ~2 km AGL. While it is generally accepted that tornadoes tilt with height, presumably from the influence of vertical wind shear, virtually nothing has been documented about the vertical orientation of tornadoes in the cloud layer or, perhaps more importantly, how tornado orientation changes in time. It stands to reason that the tilt of a tornado in the cloud layer may indicate something about features internal to the tornado and/or characteristics of the environment that the tornado is located in in such a way that the latter impacts the former. For example, previous studies have suggested that the storm-relative flow a tornado/mesocyclone is embedded in is important in the cyclic tornadogenesis/mesocyclogenesis process (Dowell and Bluestein 2002b; French et al. 2008). It stands to reason that vertical changes in the environmental flow lead to height-varying effects on the tornado, which impact a tornado's tilt. As with the ΔV vertical profiles discussed above, it is unknown whether tornado tilt into storm midlevels can be used as a predictor of measurable changes in tornado strength (e.g., tornado dissipation). Investigation of volumetric data obtained at least up to midlevels (~3-5 km AGL) in tornadoes provides the opportunity to establish such relationships if they exist.

Tornado decay is another topic in which volumetric observations are rare. MWR-05XP data of the tornado decay process are studied here to learn whether tornadoes dissipate from the bottom-upward, top-downward, simultaneously at several

levels, or in some other manner. It is likely that previous volumetric observations of tornadoes could not be used to assess how TVS signatures dissipated in height because the observations lacked the appropriate time-height resolution. Also it is well known that tornadoes tend to become tilted in the dissipation stage, but not known is if the degree of tornado tilt is related to the height where a tornado first decays. Pinpointing how tornadoes dissipate in height could have important implications for real-time tornado forecasting in the future if a network of radars utilizing relatively fast (< 30 s) volumetric updates becomes a reality.

Chapter 4

Data

4.1 MWR-05XP

4.1.1 MWR-05XP Operations

The objectives outlined in Chapter 3.2 will be achieved by using data obtained by a new tool used in severe storms research, the MWR-05XP (Fig. 4.1). Much of the information about the radar system below is a summary of discussions that appear in Bluestein et al. (2010) and PopStefanija et al. (2005). The MWR-05XP is a PAR that can scan electronically in elevation and, to a limited degree, in azimuth as it rotates in azimuth like a conventional ground-based, mobile, Doppler radar system. The transmitter is a traveling wave tube amplifier and the radar antenna is a converted military radar antenna previously used for air defense by the United States Army. Following that, the antenna was given to the Naval Postgraduate School (NPS) to conduct scientific research. ProSensing, Inc. modified the radar for meteorological applications. A large part of the modification was the development of a weather radar processor. Benefits of the updated processor include improved control of radar parameters and the implementation of a new data acquisition and signal processing system.

The MWR-05XP utilizes a hybrid antenna with electronic scanning in elevation and both electronic and mechanical scanning in azimuth. Electronic scanning in elevation is achieved differently from electronic scanning in azimuth. Phase shifters are

used to alter the phase delay of the antenna elements to electronically scan in elevation. The number of waveguide elements is classified information, but the elements are stacked vertically and aligned horizontally. Frequency hopping, changing the frequency of the emitted beams to change the phase, is used to scan electronically in azimuth, though this can only be done over a limited sector of ~6-8°. The antenna also can scan mechanically in azimuth through use of a DC motor. The speed of mechanical scanning can be altered, but scanning rates as high as 180° s^{-1} can be reached, a value much higher than that of most mechanically-scanning mobile Doppler radars. Frequency hopping is used to obtain a sufficient number of independent samples and mitigate beam smearing while maintaining high scanning rates. Frequency hopping occurs with every other radar pulse, so pulse pairs use the same frequency in determining Doppler velocity estimates. The frequencies utilized in the frequency hopping process are separated by $1/\tau$ at a minimum, where τ is the pulse duration. The $1/\tau$ separation leads to statistically independent samples for radar distributed targets. In order to give the radar system enough time to collect independent samples at each azimuth, the system utilizes back scanning, in which the antenna electronically scans in the opposite direction of its mechanical scanning in azimuth. Between 10-32 independent samples were obtained for datasets collected using frequency hopping in 2009 and 2010.

Estimates of Doppler velocity are made using pulse-pairs. As is typical, errors in velocity estimates are introduced through ground clutter and bimodal velocity spectra. Velocity spectra are not computed using a fast Fourier transform (FFT) algorithm for two reasons. First, the main advantage of the radar system is its fast volumetric update time, which would be reduced by using a FFT algorithm. Second, the FFT algorithm

cannot be used in a radar system that utilizes frequency agility, which allows for frequency hopping, an important and unique aspect of the radar's data collection process. The downside of not utilizing a FFT algorithm is that spectra cannot be computed, so features like automatic ground clutter removal algorithms cannot be implemented easily. In practice, ground clutter was not overly problematic in datasets collected from 2008-2010 since the use of optimal deployment sites (few obstructions and a level surface) was emphasized in the field. However, there are some datasets where ground clutter rendered data from the lowest one or two elevation angles unusable. The variance of velocity estimates is lower for a larger number of independent samples and a higher signal-to-noise ratio. Examples provided in Bluestein et al. (2010) using standard MWR-05XP parameter values yielded velocity errors ranging from 0.2 to 2.5 m s^{-1}. Radar moment data provided by ProSensing, Inc. included only radar reflectivity factor and radial velocity. Other moments, such as spectral width, and potentially useful fields, such as signal-to-noise ratio, were not provided. Velocity errors are a concern with this system because of the lack of a ground clutter removal algorithm and the relatively coarse spatial resolution of the radar beam; one resolution volume could contain the horizontal extent of a small tornado at even relatively close ranges.

4.1.2 MWR-05XP Parameters

Several common radar parameters for the MWR-05XP appear in Table 4.1. As mentioned previously, the radar operates at X band, and the center frequency that it uses can be adjusted. From 2007-2009, a radar center frequency near 9.5 GHz was used. In

2010, the frequency was changed to ~9.99 GHz to prevent interference from other X-band radars being used in the second VORTEX (VORTEX2; Wurman et al. 2011). The peak maximum power is ~15-25 kW, a value that is smaller than that of other ground-based, mobile, radar systems. The pulse duration (τ) is ~1 μs, so range resolution is 150 m, typically oversampled by a factor of 2. The half power beamwidth is 1.8° in azimuth and 2.0° in elevation, and the typical sampling interval in azimuth (elevation) is ~1.4° (1.5°). The mechanical motor steering the antenna only does so in azimuth, but electronic scanning in elevation angle can reach as high as 55° and even go below the horizon of the radar. In 2009 and 2010, in cases when the MWR-05XP was at a relatively high elevation and the weather target was at a relatively low elevation, sampling as low as -2° was instituted. The pulse repetition frequency (PRF) can be varied within deployments, but typically is 2500-5000 Hz. Common maximum unambiguous ranges are 30, 45, or 60 km and Nyquist velocities are usually 20-35 m s^{-1}. There are not many examples of range-folding in data obtained from 2008-2010, but velocity aliasing is a common problem. Utilizing a staggered PRF algorithm to increase the Nyquist velocity would be ideal, but increasing the volumetric update time of the MWR-05XP is antithetical to the goals of this project.

4.1.3 MWR-05XP Truck

After the MWR-05XP was converted to a weather radar, the antenna was mounted on a large truck. The antenna was placed on a platform that can be raised and lowered mechanically (Fig. 4.1). The platform allows the radar to scan over relatively short (tall) obstructions close to (far from) the radar truck, thus increasing the number of

potential deployment sites. An on-board generator is used to power the radar system. The truck has manual levelers, but they are sufficient only for stabilizing the truck's frame and are not designed to precisely level the radar antenna. A digital inclinometer, installed in 2009, is used to calculate the heading, roll, and pitch angles of the radar to within 0.1°. Unfortunately, the digital inclinometer was not functioning for datasets obtained in 2009-2010. The truck also has a waterproof cabin containing a computer system for real-time data viewing, data storage, a cooling system, and room to seat 2-3 people. The real-time data display shows reflectivity and radial velocity, but these fields are calculated using fewer independent samples than in processed data because of the large amount of data being acquired in a short amount of time. The front of the truck can fit 2-3 people, including the driver, and contains a built-in, on-board navigation system to help identify locations suitable for deployment. The navigation system is a dual-antenna GPS system. Heading accuracy is ~0.3° and position accuracy is within 60 cm 95% of the time.

4.1.4 System Strengths and Weaknesses

Unquestionably, the greatest strength of the MWR-05XP is its ability to collect volumetric, rapid updates of weather targets with a sufficient number of independent samples. Using a modified version of Eqn. 1.1, a radar time scale can be calculated; utilizing updates faster than the radar time scale no longer adds useful information about the feature in question. At a range of 10 km, the azimuthal spatial resolution of the MWR-05XP is ~250 m. Assuming that typical sampled velocities for a tornado are 65 m s^{-1}, the minimum radar time scale is ~5 sec. For the datasets that have been

examined for this doctoral work, *volumetric* update times are O(10 s) for elevation-angle ranges of either 1-20° or 1-40°, which typically represents layers 3-25 km thick. MWR-05XP volumetric update times are at least an order of magnitude finer than all other mobile, Doppler weather radars except for the Rapid-DOW system and the new Rapid X-Pol (RaXPol; Pazmany and Bluestein 2011) mobile Doppler radar.

The spatial resolution of the MWR-05XP is coarse compared to other Doppler, weather radars, fixed or mobile, and is one of the radar's weaknesses. At ranges of 10, 20, and 30 km, resolution volumes are approximately 150 m x 315 m x 350 m, 150 m x 630 m x 700 m, and 150 m x 940 m x 1045 m not factoring in oversampling. For comparison, another mobile, Doppler, X-band weather radar, the University of Massachusetts X-band, Polarimetric radar (UMass X-Pol; Kramar et al. 2005), has a resolution volume at a range of 10 km of 150 m x 220 m x 220 m. Oversampling in azimuth has been shown to improve vortex detection (e.g., Wood et al. 2001), and is used in data collection, but not to the degree that it negatively affects the volumetric update time of the radar system. The coarse spatial resolution of the radar also means attempting to obtain volumetric update times faster than the ~5 sec. radar time scale likely will not result in more useful tornado data. A detailed discussion about spatial resolution issues is provided in Chapter 4.3. Other system weaknesses, including a long setup time, signal attenuation, and a lack of a precise leveling system, are covered in Chapter 4.2.

4.1.5 MWR-05XP Scanning Modes

Between 2007 and 2010, the MWR-05XP underwent several changes and upgrades. Most notably, during that time period, new scanning strategies were continually added. In 2007, all data were obtained using the stepped frequency spiral (STF-SP) mode. STF-SP mode does not utilize sector scanning or electronic scanning in elevation angle, but does use back scanning in azimuth to mitigate beam smearing. The radar scans a full 360° in azimuth for each elevation angle scanned, similar to a WSR-88D radar. Using fast antenna rotation rates, update times of ~25 sec. could be achieved scanning from 0-20° in elevation angle. After 2008, data were obtained using a version of data collection called stepped frequency elevation (STF-E) mode. In this mode, the radar conducts sector scans instead of 360° scans in azimuth. Also, electronic scanning in elevation is accomplished by transmitting a pair of radar pulses for each elevation angle, and then repeating the process ten times (i.e., two pulses at 1.0°, then two pulses at 2.5°, etc., repeated ten times); this process takes ~10 ms. Reflectivity and estimates of Doppler velocity were attained by averaging the 10 scans at each elevation angle.

In 2008, there was no frequency hopping, so to attain the dwell time necessary to gather enough independent samples and to mitigate beam smearing, the azimuthal rotation rate was decreased such that the antenna rotated ~1° during the time the 10 samples were obtained at each elevation angle. This sub-mode is referred to as sector elevation mode (SE). From 2009 onward, frequency agility was implemented and, as a result, frequency hopping was used in data collection. By using frequency hopping, between 10 and 32 independent samples are obtained for each beam in half the amount of time as possible previously. Also, beam smearing is mitigated using frequency hopping. In turn, the rotation rate of the antenna and the volumetric update time of the

radar are increased. This mode is referred to as stepped frequency elevation, sector elevation mode (STF-SE). In 2010, the MWR-05XP oversampled less in azimuth than it did in 2009, so volumetric update times were even faster.

4.2 Data Collection

In this section, specific information about the datasets under investigation is provided, including radar parameters that were used, strengths and weaknesses of the datasets, and challenges encountered during data collection. This doctoral work utilizes datasets obtained in the springs of 2008, 2009, and 2010, the latter two year during the VORTEX2 field project. The MWR-05XP also was used in 2007, but as detailed in Chapter 4.1.5, it had not yet been configured to collect rapid, volumetric updates on the order of 10 sec.

4.2.1 Data Acquisition

Data collection using the MWR-05XP presented many challenges likely not encountered with previous ground-based, mobile, Doppler radar systems. There typically were several steps that needed to be taken before the radar could begin to acquire data in severe convection. Once a target storm was chosen, a deployment spot needed to be identified. The large size and relatively slow acceleration speed of the truck along with the myriad of steps that needed to be undertaken prior to data collection were a factor in determining a location suitable for data collection from both a meteorological and safety point of view. From a safety perspective, a longer radar

setup and take-down time compared to other systems meant the radar could not get as close to tornadoes, hail, and other potentially dangerous phenomena. However, the relatively coarse spatial resolution of the MWR-05XP necessitated placement of the system close to supercells and tornadoes so that smaller-scale features could be spatially resolved. A compromise strategy was employed by attempting to place the radar in a location 20-30 km forward and to the right of the rear-flank of a supercell. Doing so provided enough time to set up the radar system because any data collected beyond 30 km typically were too coarse spatially to be useful.

Radar placement to the right of the rear flank of the supercell also emphasized relatively long deployments (at least 20 min.), letting the storm move toward and sometimes past the radar to the north. Longer deployments were emphasized for two reasons. First, the relatively long setup and take down time (described in detail below) of the radar system and the difficulty in finding suitable deployment sites made short deployments inefficient. In obtaining longer datasets, the crew often ended up south and west of eastward-moving storms with little chance to attempt additional deployments. Second, we believed that the radar's strength, its enhanced temporal resolution and ability to resolve processes that other radars cannot, was best served by collecting at least 20+ min. of continuous data (collection of data while the truck is moving is not permitted).

Deployment spots within the identified area optimally were level, free of obstructions to the path of the storm, and out of the way of traffic. The above restrictions along with the size of the truck made deployments on the shoulders of roads difficult. Deployments on side roads, usually dirt roads or hybrid dirt-paved roads, were

common. Side roads usually were wide enough such that the truck could set up in the middle of the road where it was most level and still allow cars to pass. The adjustable antenna platform increased the number of suitable locations by allowing the antenna to see over nearby power lines. In 2007 and 2008, the manual levelers on the MWR-05XP were used to level the radar with assistance from a hand-held, electronic level. It was not known by the radar crew at the time that the levelers on the truck were not strong enough to support the large amount of weight on the truck frame. The hand-held level was crude but, if there was sufficient time, it was used to adjust roll and pitch angles to ± 2°. Rarely did the hand-held level record final pitch and roll angles above 3° in 2008 datasets. This information is used to estimate reasonable upper limits on elevation angle errors in datasets obtained from sites perceived by the crew to be level. In 2009, an inclinometer recorded the pitch, roll, and bearing angles of the truck. Unfortunately, the pitch and roll data were not properly calculated or stored. In May of 2010, it was discovered that the inclinometer was not functioning properly. Therefore, there was no method to level the radar in 2010, either through a hand-held level or an inclinometer. In all three years, every attempt was made to deploy the radar on level surfaces. In addition, for most deployments in 2009 and 2010, photographs of the radar at the deployment site were taken (e.g., Fig. 4.2).

Once a deployment location was chosen, a number of steps were taken to prepare the radar for data collection. First, the manual levelers were lowered, which was done with the aid of a power drill. Note that the levelers were lowered in 2009 and 2010, but only far enough such that they stabilized the truck from the rapidly-rotating antenna. Second, the antenna was unlocked from its secure position facing downward

toward the platform (the MWR-05XP travels with the antenna locked down, away from anything that could damage it). Then, the generator was started and the radar platform raised while the computer system was booted up and the antenna was powered on. In 2010, the generator and computer were started prior to picking a deployment location to quicken the setup process. Next, a metal rod was dug into the grass or dirt and served as a grounding rod because of fears of large electric currents injuring the crew. After lowering the levelers, the crew's navigator recorded the latitude, longitude, and bearing of the radar. Once the antenna had warmed up, data acquisition began. From 2007-2010, the time to get to the point of data acquisition improved from 10+ min. to ~5 min. Ending a deployment and taking down the radar system consisted of undoing everything detailed above and took much less time than that in setting up the radar system. By 2010, the crew could be safely moving in the radar truck ~2 min. after data collection ceased.

4.2.2 Attenuation/Radar Sensitivity

The MWR-05XP operates at X band and has relatively small power output, two factors that combine to make attenuation (e.g., Snyder et al. 2010) a problem in some datasets. Attenuation usually was a problem for high-precipitation (HP; Doswell and Burgess 1993) supercells. An example of attenuation is provided for a tornadogenesis case obtained on 23 May 2008 near Ellis, Kansas (Fig. 4.3). WSR-88D radar data at a comparable time were used to locate the back edge of storm reflectivity and provide a sense of the extent of the attenuation. In this particular case, the attenuation was especially problematic because two tornadoes identified in the data moved rearward

into the storm to a region where data were not usable (see Chapter 5.1). The MWR-05XP is not a polarimetric radar, so attenuation correction on these datasets is not possible.

A related issue is a perceived lack of sensitivity in many datasets. There is very little radial velocity data that is not noise found coincident with reflectivity less than ~0 dBZ. In general, radial velocity data from clear-air targets were not usable. As a result, analyzing, for example, velocity data in RFD gust fronts often is not possible. An automatic algorithm was used to remove noise and isolated data points. No signal-to-noise ratio data were provided, so radial velocity data were further thresholded using a conservative reflectivity cutoff of 0.0 dBZ. As mentioned previously, there was no automatic filtering of ground clutter. Ground clutter was not removed in most datasets, but in cases in which it was removed, it was done so subjectively using stationary reflectivity patterns and near-zero radial velocity. ProSensing, Inc. provided reflectivity and radial velocity PPI data in Universal Format corrected for pointing angle (i.e., up is due north in all radar PPIs images shown here). Data were translated to Dorade format and viewed and edited using the Soloii software package (Oye et al. 1995).

4.2.3 Radial Velocity Aliasing

The MWR-05XP typically obtained volumetric scans every 5-15 sec. from 2008-2010. The large amount of data increased the importance of automation in the quality control process. For example, a dataset of a tornadic supercell on 5 June 2009 contained almost 5,500 individual PPI scans. As a result, velocity aliasing that could not be corrected automatically was a major problem (e.g., Fig. 4.4) and automatic de-

aliasing algorithms were implemented. The algorithm, developed for Alexander (2010), uses a manually de-aliased input scan and an adjustable fraction of the Nyquist velocity (0.8 in this case) to correct aliased gates. The algorithm performed poorly in areas of strong radial velocity gradients, possibly because of azimuthal variation in gate locations, a problem discussed in Chapter 4.2.5. Unfortunately, tornadoes are defined via radar by tight gradients in radial velocity. As a result, most datasets had to be manually de-aliased. Manual de-aliasing of the large number of scans prolonged the radar editing process by several hundred man-hours for the three datasets studied for this project. Once it became known that velocity aliasing was a major problem, every effort was made to utilize scanning modes with higher PRFs (and therefore a higher Nyquist velocity) and restrict data collection to a maximum range of 30 km. Even in datasets with Nyquist velocities as high as ~35 m s^{-1}, significant time and effort was spent in de-aliasing radial velocities.

4.2.4 Beam Smearing

Beam smearing was observed in many datasets from 2008-2010. A likely contributing factor in MWR-05XP beam smearing is the inherent difficulty in obtaining at least 10 independent samples while maintaining a fast antenna azimuthal rotation rate. In data obtained using the STF-SE mode, beam smearing was mitigated by employing frequency hopping in azimuth. However, beam smearing was still observed in 2009 and 2010 datasets, sometimes at inconvenient locations. For example, beam smearing was found in a dataset from 5 June 2009 prior to and during the process of tornadogenesis in the area of the mesocyclone (Fig. 4.5). In half of the data, the beam

smearing was close enough to velocity maxima in the mesocyclone that unbiased numerical calculations could not be made in the area (see Chapter 5.2). When beam smearing occurred, it was at consistent locations dependent on the direction of antenna motion. In other words, beam smearing appeared for all clockwise scans at the same location and all counter-clockwise scans at a different location. It also is possible the smeared velocities were not caused by a radar hardware problem, but rather a software issue based upon the large amount of information being processed over short amounts of time.

4.2.5 Antenna Hysteresis

A final, unique problem encountered in working with data from the MWR-05XP was a consistent data "jitter" observed in both reflectivity and radial velocity. For reasons that are still unclear, the radar scanned resolution volumes at slightly different locations when it scanned clockwise compared to when it scanned counter-clockwise; offsets between scans were ~0.4°. It is possible that the offset was caused by antenna hysteresis (e.g., Tanamachi et al. 2007), a slowing and accelerating of the radar antenna as it neared the end of one volume scan and the beginning of the next volume scan. The jitter was not a major problem; the data being obtained in successive sector scans were not in error, but were obtained at slightly different locations. Based on the large sample of measurements, it is not thought that the changing location of radar bins biased measurements presented in Chapter 5 because the radar beamwidth did not change from scan to scan. For example, it is not expected that ΔV would be systematically biased depending on whether the radar antenna was scanning clockwise vs. counter-clockwise

because the relationship between the location of radar bins and the location of a tornado should be random. However, viewing data in animation became difficult to interpret because of the distracting nature of the jitter. Most animations of MWR-05XP data use every other scan, so there is no observable jitter.

4.3 Analysis Tools

4.3.1 Tornado Vortex Signatures

The MWR-05XP is best suited for the study of storm-scale features such as mesocyclones and hook echoes. Carbone et al. (1985) found that ~5 (10) independent radar samples of a feature are required to resolve 75 (90) % of the feature's flow amplitude. A common tornado core flow diameter of 300 m would necessitate azimuthal sampling every 60 (30) m to be well resolved. At typical ranges of 5 (15) km, the MWR-05XP azimuthal beam diameter is ~120 (370) m, so tornado core flow is only well resolved in very large (> 1.5 km diameter) tornadoes. The MWR-05XP still can be used to assess the bulk properties of tornadoes by assessing azimuthal shear signatures, as is commonly done using WSR-88D data (e.g., Fig. 2.1; Brown et al. 1978; Trapp et al. 1999). When the "tornado aspect ratio", the ratio of the radar beamwidth to the radius of the tornado core flow, is less (greater) than 1, the shear signatures associated with the tornado are tornado (tornado vortex) signatures (e.g., Wood and Brown 1997). It is expected that in most cases, the MWR-05XP beam diameter will be larger than the tornado diameter, so TVSs likely are the representative tornado feature under study. Poor spatial resolution also precluded objective analysis of tornado data, though there

was no obvious need for smoothed data to achieve the objectives outlined in Chapter 3.2. The focus, therefore, is on unsmoothed TVS radial velocity data.

Much of the analysis of tornado strength will rely on gate-to-gate (GTG) maximum ΔV calculations. Use of AVV is limited because, with maximum outbounds and inbounds located in adjacent gates, calculation of the distance between the measurements is not possible. In addition, the diameter of a TVS signature is an indeterminable overestimate of actual tornado diameter (e.g., Wood and Brown 1997). Maximum TVS ground-relative radial winds also will be referenced occasionally, but because of difficulty in estimating accurate vortex translational motions every ~10 sec. (see below), vortex-relative radial velocities will not be used. Strong cyclonic shear signatures coincident with tornadoes were detected in several MWR-05XP datasets, some with $\Delta V > 100$ m s^{-1}. Radar azimuthal oversampling and the relatively close range (7-15 km) to the tornadoes studied herein allows for meaningful information to be extracted from the shear signatures. However, it has been shown that when the radar aspect ratio is relatively large, the intensity of shear signatures can change not from physical changes in the tornado, but rather from the position of the radar beam compared to the vortex (Fig. 4.6; Wood and Brown 1997). As a result, caution must be used when interpreting short-time scale changes in tornado shear signatures.

Objective criteria were established to differentiate between a shear signature and a TVS. In order to qualify as a TVS in this study, the radial velocity field had to contain all of the following:

1. GTG azimuthal $\Delta V \geq 15$ m s^{-1}
2. Adjacent inbound/outbound radial velocity measurements

3. 1 and 2 must be satisfied over at least ~30 sec. of continuous data collection

The criteria above, though crude, allow for some measure of objectivity to be used in determining when vortices began and ended. *The use of these criteria is not an indication that $\Delta V \geq 15$ m s^{-1} definitely indicates a tornado.* Many studies utilizing DOW data, for example Alexander (2010), used a minimum ΔV of 40 m s^{-1} over a diameter less than 2 km as a criterion for a vortex to be considered a tornado. However, the data used in those studies came from radars with half the azimuthal beamwidth as the MWR-05XP (.9° vs. 1.8°, respectively) and azimuthal sampling typically five times as fine (.3° vs. 1.4°, respectively). As a result, finer details of tornado flow likely are being sampled and DOW-observed signatures are best described as tornado signatures (TSs) rather than TVSs. It is expected that tornadic ΔVs in MWR-05XP TVS data would be much smaller in magnitude than that in TS data from radar systems with superior spatial resolution. Therefore, the relatively small ΔV requirement is reflective of the poor azimuthal resolution of the radar. The 15 m s^{-1} TVS ΔV cutoff was found to be well-correlated with confirmed times and locations of tornadoes in data from radar's with higher spatial resolution (see Chapter 5.2.2).

The GTG ΔVs calculated in MWR-05XP TVSs likely are underestimates both of true peak tornado ΔVs and GTG ΔVs from other mobile Doppler radars. For the purposes of this study, it is more beneficial to include non-tornadic data than to eliminate tornadic data as the former still allows for examination of the pre-tornadogenesis period, even if the exact transition time remains unknown. Once a TVS was identified, it was followed until there were at least 30 sec. of continuous data in which $\Delta V < 15$ m s^{-1} and/or at least 30 sec. of data without adjacent inbound and

outbound radial velocities. As a result, often times, ΔVs less than 15 m s^{-1} were included in time series of TVS calculations. In cases where there were not adjacent inbound/outbound radial velocities for less than 30 sec., ΔV was calculated as the largest GTG shear. If a tornado were embedded within a strong, larger-scale flow, the second criterion above might preclude detection of a tornado. However, with the exception of the dissipation of the Goshen County tornado (see Chapter 5.2.4), the TVSs documented here were almost always well-defined couplets of radial velocity.

4.3.2 Tornado Location

In addition to radial velocity, the other main piece of information recorded in examining single-Doppler radar data was the position of the tornado in space. There are two coordinate systems used in analyzing radar data, one that is relative to the radar antenna and one that is relative to the ground, both in *x, y, z* space. Standard radar coordinates are azimuth angle (θ), elevation angle (φ), and slant range (r_s). Azimuth angle is measured in the x-y plane in a clockwise direction from the positive y-axis to the antenna beam. Elevation angle is measured as the angle away from the x-y plane, increasing positive along the positive z-axis. The slant range is the straight-line distance from the antenna to the point in space. In the antenna-relative coordinate system, the front of the truck points toward the positive y-axis, so the positive x-axis is at 90° azimuth and the positive z-axis is perpendicular to and pointing away from the truck toward the sky. The ground-relative coordinate system is standard, the positive y-axis (x-axis) points toward the north (east) and is parallel to a level surface. The positive z-axis points upward and is orthogonal to a level surface.

For a level radar and ignoring atmospheric and Earth curvature effects, transforming from an antenna-relative coordinate system to a ground-relative coordinate system requires only simple trigonometry:

$$x_L = r_s[\sin(\theta + H)\cos\varphi] \tag{4.1}$$

$$y_L = r_s[\cos(\theta + H)\cos\varphi] \tag{4.2}$$

$$z_L = r_s \sin\varphi \tag{4.3}$$

or in matrix form:

$$\overrightarrow{X_L} = \begin{bmatrix} x_L \\ y_L \\ z_L \end{bmatrix} = r_s \begin{bmatrix} \sin(\theta + H)\cos\varphi \\ \cos(\theta + H)\cos\varphi \\ \sin\varphi \end{bmatrix} \tag{4.4}$$

where H is the heading angle of the truck and uses the same convention as the azimuth angle (i.e., a truck facing due east has H = 90°). However, if the truck is rotated about the x-, y-, or z-axis, the transformation is more complicated. Rotation of the truck around the positive x-,y-, and z-axes is defined as the roll (R), pitch (P), and aforementioned heading (H) angles. A truck with a positive R (P) angle will have its right (back) side lower than its left (front) side. Based on Alexander (2010) and adapted from Lee et al. (1994), the antenna-relative coordinate system can be transformed to a ground-relative coordinate system using three transformation matrices, one each for the roll (M_R), pitch (M_P) and heading (M_H) angles

$$\overrightarrow{X_g} = \begin{bmatrix} x_g \\ y_g \\ z_g \end{bmatrix} = M_H M_P M_R \overrightarrow{X_L} \tag{4.5}$$

$$\overrightarrow{X_g} = \begin{bmatrix} \cos H & \sin H & 0 \\ -\sin H & \cos H & 0 \\ 0 & 0 & 1 \end{bmatrix} \begin{bmatrix} 1 & 0 & 0 \\ 0 & \cos P & -\sin P \\ 0 & \sin P & \cos P \end{bmatrix} \begin{bmatrix} \cos R & 0 & \sin R \\ 0 & 1 & 0 \\ -\sin R & 0 & \cos R \end{bmatrix} \overrightarrow{X_L} \tag{4.6}$$

MWR-05XP is not permitted to obtain data while moving and all data are corrected for pointing angle. As mentioned previously, a dual-antenna GPS was used to calculate H to within 0.3°, so in practice, it is reasonable to assume that H is known. Deployment sites for the MWR-05XP often were parallel to sides of roads so as to not to block traffic with the radar. In Chapter 4.2.1, it is noted that, in 2008, an electronic level rarely recorded R greater than 3° in navigating the MWR-05XP to what were perceived by the crew to be level deployment sites. For the purposes of this discussion, it is assumed that maximum MWR-05XP roll angles are ± 3.0°. In addition, because deployment sites often were on roads without hills, and the radar was parallel to the side of the road, it is assumed that there is no significant P. Using these assumptions for a truck facing due north (so H is 0°), the first two matrices on the RHS of Eqn. 4.6 reduce to identity matrices and the transformation is

$$\overrightarrow{X_g} = \begin{bmatrix} x_g \\ y_g \\ z_g \end{bmatrix} = \begin{bmatrix} \cos R & 0 & \sin R \\ 0 & 1 & 0 \\ -\sin R & 0 & \cos R \end{bmatrix} r_s \begin{bmatrix} \sin\theta\cos\varphi \\ \cos\theta\cos\varphi \\ \sin\varphi \end{bmatrix} \tag{4.7}$$

which simplifies to

$$x_g = r_s(\cos R \sin\theta \cos\varphi + \sin R \sin\varphi) \tag{4.8}$$

$$y_g = r_s(\cos\theta \cos\varphi) \tag{4.9}$$

$$z_g = r_s(\cos R \sin\varphi - \sin R \sin\theta \cos\varphi) \tag{4.10}$$

Unfortunately, roll angles for the MWR-05XP are unknown, so corrections cannot be made. As a result, an error analysis is appropriate, in which Eqns. 4.8-4.10 are subtracted from Eqns. 4.1-4.3. Assuming that for small R,

$$\cos R \approx 1$$

the errors are

$$\varepsilon_x \equiv x_L - x_g = -r_s(\sin R \sin \varphi) = -r_g(\sin R \tan \varphi) \quad (4.11)$$

$$\varepsilon_y \equiv y_L - y_g = 0 \quad (4.12)$$

$$\varepsilon_z \equiv z_L - z_g = r_s(\sin R \sin \theta \cos \varphi) = r_g(\sin R \sin \theta) \quad (4.13)$$

where r_g is the "ground range," the distance between the radar antenna and the reflection of a point in space vertically to the surface. Note that there is no error in the y direction because R is defined as occurring along the y-axis.

To estimate how large expected errors in the x- and z-planes are, the assumed maximum R of 3° is considered for a range of typical azimuth angles, elevation angles, and ground ranges in MWR-05XP supercell datasets. The magnitude of maximum zonal errors (Fig. 4.7) and maximum height errors (Fig. 4.8) are provided. Zonal positioning errors are generally small, even assuming the maximum R of 3° (Fig. 4.7a); errors only surpass 500 m at ranges greater than 15 km and elevation angles larger than 20° (Fig. 4.7b). Height errors can be quite large, particularly for R of 3° and ranges beyond 15 km (Fig. 4.8a). Also, note that, for a given R, the height error will vary with azimuth and the maximum error occurs at the angle orthogonal to the truck heading (Fig. 4.8b). Most of the tornado observations discussed herein occur within 15 km of the MWR-05XP and at elevation angles of 20° and lower. As a result, zonal errors should not exceed ± 200 m, a value that is less than the radar beamwidth at a range of ~10 km. Maximum height errors of ± 500 m are expected. This study does not depend on exact height calculations to glean useful results, and the height errors likely are small enough that there is reasonable certainty in categorizing most observations as coming from low- or midlevels in a storm. However, there are some observations where the TVS is in the 15-30 km range from the radar. In such cases, estimated heights may be in error by as

much as ± 1 km. Great care should be taken in interpreting quantitative heights provided for TVS observations made beyond 15 km and the focus should be on qualitative height descriptors instead.

In addition, because of the aforementioned errors in vortex position, derived quantities using positional information is a concern. For example, positional data were used in calculating tornado height, tilt and translational speed/direction. The translational speed of a vortex, Vtr, is estimated using

$$Vtr = \frac{\partial r}{\partial t} \cong \frac{x_2 - x_1}{t_2 - t_1} \tag{4.14}$$

where r is the distance the vortex translated over time t and x is the true location of the vortex center. The tornado is not fully resolved by the MWR-05XP, so there is an error ε in the MWR-05XP-indicated vortex location such that

$$x_{M1} = x_1 + \varepsilon_1 \tag{4.15}$$

$$x_{M2} = x_2 + \varepsilon_2 \tag{4.16}$$

where x_M is the position of the vortex as estimated in MWR-05XP data. As a result, the error for vortex speed as estimated by MWR-05XP is

$$\varepsilon_V \cong \frac{\varepsilon_2 - \varepsilon_1}{t_2 - t_1} \tag{4.17}$$

A rough estimate of the maximum error in vortex location for a symmetric vortex with tornado aspect ratio greater than one is one half of a radar beamwidth. In such a scenario, at a range of 10 km,

$$\varepsilon_1 = \varepsilon_2 \cong \pm 125 \text{ m} \tag{4.18}$$

Using Eqn. 4.18 and typical MWR-05XP update times, maximum translational velocity errors of 25 m s^{-1} are possible if successive volume scans are used. For maximum errors to be less than 10, 5, and 2 m s^{-1}, integration times greater than 25, 50, and 125 s are

necessary, respectively. The integration times are similar to or greater than volumetric update times of conventional mobile Doppler radars. As a result, any estimates of vortex speed and direction are calculated over a 1-2 min time period. Using the same information, tornado horizontal displacements may be in error by as much as 250 m in addition to the maximum ~200 m zonal error from an unleveled radar; running averages incorporating ~3 successive calculations will be used to focus more on trends in tornado tilt. Vortex height errors from coarse spatial resolution likely are small, O(50 m) maximum, because height calculations rely only on vortex positional range estimates and MWR-05XP range sampling is every ~75 m.

Chapter 5

Analysis

Table 5.1 includes a list of all the datasets that were analyzed to answer the specific questions posed in Chapter 3.2, along with various radar parameters and the data collection mode. Only 1-2 datasets for each objective were studied for this work. It is emphasized that this is not a climatological study and the number of datasets studied for each objective is small. However, many of these datasets are extensive because of rapid, volumetric data collection, which also serves to make each dataset unique. Analysis here appears grouped by dataset. The discussion section that follows incorporates multiple datasets to generalize results.

5.1 Ellis, KS Tornadoes on 23 May 2008

On the night of 23 May 2008, the MWR-05XP obtained data on a tornadic supercell. Damage surveys completed following the storm indicated that several tornadoes formed as a result of the supercell. The MWR-05XP was located about 15 km north of Hays, Kansas, east of the supercell as it moved northeastward toward the radar. The storm was large in areal extent and was the result of the merger of two supercells (Fig. 5.1a). The deployment north of Hays was the only deployment on this supercell by the team. Data collection began at ~0148 UTC (Fig. 5.1b; hereafter all times given in UTC) and ended at ~0300 on 24 May 2008. Update times were 14 sec. for data collection out to 60 km and from 1-20° in elevation. The entirety of the deployment

took place at night, so there were no visual sightings of any tornadoes by the MWR-05XP crew.

A damage survey was completed after the passage of the storm by employees from the National Weather Service (NWS) in Dodge City. They found damage consistent with five tornadoes from the storm, two rated EF-1 on the Enhanced Fujita scale (Marshall 2004) and three rated EF-0. The MWR-05XP obtained data on three of the tornadoes and another strong vortex during the deployment. One of the tornadoes was located at the edge of the MWR-05XP's viewable range when data collection began and quickly moved rearward out of view of the radar because of attenuation (see Chapter 5.1.3). Based on previous studies, the tornado's rearward movement likely indicated it would soon dissipate (e.g., Dowell and Bluestein 2002a; French et al. 2008). Therefore, the focus here is on the other two tornadoes and the vortex. One tornado was cyclonic and formed northwest of the radar completely embedded in precipitation in the northern part of the combined storm. The second tornado was an anticyclonic tornado that formed southwest of the radar, likely along the RFGF of the storm's southern flank. The first tornado is referred to as the Hog Back tornado (for the town near where it formed) and the second tornado is referred to as the Ellis anticyclonic tornado (hereafter EAC tornado). In addition, an anticyclonic vortex could be identified to the east of the first tornado that moved westward out of the radar's viewable range; the vortex is referred to here as the Hog Back anticyclonic vortex (HBAV).

A comparison of the surveyed damage paths with MWR-05XP radial velocity data from 1.0° elevation angle is shown in Figure 5.2. The mismatch between the surveyed paths and the radar-indicated vortices is noticeable for both tornadoes.

Previous attempts to compare mobile, Doppler radar data with damage surveys have been met with similar inconsistencies (e.g., French et al. 2009), likely from the inherent difficulty in determining tornado paths from damage in cases when tornadoes occur at night, and therefore without sightings of the tornadoes. For the Hog Back tornado, the surveyed path crosses the radar-indicated vortex at one time and the two are fairly close for other times. Based on radar data, the TVS associated with the EAC tornado was located several kilometers to the east of the surveyed path. There are sources of error in both the damage survey and the radar data. In the damage survey, damage indicators are used to estimate the wind speed of the tornado, but if there is nothing to be damaged, the survey may underestimate the tornado's strength or miss it all together. In addition, the latitude and longitude of the surveyed path are rounded to the nearest geographic minute, so the documented path may be different from what appears in *Storm Data*. The MWR-05XP should not have zonal errors exceeding ~50 m for this case (Fig. 4.7b), so assuming negligible tornado tilt in the lowest levels, the location of the tornado in the MWR-05XP data is assumed to be accurate. Nonetheless, neither sources of error are likely large enough to explain the differences between the radar observations of the EAC tornado and the damage survey results.

Another possibility is that the damage path surveyed is from a different tornado. In the MWR-05XP data, a very large and strong cyclonic circulation can be identified passing very near the damage path in question (Fig. 5.3). Within the larger-scale circulation, TVSs were transient and could not be tracked. Also, several attempts to obtain additional information about the damage survey from the NWS office in Dodge City were unsuccessful. The MWR-05XP consistently recorded radial velocities over 30

m s^{-1} and GTG ΔVs of 40-50 m s^{-1} at 1.0° elevation angle. Also, shear signatures met the criteria for an anticyclonic TVS. For the purposes of this study, it is assumed that the strong anticyclonic shear is representative of a tornado, but with ambiguous damage survey confirmation and no visual sightings, it is plausible that there was no anticyclonic tornado.

5.1.1 Hog Back Tornado

The Hog Back tornado (Fig. 5.4) was rated EF-1 based on damage to some trees and power lines. The tornado was estimated as beginning at ~0208 based on the damage survey, though it may have started several minutes before that based on MWR-05XP radial velocities greater than 50 m s^{-1} at 1.0° elevation angle (Fig. 5.4g). Regardless of the exact tornadogenesis time, the MWR-05XP was scanning during tornado formation. The vortex signature was ~17 km away from the radar during tornadogenesis, so spatial resolution is not fine enough to examine details of the tornadic flow; the focus here is on observations of the TVS leading up to and at the time of tornadogenesis. Unfortunately, because of attenuation, shortly after the tornado formed, it moved rearward (westward) into a location of radially diminishing reflectivity and noisy, if any, radial velocity. After 0207, TVSs could still be identified coincident with the tornado, but they were poorly resolved and undergoing seemingly random fluctuations in strength. Reflectivities in the TVS locations were ~0-10 dBZ and because of assumed low SNR, the signatures were not examined after 0207. As a result, the time period under examination is ~0150-0207 in which tornadogenesis is assumed to be at ~0203-0205. In addition, de-aliasing radial velocities in and around the tornado was

particularly difficult for this case, so there are limited calculations presented here because of the likelihood of errors. Data from the Hog Back tornado only meet the criteria for the tornadogenesis objective of this study.

Formation of the Hog Back tornado occurs within relatively high values of reflectivity (Fig. 5.4h) in a region that, ~15 min. prior to tornadogenesis, contains a smooth area of outbound radial velocities (Fig. 5.4a). Only weak cyclonic shear associated with a midlevel mesocyclone is identified, even 15 min. prior to tornadogenesis. The dataset is investigated (i) for evidence of a descending TVS as in type I tornadogenesis and (ii) to determine the progression of any observed scale contractions at low levels.

In order to better visualize scale contractions and vertical directionality of cyclonic shear development, a new type of radar image that is a hybrid between an RHI and a vertical cross-section is constructed. The image is called an azimuth-height indicator (AHI) display and is similar to an RHI except range is taken to be constant for a set of azimuths. The AHI takes advantage of the unique volumetric sampling of the MWR-05XP. Azimuths are plotted on the abscissa and height is plotted on the ordinate. It is important to point out again that the MWR-05XP was not leveled. There are no pictures of the deployment location for this dataset, however, based on the author's recollection, a relatively level spot on a hybrid dirt-paved road was chosen for data collection and the radar was not noticeably tilted. Nonetheless, at a 17 km range, significant errors in height of ±1 km are possible (Fig. 4.8a) and all heights that are shown for this dataset are approximations. AHIs are constructed from PPI scans, but no time correction is necessary because all of the PPIs at a given azimuth are obtained in

less than 1 sec. Finally, AHIs give the impression that one is looking at a vertical slice of the atmosphere, but because AHIs are constructed from PPIs, they are actually showing a vertical slice that is tilted; they should be used as a rough indicator of the vertical layout of radar variables.

AHIs showing the development of the Hog Back tornado at a range of 17 km are shown in Fig. 5.5. AHIs are shown every 28 sec. for the purposes of brevity, but were considered every 14 sec. for the analysis. Using AHIs is ideal for this case because the mesocyclone/tornado cyclone/tornado do not have a significant motion normal to the radar beam during their formation. AHIs are constructed at several ranges from 15.75 km to 18.75 km (not shown) and the results are qualitatively similar. Identifiable in all of the AHIs is a curved area of azimuthal shear in the velocity field all the way up to the top of the observed domain. This shear feature moves from left to right, equivalent to clockwise motion in a PPI image. The strongest outbounds are consistently in the 3-5 km range above radar level (ARL; hereafter all heights are above radar level) initially, but the only observable inbound radial velocities are at the lowest level in the 10 min. preceding tornadogenesis. By 0202:39, just prior to tornadogenesis, a rapid strengthening in outbounds is located between 2-3 km height with a corresponding small increase in the magnitude of inbounds. At 0203:36, azimuthal shear increases between 1-2 km, but increases more in the lowest 1 km. In the next 30 seconds, azimuthal shear in the lowest 1 km increases even more while azimuthal shears in the 1-3 km layer remain steady or decrease. Also, between 0202:39 and 0204:04, the distance between the inbound and outbound maxima decrease in the lowest 2 km, indicative of a scale contraction that occurs rapidly (0202:39 in Fig. 5.5). Most of the velocity maxima

do not occur in adjacent gates. As a result, the sequence detailed above best describes a process that occurs on a scale smaller than a mesocyclone but larger than a tornado. After 0204, a TVS is identified with tornado-strength radial velocities; shortly after the TVS forms, it moves out of view of the radar.

Prior to tornadogenesis, ΔV is recorded at several heights for the Hog Back case (Fig. 5.6). *All ΔV calculations are made by examining PPIs at each elevation angle, and are not made using the AHIs.* Further, ΔV in this case was not GTG TVS ΔV but instead was calculated as max. inbound/outbound magnitude. In the 5 min. prior to tornadogenesis, ΔV increases above 1 km; this increase is followed by a large and rapid increase in ΔV in the lowest 1 km. Between 0202:26 and 0203:52, ΔV increases from ~55 to 80 m s^{-1} with another increase to ~90 m s^{-1} by 0205:15. While the increase in ΔV at 1.0° elevation angle is large and occurs quickly, the change every ~30 sec. (Fig. 5.7a) is not abrupt between time periods. Rather, steady increases of 5-10 m s^{-1} occur with every time step. It may be tempting to view the AHIs and spot the strongest shear descending in the lowest 3 km just prior to tornadogenesis, but during that same time period, ΔV between 1-3 km also increases, just not as much (from ~70 to 80 m s^{-1}) and not as quickly as that below 1 km. The TVS then moves rearward after forming, consistent with the cyclic tornadogenesis process.

The Hog Back radial velocity data illustrate well the increased value provided by the MWR-05XP compared to other radar systems. As an example, data values from different elevation angles at different times are used to construct a hypothetical height profile of ΔV obtained by a radar similar to the MWR-05XP, but using ~90 sec. updates (i.e., scanning one elevation angle at a time; Fig. 5.7b). The time period covered by Fig.

5.7b is the same as that covered in Fig. 5.7a. *The vertical profile shown in Fig. 5.7b does not accurately reflect the actual profile at any one time, so it is easily observed how the MWR-05XP might resolve volumetric processes that other radar systems cannot.*

Significant ΔVs are not observed between 5.4-15.6° elevation angle (~1.5-4.5 km ARL) at any time. It is likely that attenuation already has affected the quality of the data at increased heights, and in fact, the effects of attenuation are seen between ~5.4-15.6° elevation angle first. In a series of PPIs at 20.0° elevation angle, no TVS or inbound radial velocities can be identified at midlevels in the storm until ~5 min. prior to tornadogenesis (Fig. 5.8). Only broad cyclonic shear can be observed at the approximate time and location of tornadogenesis in radial velocity data at the top of the MWR-05XP domain (Fig. 5.9). A TVS can be observed by ~0209 at 20.0° elevation angle following a longer period of broad cyclonic shear (Fig. 5.10). The lack of a TVS at midlevels before the tornado forms and the appearance of one ~4 min. after the tornado is thought to have formed is convincing evidence that there is no descending TVS in the formation of the Hog Back tornado.

As first shown in Fig. 5.6, in the ~5 min. preceding tornadogenesis, ΔV increases in the lowest levels, first between 1-2 km and then in the lowest 1 km. There are no individual ΔV jumps greater than 15 m s^{-1}, rather increases in ΔV are typically ~5 m s^{-1} between updates. After the tornado forms, ΔV calculated from the lowest four elevation angles stays relatively stable (Fig. 5.11a). As mentioned previously, strong cyclonic shear in the low-level mesocyclone or tornado cyclone undergoes a scale contraction around the time of tornadogenesis. The distance between the maximum

inbound and outbound radial velocities (Δx) is calculated for the lowest four elevation angles in the 10 min. period centered on the time of tornadogenesis (Fig. 5.12a). During the three minutes preceding the estimated time of tornadogenesis, Δx decreases ~1.5 km. After 0205, Δx continues to decrease, but at a much lower rate. The decreases in Δx occur first at 2.5° and 3.9° elevation angle, and then occur ~45 sec. later at 1.0° and 5.4° elevation angle (Fig. 5.12b). The Δx values are noisy, even after using a running average, because of the coarse azimuthal resolution of the MWR-05XP data. Therefore shear and AVV values also are very noisy and not shown. Also, there are no data available above 5.4° elevation angle to see if there is a vertical progression of the scale contraction that continues upward with time. As a result, it cannot be determined if there is vertical directionality in the progression of the scale contraction.

5.1.2 Ellis Anticyclonic Tornado

In radial velocity data, there is a strong, tight, anticyclonic low-level circulation at the southwestern extent of what is likely the rear-flank gust front of the Ellis supercell (Fig. 5.13). At some times, GTG ΔVs are greater than 50 m s^{-1} at 1.0° elevation angle. The unique nature of both the observing platform and of anticyclonic tornadoes in general makes the EAC tornado worth investigating. Unlike with the Hog Back tornado, the entire life cycle of the EAC tornado was captured encompassing approximately 15 min. worth of data. The MWR-05XP data are used to address the tornado research questions posed in Chapter 3.2.

To follow the progression of the EAC tornado, AHIs again are constructed and examined (Fig. 5.14). Unlike the Hog Back tornado, which is nearly stationary during

tornadogenesis, the EAC tornado is moving toward the radar when it forms and afterward (Fig. 5.13). As a result, the AHIs for the EAC tornado are at different ranges for each plot and centered at the location of the maximum ΔV at 1.0° elevation angle. The change in range also means the spatial resolution changes in the plots. As the range decreases and the EAC tornado approaches the radar, there is a noticeable increase in vertical spatial resolution. The maximum height is kept steady in the plots so that easy comparisons can be made between successive times. Prior to any observed vortex, there is a curved layer of anticyclonic shear up to ~6 km at 0204:20. Even with enhanced temporal resolution, strong azimuthal shear develops in the lowest 2-3 km at roughly the same time between 0204:48 and 0205:45. The strongest azimuthal shear is consistently confined to the lowest 3 km, but there is no obvious pattern to the progression of the azimuthal shear after 0205 in the AHIs (Fig. 5.14). Only from 0206-0208 is there an identifiable vortex signature above 3 km. No scale contraction is observed in this case.

A set of ΔV calculations are made using the EAC tornado data. The EAC tornado ΔV calculations span the entirety of the tornado's lifecycle and are GTG calculations. In the Hog Back tornado calculations, ΔV is defined as the difference between the maximum outbound and maximum inbound radial velocities in the mesocyclone/tornado cyclone and were calculated only at and before tornadogenesis because of poor data quality after these time periods. For the EAC tornado and all discussions that follow, ΔV is defined as the maximum GTG difference in radial velocities in the TVS. In this instance, the use of GTG ΔV reflects the higher quality of the data (i.e., less attenuation) used in the calculations and a higher confidence that the

bulk properties of the tornado are being resolved. In practice, GTG ΔVs either are equivalent to the maximum inbound and outbound radial velocities or are very close in value to ΔVs calculated using maximum inbound and outbound radial velocities.

In total, 283 TVS ΔV calculations are made at elevation angles from 1.0-9.8°, spanning heights of ~0.3-3.3 km ARL (Fig. 5.15). There is relatively little variation in ΔV with time, 67% of the ΔV observations are in the 35-45 m s^{-1} range. The one exception is the cluster of ~20 data points in the 10-20 m s^{-1} range from 0207-0214. The group of weaker ΔVs is associated with two oscillations in the elevation-angle averages from 0208-0213 before the average stabilizes (Fig. 5.15). The ΔV data are grouped further into two elevation angle subsets (Fig. 5.16a) and then averaged (Fig. 5.16b) to look for where rapid changes in TVS strength are occurring. It can be seen that the low-level ΔVs (lowest ~2 km) undergo little change until a sudden drop off before the TVS dissipates. The cluster of lower-ΔV data points come exclusively from the higher elevation angles (~1.5-3.3 km) and are associated with the oscillations in the averaged ΔV field. Time series of ΔV from three individual elevation angles also are provided (Fig. 5.17). The 1.0° and 5.4° elevation angle ΔV time series are very similar with minimal abrupt changes in ΔV and values consistently between 30 and 45 m s^{-1}. However, above ~2.5 km (data mostly from 8.3° and 9.8° elevation angle), ΔVs undergo rapid changes much more frequently. At 8.3° elevation angle, changes in ΔV of as much as ~25 m s^{-1} occur in as little as one scan (~14 sec.) and ΔVs range from ~15-50 m s^{-1}.

Based on several ΔV time series (Figs. 5.15-5.17), the strength of the EAS TVS is relatively constant with height outside of the top two elevation angles. Vertical

profiles of ΔV also are examined (not shown), but there is no identifiable pattern to changes in vertical profiles of ΔV at individual times. All of the individual ΔV profiles are combined and plotted together (Fig. 5.18a). There is a very weak, negative linear relationship between the height of the TVS and its strength. The cluster of weaker ΔVs from the top two elevation angles again can be identified; they are the only indication that there may be general weakening of the EAC TVS with height. In addition, the strength of the EAC TVS from 2.5-9.8° elevation angle is compared to the strength of the TVS at the level closest to the surface (1.0° elevation angle) for every data point (Fig. 5.18b). Again, there is no evidence that the TVS is systematically stronger or weaker relative to the TVS close to the surface, outside of the weaker ΔVs above 2.5 km.

In an effort to synthesize all of the above information, a height-time series of color-coded ΔV is constructed (Fig. 5.19). As noted previously, ΔVs in the lowest ~2 km are relatively steady, while, above 2 km, ΔV fluctuations of greater than 10 m s^{-1} in one scan occur ~5 times. Also, it now can be seen that the TVS requirement is first met at 3.9° elevation angle (~1.9 km), progressing upward one elevation angle every ~30 sec. thereafter. The TVS criteria are not met in data from the lowest two elevation angles for another ~90 sec. *The TVS criteria being met at time t is not necessarily an indicator that tornadogenesis occurred at time t.* Also, anticyclonic shear is present in the lowest 3 km inclusive prior to TVS formation. Regardless, the consistent upward progression of TVS formation with time and the relatively long amount of time between TVS formation at 3.9° elevation angle and that at 1.0° and 2.5° elevation angle are both potentially important observations. Also of note is that the anticyclonic shear at 8.3°

elevation angle does not meet the TVS criteria for another ~30 sec. at ~0213; this period is followed by another 4 min. period in which it does meet the criteria before it can no longer be tracked. The TVS criteria are met for about four minutes longer at the higher elevation angles, though there are only three data points in the last ~2 min. prior to TVS dissipation at all levels.

The path the EAC tornado took is recorded for each elevation angle. An example comparing the paths at 1.0° and 6.8° elevation angle is shown in Figure 5.20. The EAC tornado generally moves toward the northeast, though higher above the surface, the tornado moves more toward the north at the end of its lifecycle. The TVS location at 6.8° elevation angle is displaced to the west and north of the TVS location at 1.0° elevation angle, an indication that the tornado is tilted. Vertical cross-sections of the TVS location are plotted at several times in the east-west (Fig. 5.21a) and north-south (Fig. 5.21b) direction. Again, the radar may have been tilted by as much as ~3°, so the absolute magnitudes of the tilt may be off, though relative changes likely are robust because the EAC tornado was moving very little in azimuth. The EAC tornado becomes increasingly tilted toward the west and the north with increasing time and height. In each case, the TVS dissipates when tilt is greatest.

5.1.3 Hog Back Anticyclonic Vortex

Prior to the formation of the EAC tornado and the Hog Back tornado, the HBAV could be identified to the east of the first observed tornado that moved out of range of the MWR-05XP (Fig. 5.22a). The anticyclonic vortex moved northwest towards the cyclonic tornado. It is not known whether this feature was a tornado or not. The

anticyclonic vortex was very shallow, typically confined to the lowest 2 km (Fig. 5.22b) and occasionally to the lowest 3 km in PPIs and AHIs. As with the EAC tornado, there was an intermittent weak minimum in reflectivity, but it was not a feature that could be tracked in time (not shown). The anticyclonic vortex weakened slowly as the larger-scale circulation associated with the Hog Back tornado began to strengthen. Again, because observations of small-scale, convective anticyclonic vortices are rare, the HBAV is worthy of study here.

The HBAV was observed when data collection began, so there is no MWR-05XP data to investigate how the vortex formed. During the ~16 min. time period when the vortex shear signature is identified, a total of 252 ΔV calculations are made from 1.0-8.3° elevation angle (lowest ~3 km). The HBAV undergoes a 7 min. period of gradual weakening from 0150-0157 followed by ~4 min. of strengthening before it weakens again and dissipates (Fig. 5.23). As was seen for the EAC tornado, the ΔV calculations in the lower elevation angles have less spread than that of the higher elevation angles (Fig. 5.24a). The large shifts in ΔV at higher elevation angles make it difficult to gauge if there is any trend in the strength of the vortex prior to ~0157 (Fig. 5.24b). Short-time-scale changes in ΔV are not observed frequently in the lowest elevation angles.

The aggregate of the ΔV vertical profiles for the HBAV display little to no linear relationship between vortex strength and height (Fig. 5.25a), again like the EAC tornado. At each of the six elevation angles in which a TVS is observed, ΔVs ranged from 10-40 m s^{-1}. The ratio of TVS ΔV above the surface to that near the surface also is not linearly related to height (Fig. 5.25b). Through inspection of a color-coded time-

height profile of the HBAV ΔV (Fig. 5.26), it can be seen that the ~7 min. decrease in HBAV strength occurs first at 3.9° and 5.4° elevation angle and then the lowest two elevation angles. The HBAV TVS criteria are no longer met in the lowest 1 km first before dissipating above 1 km, as was seen in the EAC tornado. The TVS already can be identified in the lowest four elevation angles when data collection began.

The paths of the HBAV at 1.0° and 5.4° elevation angle are similar but displaced in the east-west direction (Fig. 5.27). Also of note is the unusual path the vortex takes, first moving north-northeast, then northwest, and finally northeast again. The unusual vortex motion is discussed further below. The HBAV consistently tilts toward the north with height (Fig. 5.28a). The EAC tornado also tilted toward the north, but its tilt became more pronounced with time. The tilt in the HBAV does not change significantly during the time it is tracked, even after TVS criteria are no longer met close to the surface. The HBAV has almost no vertical tilt in the north-south direction for most of the time it is tracked (Fig. 5.28b). However, as its translational motion slows, the vortex begins to tilt, first toward the south and then toward the north before it dissipates.

Between 0150-0153, the HBAV appears to move cyclonically around the cyclonic tornado located to its west (Fig. 5.29). The HBAV is moving north as data collection begins, then northwest for a time, and then slows down considerably as it moves northeast while the cyclonic tornado moves west-northwest (Fig. 5.30). Binary interaction between tropical cyclones has been observed when the systems are located close enough to each other (Fujiwhara 1931; Dong and Neuman 1983). In addition, French et al. (2008) observed mesocyclones within a cyclic supercell rotating around each other for a brief time. A comparison between the direction of motion of the HBAV

and the distance between itself and the cyclonic tornado is shown in Figure 5.31. When the two vortices are close to each other, the HBAV moves toward the northwest and moves from due east of the tornado to north-northeast of the tornado (Fig. 5.29). However, as the occluding tornado continues to move almost due west and the distance between the two vortices increases, the HBAV first moves very little and then moves slowly toward the northeast. Though the general location of the cyclonic tornado is identified in the MWR-05XP data, the tornado's strength cannot be reliably determined owing to noisy, attenuated data. Thus, a relationship between the relative vortex strength and vortex motion cannot be established, and the evidence here for binary interaction is merely circumstantial.

To summarize Chapter 5.1, the formation of at least one and possibly two tornadoes is sampled by the MWR-05XP. In the cyclonic Hog Back tornado, very little cyclonic shear is observed at midlevels and above prior to tornadogenesis. There is no evidence that mode I tornadogenesis occurs. The strongest shear is observed in the lowest 3 km and a low-level scale contraction is observed just prior to tornadogenesis; both observations are consistent with the mode II tornadogenesis process. In addition, a strong anticyclonic vortex is observed for ~15 min. The vortex is referred to here as a tornado because of the strong ground-relative radial velocities and ΔVs associated with the vortex. The TVS associated with the anticyclonic tornado is observed first at ~2 km and then above and below that level. The strength of the vortex varies little except at its highest-observed levels (~3-4 km). The TVS becomes increasingly tilted toward the northeast with height prior to dissipation. Finally, a well-defined low-level anticyclonic vortex is observed to the east of a cyclonic tornado. The vortex is confined to the lowest

~2 km and is relatively weak. The vortex may rotate briefly around the cyclonic tornado before the cyclonic tornado moves westward and dissipates.

5.2 Goshen County, WY Tornado on 5 June 2009

On 5 June 2009, during year 1 of VORTEX2, the complete lifecycle of a supercell mesocyclone tornado (hereafter the GC tornado, for Goshen County) was captured by the MWR-05XP (Fig. 5.32a). Based on a damage survey and radial velocity measurements from other mobile Doppler radars, the tornado was rated EF-2 by the NWS. Volumetric scanning was 1-20° in elevation with 6-9 sec. updates. Unlike for the previous case, data collection occurred during the day and there were consistent visual observations of the tornado. MWR-05XP data collection began at 2143:41 and ended at 2230:31; this time period enclosed the entire tornado lifecycle. The deployment location was a paved road leading to an abandoned missile silo with the MWR-05XP facing almost due west. The road was relatively level and the deployment location was one of the better sites encountered in 2009 (Fig. 5.32b). The TVS signature of the GC tornado varied in range from the radar ~5.5-17 km during data collection and was easily identified from 2200-2230. To the author's knowledge, this dataset represents the most complete radar documentation of a supercell tornado's time-height evolution through midlevels and, therefore, it warrants thorough analysis.

Estimated height errors (Fig. 5.33) and horizontal position errors (5.34) based on TVS location data are provided for the 2200-2230 time period. Assuming a relatively large R of 3°, height errors are as much as ±500 m early, but as the tornado moves

closer to the radar, the errors decrease to the ±300-400 m range (Fig. 5.33a). Also, errors are insensitive to elevation angle as shown in Eqn. 4.13. For smaller R, the errors are less than ±300 m (Fig. 5.33b). The largest height errors occur orthogonal to the heading angle of the radar, in this case to the north and south in a ground-relative reference frame. However, while the tornado moves from 340° to 20° azimuth between 2214-2221, the tornado also is relatively close at these times, so height errors are mitigated. Errors in the horizontal position of the radar are greater than ±200 m only for the assumed largest R of 3°, and only at the highest elevation angles at early times when the tornado was beyond 10 km from the MWR-05XP (Fig. 5.34a). For smaller R, the errors are less than 75 m (Fig. 5.34b).

Despite the appearance of the radar on level ground, the lack of precise measurements of roll and pitch angles leave open the possibility that roll angles were greater than 3.0° and errors in TVS coordinates are larger than estimated above. As a result, the focus in discussions of the GC tornado using TVS coordinates will not be on exact locations and heights, but rather on changes in TVS location and height with time and the relationship between those changes and other radar observations. Most of the TVS observations are made in the low (~0-2.5 km) and midlevels (~2.5-5.0 km) of the storm, so observations with estimated heights close to the interface between low and midlevels may have actually occurred in either part.

The MWR-05XP set up in an ideal location both in terms of the deployment site and the location relative to the storm. The MWR-05XP was located southeast of the supercell as it moved east-southeastward. The placement of the radar allowed for a long deployment as the supercell moved toward and just north of the radar location. The

downside of setting up 20+ km downstream of the hook echo is that the storm was relatively far from the radar initially. Early on, the maximum range used was 45 km in order to capture the whole storm. The volumetric update time was 9 sec. during the whole pre-tornadogenesis and tornadogenesis period. The relatively small PRF used for the large unambiguous range necessitated a smaller Nyquist velocity of ~24 m s^{-1}. Beyond 20 km, the spatial resolution of the radar begins to noticeably suffer (see Chapter 4.1.4), and at the time of tornadogenesis, the tornado was ~17 km away from the radar origin. However, a TVS was identified at the time of tornadogenesis and continually after that until tornado dissipation. At ~2200, the maximum range was decreased to 30 km and the Nyquist was increased to 34.75 m s^{-1}. In the 2200-2230 time period, the tornado was typically within 5-10 km of the radar with a well-defined TVS.

As mentioned previously, beam smearing is an occasional problem in examining the MWR-05XP datasets. Unfortunately, for the early part of the GC tornado dataset (2143-2157), beam smearing was identified in the area of the mesocyclone (Fig. 5.4) with a ~20° smearing offset depending on whether the radar antenna was scanning clockwise or counter-clockwise. In half of the scans, the northern part of the mesocyclone is smeared to a degree that it affects the quality of any analysis undertaken (Fig. 5.35a). In the other half of the scans, the beam smearing occurs in the southern portion of the mesocyclone (Fig. 5.35b), though typically to the south of the largest radial velocities. Therefore, most of the radar images herein only use the latter data, while calculations combine data from successive scans to maximize accuracy. As a result, the mesocyclone analysis utilizes volumetric data every 18 sec. rather than every

9 sec. An update time of 18 sec. is still much faster than that of conventional mobile Doppler radars.

The large amount of data obtained during the supercell necessitates splitting the discussion up into four separate periods: the pre-tornadogenesis, tornadogenesis, mature, and dissipating phases. The time periods for each phase are subjective and line up with MWR-05XP data collection (i.e., phases tend to end prior to MWR-05XP data gaps) for convenience. However, the gaps used here are similar to ones mentioned by Markowski (2012a). They categorize the storm periods for pre-tornadogenesis, tornadogenesis, mature, and dissipating stages as occurring at 2100-2148, 2148-2202, 2202-2212, and 2212-2230, respectively. Almost 3,600 observations of the TVS associated with the GC tornado were made; to discuss the observations all at once would diminish any attempt to extract useful information from them. Chapter 6 will synthesize all of the tornado observations to generalize results.

5.2.1 Pre-tornadogenesis Phase: 2143-2150

At ~2143, the isolated classic supercell already has a well-defined hook echo on the KCYS WSR-88D (Fig. 5.36). It is at this time that MWR-05XP data collection begins. The period from the beginning of data collection to two minutes prior to tornadogenesis is considered the pre-tornadogenesis period, consistent with previous works on the GC supercell (e.g., Markowski et al. 2012a,b). Markowski et al. (2012a) presented an overview of the pre-tornadic environment of the GC supercell using DDA first from a DOW radar and the KCYS WSR-88D and then from two DOW radars. It was found that:

1. Midlevel maximum azimuthal wind shear generally increased between 2100-2140 at storm midlevels; at low levels, vertical vorticity increased the most after 2140.
2. At ~2130, the storm had both a mid- and low-level mesocyclone, and the mesocyclones were vertically disconnected; at ~2140, there was one deep mesocyclone.
3. A DRC was identified at ~2140, after which low-level vorticity and circulation increased dramatically.

Markowski et al. (2012b) examined in-depth the possible sources of increased low-level rotation prior to tornadogenesis in the GC supercell. They found that:

1. As low-level rotation increased, the mesocyclone was ingesting mostly outflow air.
2. Circulation in the low-level mesocyclone was acquired baroclinically in the forward flank downdraft region and was modulated in the hook echo.
3. The DRC may have led to mesocyclone occlusion; low-angular-momentum air east of the mesocyclone was shut out and angular momentum increased.
4. Environmental vorticity likely did not contribute significantly to the circulation in circuits that were eventually located at the low-level mesocyclone.

The focus of this study is on the vertical development of rotation in the tornado and the short-time-scale, volumetric evolution of several physical characteristics of the tornado. However, it is worth examining MWR-05XP data in the 2143-2150 period for the possibility that the data provide more information about subjects discussed in

Markowski et al. (2012a,b). The main topic investigated is the time-height evolution of the mid- and low-level mesocyclone. Markowski et al. (2012a,b) used radar data that had volumetric update times of ~300 s (KCYS WSR-88D) and 120 s (DOWs), so there is utility in examining MWR-05XP data, which had volumetric update times more than ten times greater.

An overview of what the radial velocity field looks like prior to tornado formation is shown in Fig. 5.37. Of interest is the vertical development of the mesocyclone, rapid changes in mesocyclone strength, and mesocyclone scale contraction. Cyclonic shear that meets the TVS requirements outlined in Chapter 4.3.1 (strength and temporal continuity) is outlined in white circles, though, again, a TVS marker does not necessarily indicate an incipient tornado. At 2144:23, only inbounds can be identified in the lowest elevation angles, while cyclonic shear indicative of a midlevel mesocyclone can be seen at higher elevation angles (Fig. 5.37a). Further, at the four highest elevation angles shown, TVSs can be identified, though the TVS at 18.5° elevation angle is located more than 2 km northwest of that at the other three elevation angles. Two minutes later, at 2146:21, there is mostly broad cyclonic shear at midlevels with no obvious low-level mesocyclone signal, perhaps from a lack of scatterers in the region (Fig. 5.37b). In addition, at 9.8° and 12.7° elevation angle, the TVSs identified two minutes earlier still persist; at 15.7°, a new TVS is identified and at 18.5°, there is no longer a TVS.

By 2148:20, low-level rotation can be identified in MWR-05XP data, but there are no small-scale TVSs (Fig. 5.37c). At storm midlevels, the highest five elevation angles shown, there is broad, strong cyclonic shear and vertically continuous TVSs.

However, the TVSs at 9.8°, 12.7°, and 15.6° elevation angle are different from the ones shown two minutes earlier, the latter of which all have dissipated. At 2150:36, approximately 90 sec. prior to tornadogenesis, cyclonic shear is present at all levels and there are TVSs at all levels but the lowest one (Fig. 5.37d). Contrary to previous times, the TVSs in the highest five elevation angles at 2150:36 are all the same TVSs as observed two minutes prior (Fig. 5.37c), *however none of the TVSs shown at the final time are associated with the GC tornado* (see Chapter 5.2.2). The TVSs apparently become more frequent at low levels as tornadogenesis nears, but the life span of individual TVSs, as determined by the objective criteria, is highly variable at all levels. In addition, in data from the highest elevation angles scanned (~6-7 km in height), interpreting the approximate location of the mesocyclone was difficult as there were often multiple locations of strong cyclonic shear (e.g., the 18.5° elevation angle image in Fig. 5.37b).

During the 2143-2157 time period, maximum ΔV and shear calculations in the mesocyclone are made. Criteria for mesocyclones are less restrictive than for TVSs, requiring only a local maximum outbound and inbound with distance between the two of 1-10 km. The above definition is similar to that in the AMS Glossary, which states mesocyclones have a diameter of 2-10 km with shear of ~.01 s^{-1} and higher (Glickman 2000). In the GC supercell, mesocyclone shear calculated from MWR-05XP data is typically .01-.02 s^{-1}. Calculations are not made above 15.6° elevation angle because of the aforementioned difficulty in identifying what features are representative of the mesocyclone. Data from 8.3-15.6° elevation angle still provide a thorough look at the evolution of the midlevel mesocyclone. Tornadogenesis was at ~2152, but the evolution

of the mesocyclone during both the pre-tornadogenesis and tornadogenesis period is discussed here for convenience.

The maximum mesocyclone ΔV increases steadily in the period leading up to tornadogenesis (Fig. 5.38). Mesocyclone ΔV at the lowest-observed level (1.0° elevation angle) and in the low-level mesocyclone increases slowly throughout the period (Fig. 5.38a), though there is an observable jump in ΔV at around the time of tornadogenesis at some levels (Fig. 5.38b). In contrast, ΔV in the midlevel mesocyclone begins to decrease ~5 min. prior to tornadogenesis before also slowly increasing. There is no obvious trend to the distance between the maximum inbound and outbound radial velocities in the mesocyclone (Δx; Fig. 5.39). There is a signal of a scale contraction at the lowest level prior to tornadogenesis (Fig. 5.39a), but there is no evidence that the scale contraction is vertically consistent (Fig. 5.39b). The GC mesocyclone Δx is quite variable (e.g., at 2.5° and 8.3° elevation angle in Fig. 5.39b), similar to that in the Hog Back mesocyclone/tornado cyclone. It again is likely that a combination of poor radar azimuthal resolution beyond ~15 km range and variability in the location of maximum point values leads to temporally inconsistent Δx values. Mesocyclone shear (Fig. 5.40), which is calculated using ΔV and Δx values, also is noisy. There is an exponential increase in shear at the lowest levels (Fig. 5.40a) and large increases at midlevels (Fig. 5.40b) after 2155, though by these times it may be difficult to accurately distinguish between the contracted mesocyclone and the tornado.

The quantities shown in Figs. 5.38-5.40 are shown again for the lowest four elevation angles (Fig. 5.41). The same slow increase in ΔV is seen before and after tornadogenesis, but also of note is the downward progression of low-level mesocyclone

formation (i.e., when both an outbound and inbound maximum can be identified; Fig. 5.41a). It takes ~80 sec. for the mesocyclone to meet the criterion every ~400 m, or a rate of ~5 m s^{-1}, though again the lack of scatterers in the area of the mesocyclone may adversely affect the accuracy of the criterion. Only at the very lowest level is there an obvious signal of mesocyclone scale contraction prior to tornadogenesis (Fig. 5.41b). At the next three levels (~0.6-2.3 km), Δx decreases from ~4 to ~1 km at ~2155, three minutes after tornadogenesis. As in the Hog Back case, noisy data preclude determination of vertical directionality to the Δx decrease. The large decrease in Δx is associated with an abrupt increase in mesocyclone shear at 1.0° elevation angle near the time of tornadogenesis and at the three subsequent levels after ~2155 (Fig. 5.41c).

5.2.2 Tornadogenesis Phase: 2150-2157

A tornado in visible contact with the ground was not observed until ~2205. However, by using a combination of higher-spatial-resolution data from DOW7 and information from an in-depth damage survey, it was determined that the tornado actually formed about 13 min. before a condensation funnel formed, at ~2152 (e.g., Wakimoto et al. 2011; Markowski et al. 2012a). In studying tornadogenesis, it is assumed that tornado formation occurred at ~2152; the collocation of radar data close to the ground with damage indicators provides confidence in this assumption. At 2157:19, MWR-05XP ceased data collection for ~2.5 min. to change the scanning sector, so it is a natural and convenient stopping point for the tornadogenesis period in this analysis, though again the choice is purely subjective.

The main question addressed in this section is "Did the tornado form near the surface in a bottom-up manner or at some level above the surface in a top-down manner?" This question is answered by using the criteria defining a TVS set forth in Chapter 4.3.1 and working backwards from a time period in which the tornado was well-defined. By the time of the last scan prior to the data gap, 2157:19, the tornado is easily identifiable in MWR-05XP data (Fig. 5.42). The same TVS is followed for another 30+ min. and is collocated with the tornado, thus providing near certainty that the TVS is representative of the tornado. Starting from that point (2157:19), volumetric MWR-05XP data are analyzed moving *backward in time* to follow the TVS to its origin. The TVS origin occurs when, for at least 30 sec. continuous, the TVS either (i) no longer has adjacent gates with inbound/outbound radial velocities or (ii) has a ΔV threshold below 15 m s^{-1}. In the previous sections, it was mentioned that midlevels of the storm contained numerous cyclonic shear signatures. It is occasionally difficult to interpret when one TVS begins and another one ends, particularly between 2.5-4.0 km, however, this confusion typically affects the TVS origin time by less than 1 min. Very rarely does TVS ΔV weaken to under 15 m s^{-1} prior to its origin time. Knowing that other instruments have verified the time of tornadogenesis as 2152 is advantageous in assessing the fidelity of the criteria set forth here in determining the vertical formation of the TVS.

The TVS associated with the GC tornado is followed backward in time for all 14 elevation angles (e.g., Fig. 5.43). The vertical development of the TVS is shown in Figure 5.44. The TVS develops upward in time from ~2152-2155. The TVS is identified first at the lowest elevation angle (1.0°) at 2151:54. Over the next 90 sec., the

TVS builds upward to 2 km in a relatively slow manner. Above ~2 km, however, TVS formation progresses upward rapidly, reaching the highest observable level, 20.0° elevation angle (~5.75 km), at 2155:03. Only twice are the TVS criteria first met at a higher height level before a lower height level, and on those occasions, the time offsets are only 15 sec. The consistency with which the TVS is identifiable at greater heights at later times provides strong, convincing evidence that the TVS builds upward with time. In addition, the TVS criteria being met first at 2151:54 is consistent with the ~2152 tornadogenesis time as estimated from high-resolution radar data and the detailed damage survey. Using the approximate depth of the TVS and the time period over which it formed, the "formation velocity" of the TVS can be estimated as upward at ~29 m s^{-1}. More specifically, the formation velocity in the lowest 2 km (above 2 km) is ~11.5 m s^{-1} (~76 m s^{-1}). Note that the TVS forms upward from near the surface to almost 6 km in ~3 min. During that period, the MWR-05XP completes 23 volume scans, while a conventional mobile Doppler radar (WSR-88D) would complete two (less than one) volume scan(s).

The TVS is continuously identifiable in time and height through 2157:19, providing 337 separate observations of its location and strength (Fig. 5.45-5.46). Typically, TVS ΔV increases to greater than 30 m s^{-1} within one minute of formation and generally stays at 30-45 m s^{-1}. Above 3 km, there is a tendency for the TVS to strengthen in an upward fashion with time in the first two minutes after it formed (Fig. 5.45). It is likely that the upward formation of the TVS and the manner in which the TVS initially strengthens indicates that the tornado is being driven by a central updraft that advects and stretches vertical vorticity upward with time. However, subsequent

changes in TVS strength do not always progress in a similar "bottom-up" manner. While, on average, ΔV increases after tornadogenesis (Fig. 5.46a), in the minute prior to the data gap at 2157:19, TVS strength increases above 3 km while it is highly variable below 3 km (Fig. 5.46b). During this time period, there is no linear relationship between ΔV and height (Fig. 5.47a) or normalized ΔV and height (Fig. 5.47b). Chapter 5.2.3 will discuss in detail several changes in TVS strength observed in the tornado's mature stage.

The TVS track is followed at several different elevation angles (Fig. 5.48). The location of the TVS shown above 3 km is well to the northeast of that near the surface. Also, the TVS near the surface has a translational direction toward the east-southeast, while at higher levels, the TVS has a northward component of motion. To determine the tilt of the TVS after it is identified, vertical cross sections of TVS location are constructed (Fig. 5.49). The tornado is consistently tilting toward the east (Fig. 5.49a) and north (Fig. 5.49b) with increasing height above the ground. The tilting of the vortex is immediate upon formation (Fig. 5.50-5.51) rather than a occurring after formation. Prior to the data gap, there is a signal that tilting toward the east (Fig. 5.50) and north (Fig. 5.52) is lessening. Trends in tornado tilt generally are consistent with height (Fig. 5.52a) and the inclination angle (angle from the vertical) of the vortex varies with time and height from 25-40° (Fig. 5.52b), a value consistent with previous observations of tornadoes (e.g., Alexander 2010).

To summarize, the first two phases of the GC supercell as observed by the MWR-05XP present an opportunity to examine unique rapidly-updating, volumetric data of a supercell prior to and at tornadogenesis. Prior to tornadogenesis, a well-

defined midlevel mesocyclone is observed to contain a large number of TVSs that typically lack time and/or height continuity. A mesocyclone and the aforementioned transient TVSs are observed at progressively lower levels in the MWR-05XP data. None of the low- or midlevel TVSs identified prior to tornadogenesis are an incipient tornado associated with the GC tornado. Several minutes after tornadogenesis, a strong TVS is observed at all 14 elevation angles in MWR-05XP data. From that point, the TVS is tracked backward in time to identify the origin time and height at each level. From this analysis, the TVS is observed to form first near the surface and then steadily upward to ~2 km. Above ~2 km, the TVS rapidly forms upward to ~5.5 km. The entire process of TVS formation up to ~5.5 km takes ~3 min. The TVS becomes steadily stronger at all levels after it forms and is tilted noticeably toward the north with height as it forms.

5.2.3 Tornado Mature Phase: 2200-2216

At 2157, the MWR-05XP crew decided to shift the scanning sector clockwise and reduce the maximum unambiguous range from 45 km to 30 km as the supercell approached the radar location. At the time, the crew was unaware that there was an ongoing tornado because of poor resolution in the real-time data display and the lack of a tornado condensation funnel or debris cloud. Data were lost for ~2.5 minutes, though the sector shift allowed for over 15 minutes of continuous data collection of a tornado at close range using 6.5 sec. volumetric updates and a higher Nyquist velocity (~36 m s^{-1}). The focus of data analysis during this time period is on rapid changes in TVS intensity and volumetric characteristics of the TVS.

When data collection resumed, the supercell had a well-defined hook echo (Fig. 5.53a) and a TVS that is easy to identify in radial velocity data as representative of the tornado (Fig. 5.53b). During this time period, 2161 observations of the TVS are made. A time-height plot of ΔV is shown in Figure 5.54. Note that during the mature stage of the tornado, there are no missing data. However, above 2 km, there are short time periods when the TVS can no longer be identified and other times of rapid strengthening and weakening in an oscillatory nature. Typically, ΔV values are 50-60 m s^{-1} during this stage but there are several time periods when ΔV has significant spread (Fig. 5.55). By separating TVS data points into two groups, TVS observations from above and below 2 km (Fig. 5.56a), it can be seen that TVS ΔV above 2 km is much more variable in time than that below 2 km. By averaging the ΔV values at each time (Fig. 5.56b), five separate oscillations in ΔV are identified, occurring with a period of ~2-5 minutes. In the lowest 2 km, ΔV is comparatively steady at ~60 m s^{-1}. The height-dependent oscillations identifiable in Fig. 5.56b are discussed further below.

The first oscillation occurs from ~2200-2205 and the second from 2205-2208 (Fig. 5.56b); both oscillations are relatively large in ΔV amplitude. It is the second oscillation in which the TVS criteria are not met for a period of time at some of the higher elevation angles (Fig. 5.54). The ΔV progression at several elevation angles provides a clearer picture as to how the first two oscillation progress at individual levels (Fig. 5.57). At higher elevation angles (above ~2 km), ΔV first decreases, then increases to a maximum at ~2205, followed then by a rapid and precipitous decline (Fig. 5.57a,b). In contrast, ΔV in the lowest 2 km stays at ~55-60 m s^{-1} throughout the time period in which ΔV decreases aloft (Fig. 5.57c). *In the first oscillation, it can be seen that the*

decline in ΔV occurs first at 12.7°, then at 15.6°, and finally at 18.5° elevation angle (Fig. 5.57a). The progression is similar at 14.1°, 17.1°, and 20.0° elevation angle (Fig. 5.57b) in that the ΔV decline occurs in data from the lowest elevation angle first.

The TVS criteria are not met at various times during the second decline in ΔV, so it is difficult to assess from Fig. 5.57 whether there is vertical directionality to the second oscillation as well. As a result, maximum GTG shear values are recorded at times when the TVS criteria are not met (Fig. 5.58). After including cyclonic shear data, *it can be seen that the decline and subsequent increase in ΔV in the second oscillation also progresses in a bottom-up fashion*, both in the 12.7°, 15.6°, 18.5° (Fig. 5.58a) and the 14.1°, 17.1°, 20.0° elevation angle graphs (Fig. 5.58b). Both the oscillations and the upward progression of the oscillations occur rapidly. Vertical profiles of ΔV for the first (Fig. 5.59a) and second (Fig.5.59b) oscillations also show them occurring rapidly at greater heights later in time. For example, at 2205:18, ΔV is at a minimum at ~2.2 km, while ~35 seconds later ΔV is at a minimum at ~3.5 km (Fig. 5.59b).

To better understand why there is a sudden decrease in ΔV after an increase, the radial velocity progression in the TVS at 12.7° and 20.0° elevation angle is examined every 6.5 sec. during the first (Fig. 5.60) and second (Fig. 5.61) ΔV oscillations. At 12.7° elevation angle during the first oscillation (Fig. 5.60a), the TVS weakens between 2200 and 2201 and then gradually re-strengthens. During the same time period, the secondary ΔV maximum (likely that of the mesocyclone) progresses in the opposite manner, first strengthening and then weakening. At 20.0° elevation angle, the evolution of the TVS is complicated (Fig. 5.60b). The TVS moves in a cyclonic pattern, first moving southeast (2200:19-2200:38), then north (2200:38-2201:15), northwest

(2201:34-2202:29), and south (2202:48-2203:25). While the TVS moves cyclonically, ΔV is unsteady, but generally weakens from 2200-2202 and strengthens from 2202-2205. In following the progression of the TVS at 12.7° elevation angle during the second oscillation (Fig. 5.61a), it can be seen that the TVS rapidly declines in strength (2205:12-2205:25) followed by a gap with no TVS (2205:25-2206:02). Then, *a TVS forms again, but well east of the location where the original TVS dissipated (2206:02).* The distance between the TVS locations is ~1.2 km and the time between observations is ~44 sec. As a result, unless the tornado translated at ~30 m s^{-1} during the time period shown in Fig. 5.57, *the two TVSs are different* and not resulting from poor detection by the MWR-05XP[1]. At 20.0° elevation angle, the progression is the same as that seen at 12.7° elevation angle, just delayed in time by ~1 min. (Fig. 5.61b). The TVS begins to weaken just short of 2206, followed by a period of no identifiable TVS (2206:08-2206:20), and then a TVS again is located southeast of where it was last identified (2206:20-2206:33).

The 1.0° elevation angle scans are inspected for ΔV oscillations like those seen above ~2 km (Fig. 5.62). In the case of the first oscillation, there is a modest increase in ΔV in the lowest 2 km during the time period the TVS weakens above 2 km (Fig. 5.56b). At the lowest-observed level, the increase in ΔV is readily apparent (Fig. 5.62a). Also, there is an apparent scale contraction that takes place on a scale larger than that of the tornado (2200:56-2201:15 in Fig. 5.62a). For the second oscillation, a similar evolution as that seen in the first oscillation follows at low levels (Fig. 5.62b). There is a decrease in radial velocity on the mesocyclone scale. However, there is not an obvious

[1] Average TVS translational speeds of ~9-13 m s^{-1} during the mature stage of the GC tornado were calculated using ~2 min. integration times.

increase in radial velocity in the TVS as was seen in the first oscillation. The evolution of the radial velocity field in data from 2.5°, 3.9°, and 5.4° elevation angle during the first oscillation (not shown) is similar to that described above for data from 1.0° elevation angle.

During the same time period in which the first two oscillations are occurring, the condensation funnel of the GC tornado first becomes visible (Fig. 5.63). According to Wakimoto et al. (2011), there are actually two "attempts" at the formation of a condensation funnel. The first funnel occurs from 2202:12-2202:42 and the second funnel forms at ~2206 (Fig. 5.64). After the latter time, the GC tornado has an identifiable condensation funnel or debris cloud in the sub-cloud layer until the tornado dissipates at ~2230. In Wakimoto et al. (2011), low-level ΔV and Δx calculations from DOW7 are correlated with the formation of the condensation funnels. The first condensation funnel forms at ~2202 following a sharp decrease in Δx at 0.5° elevation angle at ~2201. That funnel cloud dissipates shortly afterward and Δx increases. About two minutes later, at ~2206, the second condensation funnel forms. In the first DOW7 0.5° elevation angle scan after the second funnel forms, Δx decreases significantly. The progression of the MWR-05XP radial velocity field in the area of the TVS is qualitatively similar to that shown in Wakimoto et al. (2011; Fig. 5.64) despite the use here of data with much coarser spatial resolution.

The third and fifth ΔV oscillations observed above 2 km are relatively small in magnitude, while the fourth oscillation is comparable in amplitude to the first two oscillations (Fig. 5.56b). In addition, oscillations 3-5 are not associated with any visually striking changes in the GC tornado as with the first two oscillations. The

progression of ΔV oscillations 3-5 above 2 km are shown for several different elevation angles scans in Figure 5.65. The progression of the third oscillation, like the first two oscillations, is upward with time (e.g., Fig. 5.65a). However, the fourth and fifth oscillations do not have a discernible vertical trend (e.g., Fig. 5.65b). To examine further the apparent lack of vertical directionality to the last two oscillations, ΔV in the lowest and highest elevation angle scans where the oscillations are observed are compared (Fig. 5.66). Upward progression to the third oscillation is clearly identified, but again there is no obvious vertical directionality in the fourth oscillation. In the final oscillation, decreases in ΔV in 12.7° elevation angle scans slightly lead those in 20.0° elevation angle data, but not enough to say with certainty that there is a vertical lag. The lack of vertical directionality to the fourth oscillation also is seen from several ΔV profiles at that time (Fig. 5.67). Prior to the data collection gap, there is another downward trend in ΔV which may be indicative of another oscillation. When data collection resumes at ~2217, there are no longer rapid changes in ΔV, but rather longer-term ΔV declines (see Chapter 5.2.4). During the mature phase of the tornado, ΔV has a slight tendency to decrease with height (Fig. 5.68a). However, there are still many observations of ΔV at midlevels that are similar to or greater in value than those at low levels (Fig. 5.68b), so there is no "typical" ΔV profile during this time period.

The progression of the radial velocity field for the fourth oscillation is somewhat similar to that seen in the second oscillation (Fig. 5.69). However, in the fourth oscillation, the TVS is only absent for a single scan at 20.0° elevation angle rather than for several scans at multiple levels. Nonetheless, the TVS does "jump" south ~600 m in 13 sec. Below 20.0° elevation angle (not shown), the TVS is identifiable at all times and

simply weakens for a brief period of time. Radial velocity data above 20.0° elevation angle (~3.5 km) would be beneficial in assessing whether the oscillation is associated with a complete TVS dissipation as is observed with the second ΔV oscillation. In the radial velocity data, the third and fifth oscillations are associated only with weakening and strengthening of the TVS.

The TVS is moving toward the southeast at all levels prior to the midlevel TVS dissipation (Fig. 5.70). The gap in the paths, for example at (-7, 8.5) in Fig. 5.70 at 11.2° and 20.0° elevation angle, are times when the TVS cannot be identified at those levels. When the TVS again can be identified, the paths at all levels are very similar for several minutes. At ~2211, the TVS is moving toward the southeast near the surface but increasingly toward the east at low and midlevels. The vertical tilt of the TVS in the east-west direction during the tornado mature phase generally is modest (Fig. 5.71a). Only near the time of the second ΔV oscillation does the TVS tilt significantly, in this case, toward the west with height. Also, as the tornado enters the dissipation phase, it begins to tilt increasingly toward the east. When data collection resumes at 2200, the TVS is tilted toward the north with height (Fig. 5.71b), much as it was when data collection stopped at ~2157 (Fig. 5.49b). The TVS then becomes more vertically upright for several minutes before the northward tilt returns when data collection again stops.

The orientation of the tornado changes at the time of the second ΔV oscillation, when the TVS dissipation and secondary genesis aloft occurs (Fig. 5.70-5.71). The progression of the TVS location during this time specifically is shown through x-z (Fig. 5.72) and y-z (Fig. 5.73) vertical cross-sections of TVS position. As the dissipation

begins around 2 km, the TVS is tilted significantly toward the east and north. *However, as the TVS reforms, it is nearly vertically upright with very little tilt*. Similarly, the horizontal displacement of the vortex sharply decreases as the TVS reforms above 2 km (Fig. 5.74a). Generally, the tilt/displacement of the vortex is highly variable above ~2 km, while it remains relatively steady closer to the surface. The inclination angle of the TVS during the mature phase of the tornado (Fig. 5.74b) is ~10-30°, less than that observed in the tornadogenesis phase (Fig. 5.52b), but again is highly variable at storm midlevels. The tilt/displacement is well correlated in height (Fig. 5.75) much as the ΔV oscillations were, though the displacements do not have an obvious vertical directionality and occur almost simultaneously above 2 km. While it may be tempting to relate the intensity of the TVS to the tilt of the vortex, the results of a direct comparison of the two quantities (Fig. 5.76) are inconclusive at best. After 2211, the TVS gradually becomes more tilted as the tornado enters the dissipation phase (Fig. 5.74-5.76).

5.2.4 Tornado Dissipating Phase: 2217-2231

As the tornado moved eastward away from the radar, the MWR-05XP crew stopped data collection to shift the scanning sector clockwise. The sector shift resulted in a 64 sec. loss of data at ~2216. The volumetric update time and Nyquist velocity were unchanged. There was one additional data gap, occurring at 2221:29 for 99 sec. This data gap again was to move the sector clockwise so as not to lose the tornado in MWR-05XP data collection. A slight expansion of the data sector width resulted in volumetric update times of 7.5 sec., but there was no change in the Nyquist velocity.

The primary focus of data analysis during the dissipating stage of the tornado is on volumetric characteristics of the TVS and the dissipation of the TVS.

In Chapter 4.3.1, objective criteria for a TVS were established in order to determine when a TVS first formed at each elevation angle. In order to determine when the TVS is no longer identifiable, the same criteria are used. When a shear signature has ΔV of less than 15 m s^{-1} or does not have a couplet for more than 30 sec. of data continuously, it is no longer considered a TVS. There are no situations for the GC tornado or the Kingfisher, OK tornado (see Chapter 5.3) in which a TVS dissipates and then re-establishes itself under the criteria. A time-height plot of the ΔV field is shown in Fig. 5.77. The TVS dissipates under the objective criteria first at ~2 km. From that point, the TVS dissipates upward and downward with time, dissipating last in the lowest 1 km. During the latter half of the tornado mature stage and in the dissipating stage, the GC tornado moves within 10 km of the MWR-05XP, so that the maximum heights of TVS observations decrease. As a result, there is uncertainty as to whether the upward dissipation above 2 km is an artifact of the imperfect objective criteria or a real signal of upward dissipation above a certain level. As alluded to in Chapter 4.3.1, during TVS dissipation, there was a period of time in which there was strong cyclonic shear but no couplet aloft. The strong flow away from the radar may have masked a vortex in ground-relative data at these times. If the second criterion for a TVS were ignored, Figure 5.77 would be altered such that the TVS at the two highest elevation angles would persist for several more minutes. In the lowest ~1 km, the objective criteria of TVS dissipation match up well with visual tornado dissipation (Fig. 5.78); the tornado

is no longer identifiable ~30 sec. after the final TVS observation in MWR-05XP radar data.

Until about the time of the data gap at 2221:29, decreases in ΔV can be seen at all levels (Fig. 5.79). In addition, there is some evidence supporting the existence of a sixth ΔV oscillation that is, again, most identifiable in data from higher elevation angles (Fig. 5.80). In this case, there is a decrease in ΔV of 15-20 m s^{-1} over a few min. period in data from 12.7° and 15.6° (Fig. 5.80a) and from 14.1°, 17.1°, and 20.0° elevation angle (Fig. 5.80b). In both cases, the ΔV decrease is seen at lower elevation angles first and then at higher elevation angles. However, the time gap is small, and vertical profiles of ΔV at the time of the oscillation do not provide clear evidence of vertical directionality (Fig. 5.81). Following the data gap, general decreases in ΔV continue at all levels until TVS dissipation. The aggregate vertical profiles of ΔV decrease with height (Fig. 5.82a); the negative linear correlation is even stronger when ΔV is normalized by that observed at 1.0° elevation angle (Fig. 5.82b). In the latter case, the correlation coefficient and rank correlation between ΔV and height approach -0.60, the highest values seen in any of the MWR-05XP TVS variable comparisons.

The TVS begins to move in radically different horizontal directions at different levels (Fig. 5.83) in the ~7 min. preceding TVS dissipation. There is very little spread in the horizontal direction the TVS moves in; the TVS either moves toward the southeast or toward the east-northeast. Based on the TVS position at three individual elevation angles (Fig. 5.84), roughly representing near-ground, low-level, and midlevel observations, it can be seen that the southeast TVS movement occurs in the lowest levels and the east-northeast motion occurs above the lowest levels. An approximate

(u,v) storm motion of (10.45, -1.3 m s^{-1}) was determined in Markowski et al. (2012a); the direction also is shown in Fig. 5.84.[2] Above the lowest levels, the TVS continues to move in a direction similar to that of the storm, while close to the surface, the TVS moves well to the right of the storm.

During the tail end of the tornado mature phase, the TVS begins to tilt noticeably again toward the north and east with increasing height (Fig. 5.71). That trend continues during the tornado dissipation phase (Fig. 5.85). Eastward (Fig. 5.85a) tilt is largest leading up to the initial dissipation at ~2 km. Southward tilt (Fig. 5.85b) also is large as the TVS moves toward the south at the lowest levels. Once TVS dissipation begins, subsequent dissipation above ~2 km occurs quickly. However, at the lowest levels, the TVS is identifiable for an additional ~3 min. (Fig. 5.86-5.87). The TVS observed in data from 20.0° elevation angle (~3.5 km) is located ~3.5 km to the northeast of the TVS near the surface at the time it dissipates at midlevels (Fig. 5.88a). The large horizontal distance between the TVS near the surface and at midlevels is associated with the largest inclination angles (~45°) observed during the tornado's lifecycle (Fig. 5.88b). However, the lack of a TVS in data from several elevation angles between low levels and midlevels is evidence that the tornado may be vertically disconnected from ~2224-2226.

To summarize, data from the mature and dissipation phases of the GC tornado provide an opportunity to examine short-time-scale, volumetric processes that tornadoes may undergo as well as the volumetric evolution of tornado dissipation. In the mature phase of the tornado, the associated TVS is observed to undergo several height-

[2] In Markowski et al. (2012a), the authors observe that storm motion deviated more to the left of their estimate after 2100, in which case the TVS at low levels moves even more to the right of the storm than indicated in Fig. 5.82.

dependent intensity fluctuations. The fluctuations are observed above 2 km and, in one case, are associated with a TVS dissipation and secondary genesis during the formation of the tornado condensation funnel. At least some of the intensity oscillations are observed to occur upward with time. During the intensity oscillations aloft, TVS intensity is relatively steady in the lowest 1.5 km. TVS tilt varies during the mature phase, but often is large and toward the northeast with height. Several minutes prior to tornado dissipation, TVS intensity decreases above 2 km. The TVS criteria are no longer met first at ~1.5 km; the TVS then dissipates upward from that height. Several minutes later, the TVS dissipates in the lowest 1 km. The TVS moves increasingly southward in the lowest levels in the dissipation phase while at midlevels, the TVS continues to move toward the east. As a result, the TVS is tilted severely toward the northeast with height as it dissipates.

5.3 Kingfisher, OK Tornado on 19 May 2010

The final tornado under examination in this study occurred on 19 May 2010 near Kingfisher, OK. Data collection by MWR-05XP took place during VORTEX2 as in the previous dataset. The tornado was ongoing when MWR-05XP data collection began, but it was not viewable from the deployment location to the south of the supercell (Fig. 5.89). The tornado was rated EF-1 based on a damage survey performed by the NWS. The same survey estimated the tornado as occurring from 2233 to 2300. However, both DOW7 and the MWR-05XP contain likely tornado data ending at later times than indicated in the damage survey. The MWR-05XP was scanning from 2259:06-2314:19

and data collection was from 1-40° elevation angle with volumetric update times of 12 sec. This dataset is the first one MWR-05XP obtained of a tornado up to 40° elevation angle.

The TVS associated with the tornado was located at ranges of ~6-9 km from the radar, so heights sampled, assuming a relatively level radar, ranged from ~0.1-7.5 km. The deployment site for data collection was a relatively level (in the subjective opinion of the MWR-05XP crew) gravel road (Fig. 5.90). The tornado was within 10 km of the radar at all data collection times, so estimated height (Fig. 5.91) and horizontal position (Fig. 5.92) errors are thought to be small. Data collection was interrupted twice: at 2303:45 for 132 sec. and at 2309:10 for 133 sec. Both times, the data collection gap occurred when the radar crew changed the sector clockwise to account for the motion of the tornado/storm. Based on the radar presentation of the tornado, it is likely that only the dissipation phase of the tornado was sampled, so the focus here is on volumetric characteristics of the TVS and on TVS dissipation.

A total of 501 observations of the TVS are made for the Kingfisher tornado dataset. Interestingly, a TVS can be identified in data only up to 31° elevation angle. It is unclear whether the tornado does not extend higher, vertical velocity "contamination" complicates TVSs, or tornado dissipation already has occurred at upper levels when data collection begins. Radial velocity scans from 2.5° elevation angle at several times while the tornado is ongoing are shown in Figure 5.93. The TVS signature is easily identifiable when data collection begins, but quickly weakens at all levels as it moves toward the south. A slow, steady general decline in ΔV is observed during the dissipation phase of the tornado (Fig. 5.94). Unfortunately, there are no data or not

enough data from the tornadogenesis or mature phases of the tornado's lifecycle to assess whether there are height-dependent changes in TVS ΔV as seen in the GC tornado. During the dissipation phase, ΔV is variable at all levels (Fig. 5.95a), but once ΔV is scaled to that observed in 1.0° elevation angle scans (Fig. 5.95b), a strong signal of ΔV decreasing with height can be observed. The decrease in ΔV with height during the tornado dissipation phase also was observed for the GC tornado.

The dissipation of the TVS proceeded generally in a top-down manner (Fig. 5.96). However, TVS dissipation occurs first not at the highest-observed level, but rather at a height of ~2.75 km at ~2301. TVS dissipation then progresses upward and downward with time from that height. The upward progression of dissipation occurs much faster than the downward progression of dissipation. About ~2 min. after TVS dissipation at ~2.75 km, TVS dissipation at the highest-observed level (~7.5 km) occurs. Conversely, the downward progression of TVS dissipation takes over 10 min. to complete. The last observation of the TVS is made at 2311:58 at 7.0° elevation angle (~700 m). TVS ΔVs above 3 km are universally below 30 m s^{-1} and stay that way during the MWR-05XP observational period. In the lowest 3 km, ΔVs often are 45-65 m s^{-1}, but decrease after the TVS dissipates aloft. The TVS dissipation process is very similar to that seen in the GC tornado; the major difference between the two cases is the ~1 km disparity in height at which TVS dissipation first occurs, ~1.8 (2.75) km for the GC (Kingfisher) tornado.

During the tornado dissipation phase, the TVS moves in very different directions at different heights (Fig. 5.97). TVS motion ranges from northeastward to southeastward in the 10 min. preceding dissipation. In looking at the TVS tracks from

data at three individual elevation angles, it can be seen that the TVS moves southward at the lowest levels and more eastward up into storm midlevels (Fig. 5.98). A storm motion is estimated from KTLX WSR-88D data by tracking the forward flank reflectivity core over a ~30 min. period centered on MWR-05XP data collection times. The resulting (u,v) storm motion is (13.6, -0.7 m s^{-1}) and is provided in Fig. 5.98 as a means of comparison for TVS motion. In this case, the TVS at higher levels moves in a direction to the left of the storm, while the TVS at low levels moves well to the right of storm motion during the latter half of its dissipation. In both the path taken by the TVS and the motion of the TVS compared to that of the storm, the Kingfisher TVS (Fig. 5.98) behaves very similarly to the TVS associated with the GC tornado (Fig. 5.84).

The TVS tilts toward the east (Fig. 5.99a) and north (Fig. 5.99b) with height during the dissipation phase of the tornado. In the progression of both the east-west (Fig 5.100) and north-south (Fig. 5.101) vertical cross-sections of TVS position, the TVS above the height of the initial dissipation exhibits very little movement. In other words, after the TVS first dissipates, the TVS continues on toward the south and the east at heights below 2.75 km. However, above 2.75 km, the TVS moves very little in the east-west direction and moves slightly toward the north. As shown earlier, eventually the TVS is observable only in the lowest 1 km prior to dissipation at all levels. At upper levels, horizontal TVS displacements surpass 5 km (Fig. 5.102a) and TVS inclination angles reach as high as 50°. As the tornado decays, it is tilted severely, if the vortex is still continuous vertically.

To summarize, volumetric data from the Kingfisher tornado are used to examine a second case of tornado dissipation. The dissipation of the Kingfisher tornado is

remarkably similar to the dissipation of the GC tornado. The TVS intensity is weaker above 2 km prior to dissipation and the TVS criteria are no longer met first at ~3 km. The TVS then dissipates upward from ~3 km within 2 min. The TVS in the lowest 1 km persists for another ~10 min. before dissipating. The TVS has disparate translational motion with height. Near the surface, the TVS moves to the right of the storm (toward the south) and above that, the TVS moves in a direction similar to that of the storm. As a result, the TVS is tilted several kilometers to the northeast in the lowest 5 km as it dissipates aloft.

Chapter 6

Discussion

6.1 Cyclonic Tornadoes

6.1.1 Tornadogenesis

Rapidly-updating volumetric data of the supercell tornadogenesis process have been analyzed from two cases: 23 May 2008 and 5 June 2009. In both datasets, the objectively-defined TVS clearly built upward with time at the time of tornadogenesis (Figs. 5.5 and 5.44). There is no evidence in either case that the TVS built downward from midlevels in the storm prior to or at the time of tornadogenesis. As discussed earlier, in tornado case studies and in a climatology of DOW Doppler radar observations by Alexander (2010), there also was no evidence of a descending TVS in tornadogenesis cases. The combined results now number eight cases utilizing high spatial and/or temporal resolution data without verifying the descending TVS tornadogenesis paradigm (Table 6.1). In addition, most numerical modeling studies and many analytical modeling studies of the tornadogenesis process do not include what would be considered analogs to radar-observed descending TVSs (e.g., Trapp and Fiedler 1995; Gaudet and Cotton 2006; Davies-Jones 2008). Therefore, it is natural to ask "Why has recent research, including results from numerical and analytical models, and examination of high resolution radar data, failed to document the mode I tornadogenesis process, as proposed by Trapp and Davies-Jones (1997) and ostensibly observed by Trapp et al. (1999)?"

In order to attempt an answer to the above question, it is instructive to investigate the "two mode" tornadogenesis model in detail beyond the information presented in Chapter 2.1. Prior to Trapp and Davies-Jones (1997), there were very few proposed physical explanations of what the descending TVS might represent. Many authors expressed skepticism or confusion about the role of the TVS in any tornadogenesis model. Rotunno (1986) wrote "…the dynamical connection between the TVS and the visible funnel in 'contact' with the ground is not known. That is to say, the appearance of a TVS aloft may not be relevant." Rotunno (1993) commented "Future research will continue on the smaller scale to reach a better understanding of how the tornado fits into the thunderstorm. (I still do not know where the tornado vortex signature fits into the picture.)" In a panel discussion following the presentation of Davies-Jones and Brooks (1993), Davies-Jones responded to a question about the role of the TVS in tornadogenesis by saying "I don't know. The TVS mystifies me because, according to Doppler radar observations, it begins aloft, and I don't understand why." Wicker and Wilhelmson (1995) suggested, based on modeling results, that the midlevel TVS represents enhanced midlevel rotation that causes strong upward VPGFs. The VPGFs are associated with a strengthening low-level updraft and increased near-ground convergence such that a more favorable environment for tornadogenesis exists.

To the author's knowledge, at the time Trapp and Davies-Jones (1997) argued for a bimodal tornadogenesis model with mode I (descending) and mode II (non-descending) tornadogenesis, the only documented cases of descending TVSs coincident with tornadogenesis were those made by Brown et al. (1978) and Vasiloff (1993). Therefore, in order to determine the relative frequency of mode I and mode II

tornadogenesis, Trapp et al. (1999) used a sample of 52 tornadoes observed by the WSR-88D network. The authors found that over half of all tornadoes in their sample were associated with a descending TVS, consistent with the mode I tornadogenesis archetype (Fig. 2.1). The large percentage of tornadoes that were preceded by a descending TVS in their sample provided increased confidence that previous observations were not outlier events. However, currently the evidence cited in support of mode I tornadogenesis is still based on Brown et al. (1978), Vasiloff (1993), and Trapp et al. (1999). In fact, *a literature review conducted by this author revealed no additional observational cases of mode I tornadogenesis in peer-reviewed papers published after Trapp et al. (1999).*[3] As a result, the aforementioned three studies are the only observational examples of mode I tornadogenesis presented in the literature. In contrast, there have been several observational examples of mode II tornadogenesis documented in the literature via WSR-88D and TDWR data (Dunn and Vasiloff 2001; Burgess et al. 2002) in addition to the numerous studies documented above that used mobile, Doppler radar data, including this study. Therefore, a look at the criteria established by Trapp et al. (1999) in determining whether a tornado formed via mode I or mode II tornadogenesis is warranted.

Trapp et al. (1999) presented objective criteria to determine whether tornadogenesis was considered descending or non-descending. A confirmed tornado was necessary and approximate tornado start times from *Storm Data* and damage surveys were used to estimate tornadogenesis times. TVSs associated with the tornado

[3] Dowell and Bluestein (2002b) discuss the possibility that vertical vorticity retrieved in a pseudo-dual-Doppler analysis may have descended to low levels prior to tornadogenesis in their case. However, a local maximum in vorticity also was observed at low levels prior to tornadogenesis and a time-height analysis of GTG shear could not be undertaken because of irregularly-spaced data. As a result, their example is considered incomplete.

were manually identified to assure they matched with the approximate location of tornado damage. In order to qualify as a TVS, there had to be

1. three consecutive adjacent gates in range with $\Delta V \geq 15$ m s^{-1}
2. time and height continuity

Once that information was recorded, a parameter, S, was defined

$$S = \frac{\Delta V_{peak} - \Delta V_{low}}{z_{peak} - z_{low}} \quad (6.1)$$

where ΔV_{peak} is the largest ΔV within a volume, occurring at height z_{peak}. ΔV_{low} is the maximum ΔV at the lowest elevation angle in which a TVS was identified; the height of that ΔV observation is ΔV_{low}. A TVS was said to be descending if

1. $S \geq 2.25$ m s^{-1} km^{-1} and
2. $z_{peak} \geq 3.0$ km

in at least one volume scan prior to tornadogenesis else the TVS was categorized as non-descending. *Eqn. 6.1 is based on empirical models of mode I and mode II tornadogenesis developed by the authors* (Fig. 6.1). It was determined that *S* values less (greater) than 2.25 m s^{-1} km^{-1} better matched the authors' empirical model for mode II (I) tornadogenesis.

In order to gauge the validity of the Trapp et al. (1999) criteria, WSR-88D data of the Hog Back and GC tornadoes are examined in the time period prior to tornadogenesis. In both cases, strong evidence (MWR-05XP data) was presented that tornadoes developed near the surface and built upward with time. If the Trapp et al. (1999) criteria are accurate, the TVSs associated with both tornadoes should qualify as non-descending. For the Hog Back (GC) tornado, KDDC (KCYS) data are examined; the radar is located ~150 (~60) km from the location of the tornado. At each level, it is

first determined if there is a qualifying TVS. If there is a TVS, then ΔV values are recorded along with approximate beam heights. Once ΔV values are recorded, the S parameter is calculated and a determination of whether the TVS is descending or non-descending is made.

For the Hog Back tornado, inspection of the WSR-88D data is complicated by two factors. First, the closest radar is over 150 km away from the approximate location of tornadogenesis, so there are no near-ground radar observations, azimuthal spatial resolution is coarse, and midlevel radial velocity observations are extremely noisy (Fig. 6.2). Second, the supercell likely is undergoing cyclic tornadogenesis during the formation of the tornado. As discussed in Chapter 5.1, when MWR-05XP data collection begins, there is a well-defined TVS associated with a tornado that quickly moves rearward (westward) out of radar view (Fig. 5.2). It is shortly afterwards that the Hog Back tornado forms and also moves rearward; this behavior is consistent with the cyclic tornadogenesis process (e.g., Dowell and Bluestein 2002a). The combination of poor spatial resolution and noisy data prevent the examination of midlevel data prior to tornadogenesis. However, even if midlevel radial velocity data were investigated, it is likely that the unique processes inherent to the cyclic tornadogenesis process would have complicated any generalizations made about observed midlevel TVSs.

Analysis of the GC supercell is not impacted by range-related data issues because the storm is located ~60 km away from KCYS radar during tornadogenesis. In addition, the GC tornado is the first tornado produced by the supercell, so tornado cycling need not be considered. Radial velocity data from three volume scans prior to

tornadogenesis are inspected[4]. In the volume scan prior to tornadogenesis (beginning at 2148:34), TVSs are identified in data from 0.55°, 2.48°, 3.16°, 4.05°, 5.14°, 6.46°, and 8.05° elevation angle (Fig. 6.3). The TVS criteria are not met in data from 0.94°, 1.38°, 1.86°, and above 8.05° elevation angle. The maximum TVS ΔV is 45 m s^{-1} at 4.05° elevation angle and the approximate height of the observation is ~4.7 km. The lowest TVS ΔV is 27 m s^{-1} at 0.55° elevation angle and the height of the observation is ~800 m. *Using the above values gives an S value of ~4.6 and* z_{peak} *of ~4.7 km, indicating a descending TVS.*

There are two caveats to consider in the above calculations. First, when Trapp et al. (1999) developed their TVS criteria, "Super Resolution", oversampling WSR-88D radial velocity data in azimuth by a factor of two, had not been implemented. As a result, a TVS (couplet in adjacent gates) as viewed in legacy data now may be spread among three or four azimuths in oversampled data. To account for the possibility that ΔV values are being depressed by oversampling, the TVS criteria are relaxed such that the ΔV inbound/outbound maxima are no longer restricted to adjacent gates, but rather to within 3 gates (i.e., a maximum inbound and outbound separated by two gates in between). When the low-level radial velocity data are re-examined, the lowest TVS ΔV increases slightly to 31 m s^{-1}, but S is ~3.9, a value that still categorizes the TVS as descending. Second, in data from 4.0° elevation angle, where the maximum TVS ΔV value is observed, there are a series of gates in which radial velocities may be aliased (Fig. 6.3). The radial velocities are close to the Nyquist velocity (~26.5 m s^{-1}) and so

[4] In Trapp et al. (1999) the authors treat the beginning time of the volume scan in which tornadogenesis occurred as the time of tornadogenesis. In this case, the tornado formed at ~2152. The volume scan beginning at 2148:34 was not completed until 2152:33, which may have been after tornadogenesis. As a result, Trapp et al. (1999) may not have considered the volume under consideration here as occurring prior to tornadogenesis.

values of approximately -21 m s^{-1} or 31 m s^{-1} are both realistic. In this case, the velocities are not de-aliased. However, if they were, the only change in the calculations would be a 1 m s^{-1} drop in the maximum ΔV. Again, the S parameter would be nearly unchanged and the TVS would still be categorized as descending. As a result, it is not thought that changes in WSR-88D sampling or aliased radial velocities bias the calculation of S.

Trapp et al. (1999) openly discuss the imperfect nature of the criteria they use in determining the tornadogenesis mode using WSR-88D data. Some of the reasons they provide are: the low ΔV threshold for TVS identification, the development of an objective criteria based on a subjective classification scheme, and a priori knowledge of tornado formation location and time. Therefore, it should not necessarily be surprising that a radar system utilizing 40-50 times the volumetric temporal resolution of the WSR-88D provides evidence of shortcomings in their criteria. Instead, it is more instructive to investigate *what* the WSR-88D is observing at midlevels and *how* that relates to the underlying theory of a midlevel incipient tornado that descends to the surface via the DPE.

The strong midlevel TVS that is observed in KCYS data from 2.4-8.0° elevation angle is matched up with MWR-05XP data to explore the midlevel TVS in more detail. For example, the midlevel TVS at 5.1° elevation angle in KCYS data is located at a height of ~5.5 km (Fig. 6.4a). In qualitatively matching heights, the corresponding MWR-05XP scan is estimated to be from 18.5° elevation angle where the TVS is located at a height of ~6.0 km (Fig. 6.4b). The main radial velocity features that can be identified in the area of the mesocyclone in KCYS data are three areas of cyclonic

rotation, the middle of which is the previously identified TVS (Fig. 6.4a). The same three areas of cyclonic rotation within the larger scale mesocyclone can be identified in MWR-05XP data (Fig. 6.4b) despite the differing radar frequencies, radar resolution volumes, and viewing angles. Again, a TVS can be identified between two weaker areas of cyclonic rotation as in the KCYS data from the same time and similar height. The next PPI scan in the KCYS data at that height is not available for another 4.5 min., however the MWR-05XP dataset allows for a unique look at how the midlevel TVS in the KCYS data evolves before the next KCYS volume scan (Fig. 6.5). *In the MWR-05XP data, the TVS identified in both sets of radar data completely dissipates less than a minute later (Fig. 6.5d).* The area of cyclonic rotation east of the old TVS strengthens as the initial TVS dissipates.

In Chapter 5.2.1, the variable nature of observed midlevel TVSs prior to formation of the GC tornado is discussed. In order to quantify this effect, TVSs were tracked during the 9 min. of data obtained by the MWR-05XP prior to tornadogenesis. However, because the WSR-88D network is only obtaining "snapshots" of TVSs at any given height every 4-5 min., the time continuity requirement for TVS tracking is neglected. In this way, the evolution of TVSs that may be observed by the WSR-88D network at a given time can be tracked. When viewing the time evolution of individual TVSs (Fig. 6.6), it can be seen that TVSs are ubiquitous and yet rarely exhibit time or height continuity. TVSs are constantly forming and dissipating within the larger-scale mesocyclone. Figure 6.6 displays TVSs with a more stringent ΔV cutoff of 25 m s^{-1} because of the large number of short-lived TVSs observed within each PPI scan. Results using the original 15 m s^{-1} cutoff progressed in the same manner, but are more difficult

to interpret without the aid of animation. Only at the time of tornadogenesis is a consistent (in time and height) TVS seen, first at low levels and then at progressively higher levels, as discussed in Chapter 5.2.2.

In the GC supercell, enhanced areas of rotation within the mesocyclone formed and dissipated quickly, and no single TVS built downward. Despite the appearance of a dominant midlevel TVS prior to tornadogenesis in KCYS data, the sudden formation and dissipation of TVSs in MWR-05XP data provide strong evidence that the midlevel TVS was not an incipient tornado. Further, *the DPE cannot act on vortices that constantly form and dissipate, rather one vertically and temporally continuous vortex is necessary for a tornado to build downward in this manner.* As a result, for this particular case, the explanation for the dynamical connection between the midlevel descending TVS and tornadogenesis provided by Trapp and Davies-Jones (1997) and Trapp et al. (1999) is not supported by the observational evidence.

In light of the increasing number of observational cases failing to document mode I tornadogenesis and the radar observations presented above for the GC supercell, the following is speculated (Fig. 6.7): Mode I tornadogenesis, in which a midlevel incipient tornado forms at storm midlevels and descends to the surface via the DPE, does not occur in nature. In some supercells, vertical vorticity within the midlevel mesocyclone increases and decreases over short periods of time at small spatial scales, perhaps from natural cycles caused by a constantly-changing storm environment (e.g., updraft pulses, sfc. thermodynamic changes, etc.). As the storm strengthens and the low-level mesocyclone forms, enhanced areas of rotation become more common closer to the surface. After the low-level mesocyclone strengthens, tornadogenesis occurs.

However, the relatively coarse spatial and temporal resolution of the WSR-88D network is such that the areas of enhanced rotation appear to be temporally and vertically continuous TVSs that descend to the surface at around the time of tornadogenesis, particularly if the data are objective analyzed (e.g., Fig. 6.8). In reality, there is no temporal TVS continuity, no vertical TVS continuity, and, as a result, no DPE.

To the author's knowledge, the GC supercell dataset is currently the only one with rapid-scan, volumetric data of storm midlevels prior to tornadogenesis. As a result, the above hypothesis remains thoroughly untested as it is based on a single case. For example, it is feasible that the lack of observed mode I tornadogenesis cases by mobile Doppler radars results from the small sample of documented cases. It is hoped that future rapid-scan observations of storm midlevels prior to tornadogenesis can be obtained by the MWR-05XP and other rapid-scan radars and used to determine whether the evolution documented above is common. In addition, there is no argument put forth here that a descending TVS should or should not be used as a tool in the tornado warning process by local NWS offices. Even if the conceptual model shown in Fig. 6.7 is accurate, it is plausible that the hypothesized enhanced levels of vertical vorticity within mesocyclones are associated with an environment that is more conducive for tornadogenesis. Ideally, a large sample of rapid-scan, volumetric supercell observations can be used to relate patterns in mid- and low-level mesocyclone evolution to tornadogenesis.

In previous observations of mode II tornadogenesis, tornadoes appeared to form in the lowest levels very quickly after a scale contraction. In neither MWR-05XP cyclonic tornadogenesis case could a vertical directionality of scale contraction be

observed. In the Hog Back tornado case, mode I tornadogenesis was not observed, but vertical directionality to mode II tornadogenesis could not be determined because of poor data quality. However, for the GC tornado, the TVS was observed to build upward over a 3 min. period. Since most mobile, Doppler radar observations utilize ~90 sec. update times, it is conceivable that previous mobile radar observations of mode II tornadogenesis lacked the volumetric temporal resolution to resolve vertical directionality in the tornadogenesis process. Another possibility is that MWR-05XP spatial resolution is too coarse beyond 15 km and the TVS method used here is not suitable for tornado-scale processes. Future observations of mode II tornadogenesis can be used to determine if upward tornado formation occurs frequently.

6.1.2 Fluctuations of Tornado Horizontal Wind Speeds

Rapid changes in tornado winds were observed several times during the mature phase of the GC tornado. Oscillations occurred every 2-5 min. and were relegated to heights above ~2 km. At no time did rapid changes in tornado ΔV occur in the lowest 2 km. In the second oscillation, the TVS was shown to dissipate and then reform ~45 sec. later ~1 km east. When the TVS dissipated, it was tilted significantly to the northeast with height, but reformed nearly vertically upright. The first three oscillations all occurred upward with time. In the lowest 2 km, the TVS was relatively steady, though there was evidence of a scale contraction on the mesocyclone or tornado cyclone scale during the first two oscillations. During this time period, the condensation funnel of the GC tornado formed. Another instance in which the TVS dissipated and then reformed was seen several minutes later, but only in data from the highest elevation angle

scanned, 20.0°. To the author's knowledge, the tornado dissipation and secondary "genesis" observed above 2 km and the additional height-dependent oscillations in tornado strength have not been documented previously. Ideally, any attempt to explain the cause of the oscillations should account for all of the observations listed above.

Additional tornado data would be beneficial in determining the cause of the oscillations, however even with the suite of instruments used in VORTEX2, rapid-scan volumetric observations of the tornado were obtained only by the MWR-05XP. As a result, the discussion herein is mainly speculative. Consider the frictionless form of the perturbation vertical equation of motion:

$$\frac{dw}{dt} = -\frac{1}{\overline{\rho}}\frac{\partial P'}{\partial z} + B \tag{6.2}$$

where w is the vertical velocity, $\overline{\rho}$ is the base state density, P' is the perturbation pressure, and B is the buoyancy. Air parcels near the surface being ingested by a supercell likely lack the buoyancy to reach the level of free convection (LFC) without the aid of a dynamically-driven updraft. If parcels do not rise to the LFC, the updraft weakens or is not strong enough for associated convergence to amplify vertical vorticity to tornadic levels. For example, Markowski et al. (2011) found that trajectories in nontornadic mesocyclones did not reach the LFC and rose only a few hundred meters. In addition, observations of relatively warm (cold) RFDs associated with tornadic (nontornadic) supercells (e.g., Markowski et al. 2002; Grzych et al. 2007) may be circumstantial evidence of the need for dynamically-driven updrafts of varying strengths for tornadogenesis to occur. However, it stands to reason that, *even after a tornado forms*, the character of the tornado inflow often is changing.

The buoyancy of air parcels ingested by the tornado may be affected by variable parcel source regions or thermodynamic changes in the area of parcel source regions. For example, recent observations have shown that RFD surges are common (e.g., Marquis et al. 2008; Lee et al. 2011) and that they alter the thermodynamics of air parcels (e.g., Skinner et al. 2011) that may be ingested by an ongoing tornado. For an existing tornado, the buoyancy of ingested parcels is such that a dynamically-driven updraft is strong enough for parcels to reach close to their LFC. However, perhaps at the margins, even small changes in the thermodynamics of inflow air can have a large impact on the updraft at the level in which buoyancy is the main source of vertical motion. As a result, a tornado that suddenly ingests slightly less buoyant air will not dissipate in the lowest levels where the dynamically-driven updraft is strong enough to offset the lack of buoyancy. However, if less buoyant parcels can no longer be brought to the LFC or their vertical motion is substantially decreased above the LFC, the tornado may then weaken as a result of less stretching of vertical vorticity.

What follows below is a hypothesis for the cause of the height-dependent changes in tornado strength observed in the case of the GC tornado (Fig. 6.9). In the developing tornado, air parcels near the surface cannot buoyantly rise and thus a dynamically-driven updraft is necessary for parcels to reach their LFC. As a result, once the tornado forms near the surface, it develops slowly upward, taking ~2 min. to reach ~2 km. Based on a modified sounding of the storm environment (Markowski et al. 2012; Fig. 6.10), and estimating the height of the surface in Goshen County as ~1300 m, the height of the LFC can be estimated as ~1.8 km. Above this height, parcels rise faster because of positive buoyancy, reaching ~6 km in ~1 min. (Fig. 6.8).

After the tornado enters its mature phase, there are periodic changes in the buoyancy of air being ingested by the tornado. This may be due to RFGF surges, descending reflectivity cores (DRCs; Rasmussen et al. 2006), or other dynamical or microphysical changes in storm outflow that affect the thermodynamics of the parcels in source regions. When less buoyant air is ingested by the tornado, parcels struggle to reach the LFC, and if they do, they rise slowly. The effect on the tornado is observed first at or near the LFC (~2 km) and then upward from there, where decreased updraft strength weakens vorticity stretching and rotation. Weakening progresses to a point such that the tornado dissipates above the LFC in an upward manner. When the buoyancy of the inflow increases again, an updraft "pulse" results. At low levels, the increase in the strength of the tornado updraft increases vorticity stretching and rotation such that the pressure drops in the vortex and a condensation funnel forms. Above the LFC, the updraft pulse is strong enough that it stretches and advects vertical vorticity upward and the tornado reforms in an upward direction and is (briefly) vertically oriented as a result.

It also is possible that the causes of the oscillations are axially-traveling centrifugal waves downstream of the LFC (A. Shapiro, personal communication). In this scenario, the waves are induced by perturbations in the flow that occur at the LFC. Shapiro (2001) provided an exact solution to the Euler equations for an axially-traveling wave in solid-body rotation. The phase speed, c, and period, T, of the wave were found to be

$$c = \frac{2\overline{\Omega}}{k} \tag{6.3}$$

$$T = \frac{\pi}{\overline{\Omega}} \tag{6.4}$$

where $\overline{\Omega}$ is the base-state angular velocity and k is the wavenumber. For solid-body rotation, the vertical vorticity is twice the angular velocity, so the phase speed can be calculated as the base-state vorticity divided by the wavenumber. To see if the GC tornado intensity oscillations discussed in Chapter 5.2.3 are consistent with a centrifugal wave in a rotating fluid, the second oscillation is examined further.

For the second oscillation, an observable change in intensity is observed from 9.8-20.0° elevation angle. To estimate the base-state vorticity, AVV (Eqn. 1.2) is calculated at each time for the mature phase of the GC tornado at these levels. The average AVV value in time and height is 0.43 s^{-1}. To estimate the observed wavenumber, Fig. 5.59b is used; the wavelength of the modulated flow is ~1500 m in height. Using these values in Eqns. 6.3 and 6.4, respectively, gives a phase speed of ~100 m s^{-1} and a period of ~15 sec. To see how these values match the observations, a phase speed and period are estimated from the ΔV time series. Five distinct oscillations in the ΔV field are observed over a period of ~15 min. (Fig. 5.56b), for an observed period of ~180 sec. To estimate the phase speed, beginning and ending times and heights for the second oscillation were specified based on local maxima/minima in ΔV at 9.8° and 20.0° elevation angle. It is hoped that the relatively large height difference between the two levels at the time of the second oscillation (~2.5 km) provides an accurate estimate of the phase speed of any wave modulating the flow. Using the two ΔV maxima and one ΔV minimum, phase speeds of 55, 33, and 24 m s^{-1} are estimated. The calculated phase speeds are off by a factor of ~2-3 compared to the phase speeds derived from ΔV observations. The calculated period of the waves is an order of magnitude faster than the period of the intensity oscillations from ΔV observations.

However, the centrifugal wave solution derived in Shapiro (2001) does not include the ground as a lower boundary and assumes zero mean vertical velocity. Accounting for a lower boundary likely reduces the phase speed and increases the period from that calculated using Eqns. 6.3 and 6.4. Further, if there were a strong downdraft in the tornado, the observed phase speed would be even closer to that calculated theoretically.

Centrifugal waves are transverse waves, so there also would be observed effects in the tornado perpendicular to the direction of wave propagation. For axially-travelling waves, there is oscillatory behavior to the radial flow outward away from the center of the vortex, which is manifested as divergent velocity signatures. In single-Doppler radar data, this can be estimated using ΔV calculations but calculated from gates within a radial rather than from adjacent radials at the same range. Unfortunately, divergence signatures are best calculated in the gates located between the inbound and outbound maxima in a TS. Here, divergence is estimated at a larger spatial scale by calculating the velocity difference between the inbound maxima in the TVS and the gate 300 m (Fig. 6.11a) and 600 m (Fig. 6.11b) closer to the radar origin in range. Larger (smaller) values indicate flow that is more divergent (convergent). The results are quite noisy, so to see if periods of weaker TVS intensity are correlated with more divergent flow, scatterplots are constructed (Fig. 6.12). At 300 m (Fig. 6.12a), there is a weak negative linear relationship between TVS intensity and divergence. At 600 m (Fig. 6.12b), the negative linear relationship is much stronger. The crude divergent measurements estimated here are consistent with centrifugal waves traveling axially and modulating the flow. However, the data are too noisy to determine if there is vertical directionality to divergence signatures. In short, there are too many discrepancies in the observational

data to say with certainty that the intensity oscillations are the result of centrifugal waves, but that possibility cannot be ruled out.

A related idea is that the height-dependent changes in tornado strength are caused by wave-induced symmetric oscillations of the flow downstream of a vortex breakdown (D. Nolan, personal communication). Symmetric oscillations are one type of eddy that can result downstream of a vortex breakdown. There is not an obvious change in the radar-observed structure of the radial velocity field at the interface where the oscillations begin. It would be expected that downstream of a vortex breakdown, the core flow would be larger than it is upstream of the breakdown. However, still images of the tornado do show what appears to be a broadening of the tornado circulation close to cloud base (Fig. 5.63). Future studies of the GC tornado using higher-spatial-resolution radar data and advanced analysis techniques such as GBVTD should provide more certainty about the axisymmetric structure of the GC tornado. That information can then be used to further evaluate the potential that centrifugal waves and symmetric oscillations associated with a vortex breakdown are occurring.

Efforts to relate ΔV oscillations in the GC tornado to storm-scale features observed by radars with higher spatial resolution than that of the MWR-05XP were unsuccessful (K. Kosiba and J. Wurman, personal communication). Furthermore, dual-Doppler analyses can be synthesized only every 2 min. based on the scanning strategies of the radars used in VORTEX2, so it would be difficult to correlate derived fields with processes documented above. Efforts are ongoing to incorporate radial velocity data from other radar systems into the analysis of the ΔV oscillations for two reasons. First, even though any given system will have ΔV data at a certain level only every ~2 min.,

the values can be used as a "check" of the ΔV observations made by the MWR-05XP. Second, increased spatial resolution data, even if the data are only from a single time, may provide additional clues as to what is causing the periodic changes in tornado strength.

There are several other potential causes for the ΔV oscillations seen in the GC tornado. One possible cause is multiple vortices that are not being spatially resolved by the MWR-05XP. However, multiple vortices likely are not the cause of the variable tornado strength for two reasons. First, the oscillations occur every 2-5 min., while multiple vortices, even in large tornadoes, modulate the flow of the tornado over a much shorter period of time (e.g., Wurman 2002). Second, when ΔV decreases (increases), there is not a corresponding increase (decrease) in either inbounds or outbounds as one might expect if a multiple vortex were embedded within the larger scale tornado core flow. Another possibility is that the changes in ΔV at higher levels result from increased sampling of vertical velocities as elevation angle increases. However, the amplitudes of the oscillations do not increase as the elevation angle increases, so this explanation also is unlikely. Eliminating multiple vortices as the cause of the intensity oscillations would mean that the hypothesis proposed in Chapter 3.2.2, that tornadoes without multiple vortices reach a steady-state intensity in their mature phase, can be rejected.

As discussed in Chapter 6.1.1, we await more rapid-scan, volumetric observations of tornadoes, *particularly at midlevels*, so that the frequency of the behavior discussed above can be determined. Preferably, high-spatial-resolution data also would be used so that processes that may be occurring at small spatial scales, which may be impacting the tornado oscillations, can be observed thoroughly.

6.1.3 Volumetric Observations of Tornadoes

Three additional, though ancillary, topics relating to tornadoes were explored. The motivation for each of the three topics is that midlevel observations of tornadoes are relatively rare. The MWR-05XP obtained data into midlevels and above for the GC tornado and the Kingfisher tornado, so additional aspects of the tornado could be explored using unique data. The first topic explored was the vertical profile of tornado winds (ΔV) into storm midlevels. Profiles were examined for the entire lifecycle of the GC tornado and the dissipation phase of the Kingfisher tornado. For the GC tornado, ΔV was highly variable in height for both the tornadogenesis and mature phases. Generally, ΔV decreased with height, but there were many observations of ΔV into storm midlevels that were similar to or greater than those near the surface. In the dissipation phase, ΔV decreased with height, particularly when ΔV was scaled by that observed at the lowest-observed level. In the Kingfisher tornado, ΔV also decreased with height, though the signal was not quite as clear as in the dissipation phase of the GC tornado.

The second volumetric topic discussed was tornado vertical orientation. The vertical orientation of the GC tornado and Kingfisher tornado were examined at specific times rather than in the aggregate as done for the vertical ΔV profiles. Upon formation, the GC tornado already was tilted toward the northeast. During the mature phase, the tornado continued to tilt toward the northeast, but also was nearly vertically upright at other times. Tornado tilt increased in the dissipation phase to the point that the tornado likely was disconnected between storm low and midlevels. In the Kingfisher tornado, the tornado also tilted dramatically upon dissipation and likely became disconnected.

The general tilt of tornadoes toward the northeast with height in both cases is consistent with previous observations and likely results from the impact of vertical wind shear on the vortex. The large TVS tilt in the dissipation phase for both cases may be the result of low-level RFGF outflow advecting the tornado to the right of the storm near the surface (see below).

It was hoped that observed midlevel ΔV profiles and tornado orientation could be used as a real-time indicator or short-term predictor of tornado behavior. The shift in the aggregate ΔV profile from one that is variable in height to one in which ΔV decreases with height in the dissipation phases of both tornadoes is one such possibility. However, there were several time periods when ΔV decreased dramatically with height into storm midlevels and tornado dissipation did not occur. For example, during the second ΔV oscillation (Fig. 5.54), ΔV was only ~25 m s^{-1} above 2 km and ~50-60 m s^{-1} below ~2 km for a period of ~1 min. After that ΔV profile was observed, tornado maintenance continued for another 20 min. As a result, sudden and large transitions to negative linear ΔV profiles may not be indicative of imminent tornado dissipation. However, a mature tornado in which the ΔV profile decreases in height *over a several minute period* may be an indication that the tornado has entered its dissipation phase and may be within several minutes of decay. Unfortunately, a similar result cannot be made from the vertical orientation data. Even as tornadogenesis is occurring in the GC supercell, the tornado is tilted toward the northeast. There are several times during the GC tornado mature phase when TVS horizontal displacements were several kilometers and tornado maintenance continued for an additional 20+ min. In the dissipation phase, TVS tilt was increasing but still mimicked similar observations made in the tornado

mature phase. The largest TVS tilts did occur in the dissipation phase, but only after dissipation already had begun aloft.

The final topic under consideration is the volumetric evolution of tornado dissipation. To the author's knowledge, no previous studies have investigated tornado decay through the use of volumetric mobile, Doppler radar data. Both the GC tornado and Kingfisher tornado dissipated generally in a top-down manner. However, in both cases, the TVS dissipated first in the 2-3 km layer before dissipation proceeded both upward and downward with time from the initial TVS dissipation point. As mentioned above, tornado dissipation occurred after a several minute period in which the tornado ΔV profile was approximately negative linear and tornado tilt was very large. One explanation is that increasing rear-flank storm outflow from an accelerating RFGF at low levels advected the tornado to the right of the storm in both cases, while the tornado at midlevels continued to move in a direction similar to that of the storm. In single-Doppler radar data from both cases, there is no obvious change in the radial velocity structure around and near the tornado at the approximate time of the southward shift in translational direction. Further inspection of higher-spatial-resolution data from UMass X-Pol for the GC supercell also did not show obvious changes in the radial velocity structure, however radar sensitivity may preclude accurate retrieval of often subtle boundaries.

Regardless of the mechanisms involved in the southward transition of the tornado at low levels, the increasing tornado tilt that resulted from the shift likely played a contributing role in the initial dissipation. The following is proposed for both tornado dissipation cases (Fig. 6.13): The tornado becomes so tilted at the interface

between the southward advection at low levels and the continued eastward motion at midlevels that it becomes vertically disconnected. After the tornado disconnects at 2-3 km, the tornado aloft is cut off from its source of vertical vorticity generation and quickly dissipates in an upward manner. The tornado below 2-3 km is still able to access inflow, and so does not quickly dissipate. However by this point, the tornado has become completely occluded and inflow is contaminated by precipitation and cooler outflow air that is responsible for the initial advection of the tornado toward the south. The tornado near the surface eventually dissipates as a result. Previous visual documentation of a tilted tornado disconnecting were made by Bluestein et al. (1988; Fig. 6.14).

It is noteworthy that tornadoes have at least two different modes of dissipation. It is often observed that tornadoes tend to bend to the left of storm motion when they dissipate, particularly when cyclic tornadogenesis is ongoing (e.g., Dowell and Bluestein 2002a, Bluestein 2009). Conversely, in the two cases presented here, the tornadoes moved well to the right of the storm at low levels as they dissipated. The differing modes of tornado dissipation likely were first observed by Agee et al. (1976) when they discussed tornadoes that were both right-and left-turners. Increases in rear-flank outflow have been hypothesized to play a role in both the advection of tornadoes to the right of the storm and in the cessation of cyclic tornadogenesis (e.g., Dowell and Bluestein 2002b; French et al. 2008). One possibility is that a spectrum of rear-flank outflow exists that modulates tornado behavior (Fig. 6.13). Weak rear-flank outflow is associated with cyclic tornadogenesis as storm inflow advects tornadoes rearward and to the left of the storm, cutting them off from their source of vertical vorticity

generation. Stronger rear-flank outflow ends the cyclic tornadogenesis process and is associated with longer-lived tornadoes. As the rear-flank outflow increases even more, the tornado is advected to the right of the storm, also removing the tornado from one of its maintenance sources (Marquis et al. 2012).

6.2. Anticyclonic Tornadoes

The EAC tornado was relatively shallow, but consistent for ~15 min. with the strongest azimuthal shear in the lowest 3 km (Fig. 5.14). Most anticyclonic tornadoes occurring in the vicinity of the RFGF are thought to form as the result of a collocation of anticyclonic shear and a developing updraft. The AHIs for the EAC tornado show that, before a vortex signature could be identified, there was a relatively deep layer of anticyclonic shear. Of interest is the source of this layer of enhanced shear and (likely) vertical vorticity. Also, there is strong evidence that the tornado did not form first near the surface, but rather at ~2 km (Fig. 5.19). After the tornado formed, it became gradually more tilted, both to the north and to the west with increasing height (Fig. 5.21). Possible explanations for the above observations are provided below.

The layer of anticyclonic shear may have resulted from horizontal wind shearing at the southern interface of the RFGF in the supercell, similar to a wake vortex. The Ellis storm was a very large HP supercell, so the edge of the RFGF is easily identifiable from heavy precipitation in MWR-05XP data (Fig. 6.15). The strongest radial velocities in the rear-flank of the supercell are not located at the boundary interface but are displaced several kilometers west of the edge of the gust front (Fig. 6.16). The strongest

inbound velocities are located southwest of a weakening mesocyclone (Fig. 6.16a). The juxtaposition of the strong inbound radial velocities just to the north of the southwest tip of the rear-gust front, where winds likely were weaker and contained a storm-relative component from the east, is a location of potentially strong anticyclonic shear.

There is another possible source of anticyclonic shear in for the EAC tornado. RHIs of radial velocity along an azimuth near where the EAC tornado formed are shown in Figure 6.17. There is a consistent, large vertical gradient in inbound radial velocity above 3.9° elevation angle. Above ~2 km, the radial velocities increase significantly for another ~2 km before they decrease again. The distinct increase in inbound radial velocities from data at 3.9° to 5.4° elevation angle also can be seen in PPIs of radial velocity (Fig. 6.18). This strong vertical gradient in inbound winds could create horizontal vorticity vectors pointing approximately northward. A strong downdraft (as would be likely in the rear-flank of the supercell) interacting with the horizontal vorticity would create anticyclonic vertical vorticity to the south of where the horizontal vorticity is located and cyclonic vertical vorticity to the north. In addition, it would be expected that the strongest vertical vorticity initially would be at the location of the strongest horizontal vorticity, likely where the interface of the rear-flank jet in approaching radial velocities is located. In this case, it is expected that the strongest vertical vorticity initially would be located in data from between 3.9° and 5.4° elevation angle. *The TVS of the EAC tornado forms first at 3.9° elevation angle and is not identifiable at the lowest levels for another 90 sec*. Any enhanced upward vertical velocity, such as forced ascent along the southern extent of the RFGF, would stretch that vertical vorticity, perhaps to tornadic strength. The mechanism for anticyclonic

vertical vorticity production detailed above is similar to the model for vorticity production in bow echoes by Weisman and Davis (1998). This idea is consistent with the likely height that tornadogenesis occurs at first and the general location of anticyclonic shear in HP supercells.

The only evidence of short-time-scale changes in wind speeds with height in the anticyclonic vortices is some rapid changes in ΔV at the highest extent of the TVS (e.g., Fig. 5.17). These changes in strength likely have more to do with the intermittent nature of the tornado at those levels than internal changes to the tornado itself. Changes in updraft strength likely determine to what extent anticyclonic vertical vorticity is advected/stretched to higher levels in the storm. Also, there is no observed relationship between tornado strength and height at levels in which the TVS can be consistently identified.

The northwestward tilt of the EAC tornado (Fig. 5.21) with height is consistent with previous observations of tornado tilting, but as mentioned previously, the EAC tornado was not a typical supercell mesocyclone tornado, so the similarity to past observations may just be a coincidence. In this case, a series of radial velocity PPIs are used to show that the progression of the radial velocity field in the rear-flank of the supercell is different at low levels than it is at midlevels (Fig. 6.19). During and just after formation of the EAC tornado, the maximum inbound radial velocities are located to the north of the EAC tornado (Fig. 6.19a,b). However, shortly after the tornado forms, an area of very strong inbound radial winds forms east of the tornado just behind the very southern portion of the RFGF close to the surface. Higher up in the storm, above ~2 km, the strongest inbounds behind the gust front are still to the north or

northeast of the EAC tornado (Fig. 6.19c,d). Previous studies have shown that tornadoes tend to move in the direction of the flow they are embedded in (e.g., Dowell and Bluestein 2002b). In this case, as the new low-level wind maximum pushes southeast (in a storm-relative sense), the tornado follows a similar direction. At higher levels, without the new wind maximum, the tornado moves more in the direction of the parent storm. As a result, the tornado becomes increasingly tilted toward the north and west with height. It is not clear if the tornado becomes disconnected because of the increased tilt as is hypothesized for the GC and Kingfisher tornadoes. However, the TVS can still be identified in the data at higher elevation angles after it dissipates at low levels, so it is possible that the new radial wind maximum brings the EAC tornado away from areas rich in vertical vorticity production at low levels.

Chapter 7

Conclusions

7.1 Summary

Unique rapid-scan volumetric observations of four tornadoes made by the first mobile phased-array radar in weather research have been presented and analyzed. Radar data of the four tornadoes were obtained from 2008-2010 by a team from the University of Oklahoma, ProSensing, Inc., and the Naval Postgraduate School. In these deployments, data were obtained from 1° up to 20° and as high as 40° elevation angle with volumetric update times of 6-14 sec. The volumetric update time for these datasets was an order of magnitude faster than that of most other mobile Doppler radars. Research questions centered on topics in tornado science that may be addressed by utilizing unique rapid-scan and/or volumetric observations. These topics were (i) the time-height evolution of the tornadogenesis process, (ii) short-time-scale changes in tornado wind speeds, and (iii) volumetric observations of tornado horizontal wind profiles, tornado orientation, and tornado dissipation.

Some of the findings made from examination of MWR-05XP observations of tornadoes are unique and prompted new ideas, while many observations are consistent with previous work. The main conclusions from this project are as follows:

1. There is little observational support for the mode I tornadogenesis process as discussed in Trapp and Davies-Jones (1997).
2. Previous radar observations of mode I tornadogenesis by the WSR-88D network

may be the result of insufficient temporal and spatial sampling of enhanced areas of vertical vorticity within midlevel, and eventually low-level, mesocyclones.

3. During the tornado mature phase, tornadoes can be relatively unsteady above low levels, even in the absence of multiple vortices.
4. Above the LFC, tornado evolution can be completely different from that observed at low levels.
5. A negative linear ΔV vertical profile observed consistently for several minutes may be an indication that tornado dissipation is about to occur; rapid, short-lived transitions to negative linear ΔV vertical profiles are not necessarily associated with tornado dissipation.
6. Tornadoes can tilt significantly at various times in their life cycle and increasingly large tornado tilt is not necessarily indicative of impending tornado dissipation.
7. Tornado dissipation may begin when the vortex becomes vertically disconnected as a result of disparate vortex motion at different levels; dissipation then proceeds quickly upward and slowly downward from the initial dissipation height.

7.2 Future Work

Future work will be focused on enhancing and expanding upon the results presented here. In particular, data of a violent tornado were obtained on 24 May 2011

near El Reno, Oklahoma. Data were obtained from 1-40° elevation angle with update times of ~11 sec. While tornadogenesis was not captured by the MWR-05XP, data were collected in at least parts of the tornado mature phase when wind speeds were thought to be extremely high (J. Snyder, personal communication). These data will be analyzed to see if rapid changes in tornado winds are observed and, if so, whether they are height-dependent or not. In addition, volumetric aspects of the TVS associated with the El Reno tornado will be analyzed, especially ΔV profiles and TVS tilt. Data collection continued for a long period of time as the tornado moved away from the radar. However, at the time of tornado dissipation, the TVS was ~40 km away, so the volumetric evolution of tornado dissipation may be difficult to investigate. It is hoped that the El Reno dataset can be used as a source of comparison for observations of the GC tornado during its mature phase.

The climatology of mobile, Doppler radar observations performed by Alexander (2010) is constantly being updated (C. Alexander, personal communication). The updated climatology contains additional cases of mode II tornadogenesis. One possibility is to use the Trapp et al. (1999) criteria on WSR-88D data from each of the mobile Doppler radar cases shown in Table 3 and any additional cases to see if they are categorized as descending or non-descending. There would be more confidence that the Trapp et al. (1999) criteria is flawed if there are several additional cases categorized as descending based on WSR-88D data. Also, more rapid-scan, volumetric observations of tornadogenesis obtained in the future would be highly beneficial. The number of tornadogenesis cases observed by mobile Doppler radars is still relatively small and the

number of cases in which volumetric, rapid-scan data are available prior to tornadogenesis is even smaller.

Earlier versions of this work included two additional areas of study: hook echo formation and supercell weak-echo regions (WERs; Chisholm 1973). It was hoped that the volumetric nature of data collection would allow for a unique look at these supercell reflectivity features. Vertical cross sections through raw reflectivity were to be used to determine the relative contribution of vertical reflectivity advection, horizontal reflectivity advection, and reflectivity formation/dissipation in three cases of hook echo formation. Byko et al. (2009) previously suggested that hook echo formation may best be described as a spectrum. On one side of the spectrum is hook echo formation from horizontal advection of hydrometeors around a strengthening low-level mesocyclone. The other side of the spectrum is hook echo formation from a DRC. Initial work done to determine the reflectivity source of developing hook echoes using vertical cross sections was inconclusive. Even with rapid volumetric updates, interpretation of hook echo formation from 2-D images is difficult. Future work will instead objectively analyze hook echo data with the goal to view isosurfaces of reflectivity during hook echo formation as done in Rasmussen et al. (2006) and Byko et al. (2009). Also, when available, polarimetric data form other radar systems may be used to approximate the type of hydrometeors involved in the hook echo formation process.

WERs form as a result of a persistent updraft, which prevents hydrometeors from growing to any substantial size in the time they reside in the area. Hydrometeors that do form are lofted upward away from the WER. As a result, WERs can be used as a proxy for the location of an updraft in a supercell. WERs have not been studied in much

detail since the 1980s. Most mobile, Doppler radar observations focus on low levels, so midlevel signatures such as WERs are not studied in detail. Because WERs can be used as proxies for supercell updrafts, their formation and evolution in time and height is of natural interest. In investigating WERs using MWR-05XP data, examples of WERs that form rapidly and/or dissipate rapidly at multiple levels were made. However, 2-D images of WERs were cumbersome, and it was determined that the best way to track their evolution is through volumetric imaging. It is hoped that objectively analyzed reflectivity data can be used to create isosurfaces of low reflectivity values in limited domains as estimates of WERs in supercells. Then, the formation and evolution of the WERs can be tracked and easily correlated with other storm features (e.g., mesocyclones, hook echoes, etc.). As with the hook echo work, incorporation of polarimetric data may also be useful. For example, WER evolution can be correlated to observed Zdr columns (Kumjian and Ryzhkov 2008) and other polarimetric signatures identified in supercell midlevels.

Properties of the MWR-05XP	
Transmitted frequency	9.3-10 GHz (X band)
Maximum peak power	≥ 15 kW
Half power beamwidth	1.8° (azimuth), 2.0° (elevation)
Maximum PRF	10 kHz
Pulse duration/range resolution	1 μs/150 m
Sensitivity	~-15 dBZ at 10 km (minimum)
Range sampling	75 m
Azimuth/Elevation sampling	~1.4° (azimuth), 1.5° (elevation)
Mechanical azimuth scanning rate	180° s^{-1} (maximum)
Electronic azimuth back scanning	6-8° swath (varies with elevation angle)
Electronic elevation scan capability	-18-55° with respect to the horizon

Table 4.1. Selected properties of the MWR-05XP. Exact values of some parameters are not provided because they are classified. Reproduced from Bluestein et al. (2010) and expanded.

Tornadogenesis						
Date	**Time (UTC)**	**Mode**	**Max. Range (km)**	**Nyquist Velocity (m/s)**	**Elevation Angles**	**Vol. Update Time (s)**
24-May-2008	0149-0205	SE	60	19.53	1-20°	14
24-May-2008	0200-0205	SE	60	19.53	1-20°	14
05-June-2009	2143-2155	STF-SE	45	24.03	1-20°	8.5
Tornado wind speeds and volumetric observations						
Date	**Time (UTC)**	**Mode**	**Max. Range (km)**	**Nyquist Velocity (m/s)**	**Elevation Angles**	**Vol. Update Time (s)**
24-May-2008	0204-0215	SE	60	19.53	1-20°	14
05-June-2009	2200-2231	STF-SE	30	34.75	1-20°	6.5
19-May-2010	2259-2315	STF-SE	30	36.5	1-40°	12

Table 5.1. List of datasets used for each of the research objectives outlined in Chapter 3.2. Datasets from 24 May 2008 are listed twice because two tornadoes from that date are being studied.

Article	Descending TVS
Trapp et al. (1999)	Yes (27 cases)
Dunn and Vasiloff (2001)	No
Burgess et al. (2002)	No
Alexander and Wurman (2005)	No
Wurman et al. (2007)	No
Alexander (2010)	No (5 cases)
French (2012)	No (2 cases)

Table 6.1. List of peer-reviewed articles published since 1999 that discuss the vertical evolution of tornadogenesis and whether mode I (descending) tornadogenesis was observed or not. If more than one case was discussed within an article, the number of cases is provided in parentheses. Note that one of the five cases discussed in Alexander (2010) is the same case discussed in Alexander and Wurman (2005).

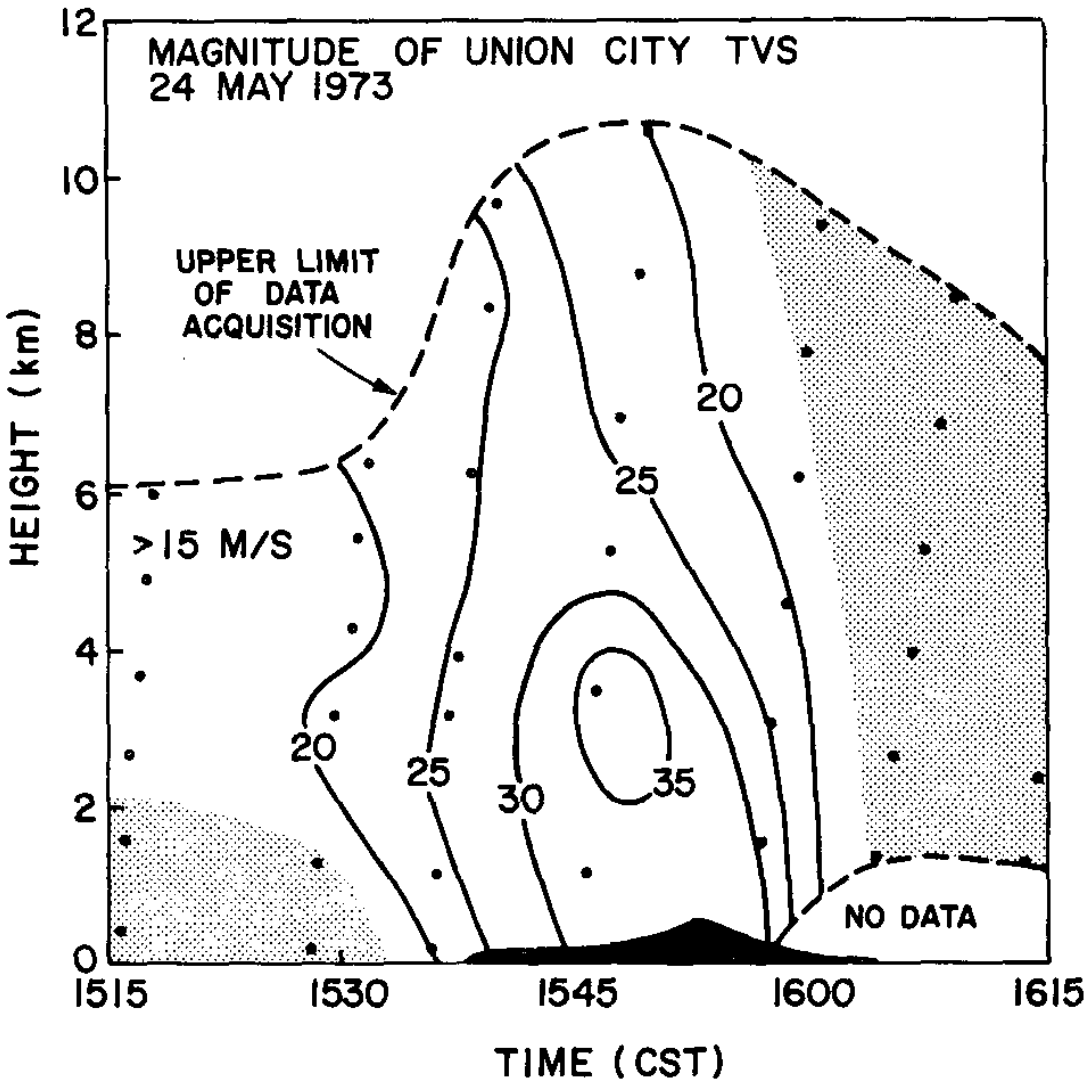

Figure 2.1. Time height profile of the magnitude of the largest Doppler velocity value within each TVS (adjusted for TVS motion). Dots indicate data points and dashed lines represent the limits of data collection. Velocity shears below the TVS detectability level are lightly shaded. The black region at bottom center is the diameter (using ordinate scale) of the Union City tornado funnel near cloud base. From Brown et al. (1978).

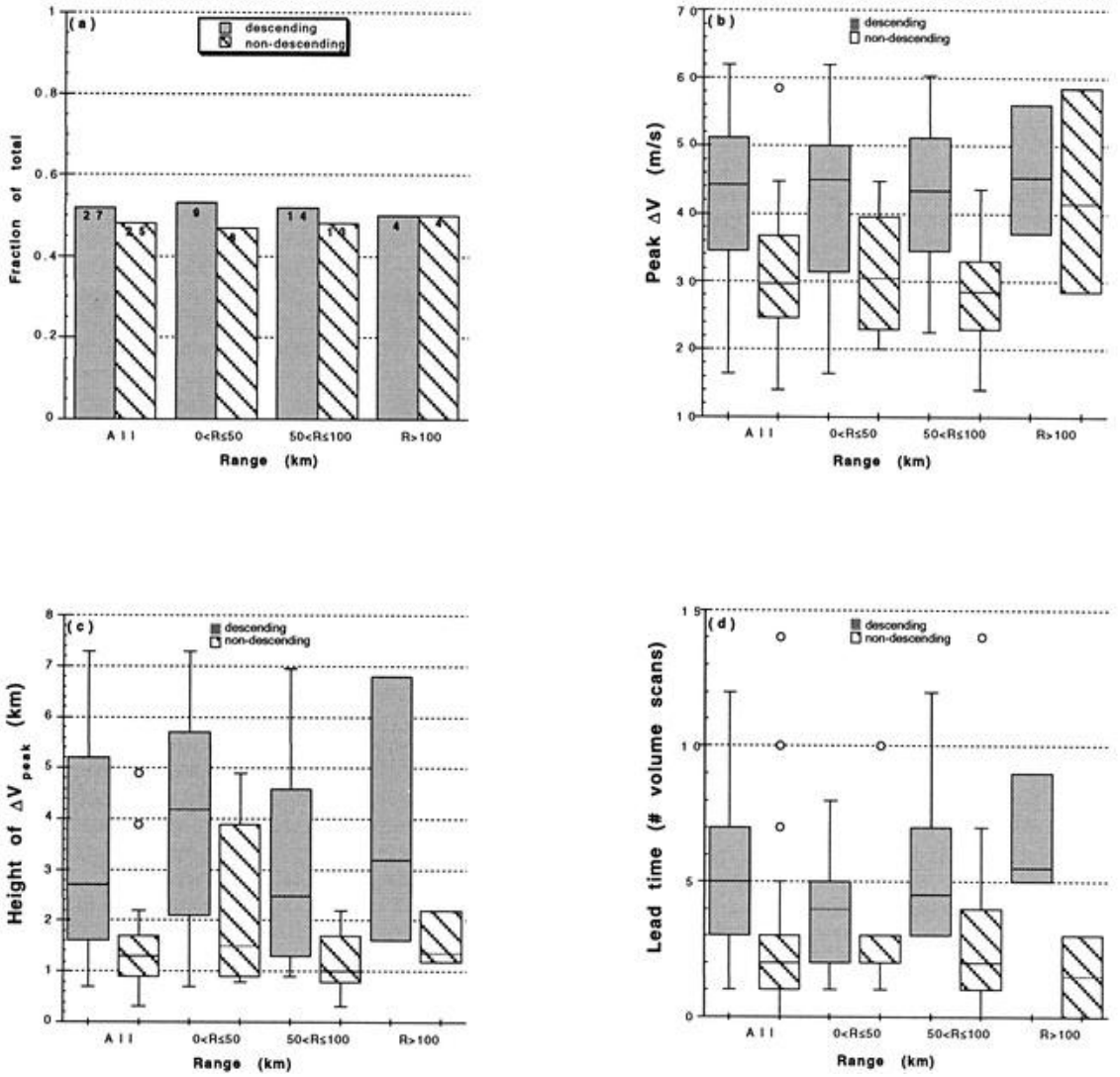

Figure 2.2. (a) Number of descending and nondescending TVSs, given as a fraction of the total occurring in a given range bin. Box plots of descending and nondescending TVS attributes, as a function of radar range: (b) peak, pretornadic gate-to-gate differential velocity (m s^{-1}); (c) height of the peak, pretornadic gate-to-gate differential velocity (km); and (d) lead time (in numbers of radar volume scans). Open circles indicate outliers, which are > the upper quartile + 1.5 × interquartile range or < the lower quartile − 1.5 × interquartile range. From Trapp et al. (1999).

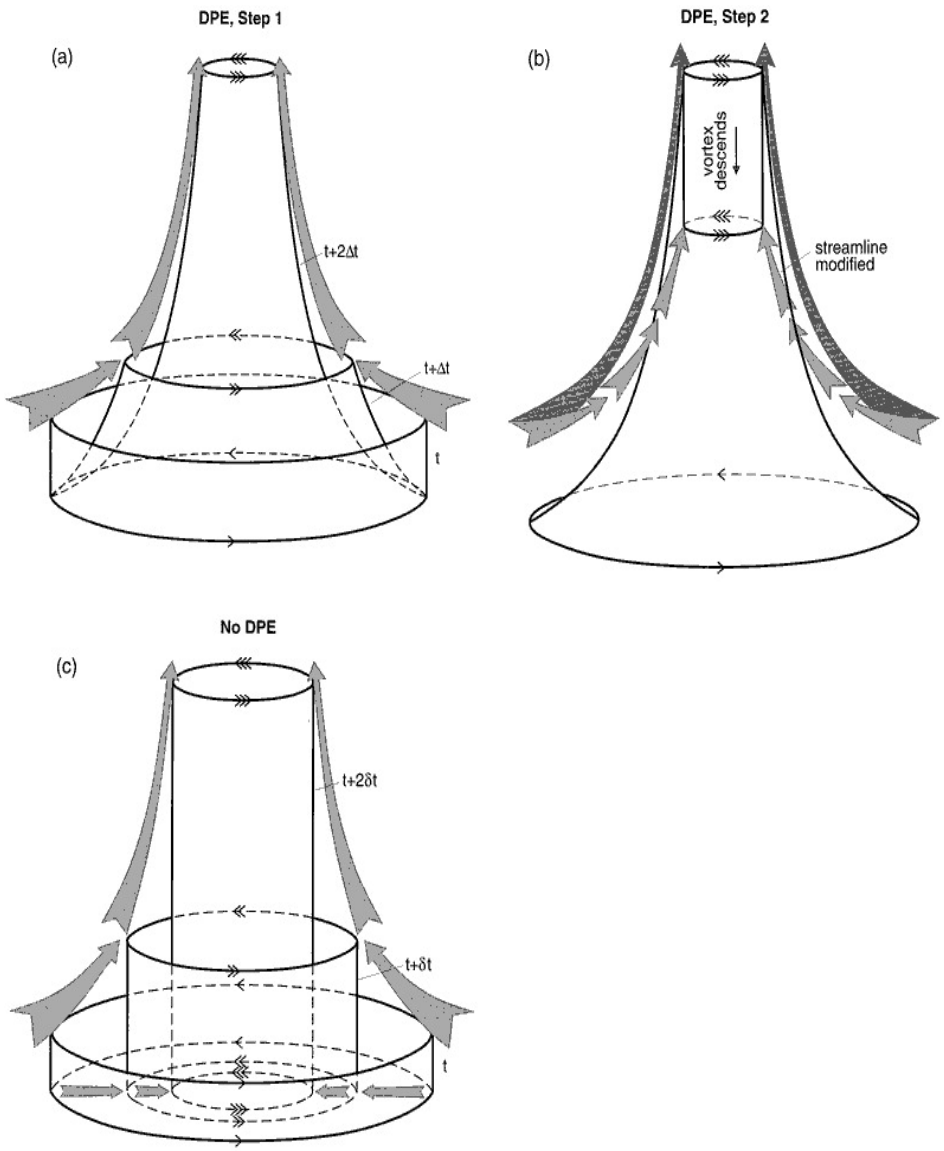

Figure 2.3. Idealization of two modes of vortex formation within a rotating updraft. Number of barbs on wind arrows indicates strength of swirling wind component. (a) Step 1 of vortexgenesis for case when maximum convergence is aloft and surface inflow is weak (or absent as depicted here). Initial cylindrical vortex tube is deformed by meridional flow (depicted by bold streamline) as shown after time $t + \Delta t$ and $t + 2\Delta t$, resulting in increased rotation aloft. (b) Step 2. Vortex begins to build down by dynamic pipe effect (see text) as it modifies streamlines (dashed) in its vicinity. In practice, steps

1 and 2 occur concurrently rather than consecutively, but step 2 only becomes a significant effect as high-angular-momentum parcels reach small radii. The vortex will contact the ground only through the slow DPE process. (c) As in (a) but for vortexgenesis when convergence is constant with height. In this case, the vortex tube is stretched but remains cylindrical, resulting in simultaneous increase in rotation throughout a large depth. Streamlines are unmodified (assuming a free-slip lower boundary). From Trapp and Davies-Jones (1997).

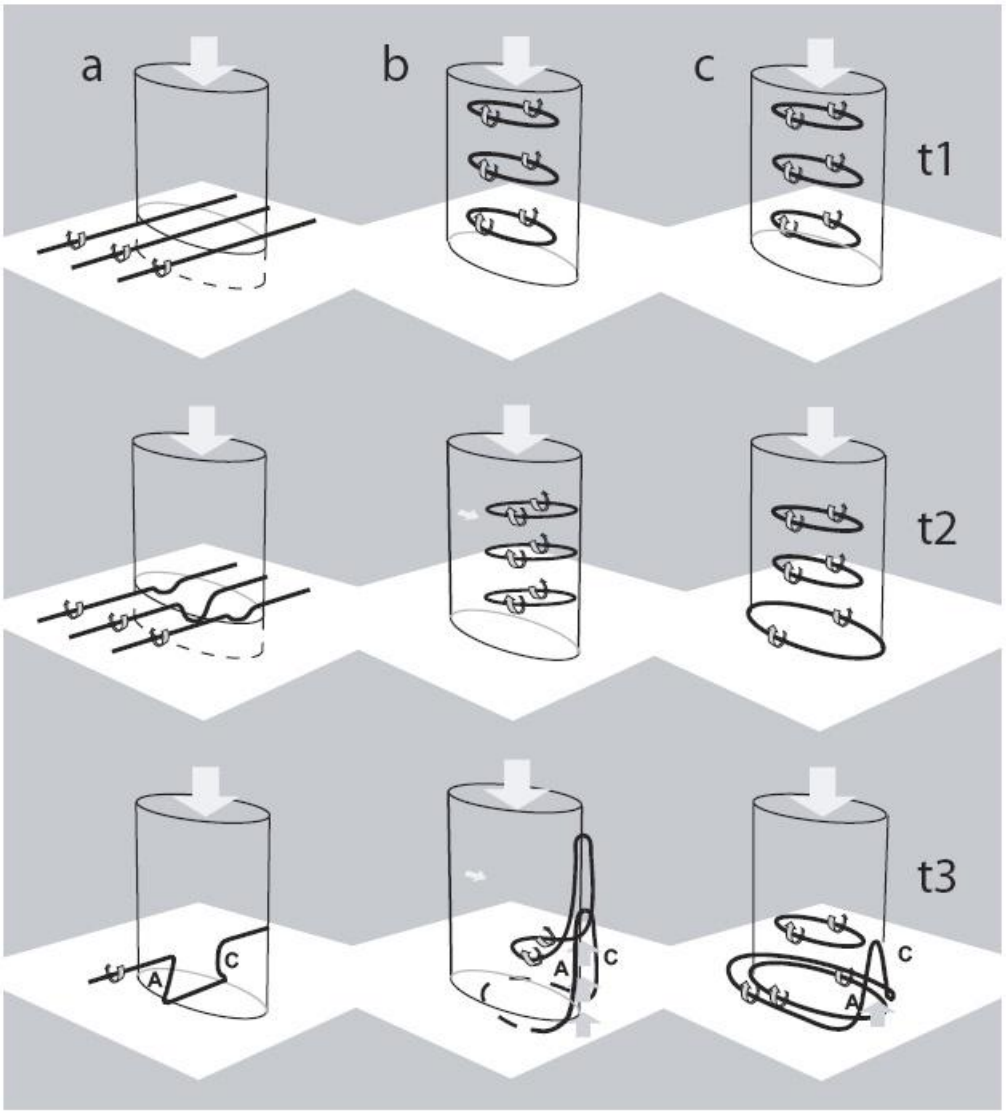

Figure 2.4. Schematic of Walko's (1993) hypothesis (a) and two versions of the arching hypothesis (b,c). The letters "A" ("C") denote cyclonic (anticyclonic), solid lines are vortex lines, and t1, t2 and t3 are increasing relative time increments. From Straka et al. (2003).

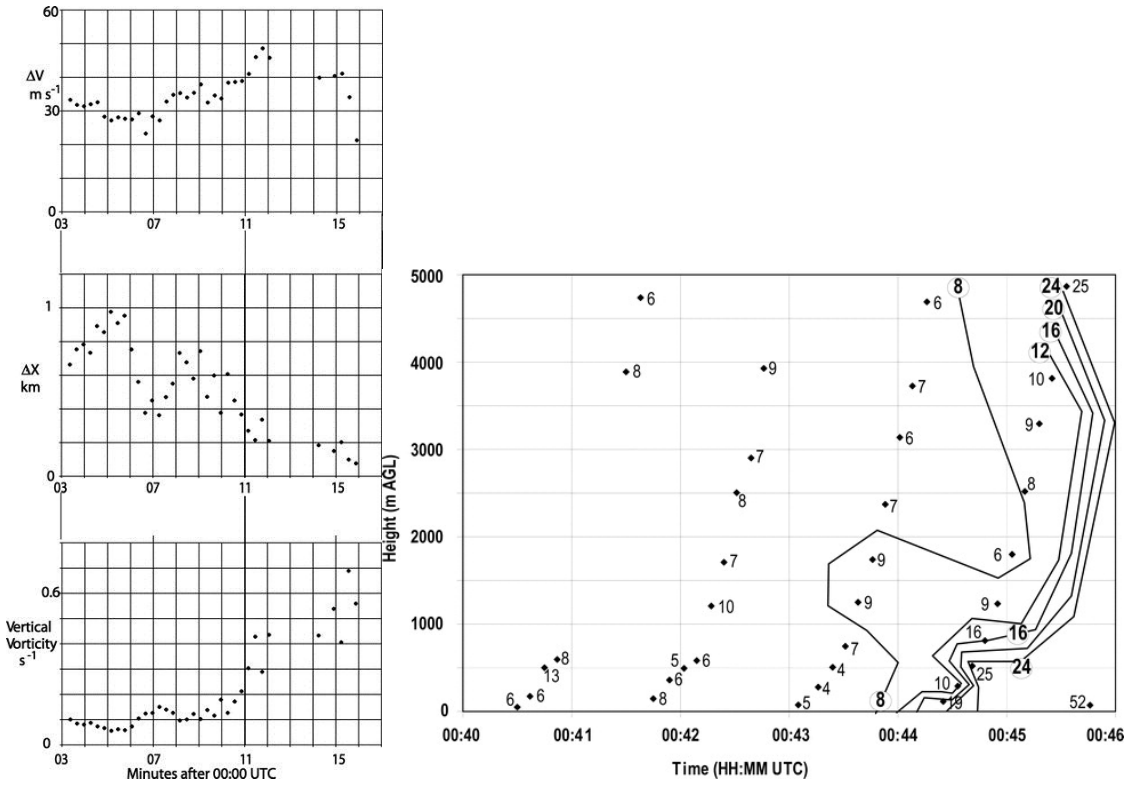

Figure 2.5. (Left) Evolution of Doppler velocity difference, spatial scale, and estimated vertical vorticity in the Glenpool tornado. Two phases of scale contraction and intensification occur during tornadogenesis. From Wurman et al. (2007a). (Right) Evolution of estimated axisymmetric vertical vorticity in developing tornado. Values are $\times 10^{-3}$ s^{-1}. Contours are drawn at 0.008, 0.012, 0.016, 0.020, and 0.024 s^{-1}. Vorticity develops very rapidly after 0044 UTC, particularly at low levels. From Wurman et al. (2007b).

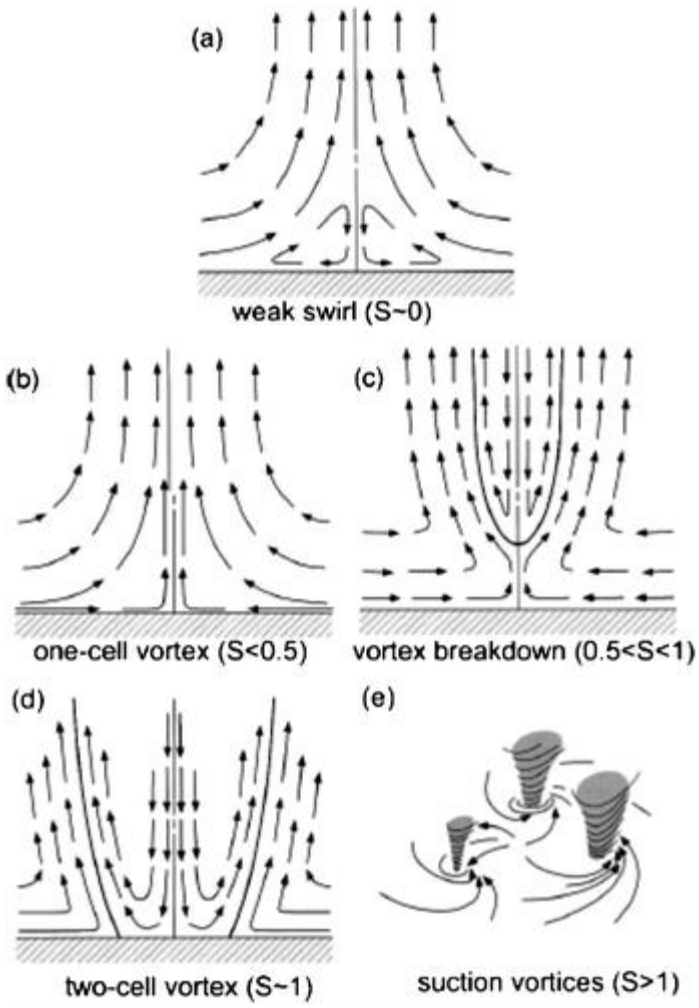

Figure 2.6. Idealized vortex structures as a function of swirl ratio (S). Vertical cross sections are shown in (a)–(d). Adapted from Davies-Jones (1986).

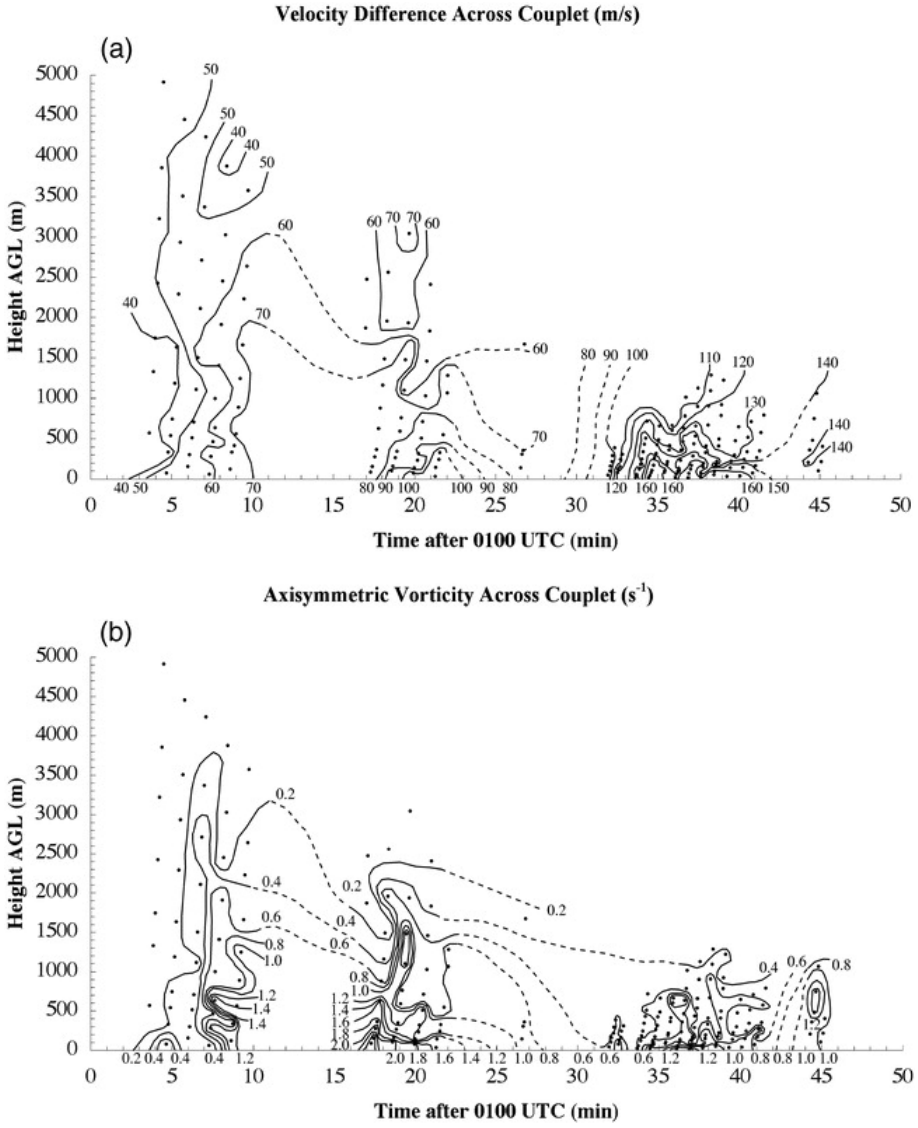

Figure 2.7. The (a) peak velocity difference and (b) axisymmetric vorticity across the Spencer, SD tornado as a function of time and height. From Alexander and Wurman (2005).

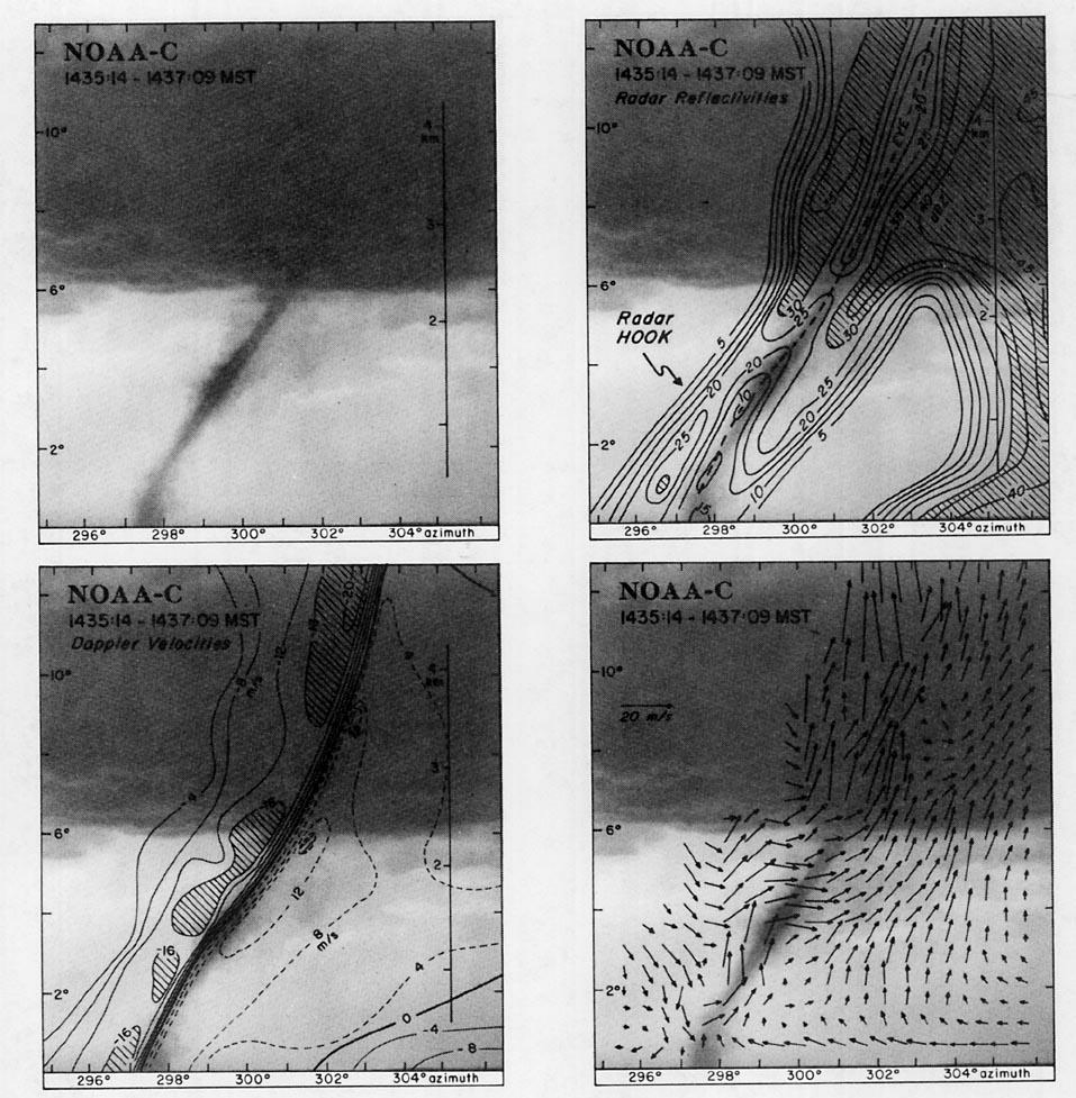

Figure 2.8. Photographs of the 2 July 1987 tornado superimposed on vertical cross sections through the center of the hook echo/misocyclone of radar reflectivity (upper right), single-Doppler velocities (lower left) from the NOAA-C radar, and dual-Doppler winds (lower right) from NOAA-C and NOAA-D. Radar reflectivities greater than 35 dBZ are hatched. Solid and dashed contours represent Doppler velocities out of and into the photograph, respectively. Dimensions of the beam and tornado core are also shown on some of the diagrams. Heights are in kilometers (AGL). From Wakimoto and Martner (1992).

Figure 4.1. The MWR-05XP radar as it would appear in data collection mode, from May of 2007. The National Weather Center appears in the background. Photo © Michael French.

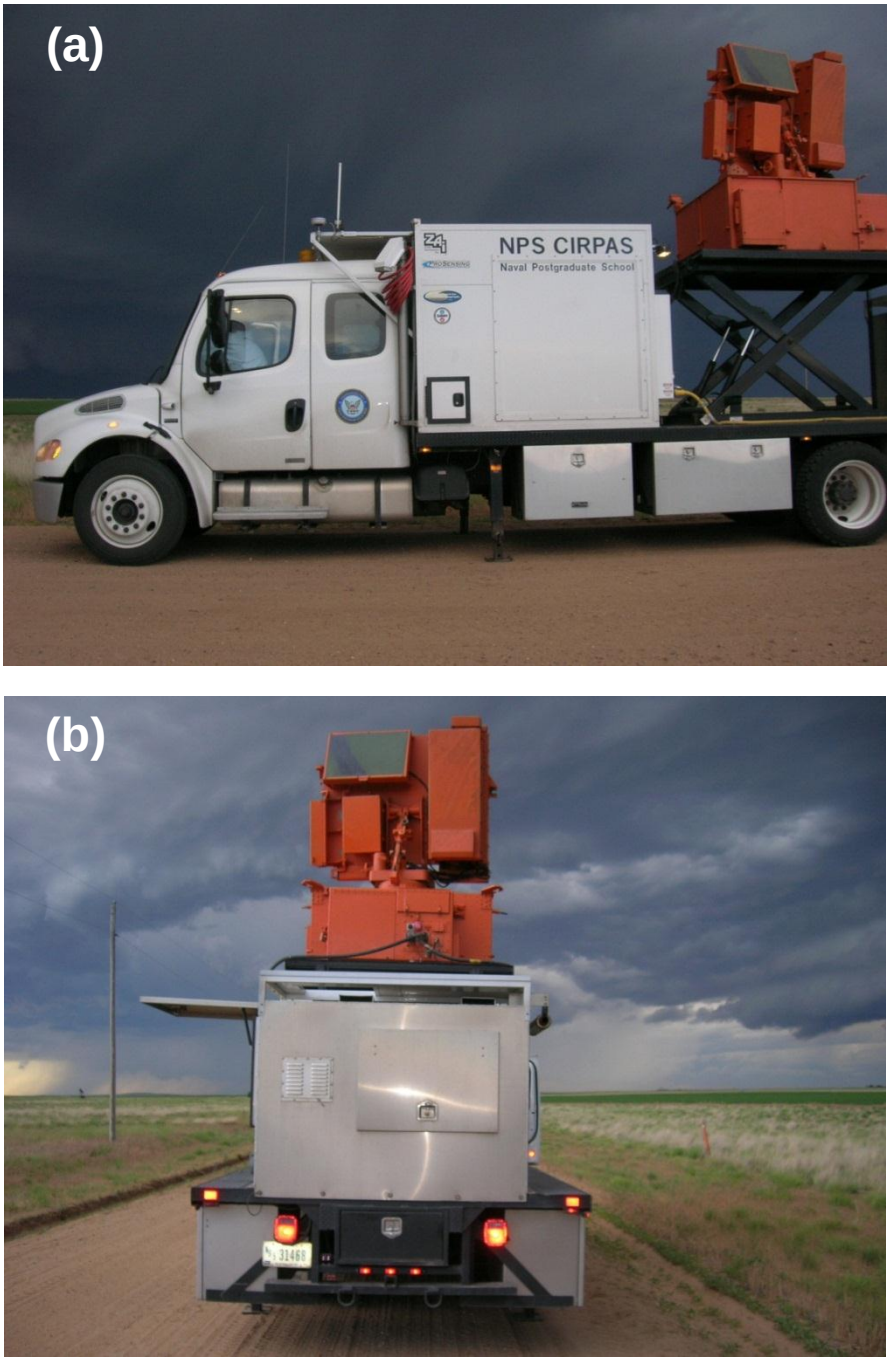

Figure 4.2. An example of photographs taken at deployment sites in 2009 and 2010 looking approximately (a) west and (b) south. The pictures are not intended to be used to estimate pitch and roll angles, but rather to show that the radar system was relatively level (or not). From a deployment on 10 June 2009 in eastern Colorado. Photographs © Michael French.

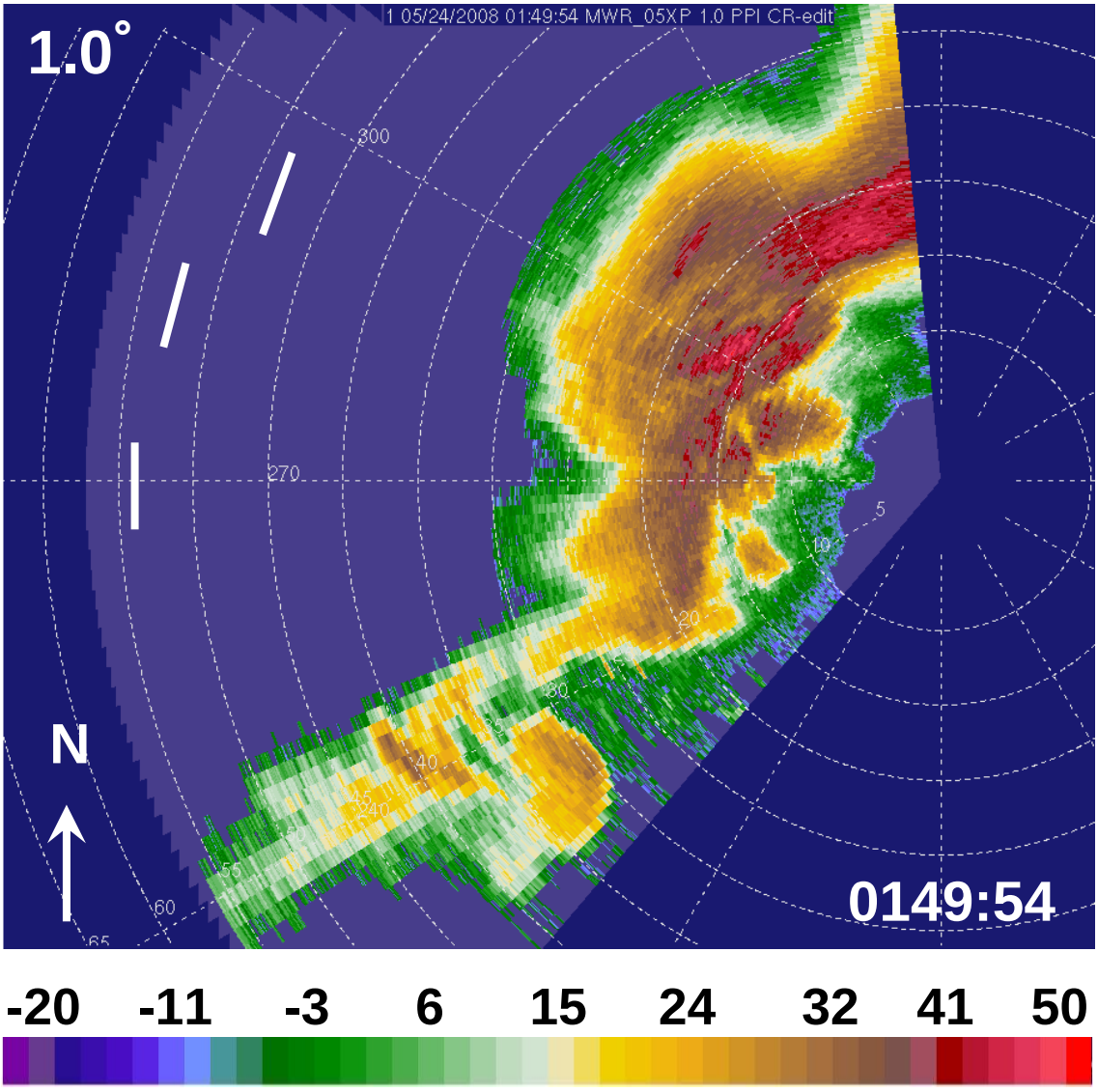

Figure 4.3. MWR-05XP reflectivity (dBZ) at 1.0° elevation angle obtained on a tornadic supercell at 0149:54 UTC on 24 May 2008 from near Ellis, Kansas. Attenuation is illustrated by the white lines, which mark the approximate westward extent of reflectivity as sampled by the WSR-88D in Dodge City, Kansas. Attenuation likely explains the unnatural gaps in reflectivity in the hook echo as well. Range rings are every 5 km. The colorbar for radial velocity appears below the figure.

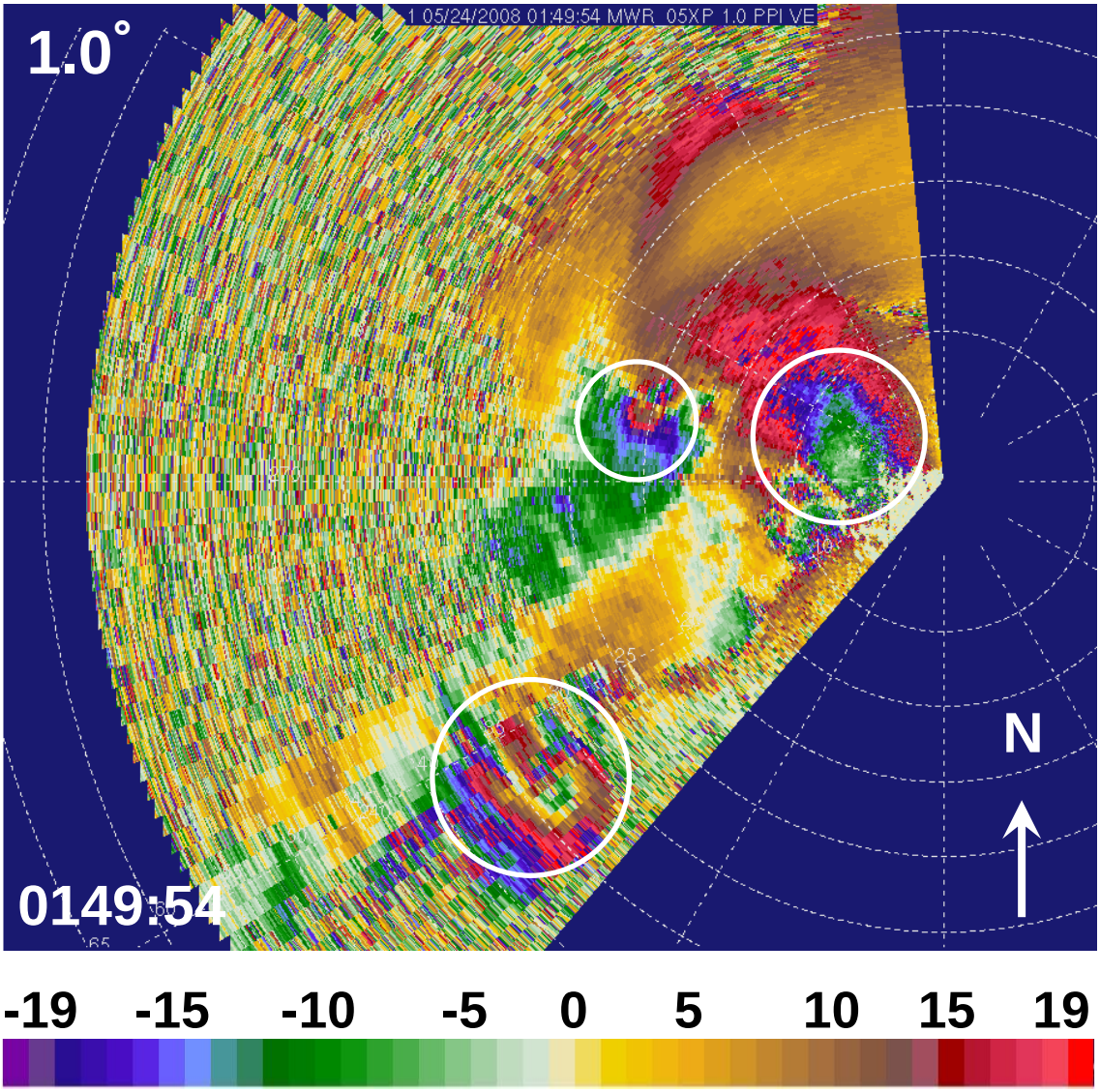

Figure 4.4. As in Fig. 4.3, but for unedited radial velocity (m s^{-1}). Areas enclosed by white circles outline regions of aliased velocities. The Nyquist velocity for this dataset is 19.7 m s^{-1}. Areas of aliased velocities had to be manually de-aliased because of poor algorithm performance in areas of tight radial velocity gradients. The colorbar for radial velocity appears below the figure.

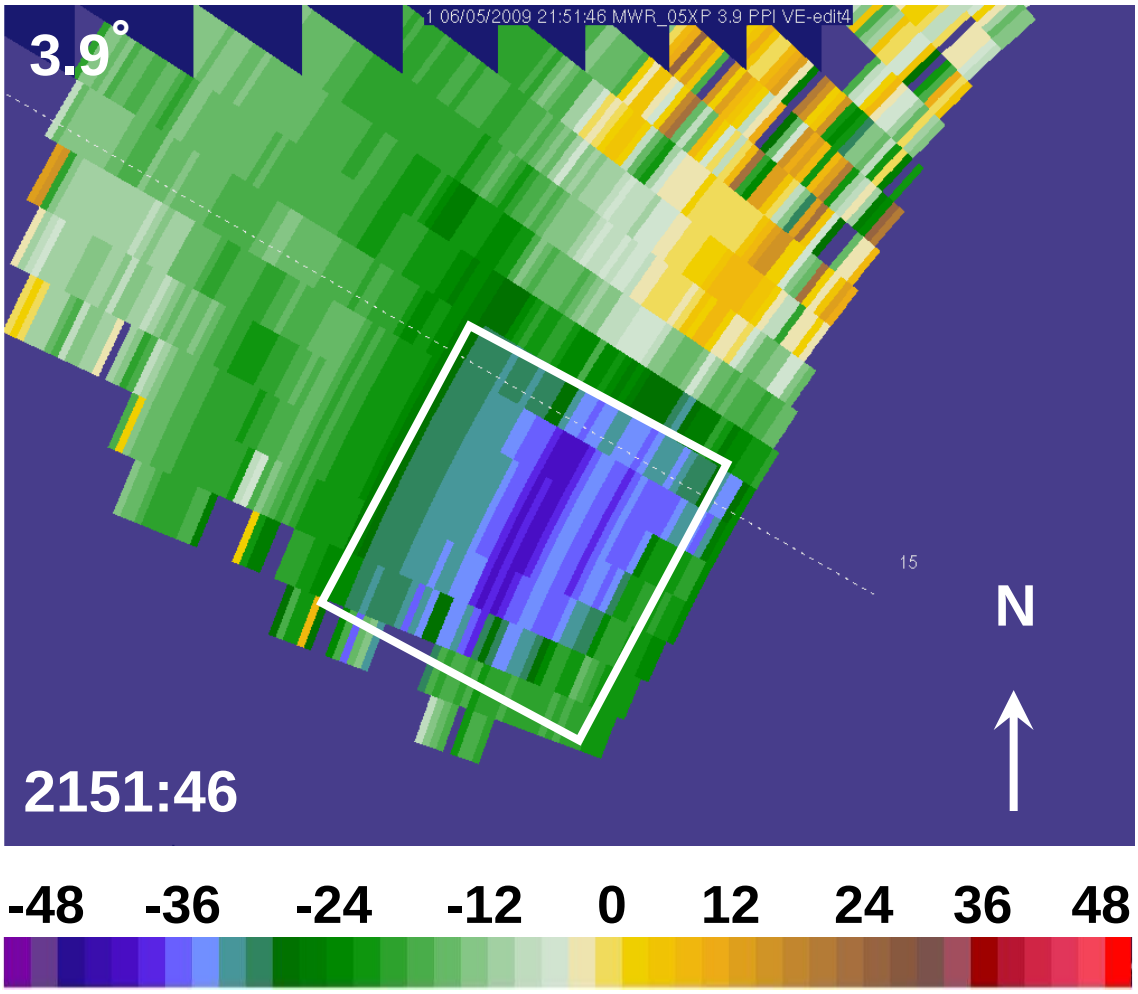

Figure 4.5. MWR-05XP radial velocity (m s^{-1}) at 3.9° elevation angle at 2151:46 UTC on 5 June 2009 near the time the Goshen County tornado formed. The area outlined by the white rectangle encompasses a region of beam smearing. The colorbar for radial velocity appears below the figure.

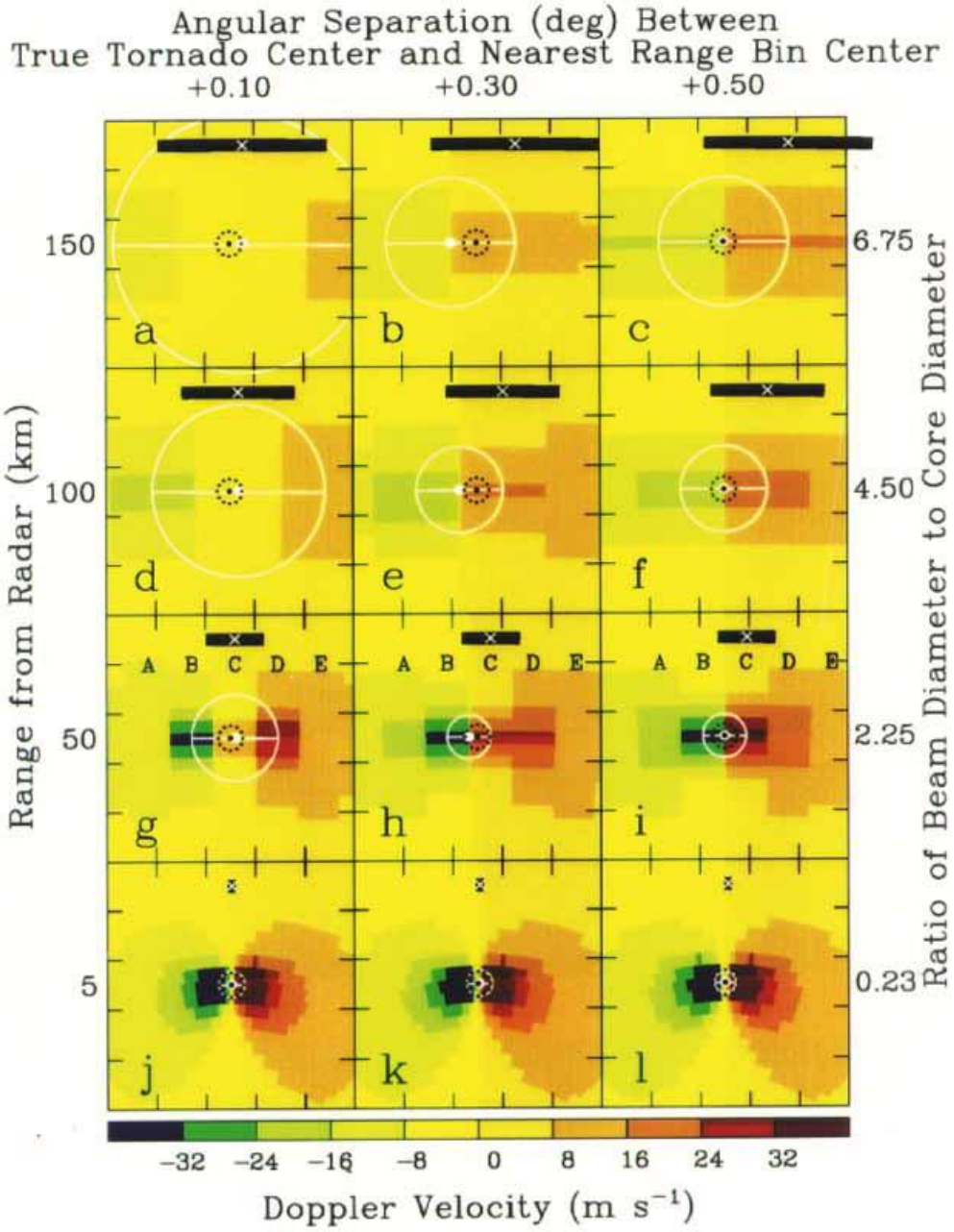

Figure 4.6. Plan view of a simulated Doppler velocity TVS for a radar located 5, 50, 100, and 150 km from a Rankine combined vortex center. Negative (positive) Doppler velocities to the left (right) of the vortex center represent flow toward (away from) the radar. Each dotted black circle, around its black center point, represents the true circle of maximum wind speed (25 m s^{-1} at radius of 2.5 km) for the model tornado. Each white circle, around its white signature center point, represents the deduced size of the

core region based on the peak Doppler velocity measurements. The black bar represents the radar resolution volume size broadened by antenna motion (effective beamwidth of 1.29°) for beam C; a white X represents the center of the resolution volume. Beams A, B, C, D, and E are identified in (g)–(i). Border tick marks are 1 km apart. Data resolution is 1° azimuth by 0.25-km range. Angular separation (°) between the true vortex center and beam center is shown at the top. The ratio of radar beam diameter to core diameter is shown on the right. The radar is located beyond the bottom of the figure. The maximum wind speed is 100 m s^{-1} and is located at 0.25 km from the model tornado center. From Wood and Brown (1997).

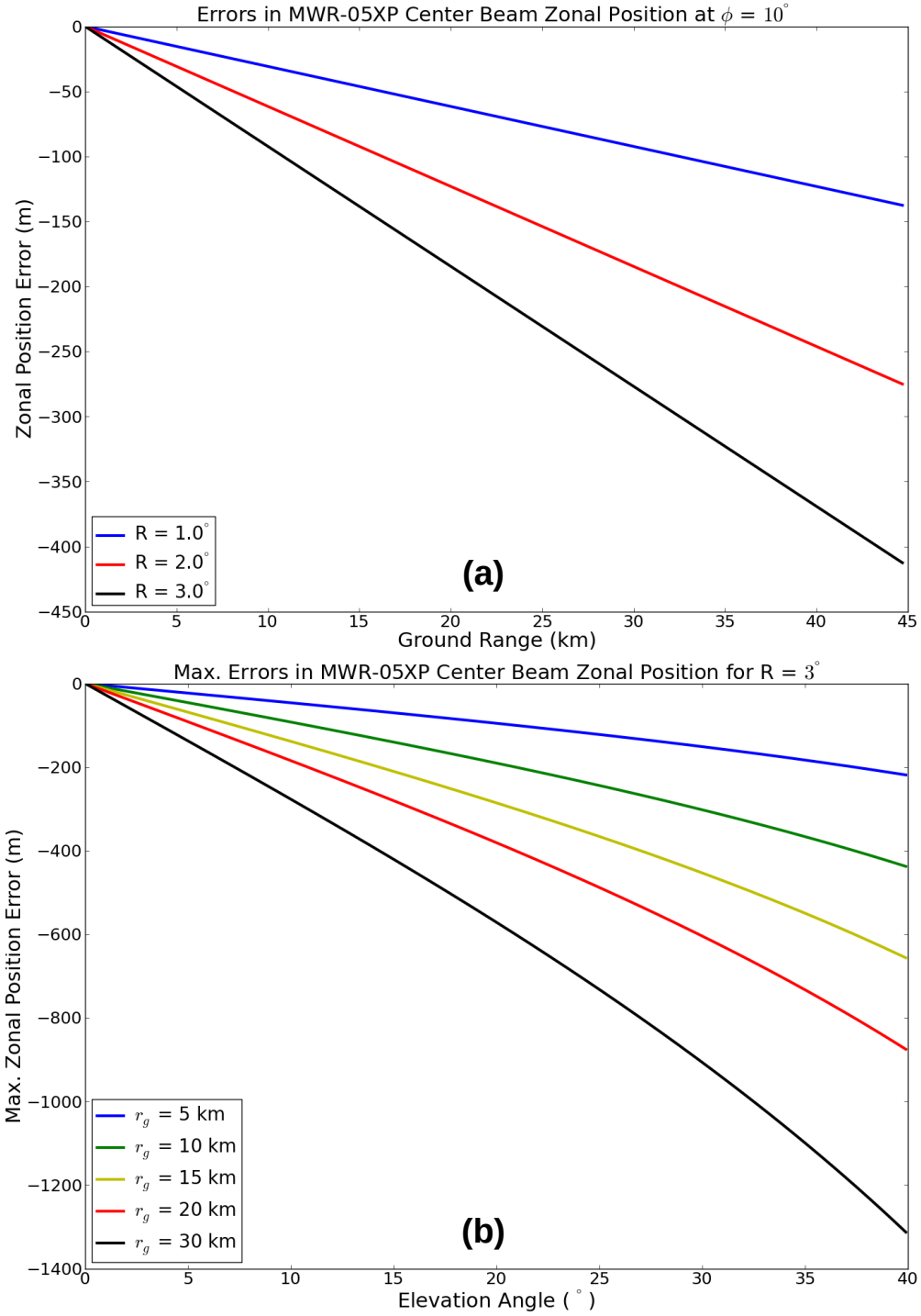

Figure 4.7. Approximate errors in radar center beam zonal locations (a) as a function of ground range at 10° elevation angle for three common roll angles and (b) as a function of elevation angle at roll angle 3° for five common ground ranges. Positive (negative) errors indicate displacement in the eastward (westward) direction.

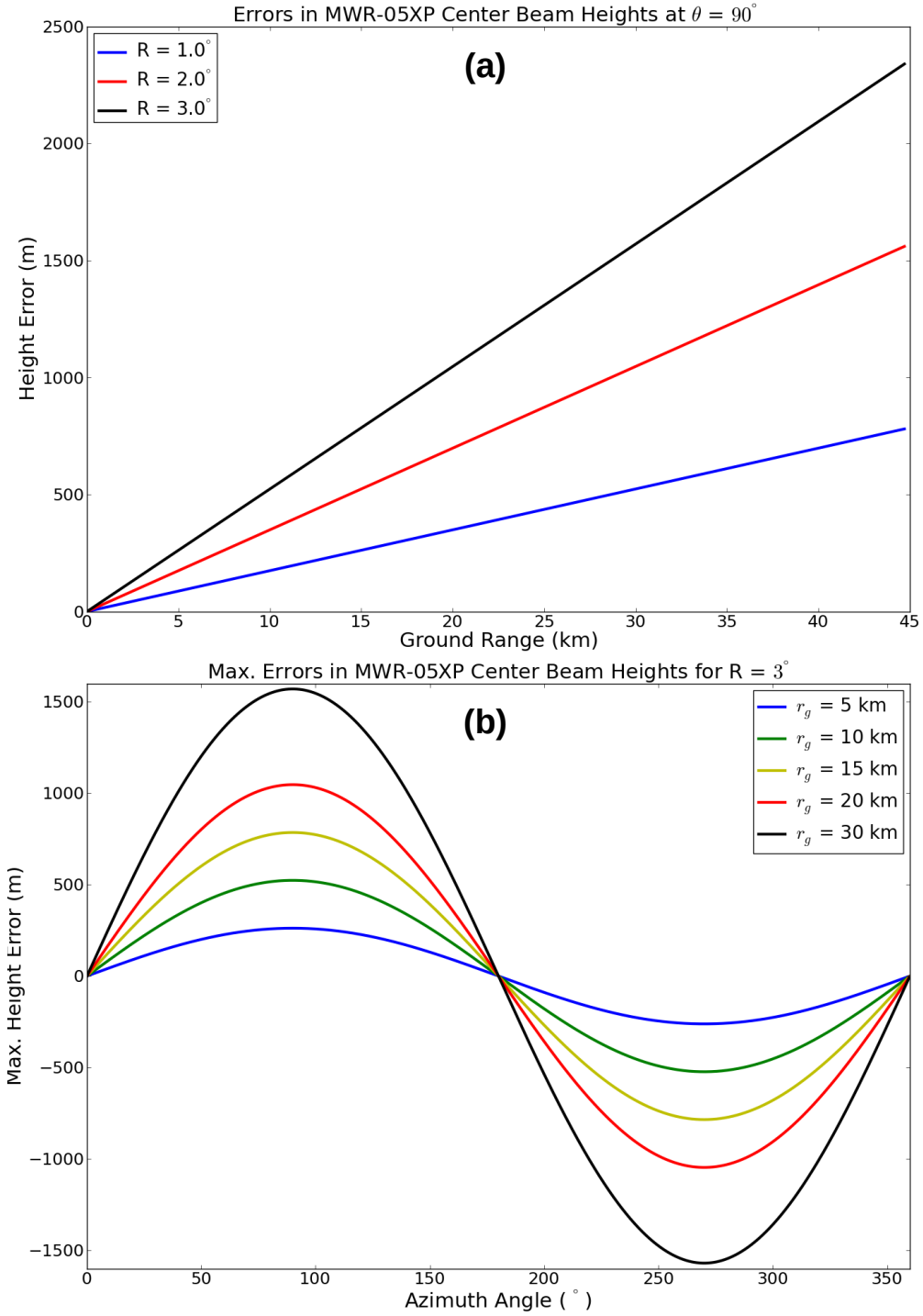

Figure 4.8. Approximate errors in radar center beam heights ARL (a) as a function of ground range at 90° azimuth angle for three common roll angles and (b) as a function of azimuth angle at roll angle 3° for five common ground ranges. Positive (negative) errors indicate displacement downward (upward).

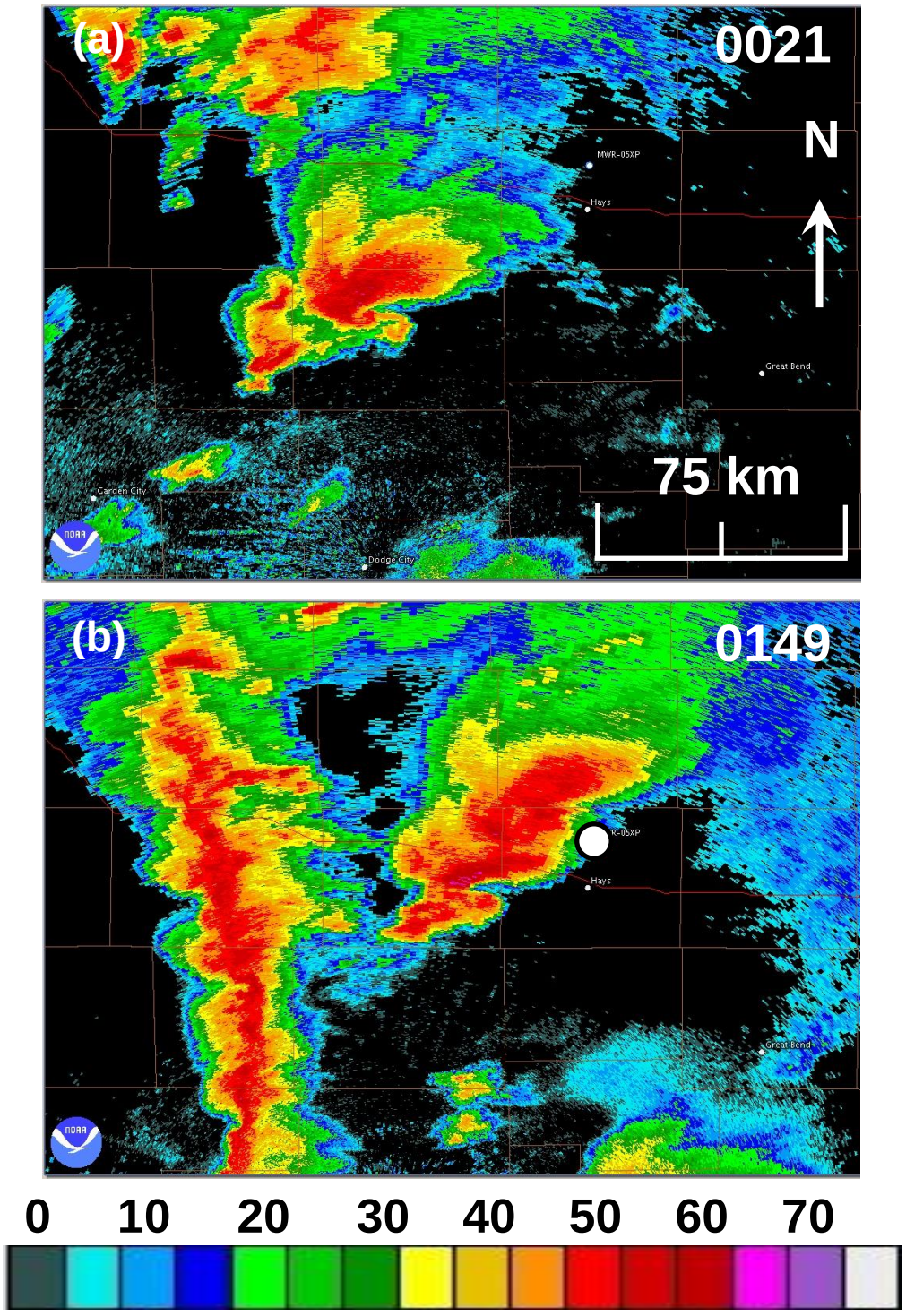

Figure 5.1. Reflectivity (dBZ) from the WSR-88D at 0.5° elevation angle in Dodge City, Kansas at (a) 0021 and (b) 0149 UTC on 24 May 2008. The location of the MWR-05XP during its deployment is approximated by a white circle in (b).

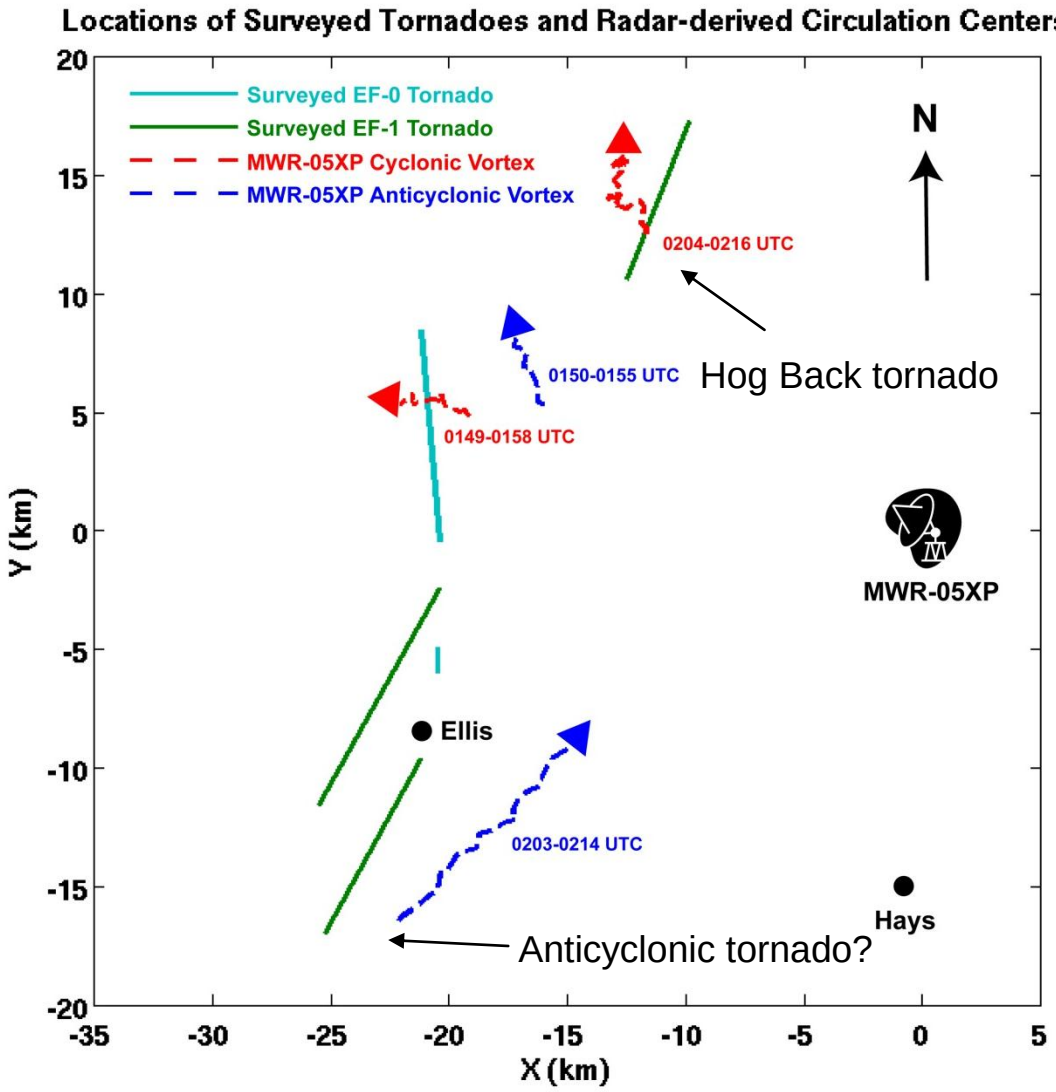

Figure 5.2. A comparison of NWS-surveyed tornado paths (straight lines) and paths of radial velocity vortex signatures at 1.0° elevation angle (dashed lines). Light blue (green) straight lines indicate damage survey ratings of EF-0 (EF-1). Red (blue) dashed lines indicate cyclonic (anticyclonic) vortex signatures in MWR-05XP data. Times indicate the beginning and end time of the vortex signatures shown in the figure. The location of the MWR-05XP is marked by the radar icon.

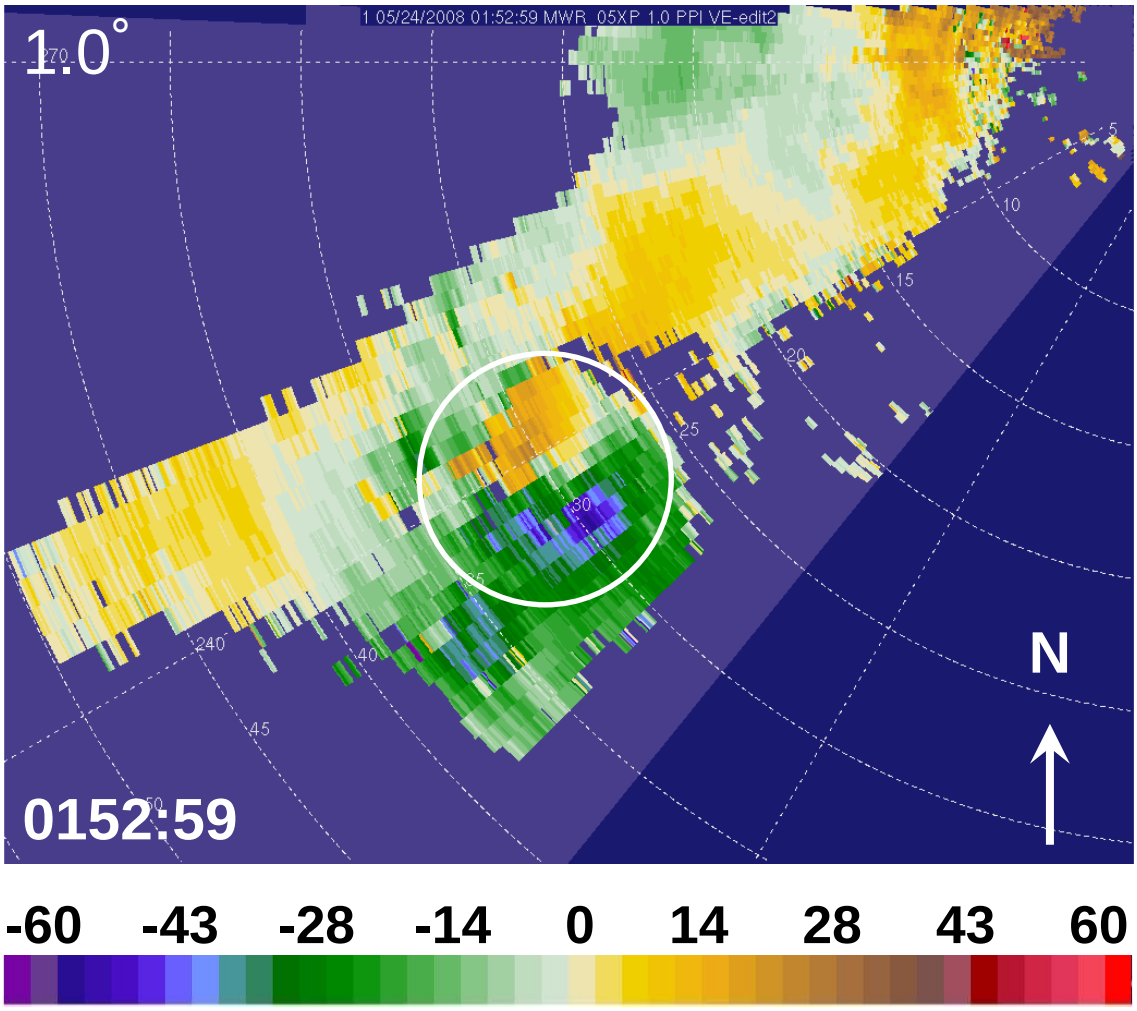

Figure 5.3. Radial velocity (m s^{-1}) PPI scan at 1.0° elevation angle at 0152:59 UTC. The large area of cyclonic rotation enclosed by the white circle may have been responsible for tornado damage as described in the text. Range rings are every 5 km. The colorbar for radial velocity appears at the bottom. The approximate center beam height at the location of the white circle is ~530 m ARL.

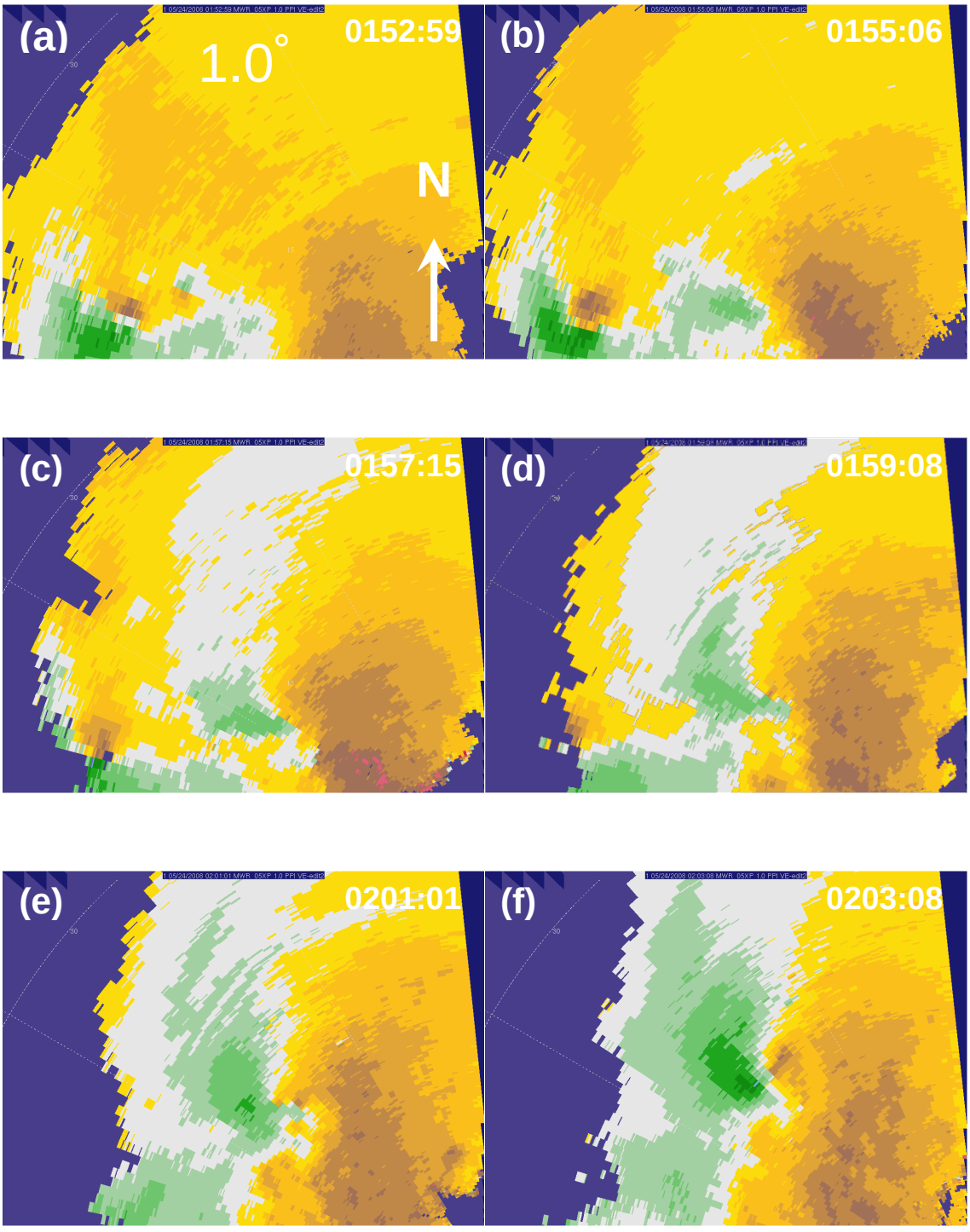
(a)
1.0°
0152:59
N
(b)
0155:06
(c)
0157:15
(d)
0159:08
(e)
0201:01
(f)
0203:08

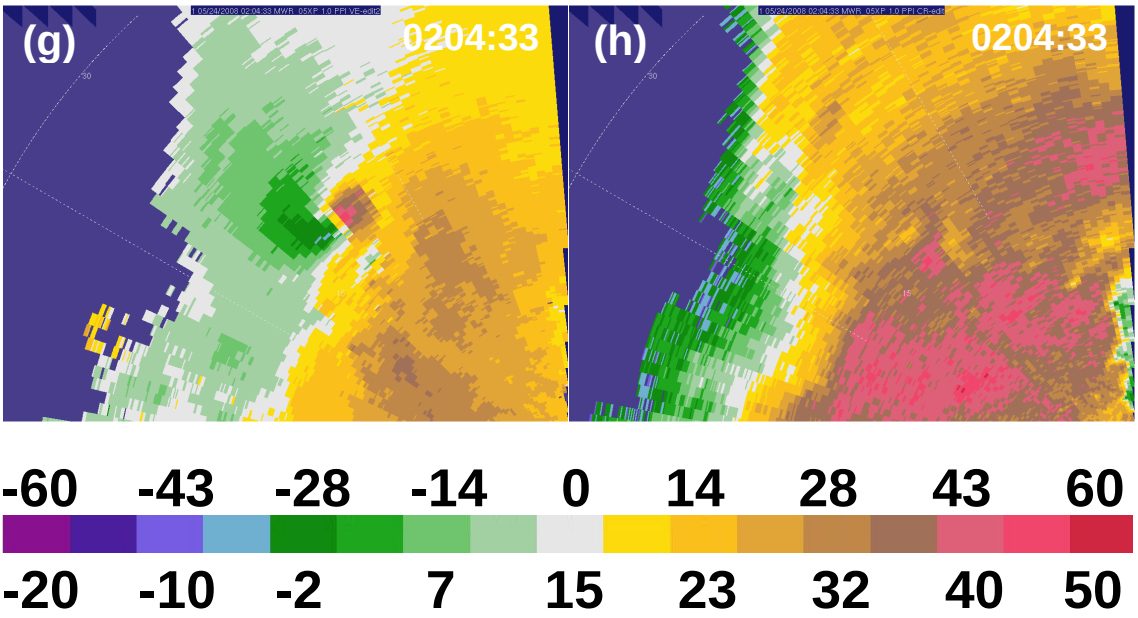

Figure 5.4. A series of radial velocity (m s^{-1}) PPI scans at 1.0° elevation angle prior to formation of the Hog Back tornado at (a) 0152:59, (b) 0155:06, (c) 0157:15, (d) 0159:08, (e) 0201:01, (f) 0203:08, (g) 0204:33, and (h) reflectivity (dBZ) at 0204:33 UTC, near the time of tornadogenesis. Range rings are every 15 km. The scale for radial velocity (reflectivity) appears on the top (bottom) of the colorbar. The approximate center beam height at the location of the vortex center in (g) is 300 m ARL.

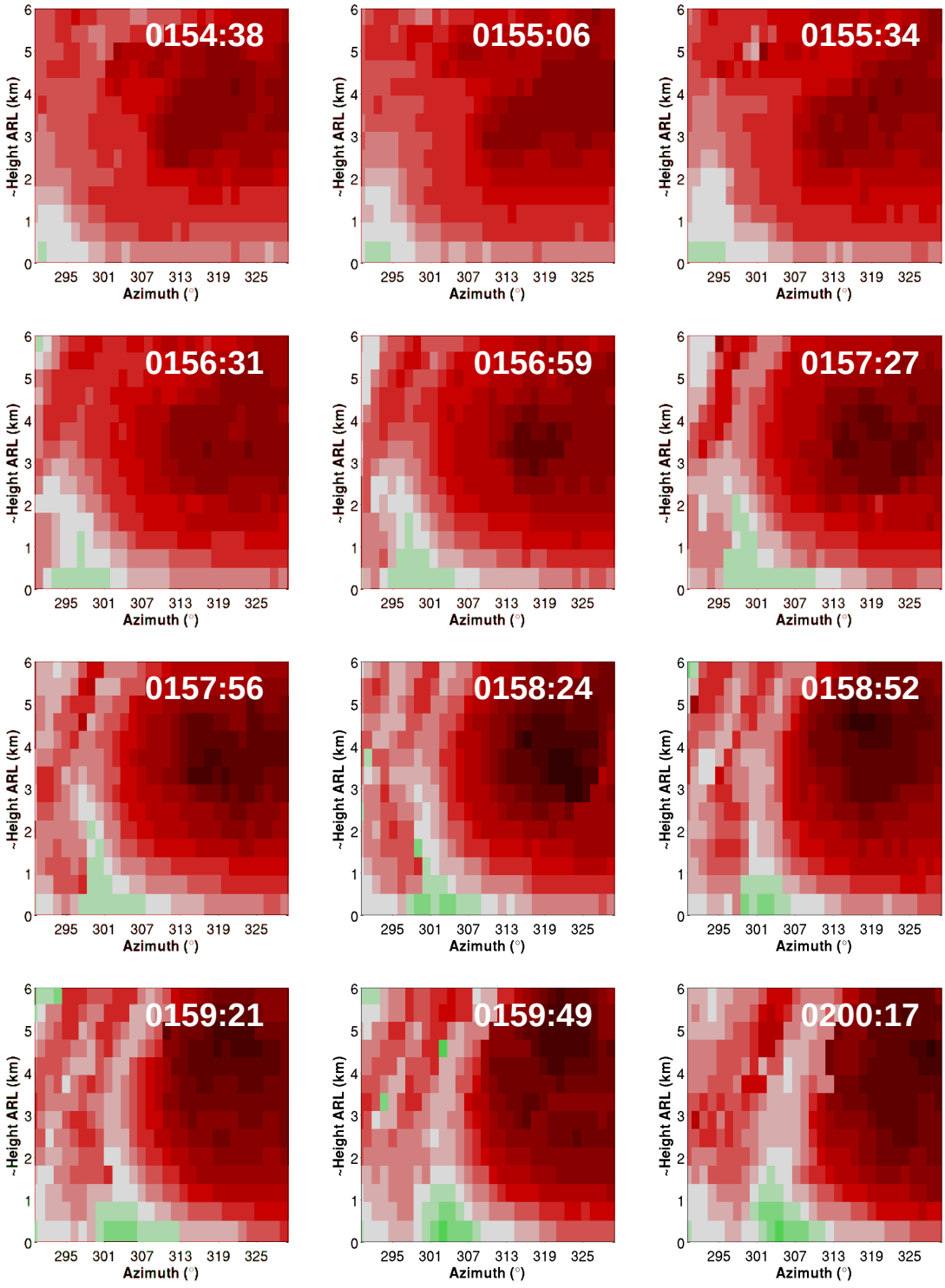
0154:38
0155:06
0155:34
0156:31
0156:59
0157:27
0157:56
0158:24
0158:52
0159:21
0159:49
0200:17
~Height ARL (km)
0 1 2 3 4 5 6
Azimuth (°)
295 301 307 313 319 325

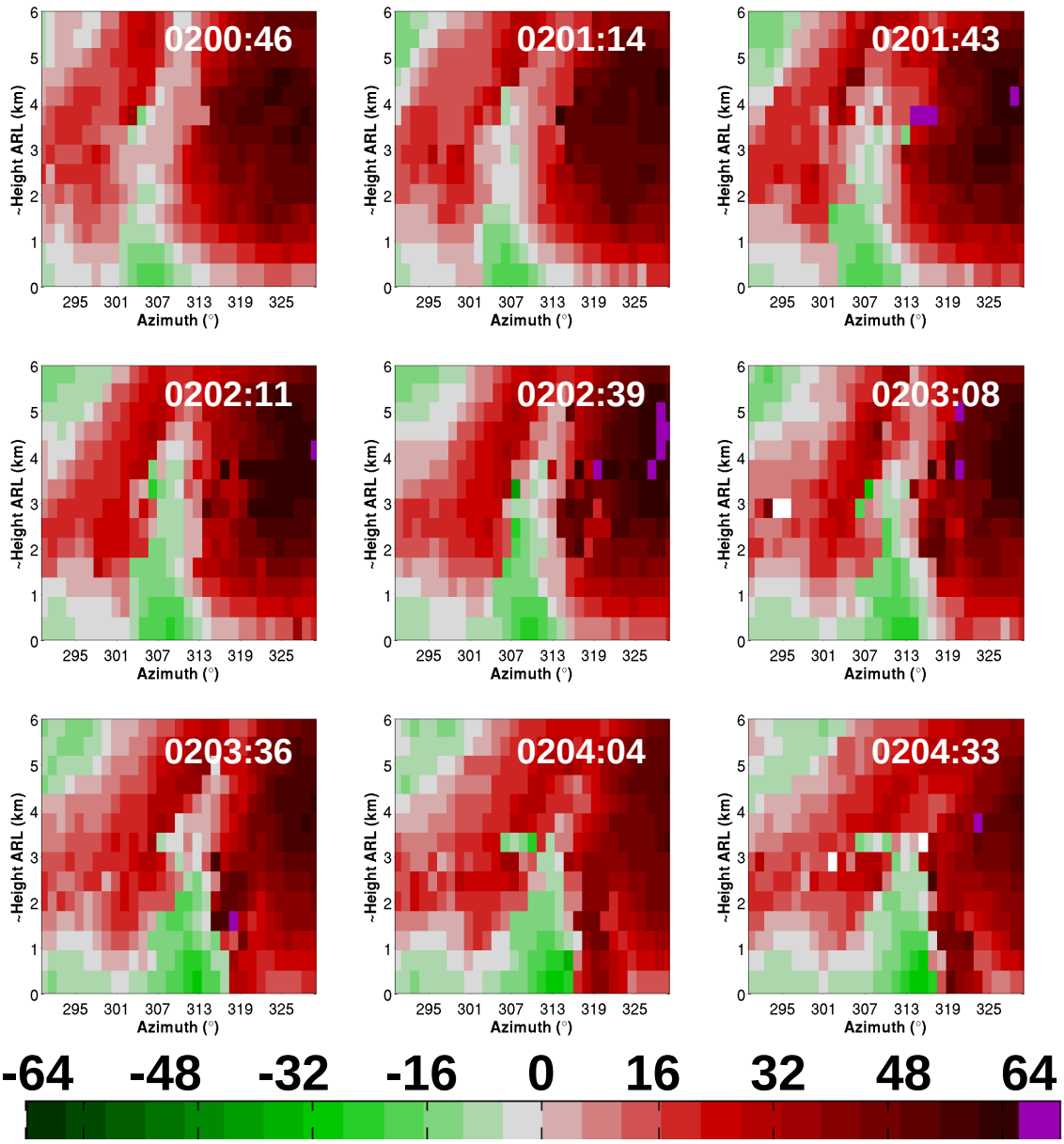

Figure 5.5. Azimuth height indicator (AHI) displays of radial velocity (m s^{-1}) at 17.0 km during tornadogenesis of the Hog Back tornado. AHIs are every 28 sec. (except for 0156:31) from 0154:09 to 0204:33 UTC. Azimuths shown are 290-330° and approximate heights extend to ~6 km ARL. The absolute location is unchanged for all plots. The vertical reference frame is not stretched. The colorbar for radial velocity appears below the figure on the first page.

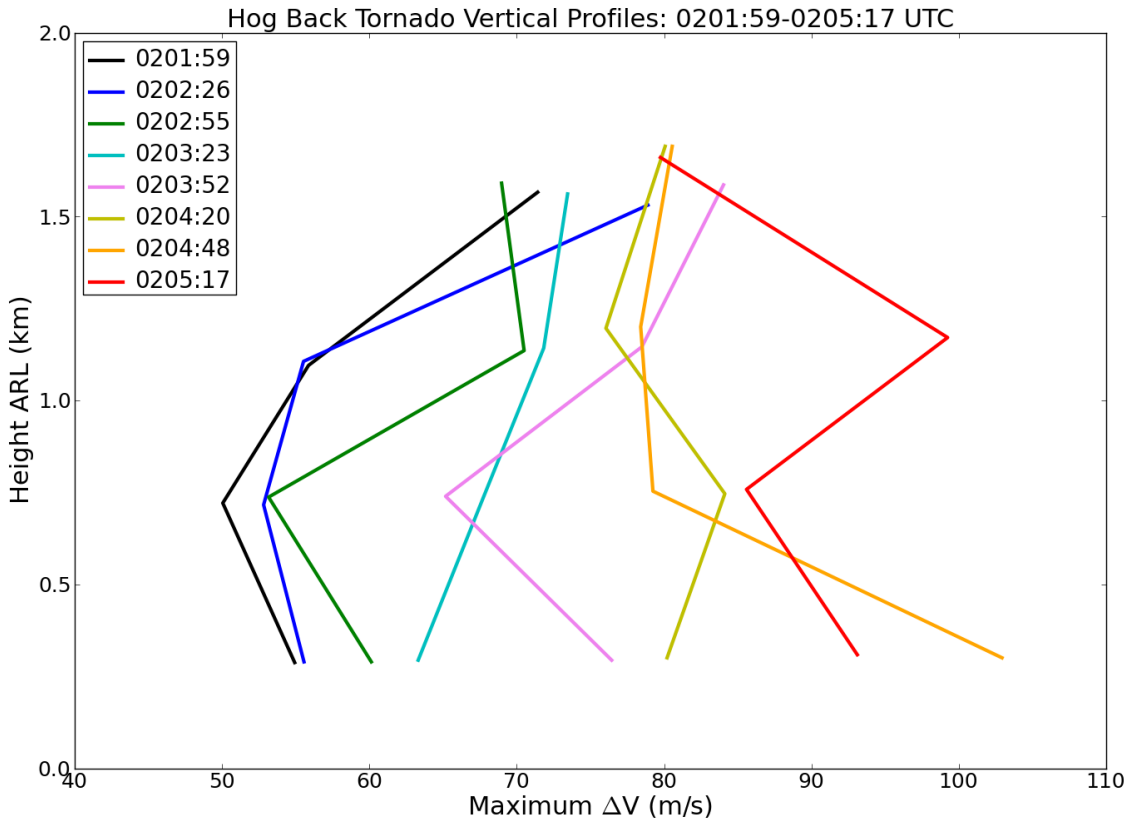

Figure 5.6. Vertical profiles of maximum ΔV (m s^{-1}) every 28 sec. from 0201:58-0205:17 UTC for the developing Hog Back tornado. Profiles move from left to right with increasing time because of consistent increases in ΔV with time.

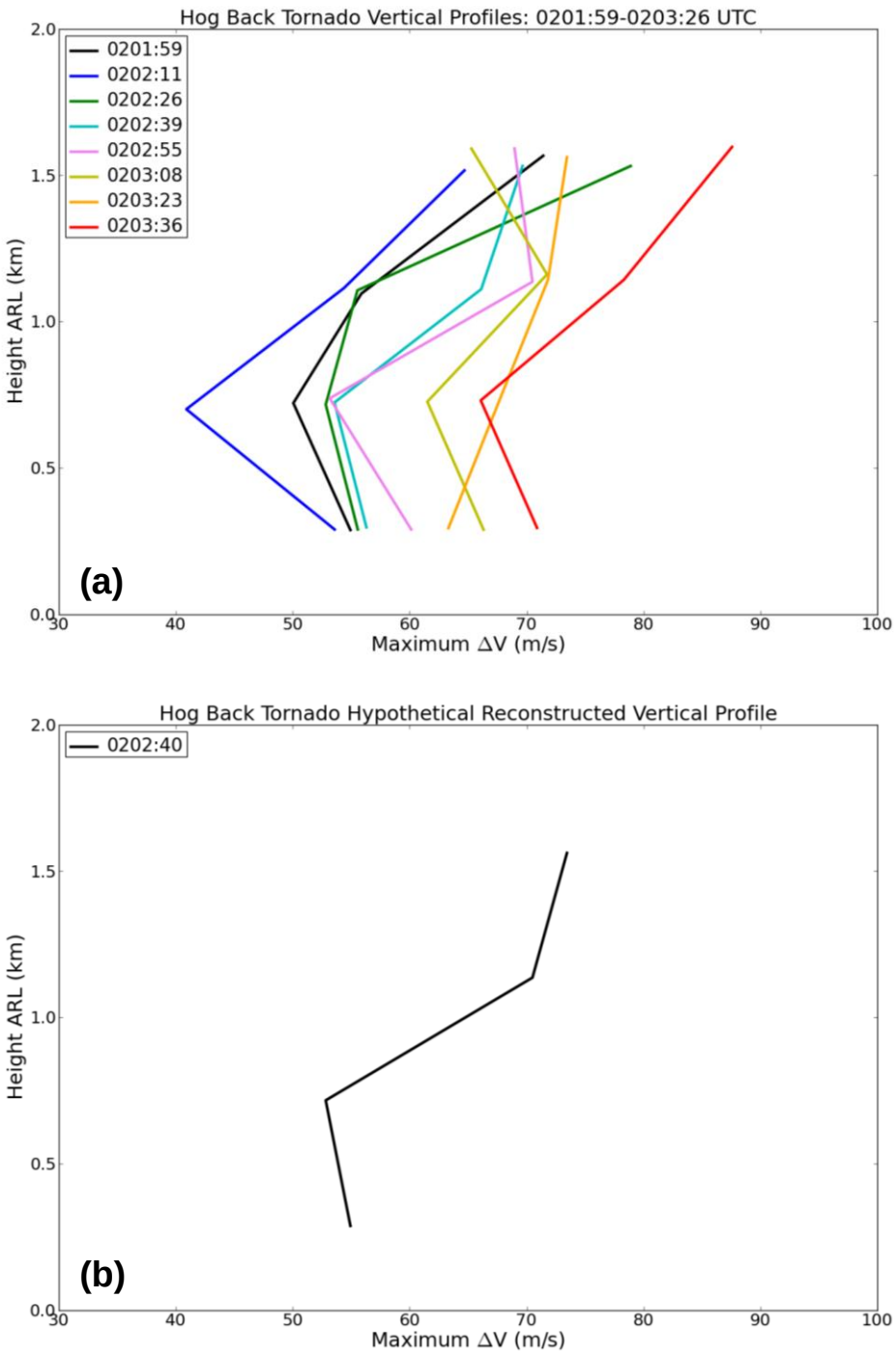

Figure 5.7. Vertical profiles of maximum ΔV (m s^{-1}) (a) time series every 14 sec. from 0201:58-0203:26 UTC for the developing Hog Back tornado, and (b) a hypothetical profile created from a traditional-scanning, mobile, Doppler radar during the same time period.

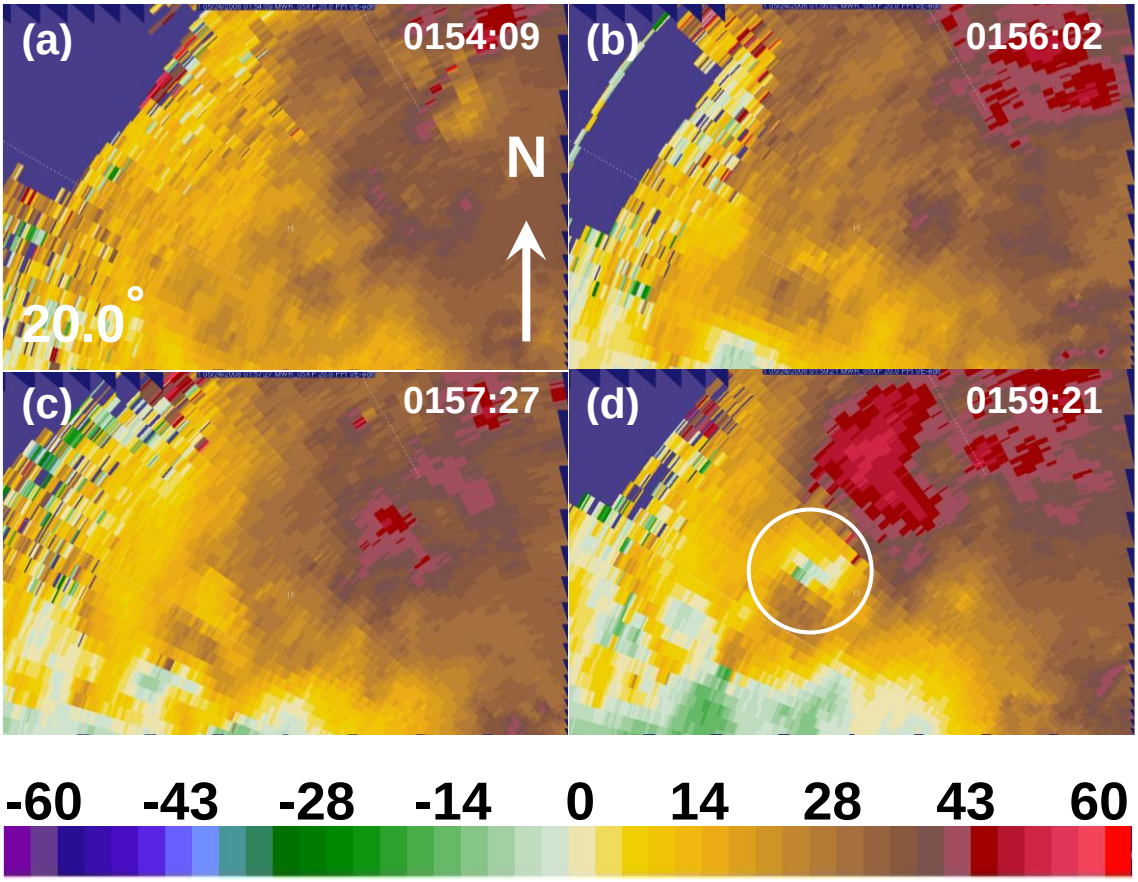

Figure 5.8. A series of radial velocity (m s^{-1}) PPI scans at 20.0° elevation angle prior to formation of the Hog Back tornado at (a) 0154:09, (b) 0156:02, (c) 0157:27, and (d) 0159:21 UTC prior to tornadogenesis. The white circle in (d) encloses the first inbound velocities associated with the precursor to the Hog Back tornado observed at 20.0° elevation angle. Range rings are every 15 km. The colorbar for radial velocity appears at the bottom. The approximate center beam height at the location of the white circle is ~5.8 km ARL.

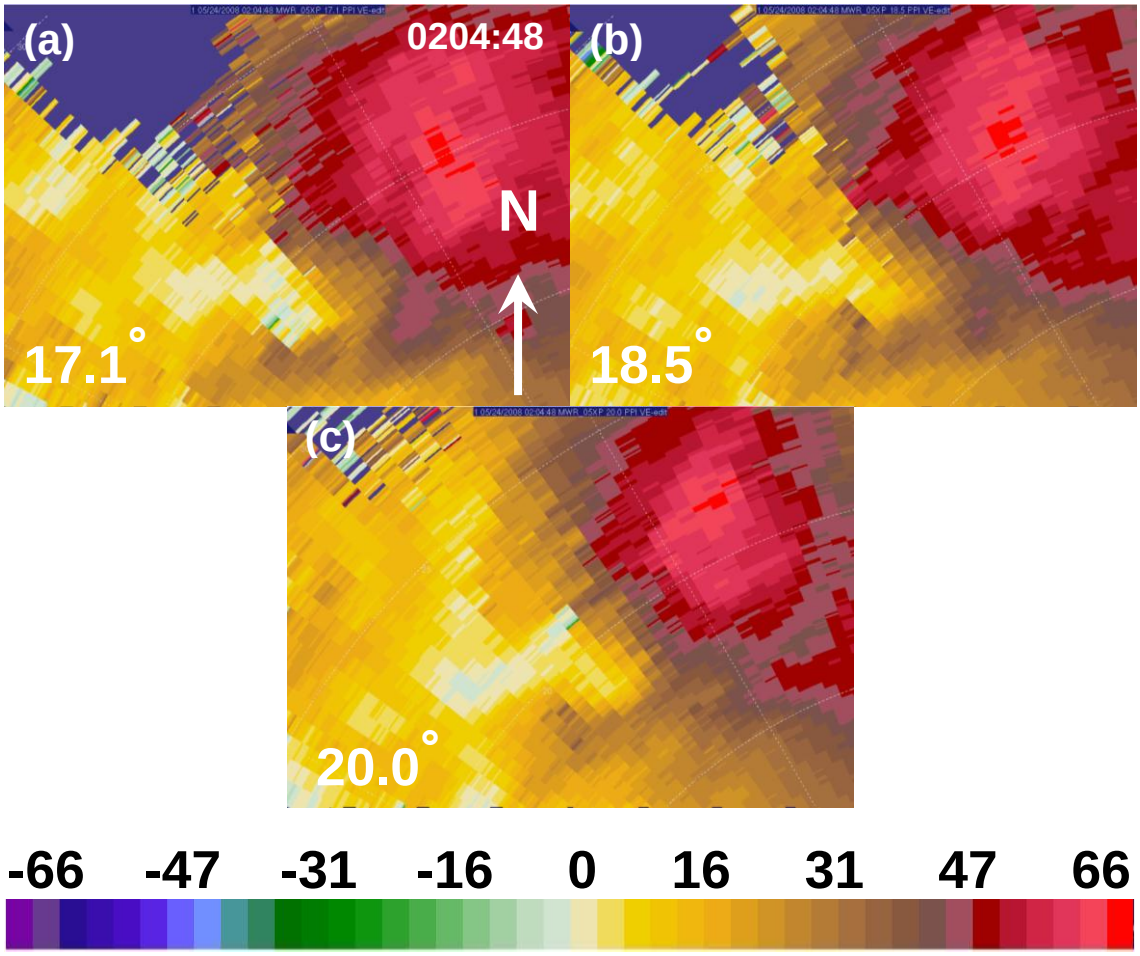

Figure 5.9. Radial velocity (m s^{-1}) PPI scans at (a) 17.1°, (b) 18.5°, and (c) 20.0° elevation angle at 0204:48 UTC after the formation of the Hog Back tornado. Range rings are every 5 km. The colorbar for radial velocity appears beneath the figure. The approximate center beam height in the area of cyclonic shear is 5.5, 6.7, and 7.2 km ARL for (a), (b), and (c), respectively.

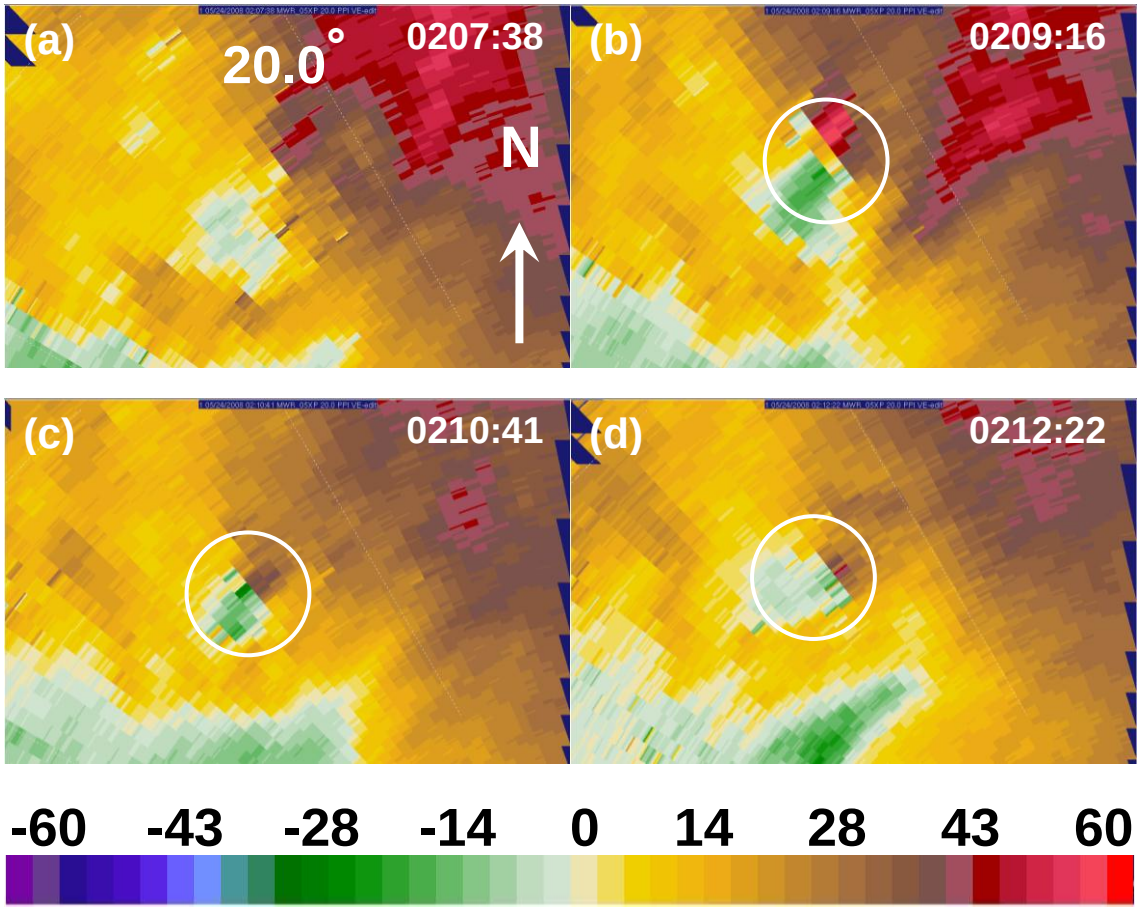

Figure 5.10. Radial velocity (m s^{-1}) PPI scans at 20.0° elevation angle after the formation of the Hog Back tornado at (a) 0207:38, (b) 0209:16, (c) 0210:41, and (d) 0212:22 UTC. Range rings are every 15 km. The white circles enclose TVSs. The colorbar for radial velocity appears beneath the figure. The approximate center beam height at the location of the TVS in (c) is 7.5 km ARL.

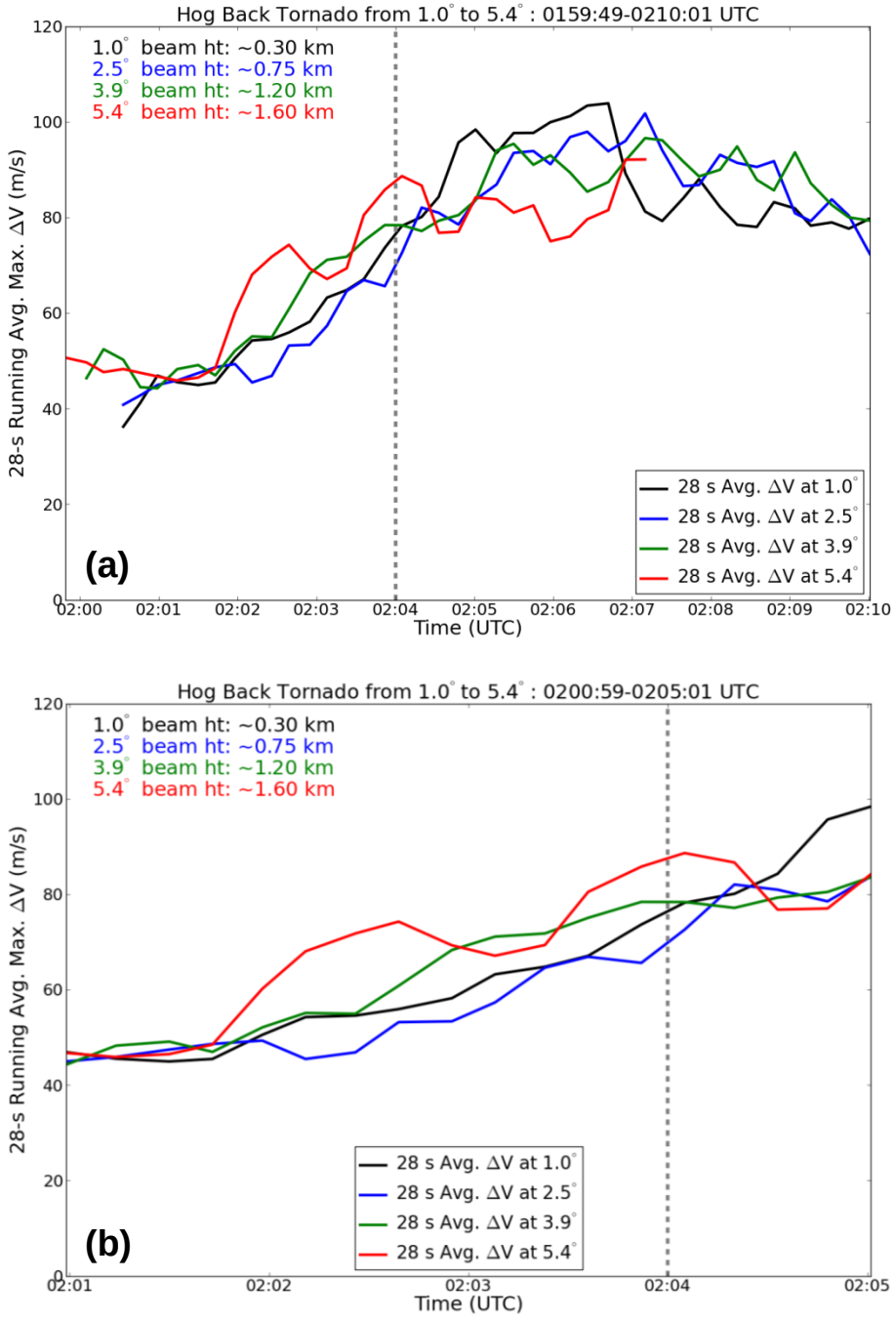

Figure 5.11. Time series of a 28-sec running average of maximum ΔV (m s^{-1}) at 1.0-5.4° elevation angle from (a) 0159:36-0210:01 and (b) 0200:59-0205:01 UTC for the developing Hog Back tornado. The dotted gray line marks the estimated time of tornadogenesis. Approximate beam heights are indicated in the upper left hand corner of each figure.

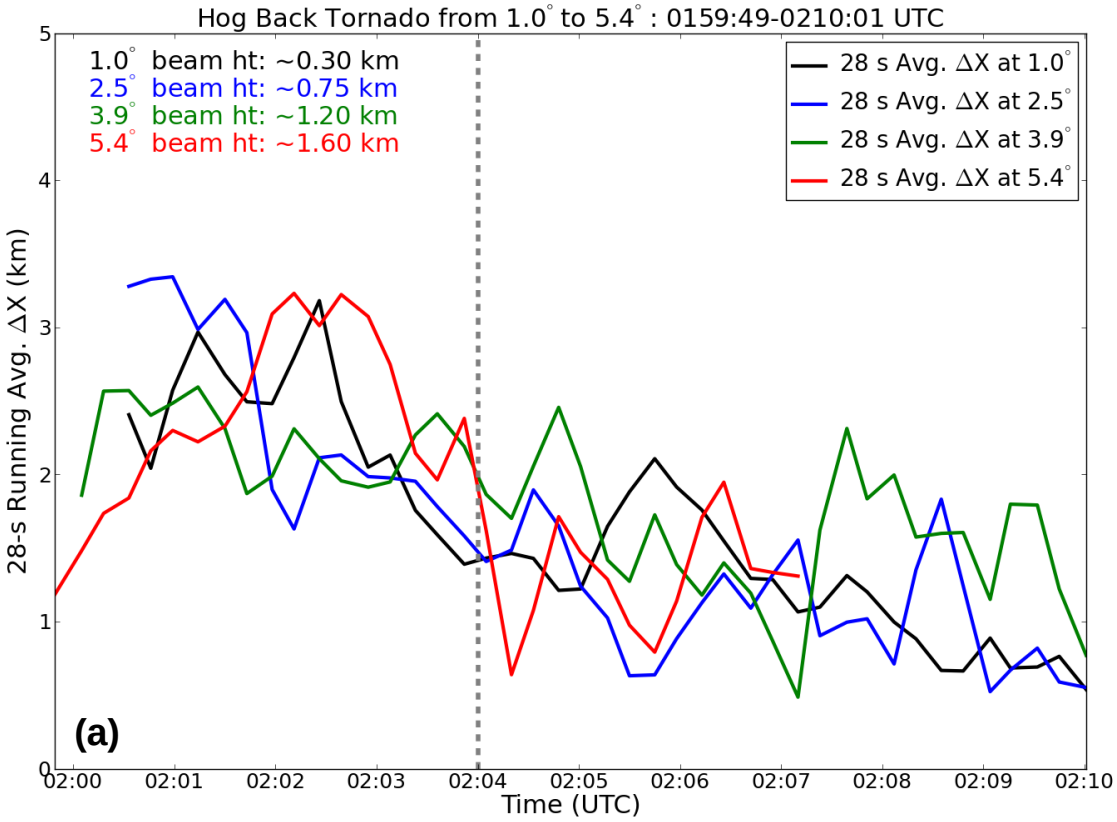
Hog Back Tornado from 1.0° to 5.4° : 0159:49-0210:01 UTC
1.0° beam ht: ~0.30 km
2.5° beam ht: ~0.75 km
3.9° beam ht: ~1.20 km
5.4° beam ht: ~1.60 km
28 s Avg. ΔX at 1.0°
28 s Avg. ΔX at 2.5°
28 s Avg. ΔX at 3.9°
28 s Avg. ΔX at 5.4°
28-s Running Avg. ΔX (km)
Time (UTC)
(a)

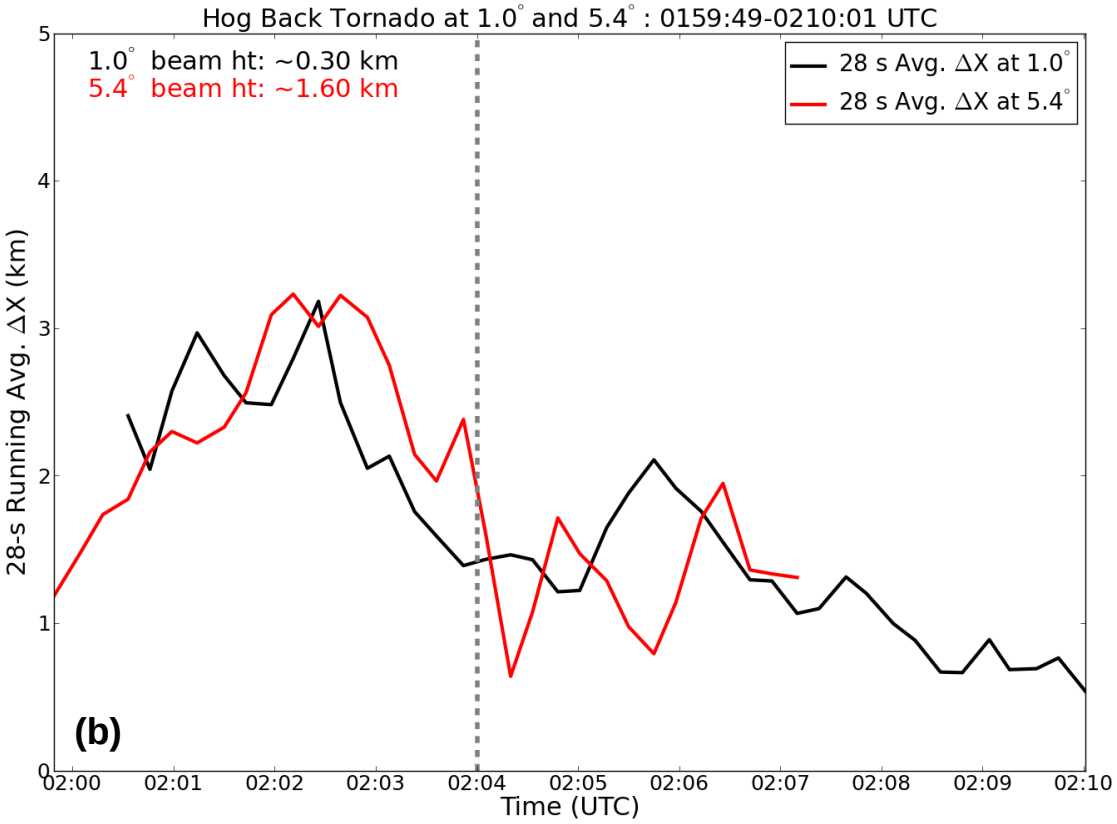
Hog Back Tornado at 1.0° and 5.4° : 0159:49-0210:01 UTC
1.0° beam ht: ~0.30 km
5.4° beam ht: ~1.60 km
28 s Avg. ΔX at 1.0°
28 s Avg. ΔX at 5.4°
28-s Running Avg. ΔX (km)
Time (UTC)
(b)

Figure 5.12. Time series of a 28-sec running average of the distance (km) between the maximum inbound and outbound radial velocities (m s^{-1}) in the Hog Back mesocyclone/tornado cyclone from 0159:36-0210:01 UTC at (a) 1.0°, 2.5°, 3.9°, and 5.4° and (b) 1.0° and 5.4° elevation angle for the developing Hog Back tornado. The dotted gray line marks the estimated time of tornadogenesis. Approximate beam heights are indicated in the upper left hand corner of each figure.

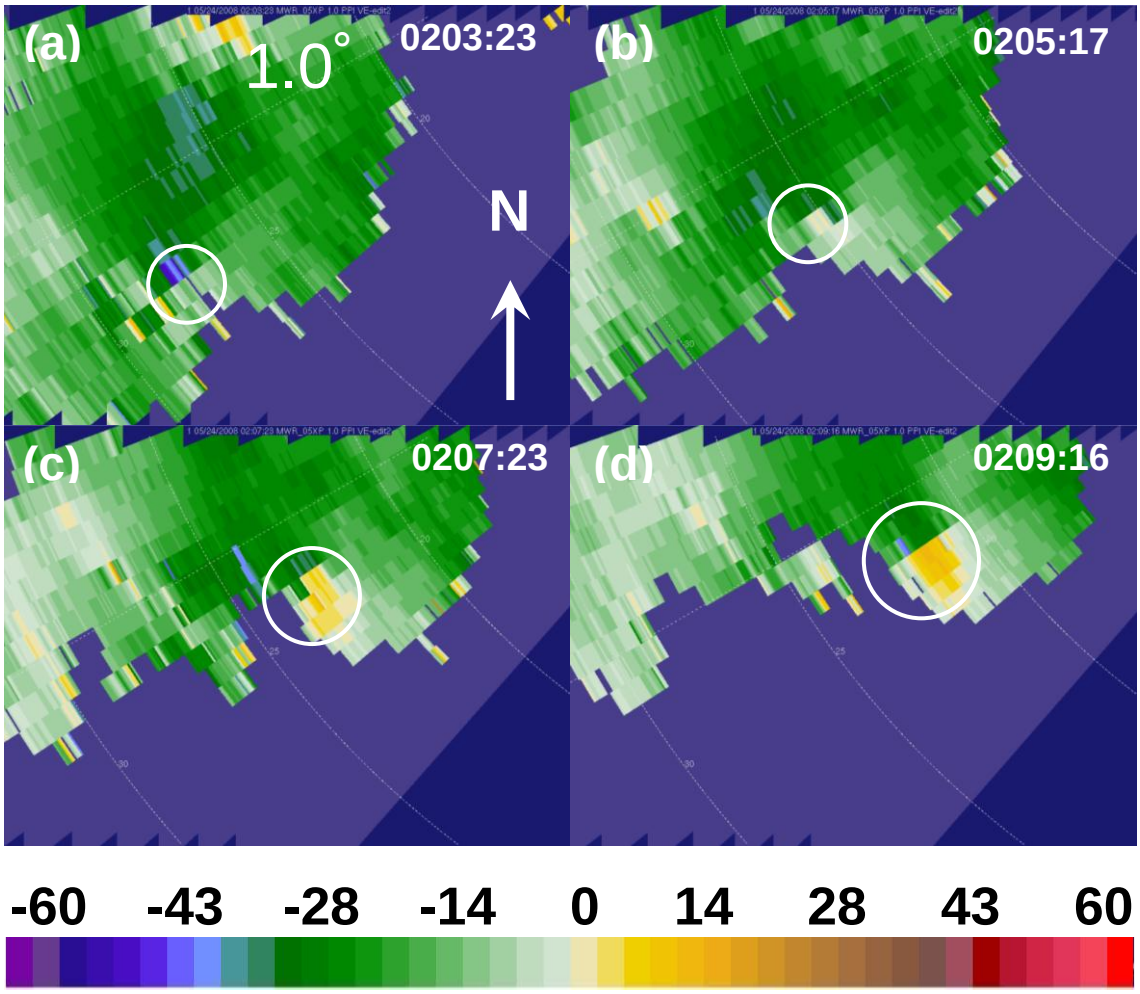

Figure 5.13. Radial velocity (m s^{-1}) PPIs at 1.0° elevation angle of the EAC tornado at (a) 0203:23, (b) 0205:17, (c) 0207:23, and (d) 0209:16 UTC. White circles enclose the TVS indicative of the EAC tornado. The transition from strong inbounds to no data (edited noisy data) at the top right in the PPI scans likely marks the rear-flank gust front. Range rings are every 5 km. The approximate center beam height at the location of the white circle is ~490, 440, 400, and 375 m ARL for (a), (b), (c), and (d), respectively. The colorbar for radial velocity appears below the figure.

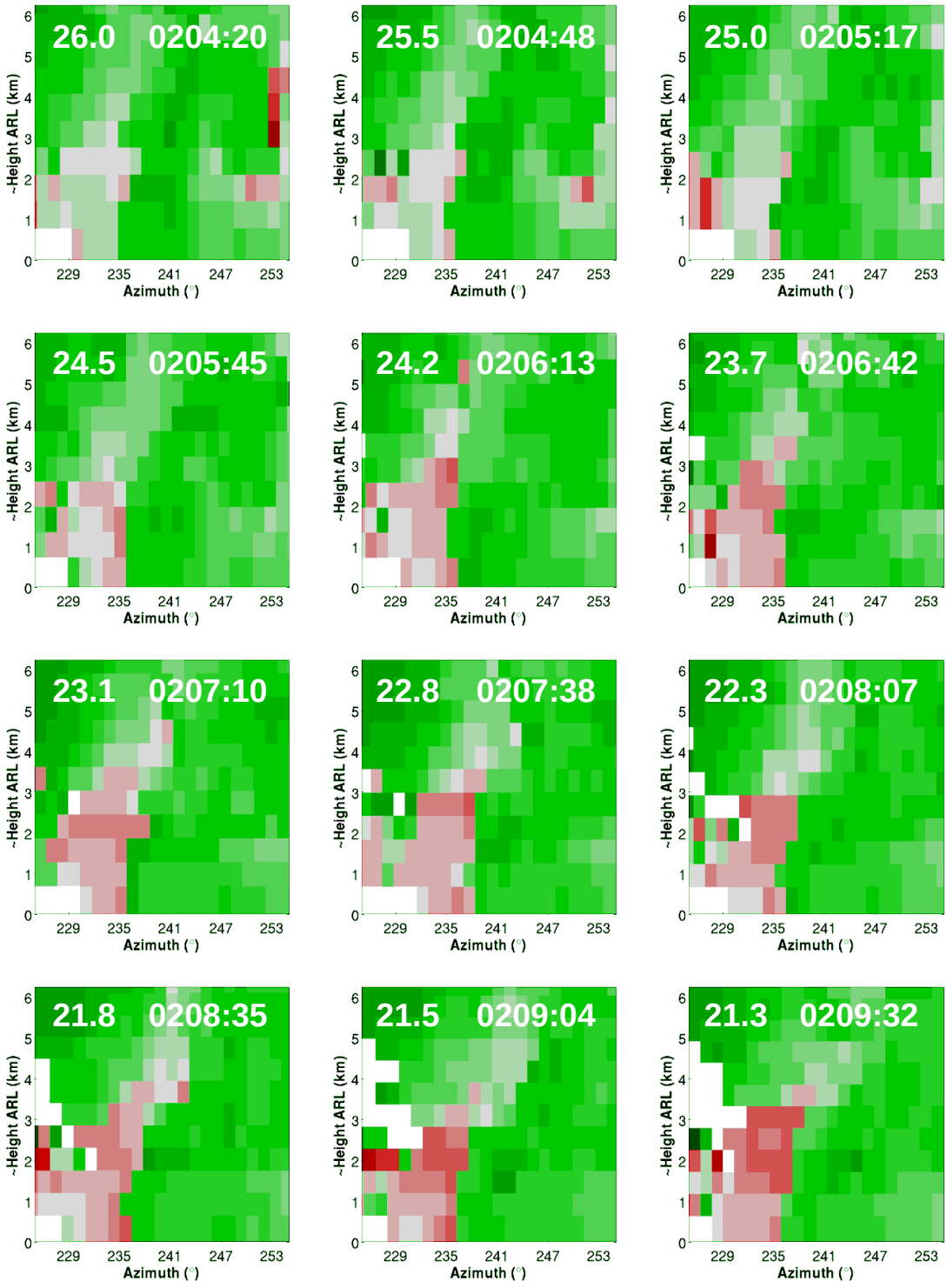
26.0 0204:20
25.5 0204:48
25.0 0205:17
24.5 0205:45
24.2 0206:13
23.7 0206:42
23.1 0207:10
22.8 0207:38
22.3 0208:07
21.8 0208:35
21.5 0209:04
21.3 0209:32
~Height ARL (km)
Azimuth (°)
0
1
2
3
4
5
6
229
235
241
247
253

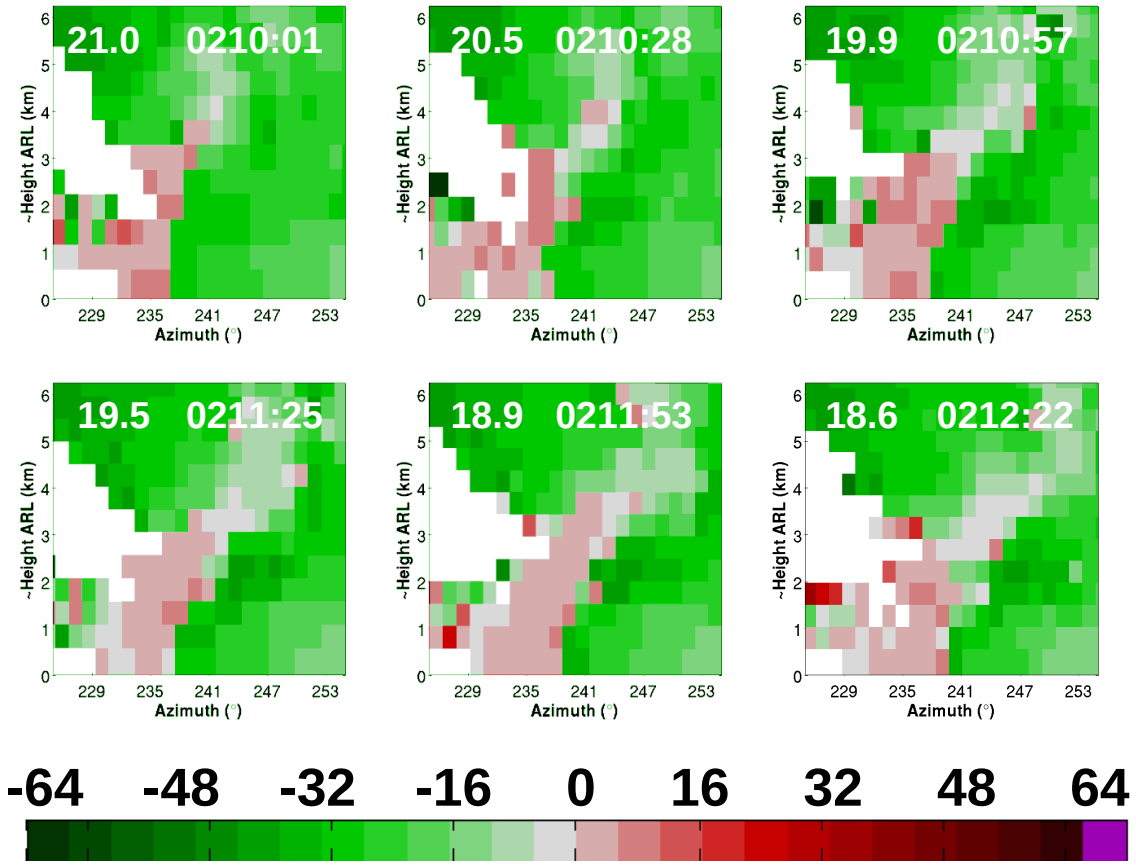

Figure 5.14. AHI plots of radial velocity (m s^{-1}) during most of the life cycle of the EAC tornado. AHIs are every ~28 sec. from 0204:20 to 0212:22 UTC. Azimuths shown are 225-255° and approximate heights extend to ~6 km ARL. The range changes for each plot, is centered at the location of the maximum 1.0° elevation angle ΔV, and is indicated at the upper left of each plot in km. The vertical reference frame is stretched to varying but similar degrees because of the change of range. The colorbar appears below the figure.

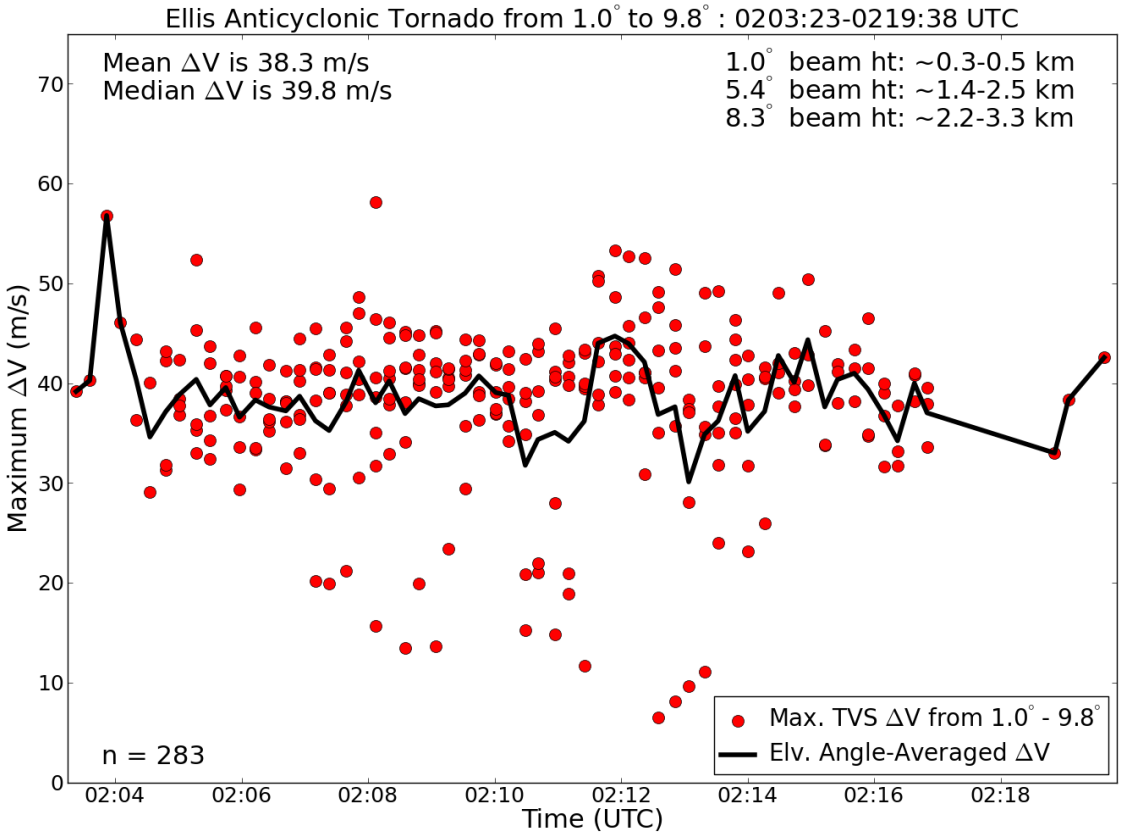

Figure 5.15. Time series of maximum GTG ΔV calculations (red circles) and elevation-angle-averaged ΔV at each observing time (black line) in the EAC tornado from 0203:23-0219:38 UTC. The number of data points, mean and median ΔV values, and approximate radar center beam heights also are provided.

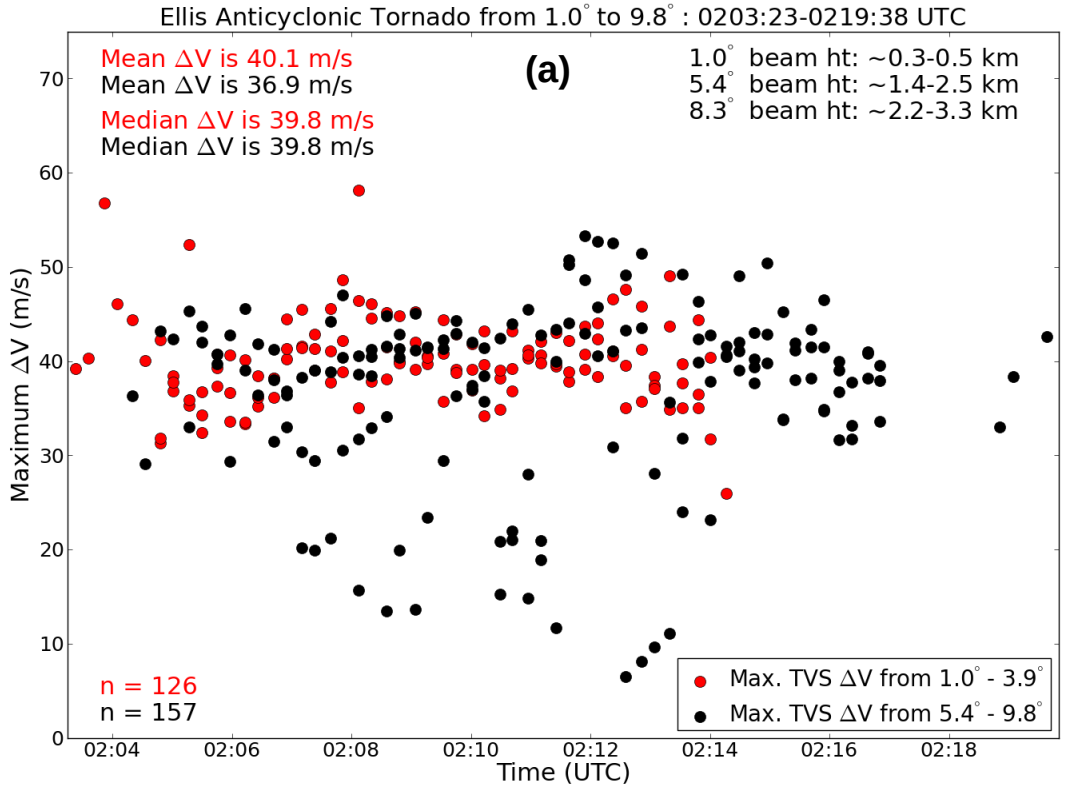
Ellis Anticyclonic Tornado from 1.0° to 9.8° : 0203:23-0219:38 UTC
(a)
Mean ΔV is 40.1 m/s
Mean ΔV is 36.9 m/s
Median ΔV is 39.8 m/s
Median ΔV is 39.8 m/s
1.0° beam ht: ~0.3-0.5 km
5.4° beam ht: ~1.4-2.5 km
8.3° beam ht: ~2.2-3.3 km
n = 126
n = 157
Max. TVS ΔV from 1.0° - 3.9°
Max. TVS ΔV from 5.4° - 9.8°
Maximum ΔV (m/s)
Time (UTC)
0
10
20
30
40
50
60
70
02:04
02:06
02:08
02:10
02:12
02:14
02:16
02:18

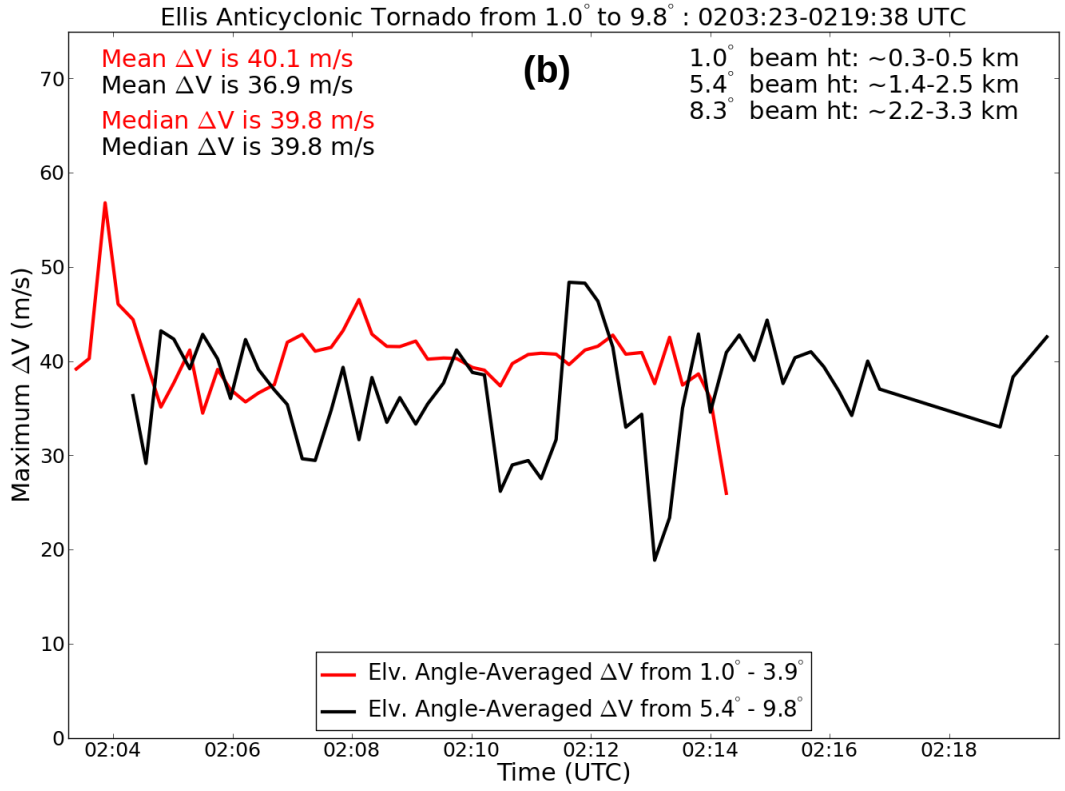
Ellis Anticyclonic Tornado from 1.0° to 9.8° : 0203:23-0219:38 UTC
(b)
Mean ΔV is 40.1 m/s
Mean ΔV is 36.9 m/s
Median ΔV is 39.8 m/s
Median ΔV is 39.8 m/s
1.0° beam ht: ~0.3-0.5 km
5.4° beam ht: ~1.4-2.5 km
8.3° beam ht: ~2.2-3.3 km
Elv. Angle-Averaged ΔV from 1.0° - 3.9°
Elv. Angle-Averaged ΔV from 5.4° - 9.8°
Maximum ΔV (m/s)
Time (UTC)
0
10
20
30
40
50
60
70
02:04
02:06
02:08
02:10
02:12
02:14
02:16
02:18

Figure 5.16. Time series of (a) maximum GTG ΔV from 1.0-3.0° and 5.4-9.8° elevation angle and (b) elevation-angle-averaged ΔV from 1.0-3.9° and 5.4-9.8° elevation angle in the EAC tornado from 0203:23-0219:38 UTC. The number of data points, color-coded mean and median ΔV values, and approximate radar center beam heights also are provided.

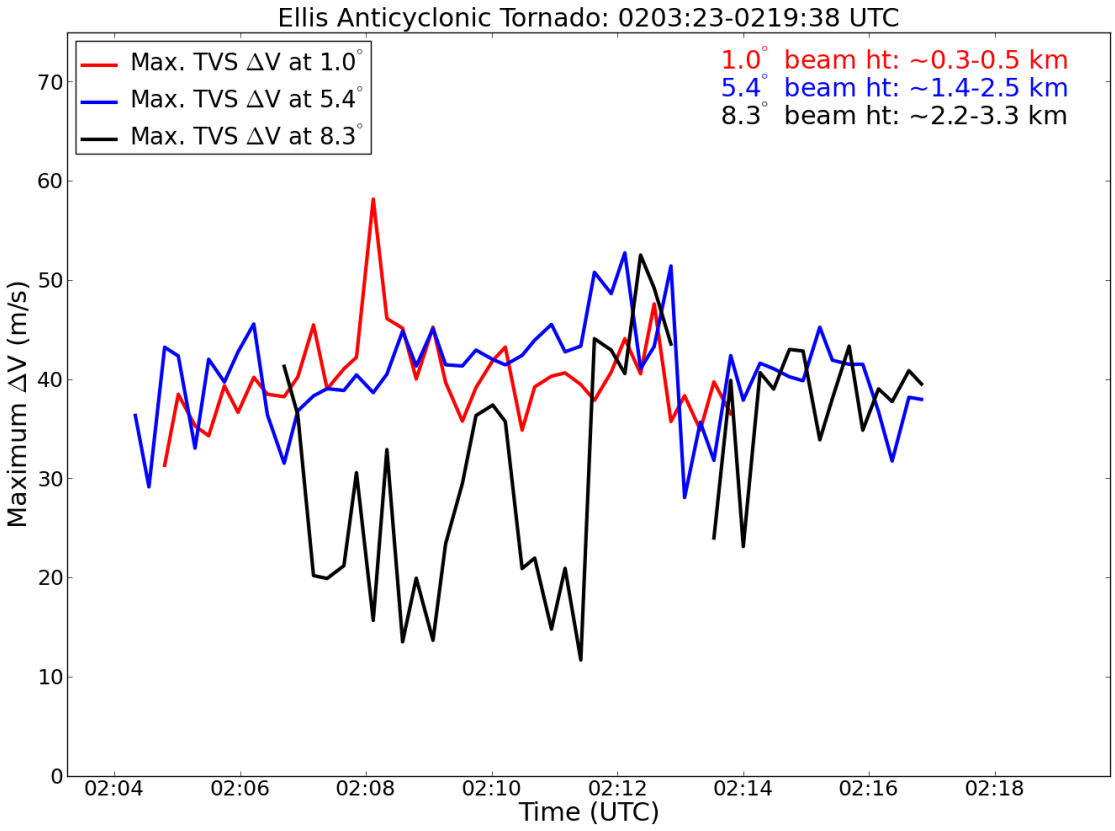

Figure 5.17. Time series of elevation-angle-averaged maximum GTG ΔV at 1.0°, 5.4°, and 8.3° elevation angle in the EAC tornado from 0203:23-0219:38 UTC. Approximate radar center beam heights also are provided.

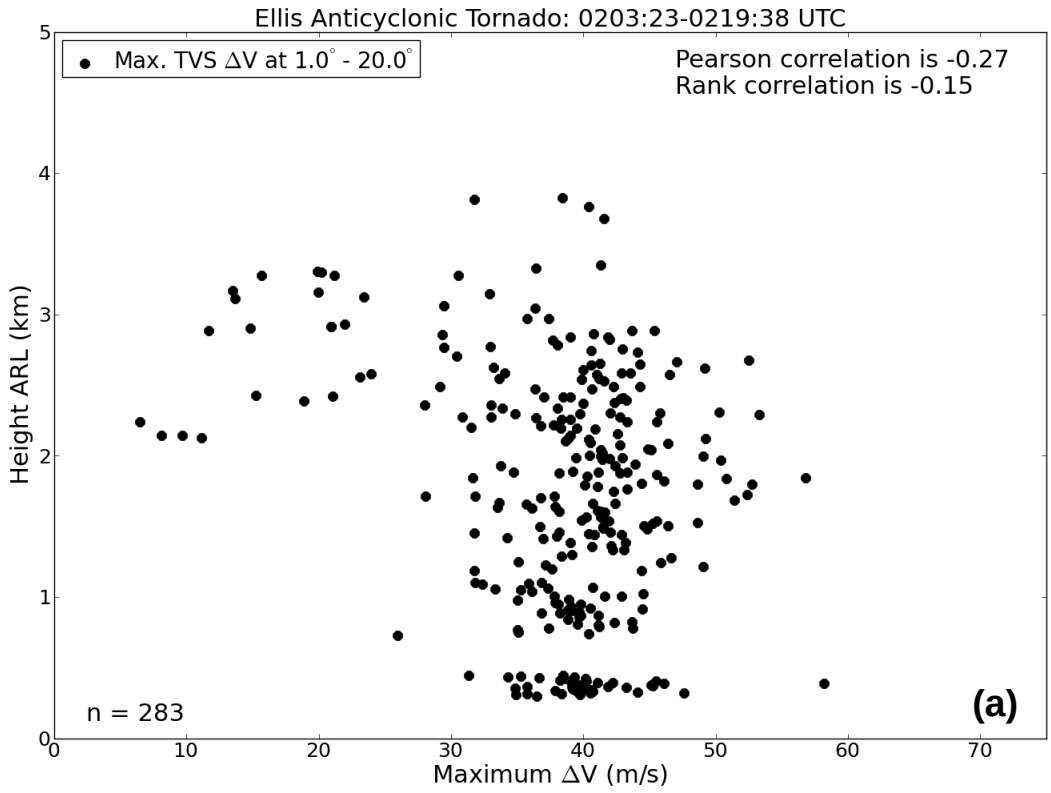
Ellis Anticyclonic Tornado: 0203:23-0219:38 UTC
Max. TVS ΔV at 1.0° - 20.0°
Pearson correlation is -0.27
Rank correlation is -0.15
Height ARL (km)
Maximum ΔV (m/s)
n = 283
(a)

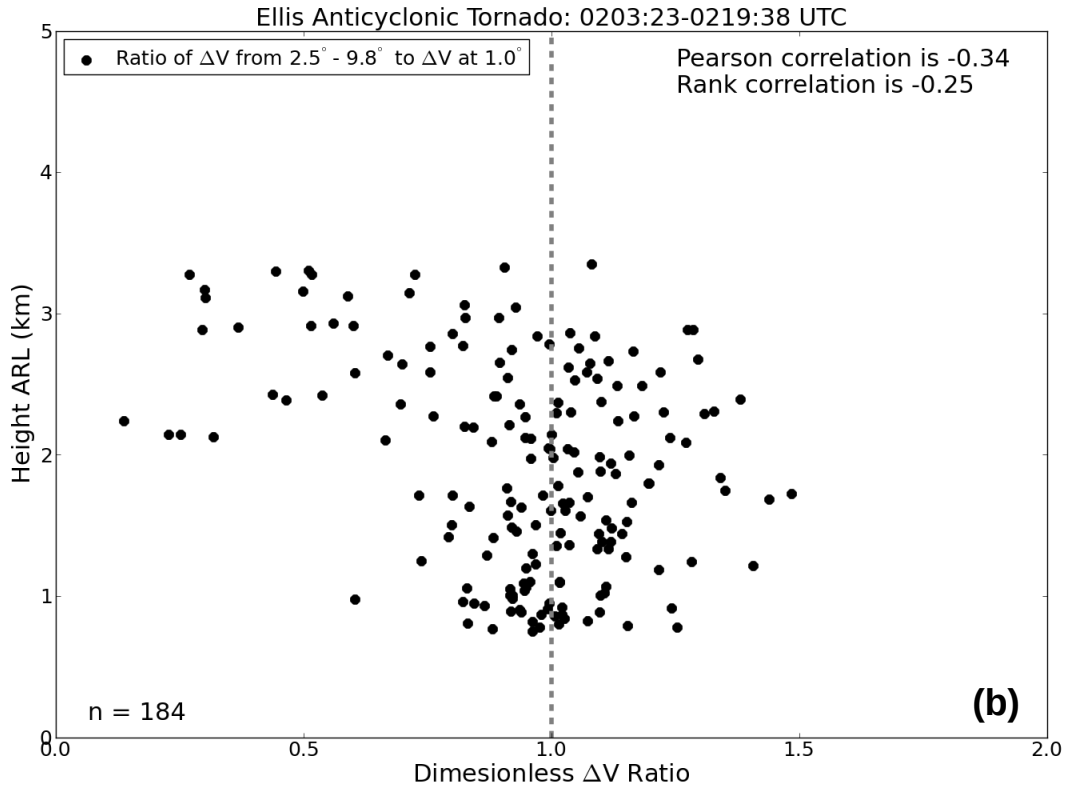
Ellis Anticyclonic Tornado: 0203:23-0219:38 UTC
Ratio of ΔV from 2.5° - 9.8° to ΔV at 1.0°
Pearson correlation is -0.34
Rank correlation is -0.25
Height ARL (km)
Dimesionless ΔV Ratio
n = 184
(b)

Figure 5.18. Vertical profiles of (a) ΔV from every TVS data point and (b) the ratio of TVS ΔV from 2.5-9.8° elevation angle to the TVS ΔV at 1.0° elevation angle for each data point from the EAC tornado. The gray line in (b) marks a ratio of 1. The number of data points and the Pearson and Rank correlations also are provided.

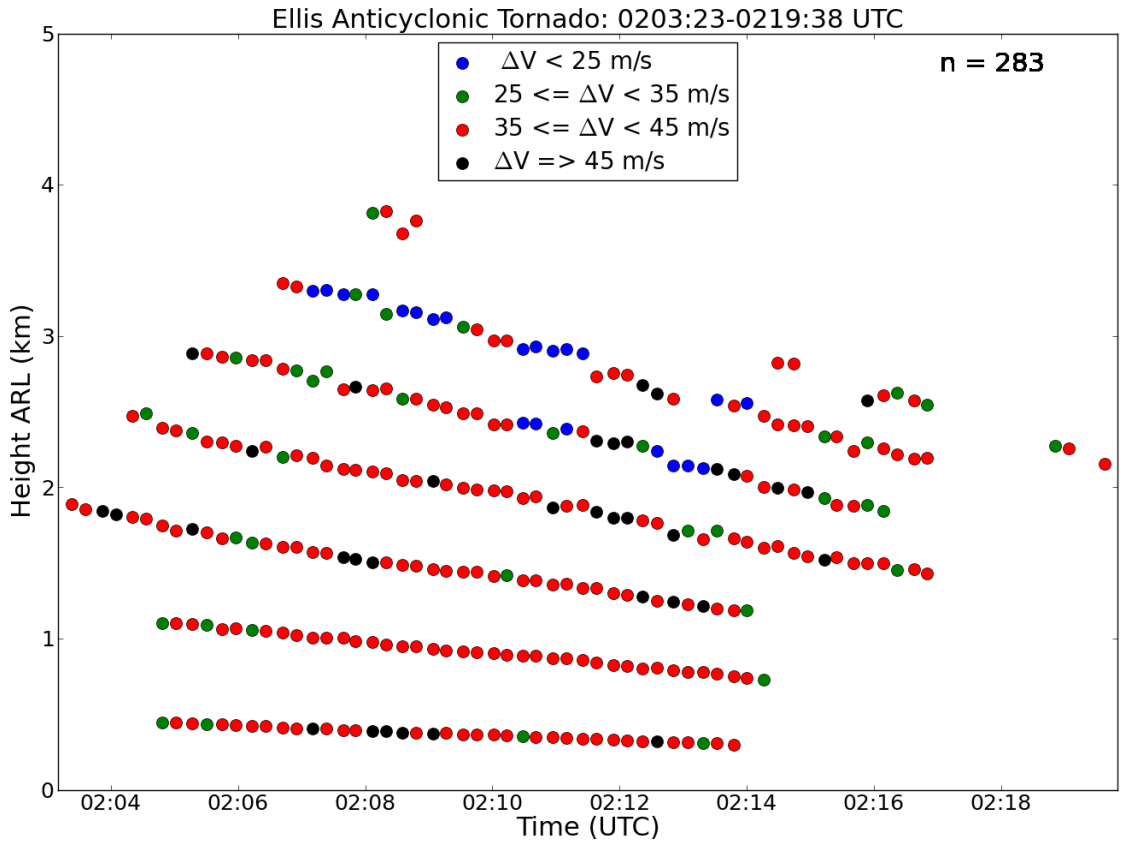

Figure 5.19. Color-coded time-height series of maximum GTG ΔV in the EAC tornado from 0203:2-0219:38 UTC. The number of data points appears in the upper right of the figure.

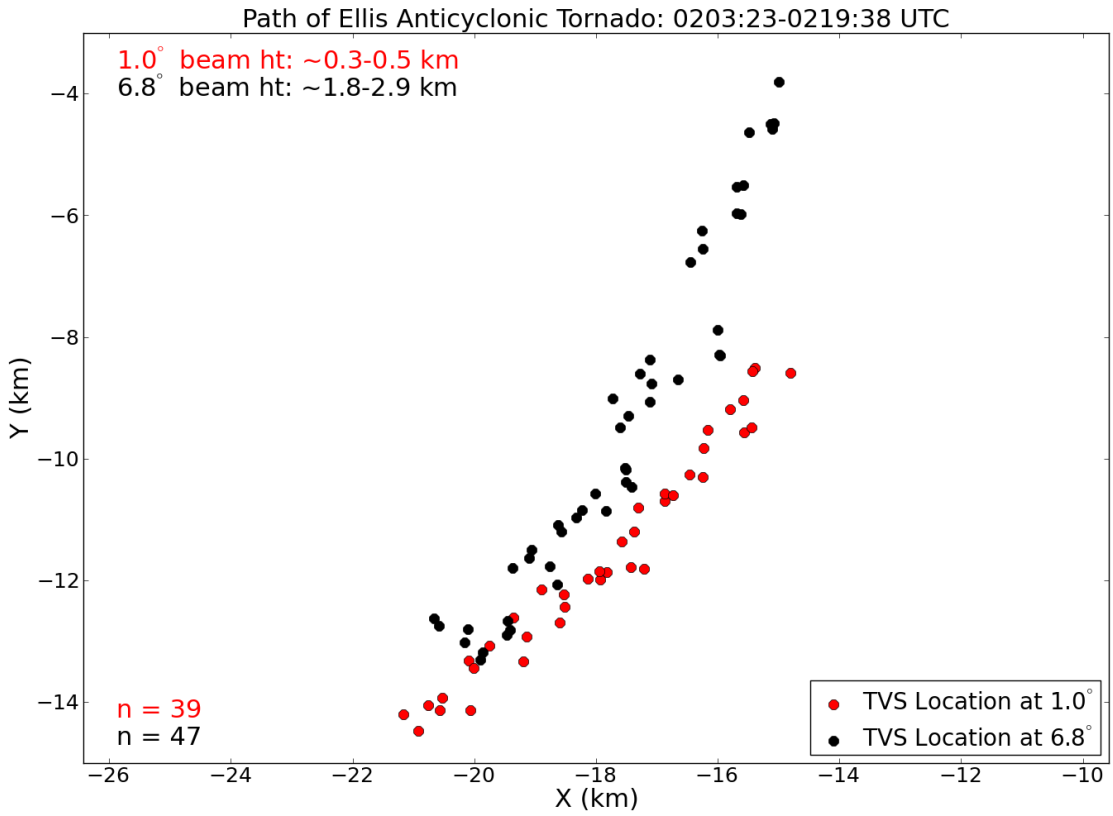

Figure 5.20. Plan view of the path of the EAC tornado at 1.0° and 6.8° elevation angle. The origin of the graph (not shown) marks the location of the MWR-05XP during the deployment. Ordinate (abscissa) increases from left to right (bottom to top) indicate eastward (northward) progression. The axes are not stretched. The number of data points and the approximate radar center beam heights also are provided.

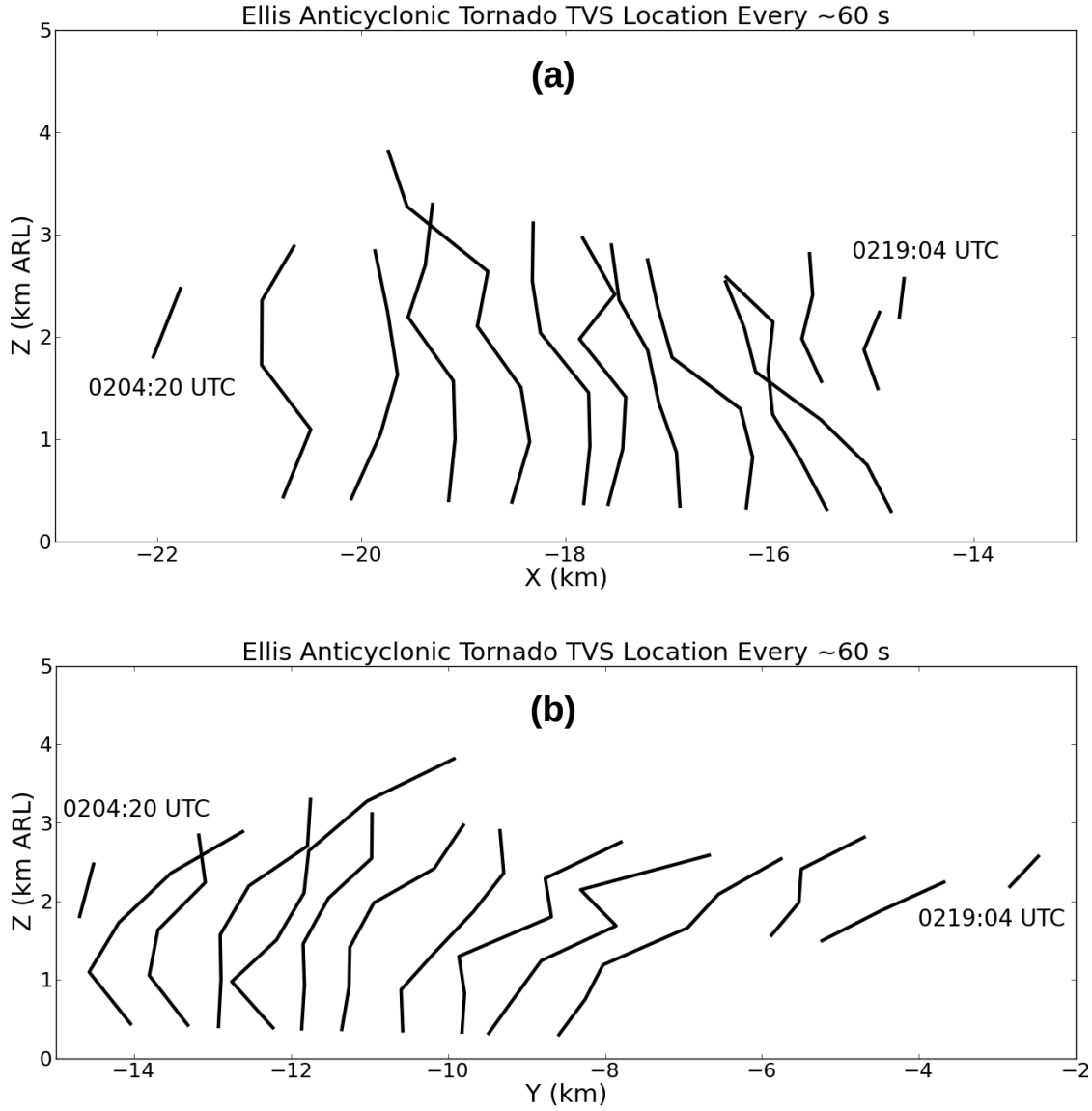

Figure 5.21. Vertical cross sections of the EAC TVS location in the (a) east-west and (b) north-south direction plotted every ~60 sec. Ordinate increases from left to right indicate eastward and northward progression in (a) and (b), respectively. The times of the first and last TVS observation included are labeled for both cross sections.

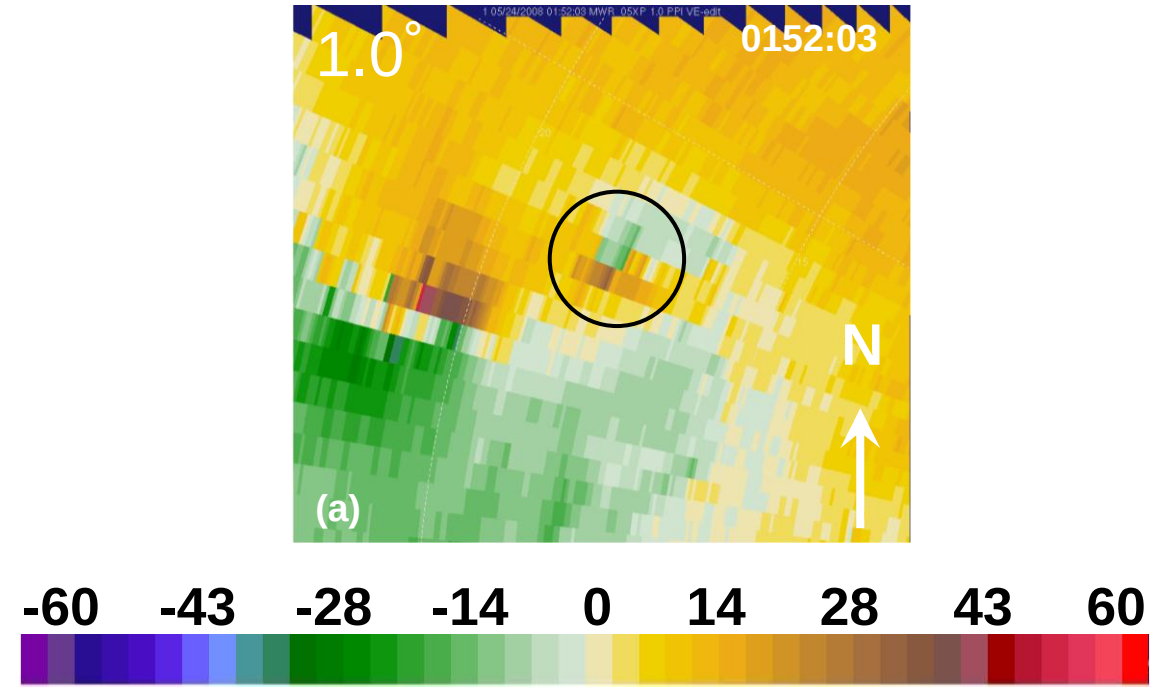
1.0°
0152:03
N
(a)
-60 -43 -28 -14 0 14 28 43 60

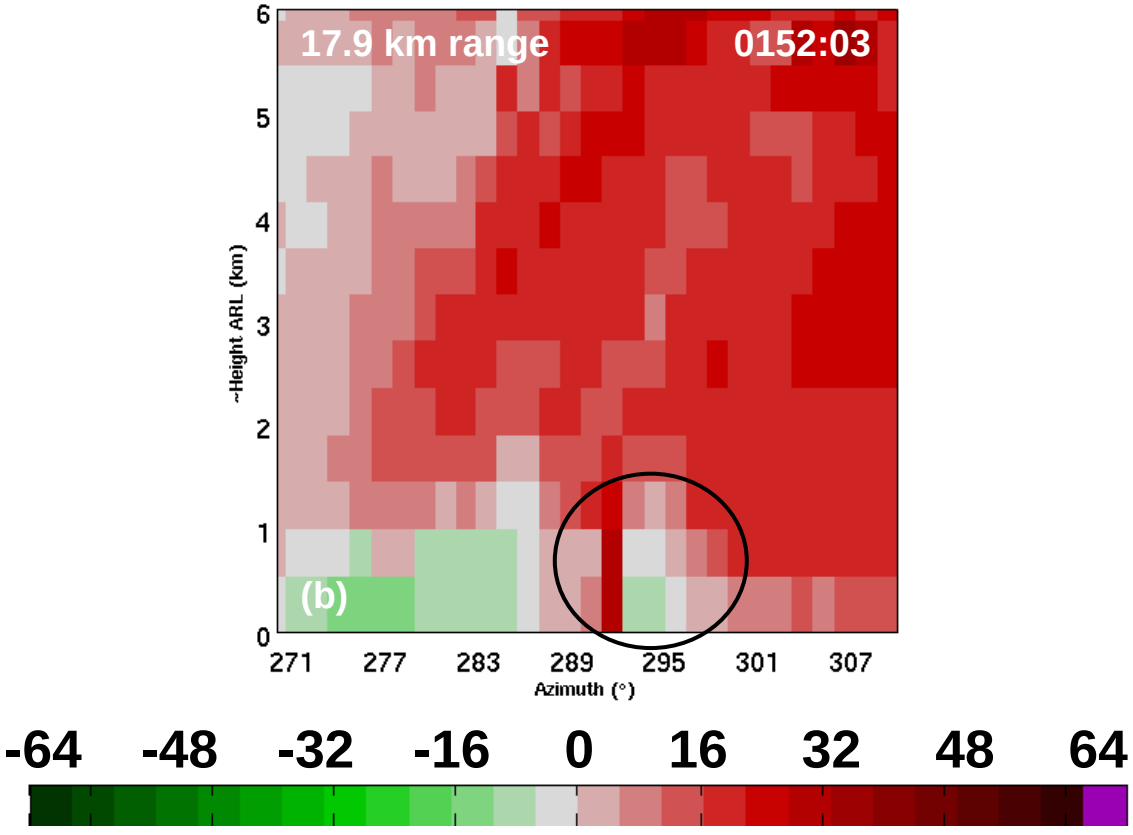
17.9 km range
0152:03
(b)
~Height ARL (km)
0 1 2 3 4 5 6
271 277 283 289 295 301 307
Azimuth (°)
-64 -48 -32 -16 0 16 32 48 64

Figure 5.22. Radial velocity (m s^{-1}) for (a) a 1.0° elevation angle PPI and (b) an AHI of an anticyclonic vortex signature located east of a tornado in the Ellis supercell at 0152:03 UTC. In both images, a black circle encloses the vortex signature. The AHI is at a range of 17.9 km, spans from 270-310° in azimuth, and extends to 6 km ARL. The colorbars appear beneath each image.

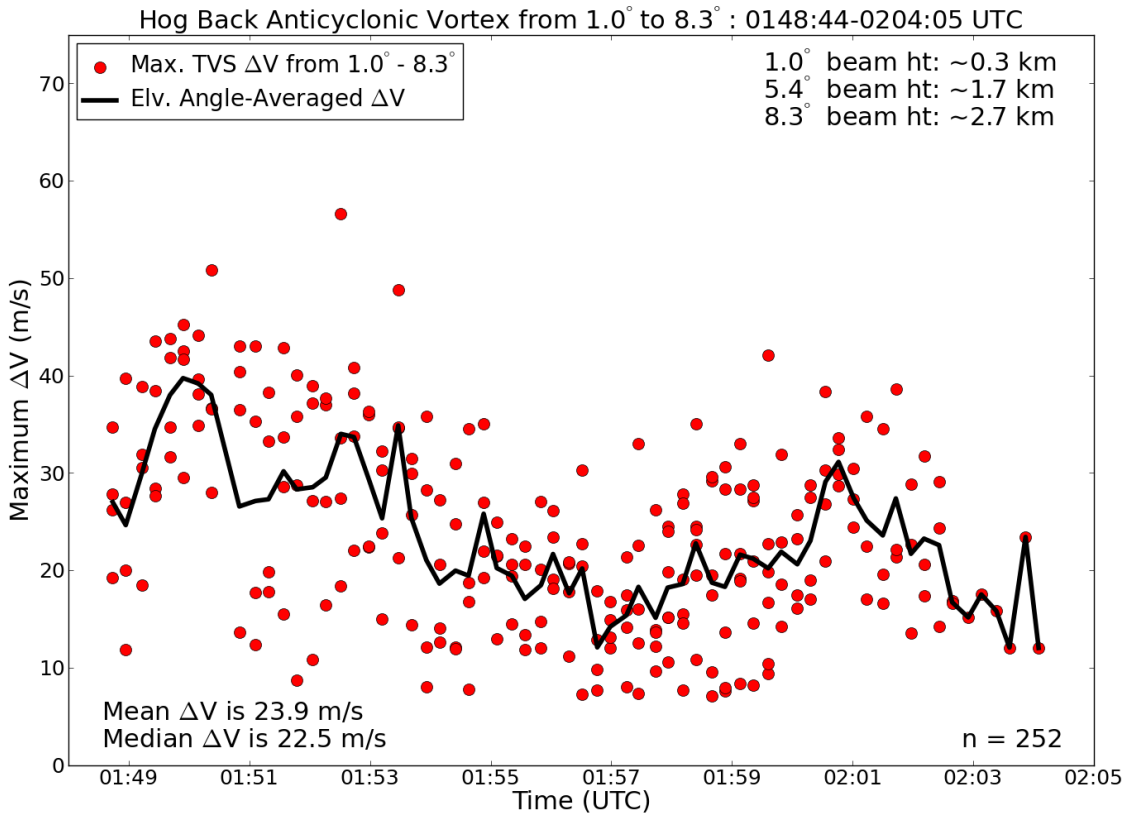

Figure 5.23. As in Figure 5.15 but for the HBAV.

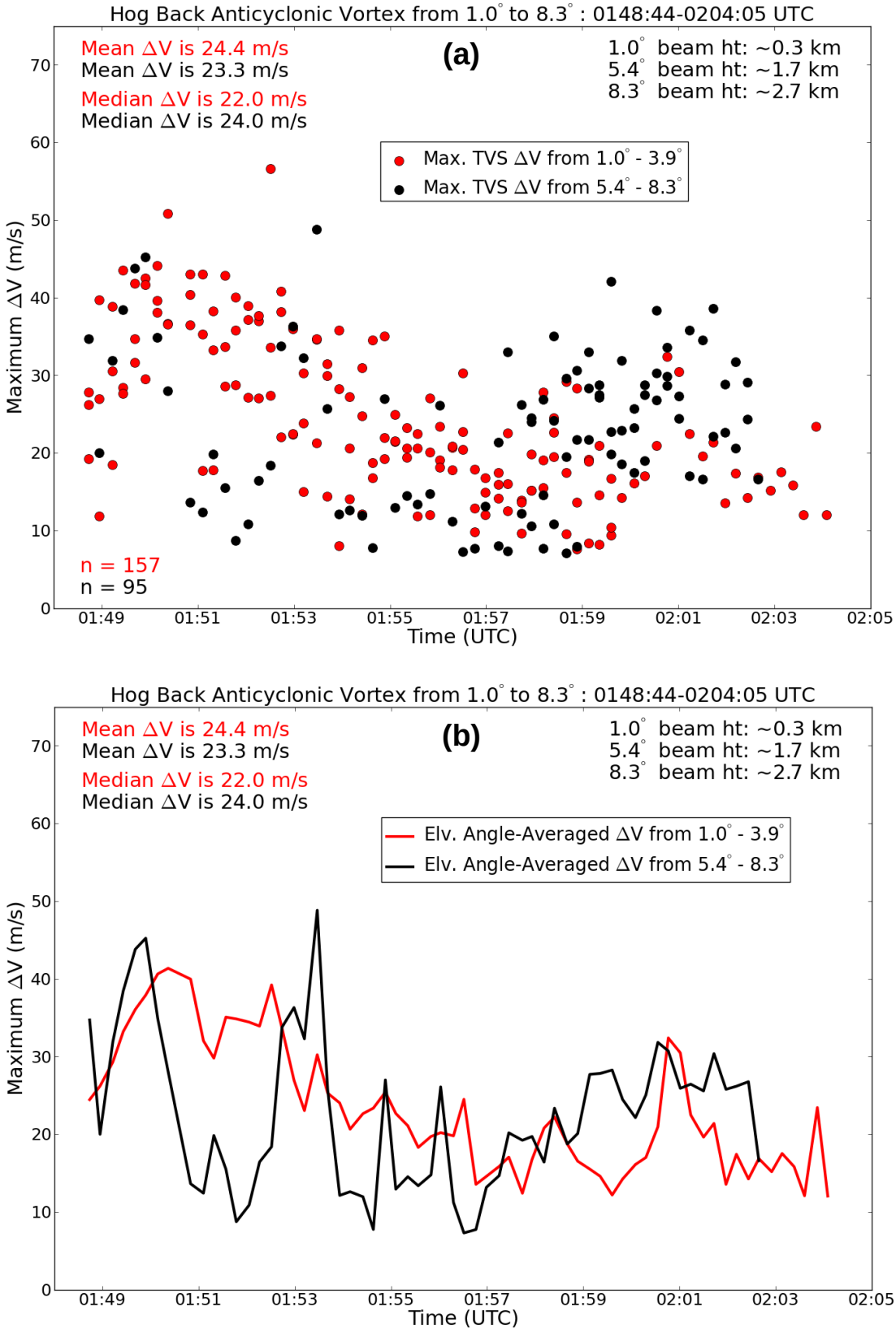

Figure 5.24. As in Figure 5.16 but for the HBAV.

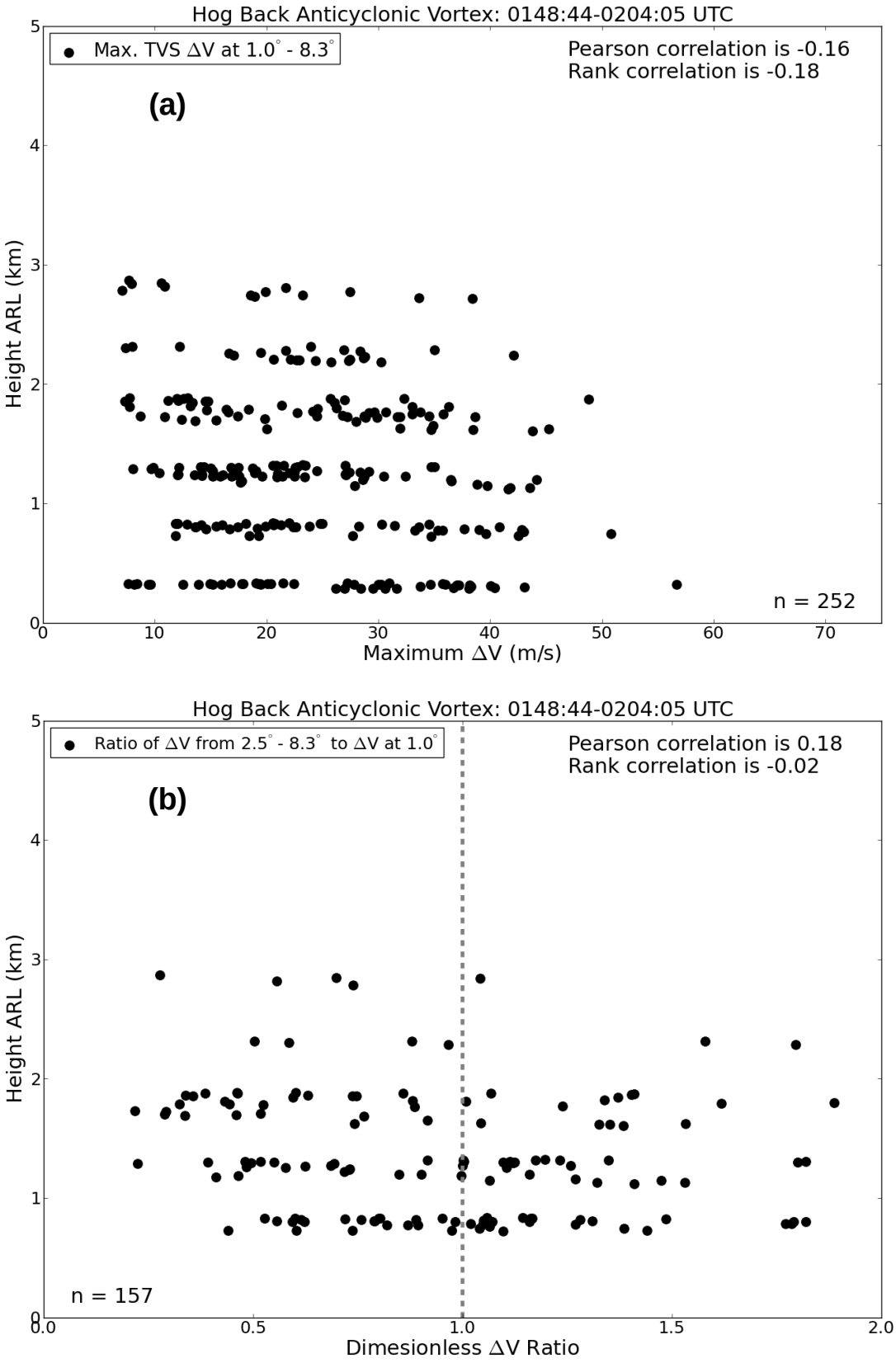

Figure 5.25. As in Figure 5.18 but for the HBAV.

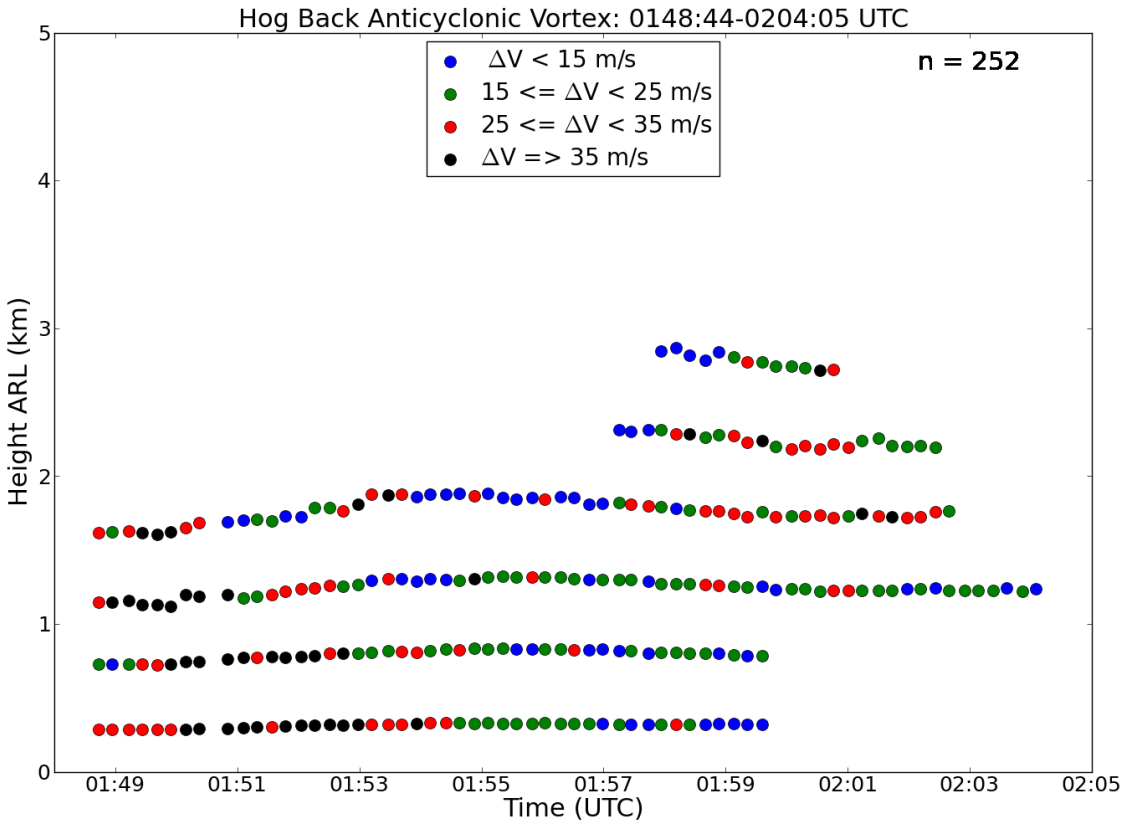

Figure 5.26. As in Figure 5.19 but for the HBAV.

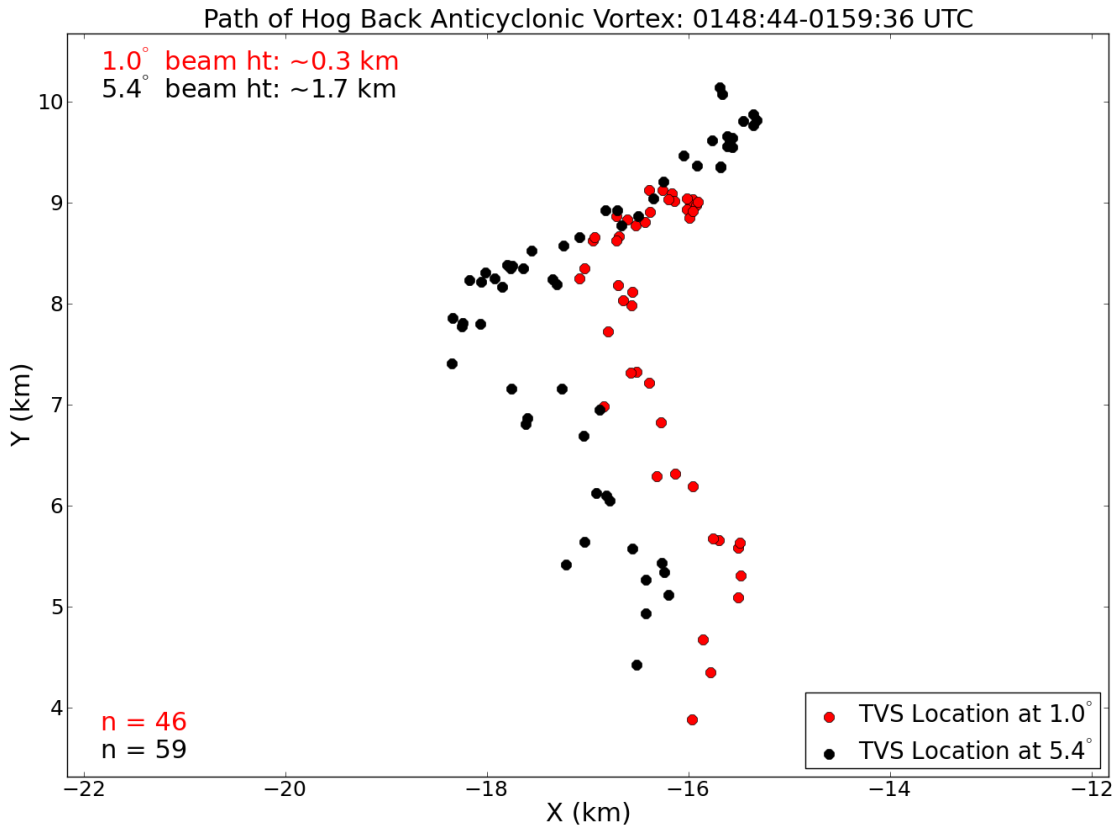

Figure 5.27. As in Figure 5.20 but for the HBAV.

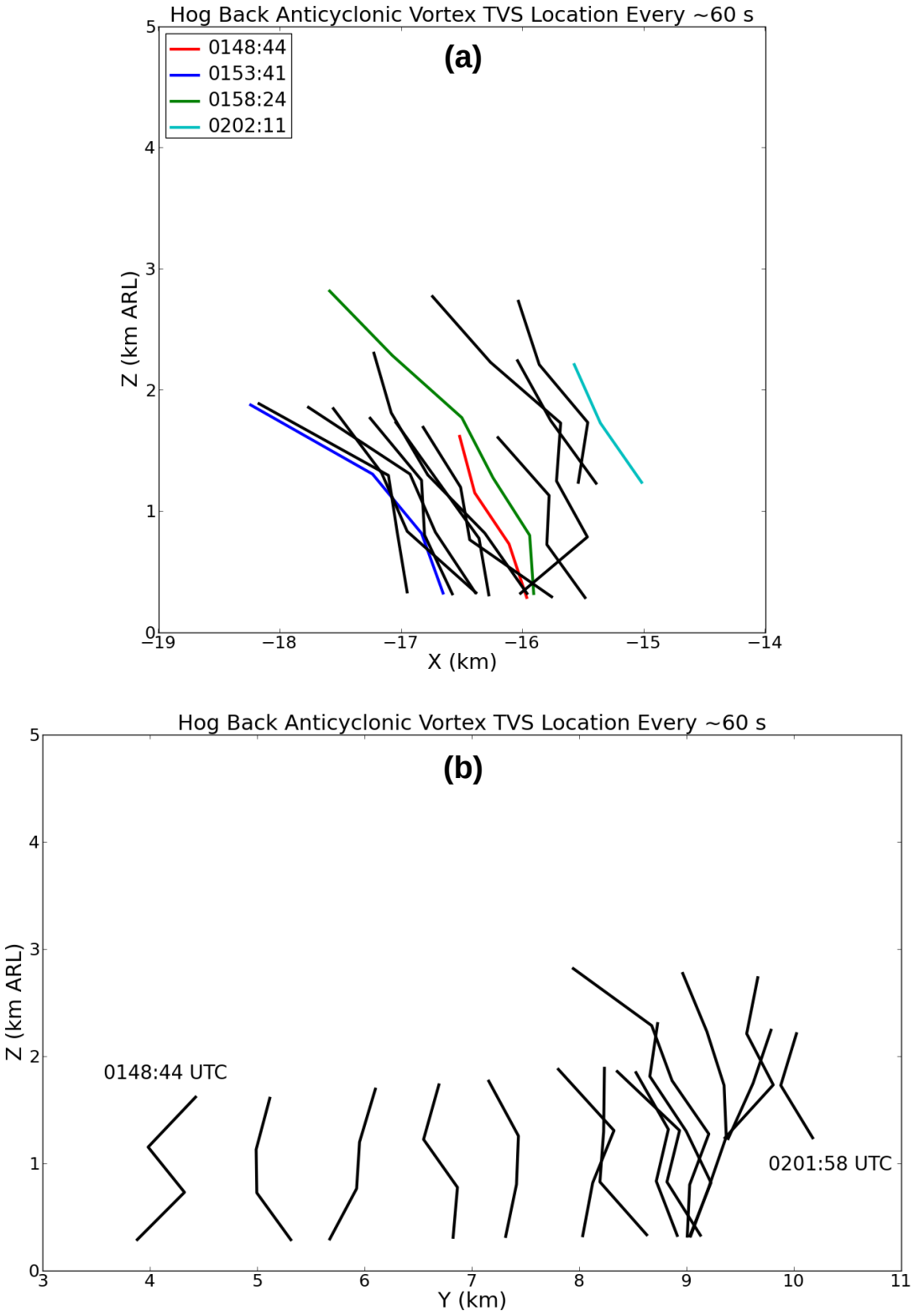

Figure 5.28. As in Figure 5.21 but for the HBAV. In (a) several different times are color-coded so that the zonal movement of the vortex can be tracked.

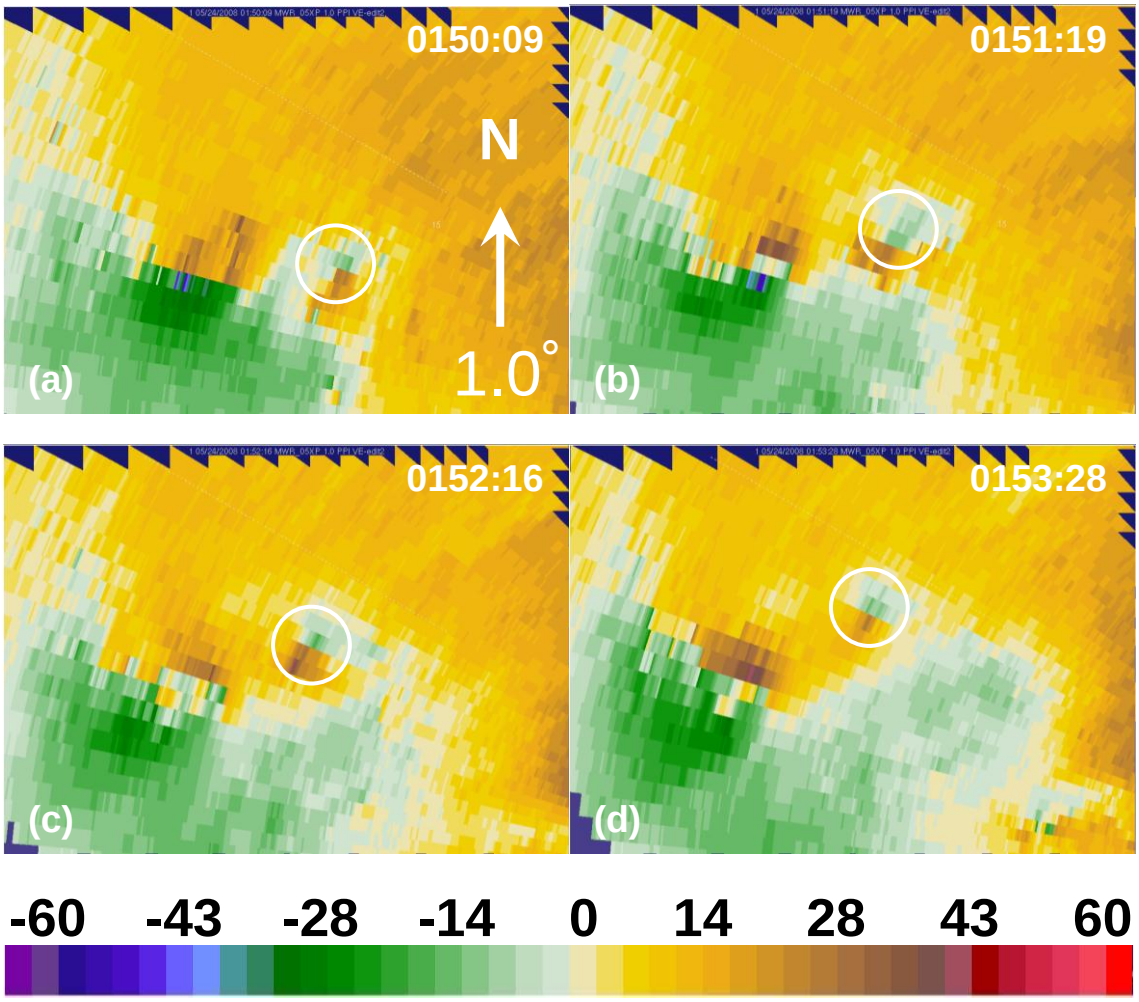

Figure 5.29. Radial velocity (m s^{-1}) PPIs at 1.0° elevation angle of a cyclonic tornado and the HBAV at (a) 0150:09, (b) 0151:19, (c) 0152:16, and (d) 0153:28 UTC. Range rings are every 15 km. White circles enclose the anticyclonic vortex. The colorbar for radial velocity appears beneath the figure.

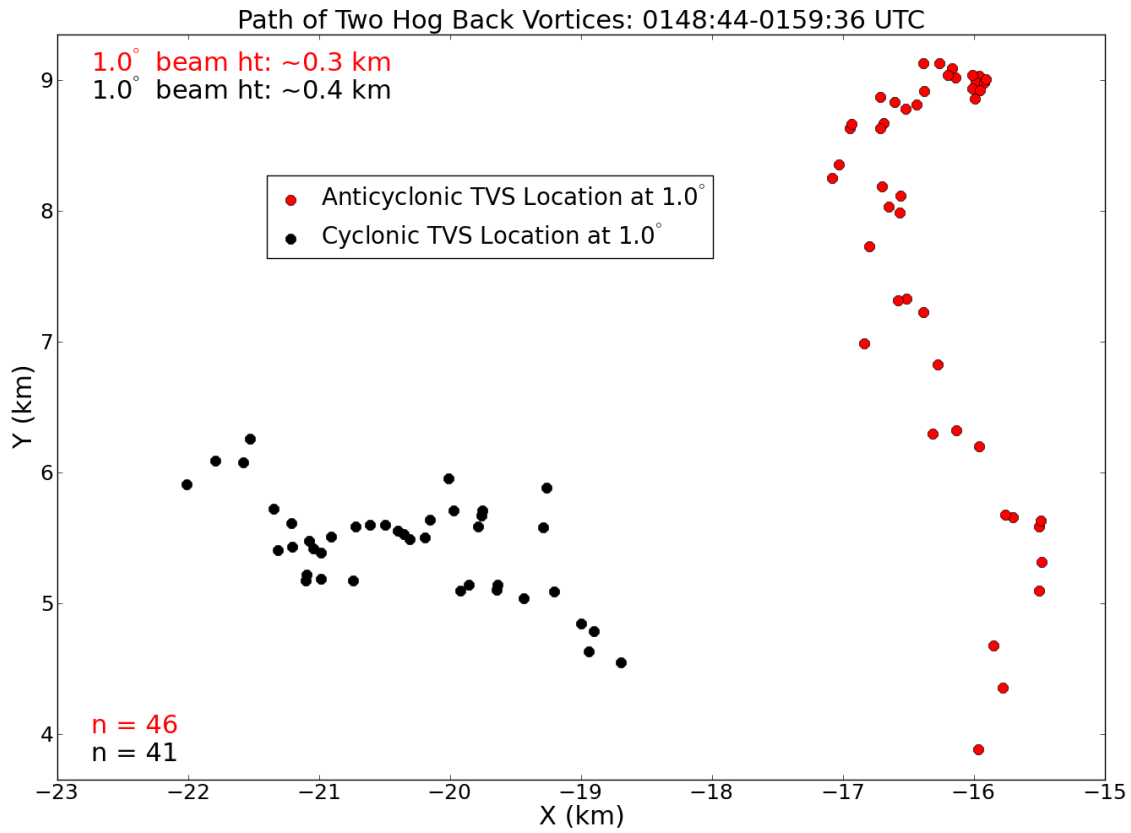

Figure 5.30. Plan view comparison of the 1.0° elevation angle paths of a cyclonic tornado and the HBAV. The number of data points and approximate radar center beam heights also are provided.

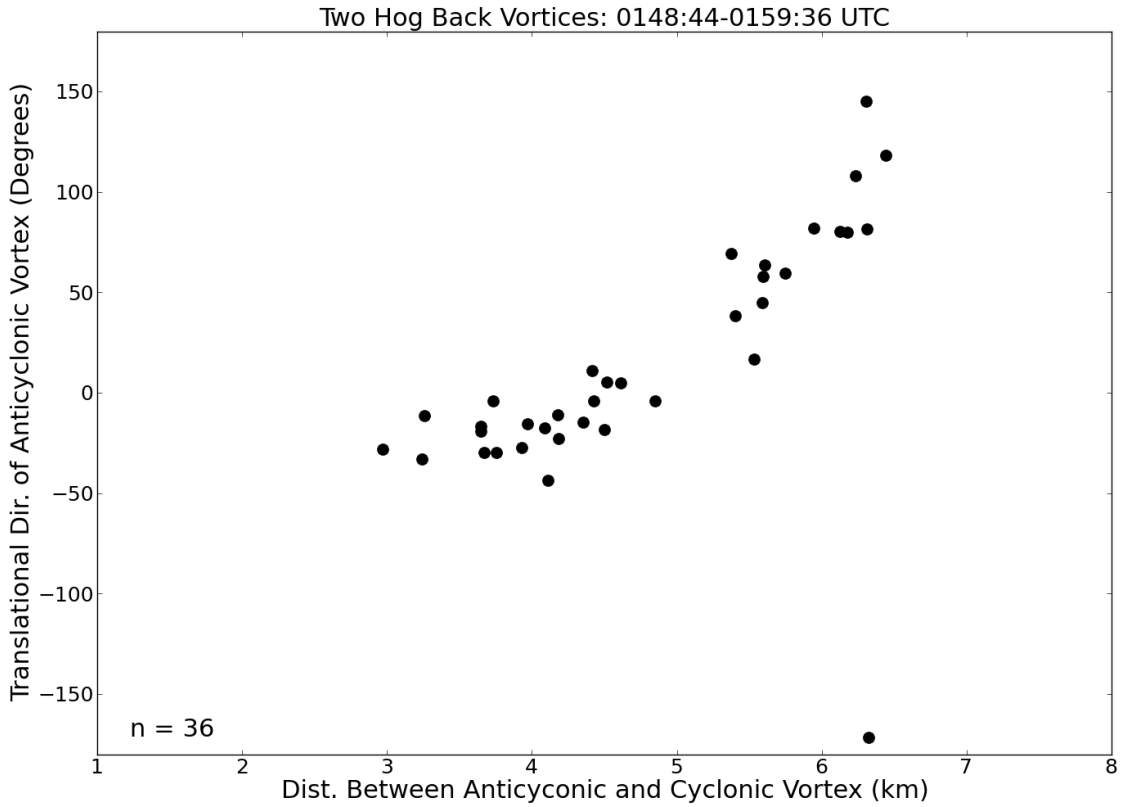

Figure 5.31. Scatterplot comparing the distance between a cyclonic tornado and the HBAV with the translational direction of the HBAV. The number of data points also is provided.

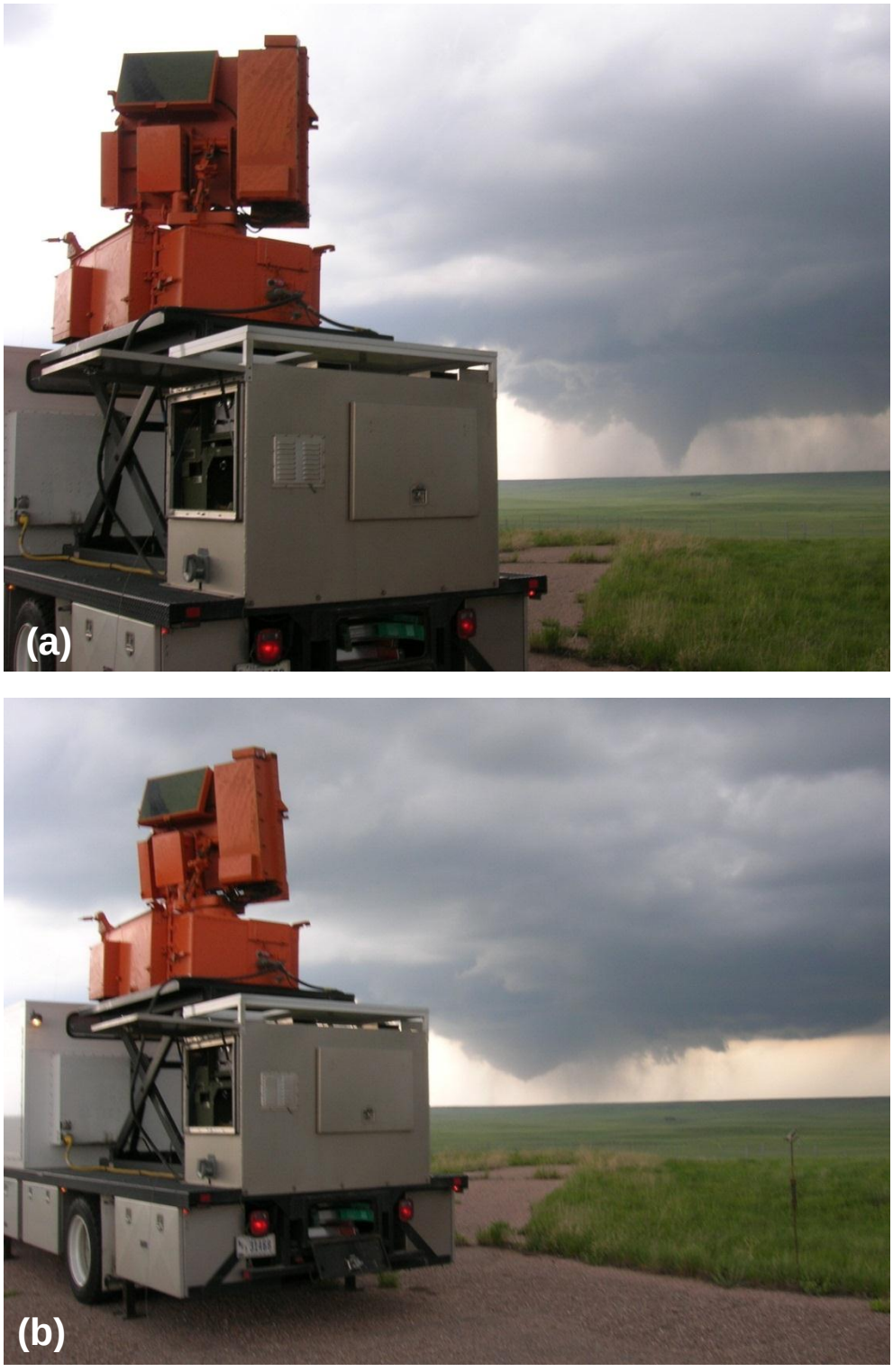

Figure 5.32. The MWR-05XP (a) scanning the Goshen County, Wyoming tornado at 2206 UTC on 5 June 2009 and (b) a wider view of the deployment site at 2201 UTC. Photographs © Michael French.

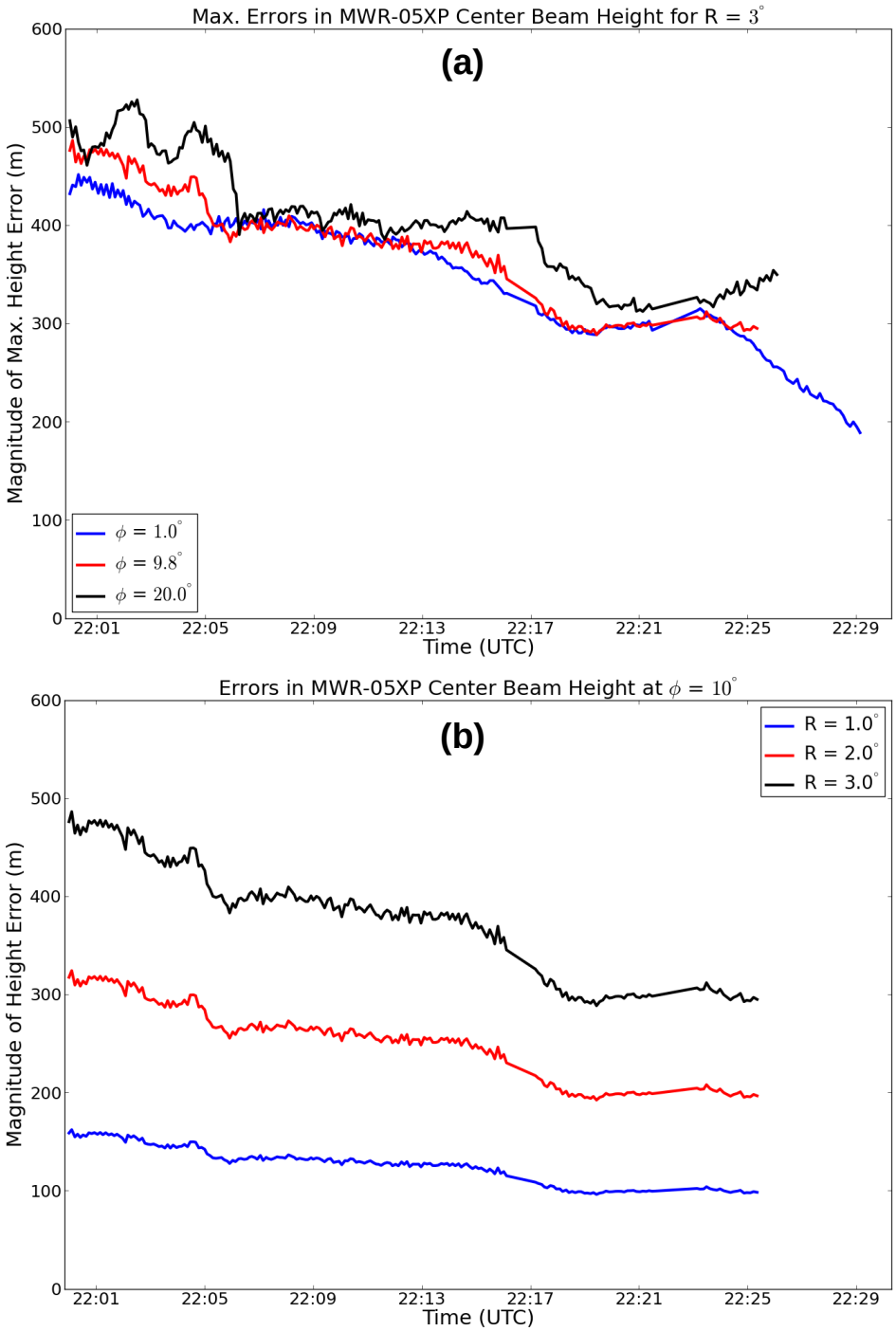

Figure 5.33. Time series of approximate error magnitudes in radar center beam heights of the Goshen County tornado (a) at three elevation angles for the assumed largest roll angle of 3° and (b) at 9.8° elevation angle for three given roll angles. Positive (negative) roll angles indicate height estimates that are too small (large).

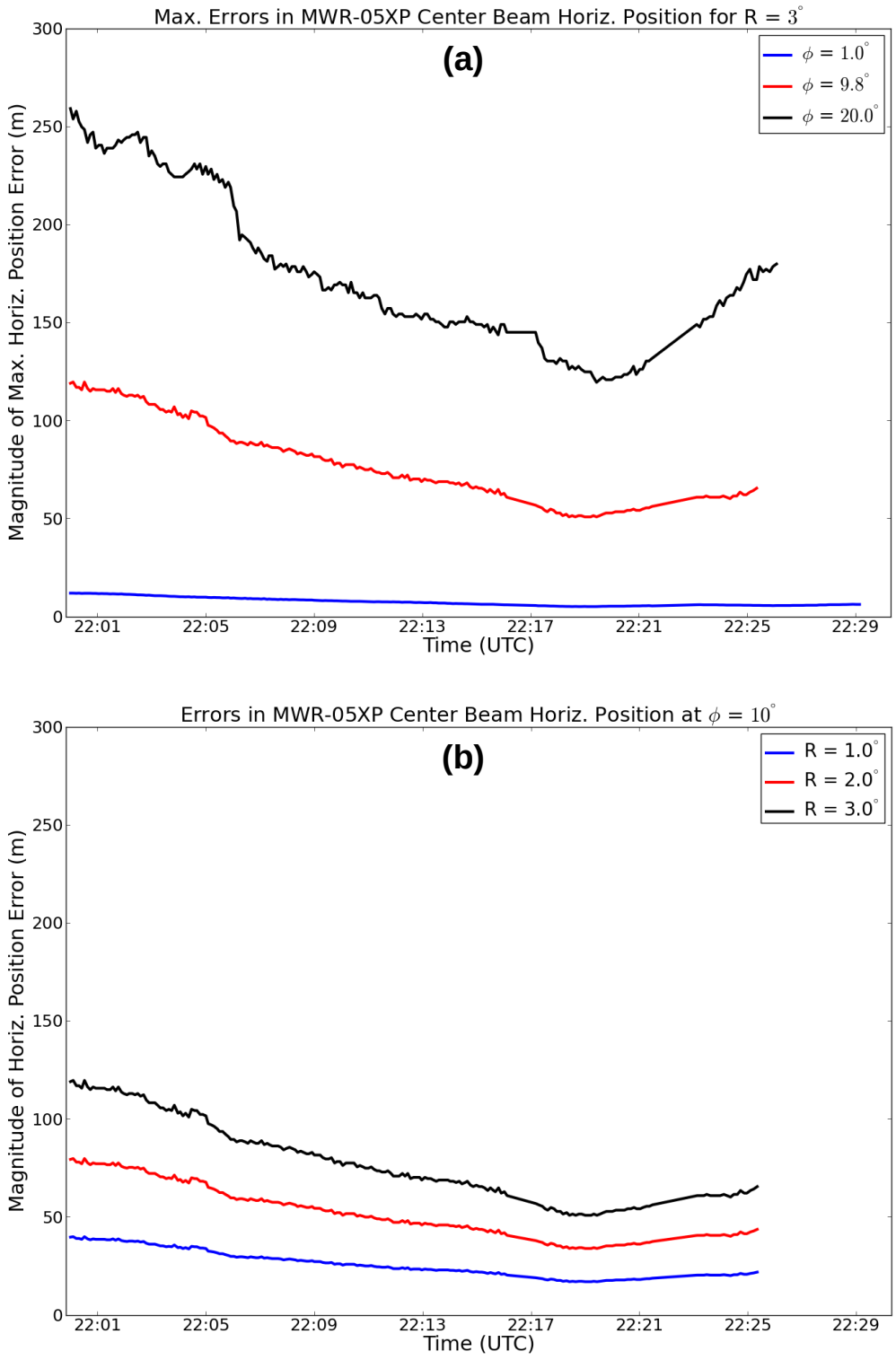

Figure 5.34. As in Fig. 5.33, but for approximate error magnitudes in radar center beam horizontal location.

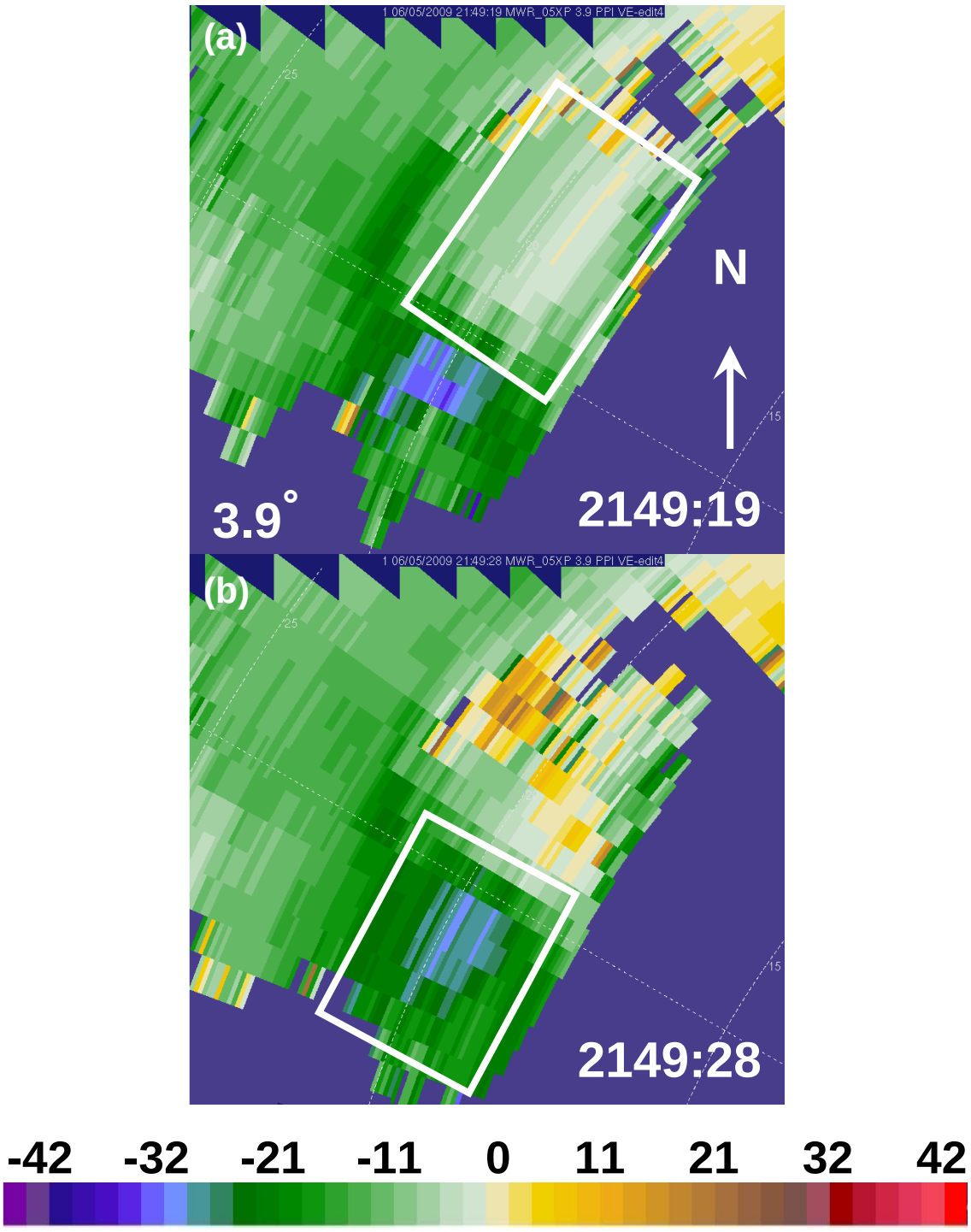

Figure 5.35. MWR-05XP radial velocity (m s^{-1}) at 3.9° elevation angle showing beam smearing (a) in the northern and (b) southern portion of the mesocyclone at 2149:19 and 2149:28 UTC, respectively. The white rectangles encompass the beam smearing. Range rings are every 5 km. The radial velocity colorbar appears beneath the figure.

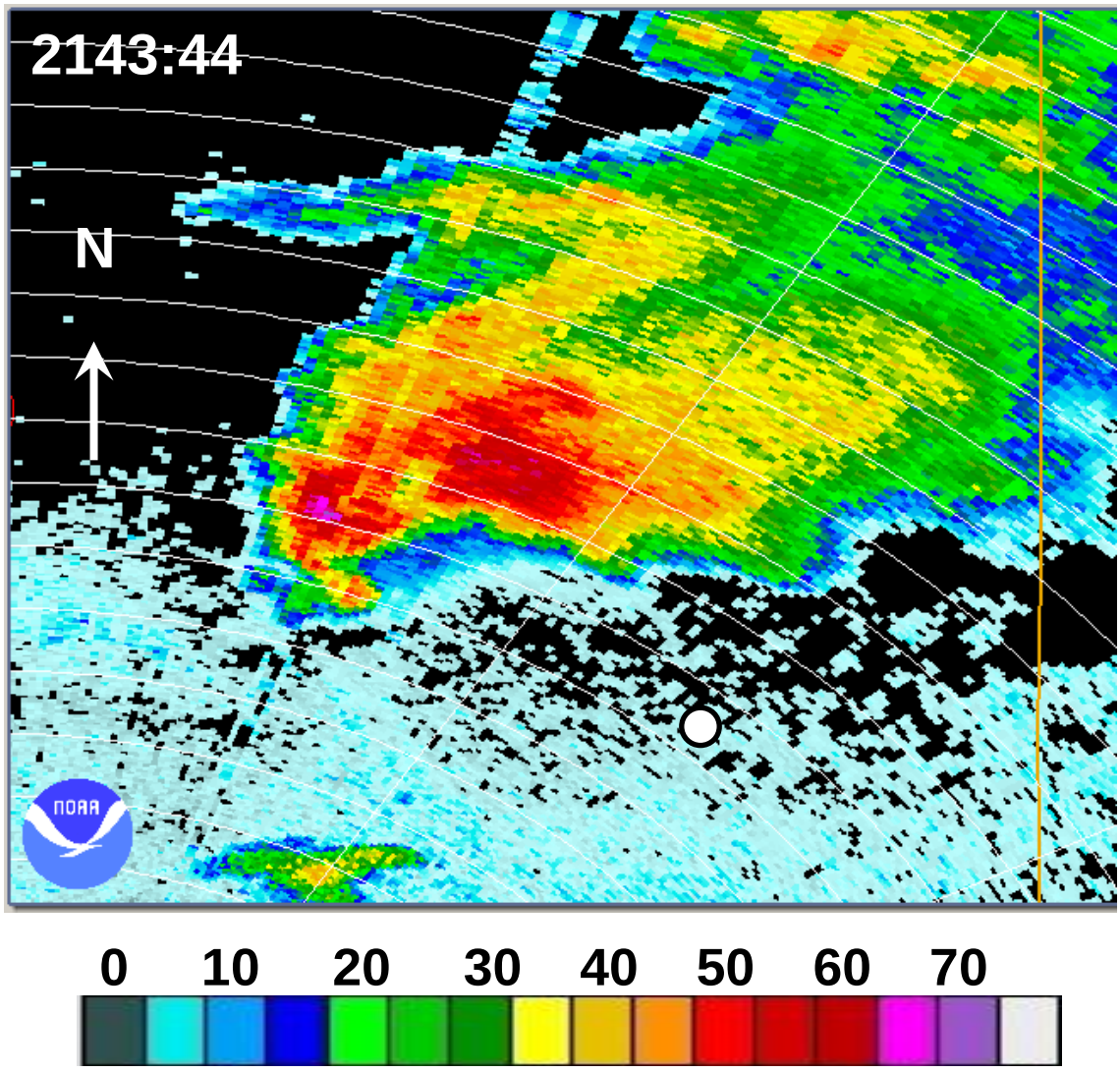

Figure 5.36. As in Fig. 5.1, but from the WSR-88D in Cheyenne, Wyoming at 2144 UTC on 5 June 2009 prior to the Goshen County tornado. Range rings are every 5 km.

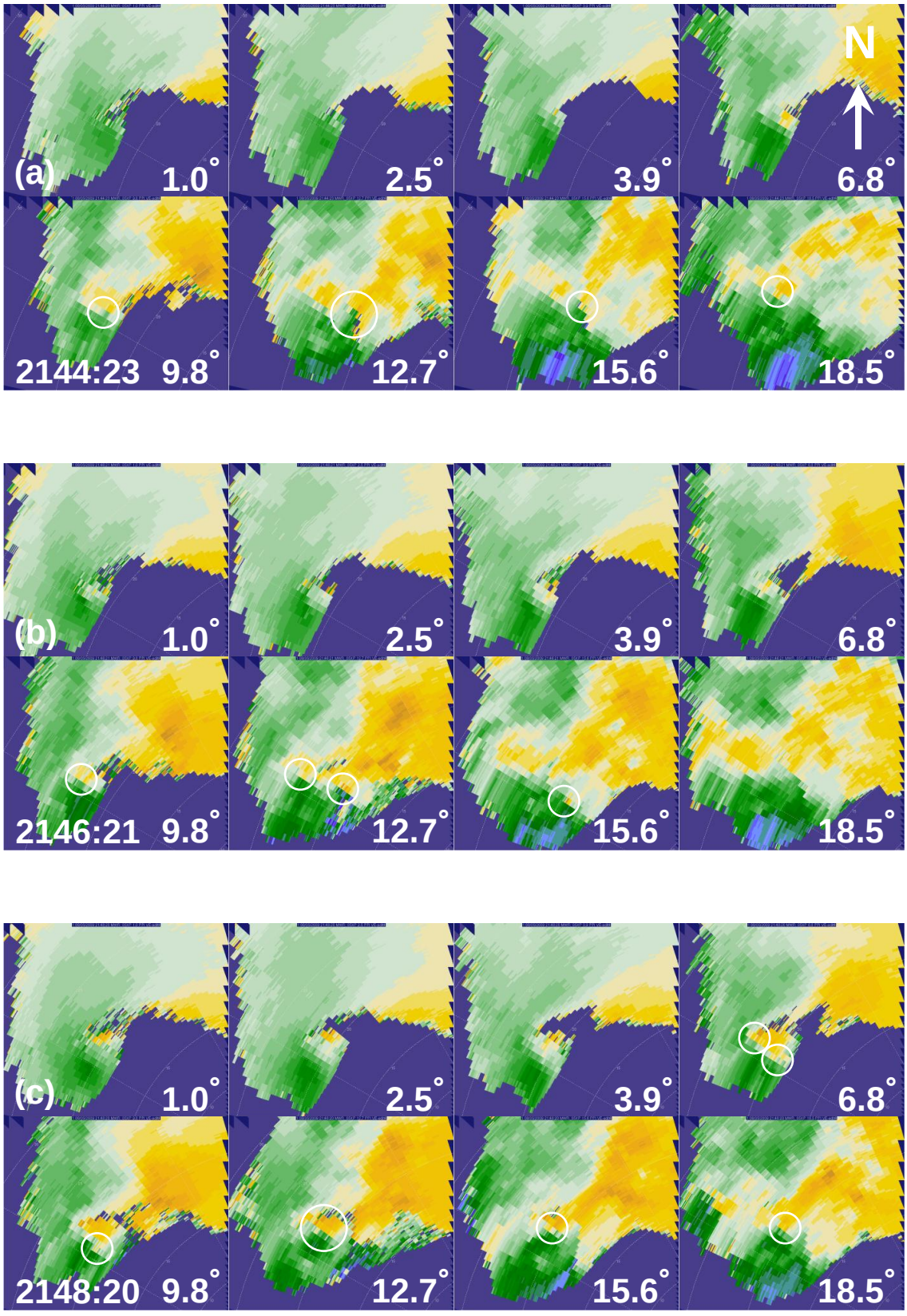
(a)
1.0°
2.5°
3.9°
N
6.8°
2144:23
9.8°
12.7°
15.6°
18.5°
(b)
1.0°
2.5°
3.9°
6.8°
2146:21
9.8°
12.7°
15.6°
18.5°
(c)
1.0°
2.5°
3.9°
6.8°
2148:20
9.8°
12.7°
15.6°
18.5°

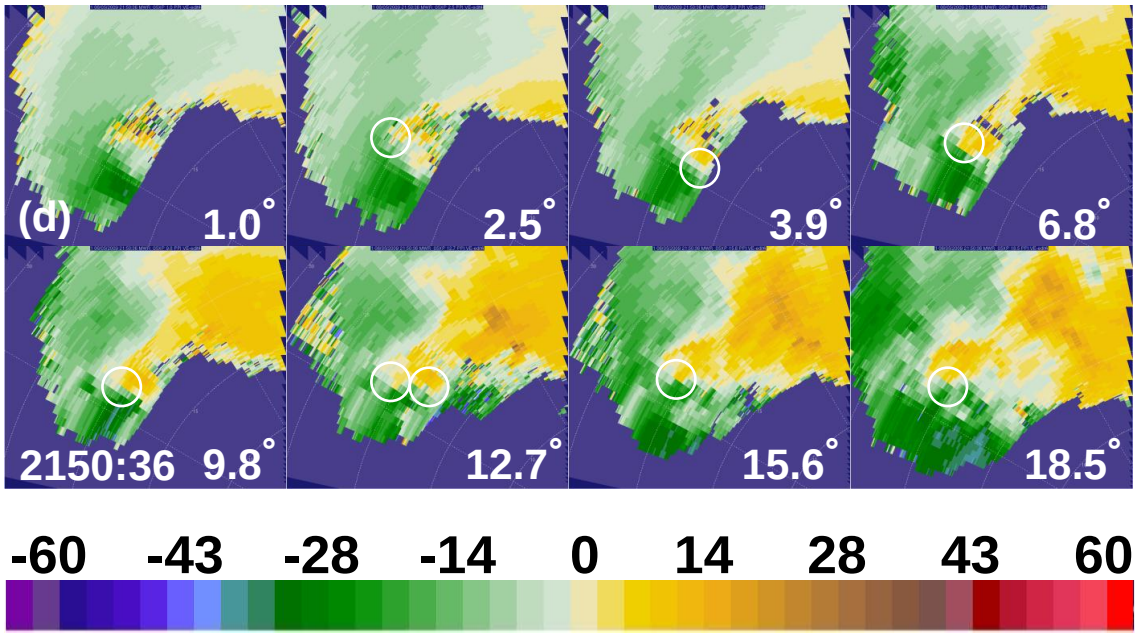

Figure 5.37. PPIs of radial velocity (m s^{-1}) at several elevation angles at (a) 2144:23, (b) 2146:21, (c) 2148:20, and (d) 2150:36 UTC prior to tornadogenesis. Areas of enhanced GTG cyclonic shear that meet the criteria for a TVS are enclosed by white circles. Range rings are every 5 km. Approximate heights at the center of the domain range from 350 m at 1.0° to 3.5 km at 9.8° to 6.7 km at 18.5° in elevation angle. The radial velocity colorbar appears beneath the figure.

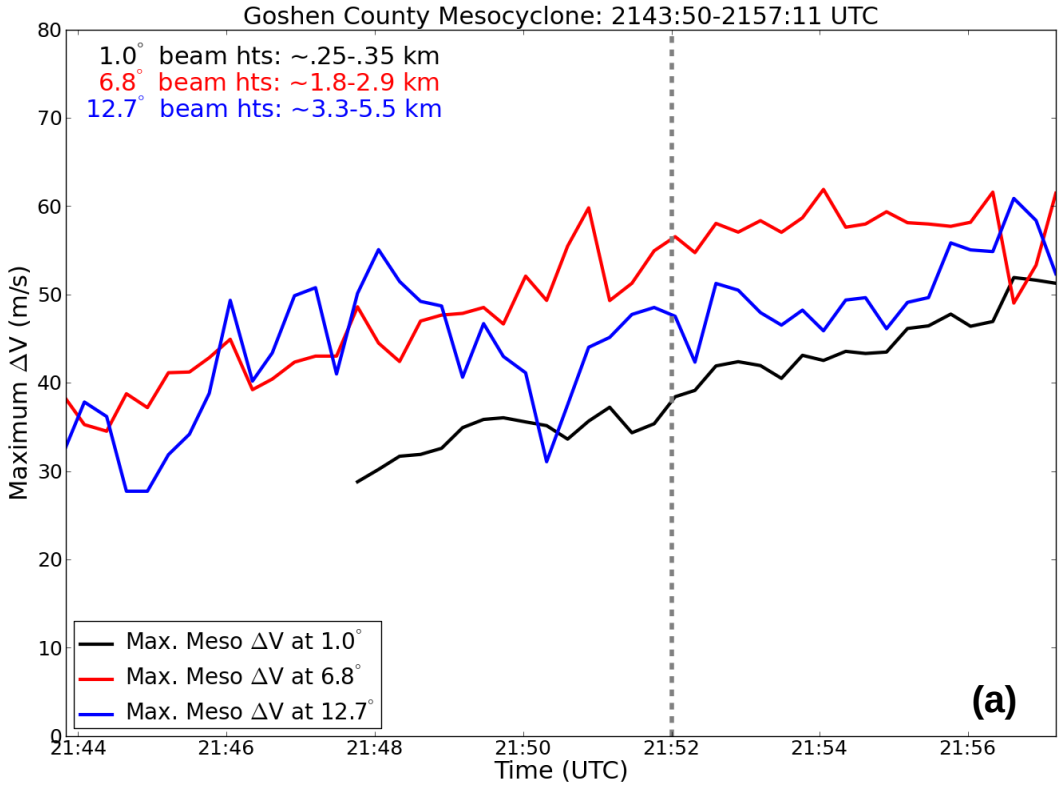
Goshen County Mesocyclone: 2143:50-2157:11 UTC
1.0° beam hts: ~.25-.35 km
6.8° beam hts: ~1.8-2.9 km
12.7° beam hts: ~3.3-5.5 km
Maximum ΔV (m/s)
Time (UTC)
Max. Meso ΔV at 1.0°
Max. Meso ΔV at 6.8°
Max. Meso ΔV at 12.7°
(a)

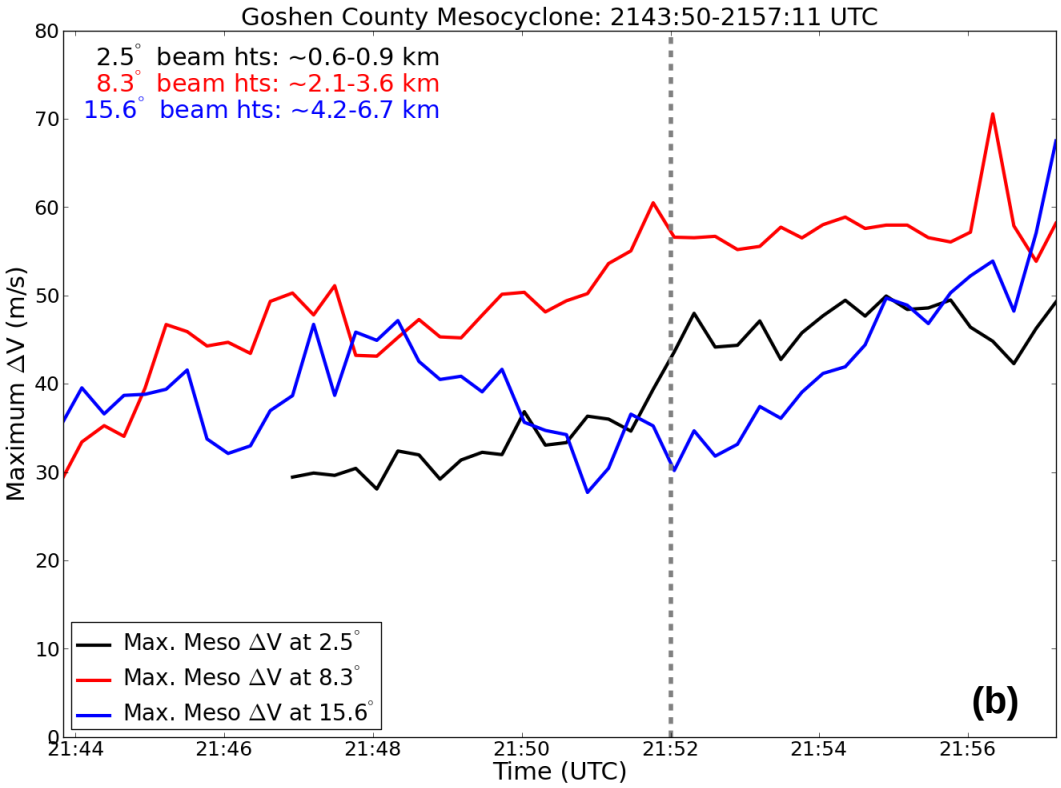
Goshen County Mesocyclone: 2143:50-2157:11 UTC
2.5° beam hts: ~0.6-0.9 km
8.3° beam hts: ~2.1-3.6 km
15.6° beam hts: ~4.2-6.7 km
Maximum ΔV (m/s)
Time (UTC)
Max. Meso ΔV at 2.5°
Max. Meso ΔV at 8.3°
Max. Meso ΔV at 15.6°
(b)

Figure 5.38. Time series of maximum ΔV (m s^{-1}) in the mesocyclone of the Goshen County supercell at (a) 1.0°, 6.8°, and 12.7° and (b) 2.5°, 8.3°, and 15.6° elevation angle from 2143:50-2157:11 UTC. The gray dashed line marks the approximate time of tornadogenesis. Approximate center beam heights are provided in the upper left of each figure.

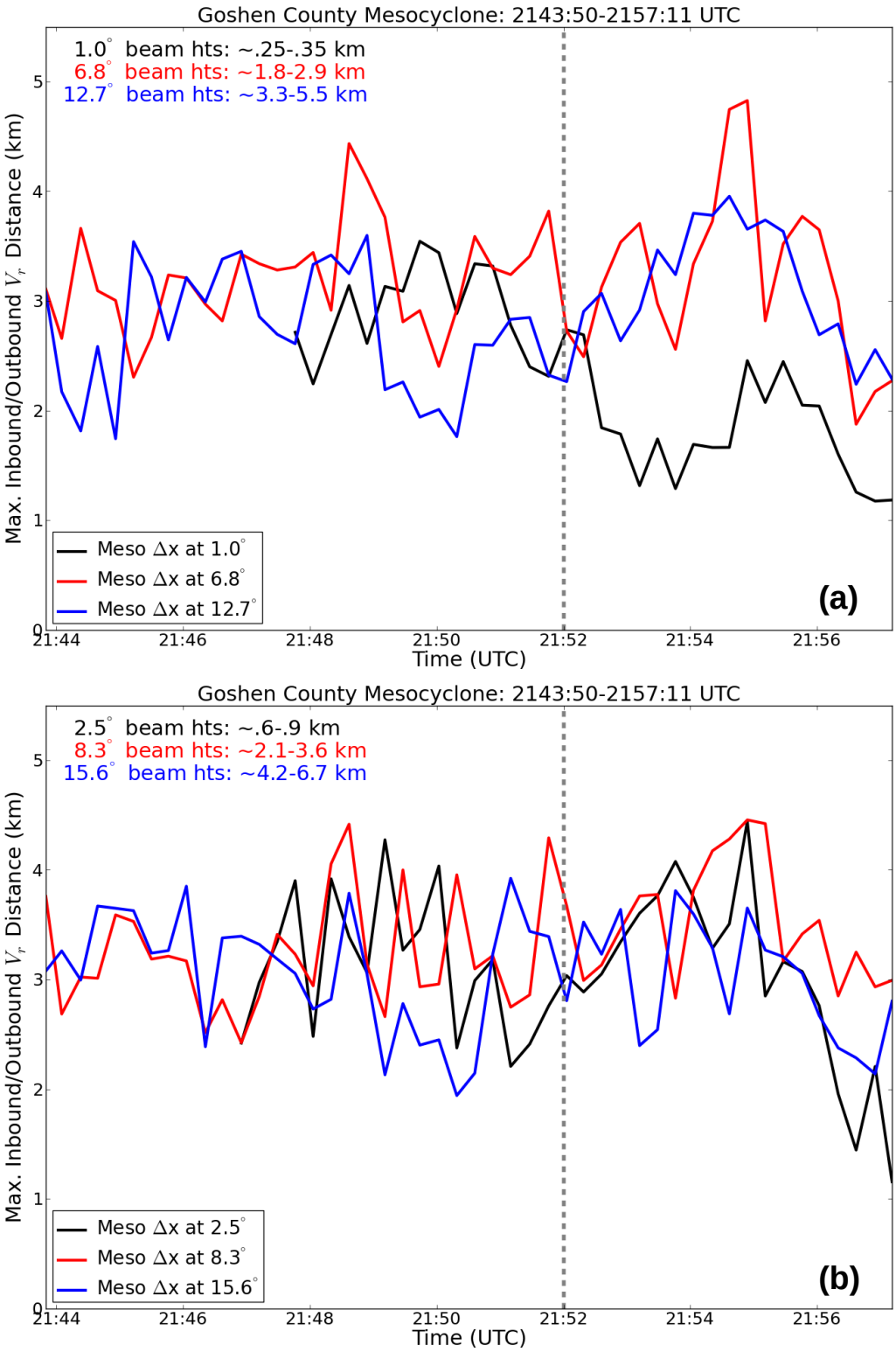

Figure 5.39. As in Fig. 5.38, but for the distance between the maximum inbound and outbound radial velocities in the Goshen County mesocyclone (Δx; km).

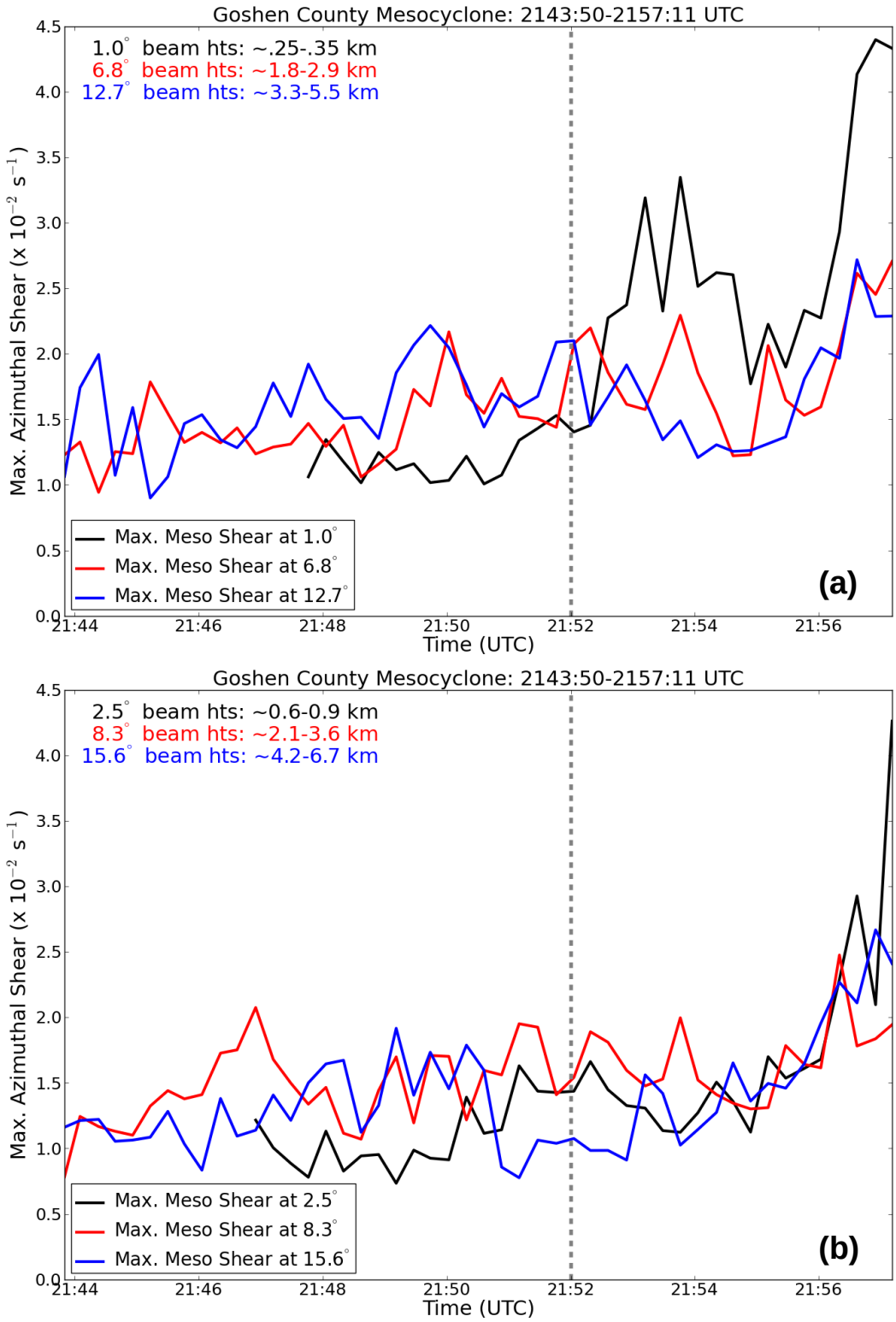

Figure 5.40. As in Fig. 5.38, but for the maximum shear in the Goshen County mesocyclone (s^{-1}).

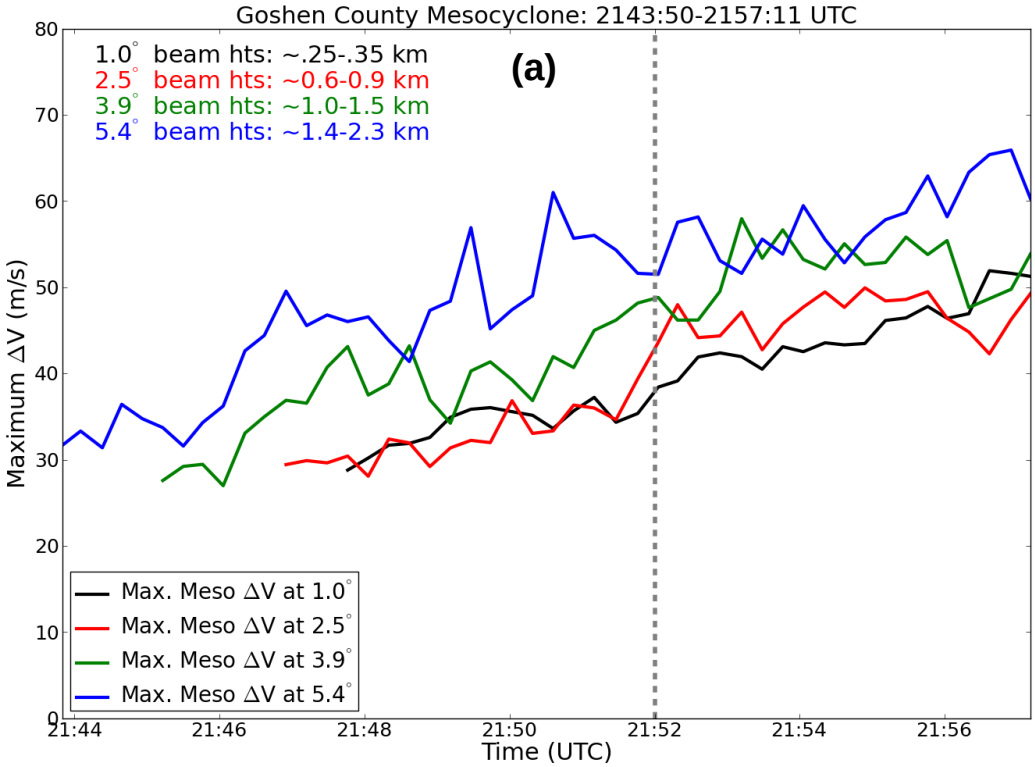
Goshen County Mesocyclone: 2143:50-2157:11 UTC
1.0° beam hts: ~.25-.35 km
2.5° beam hts: ~0.6-0.9 km
3.9° beam hts: ~1.0-1.5 km
5.4° beam hts: ~1.4-2.3 km
(a)
Maximum ΔV (m/s)
Max. Meso ΔV at 1.0°
Max. Meso ΔV at 2.5°
Max. Meso ΔV at 3.9°
Max. Meso ΔV at 5.4°
21:44
21:46
21:48
21:50
21:52
21:54
21:56
Time (UTC)

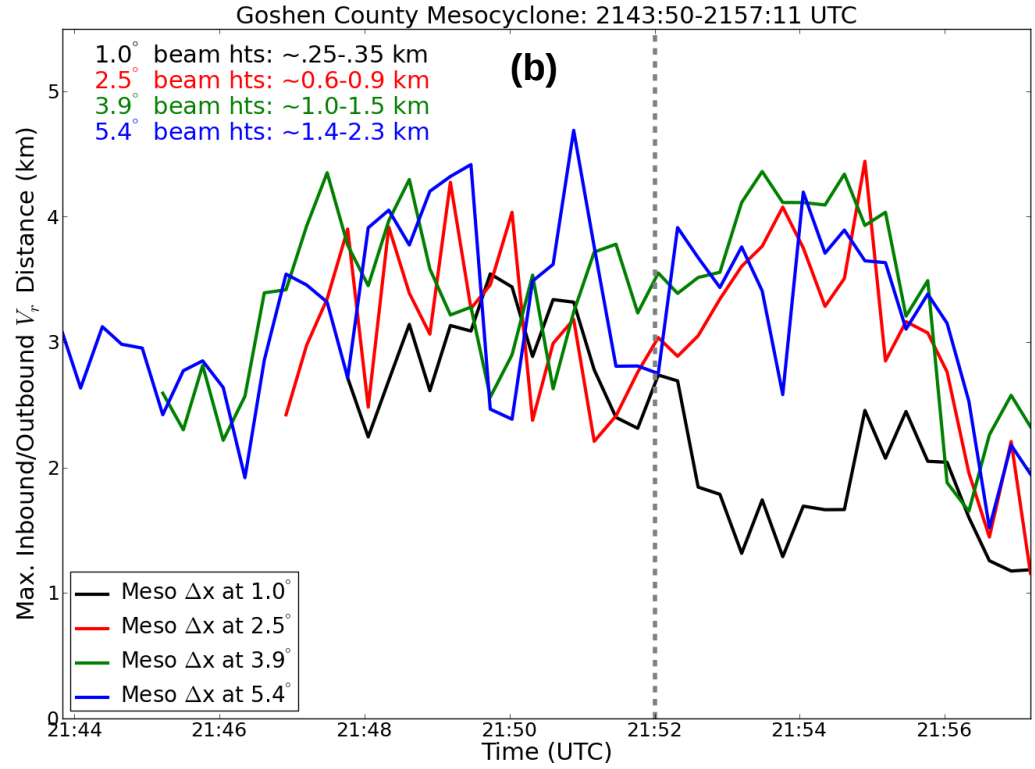
Goshen County Mesocyclone: 2143:50-2157:11 UTC
1.0° beam hts: ~.25-.35 km
2.5° beam hts: ~0.6-0.9 km
3.9° beam hts: ~1.0-1.5 km
5.4° beam hts: ~1.4-2.3 km
(b)
Max. Inbound/Outbound V_r Distance (km)
Meso Δx at 1.0°
Meso Δx at 2.5°
Meso Δx at 3.9°
Meso Δx at 5.4°
21:44
21:46
21:48
21:50
21:52
21:54
21:56
Time (UTC)

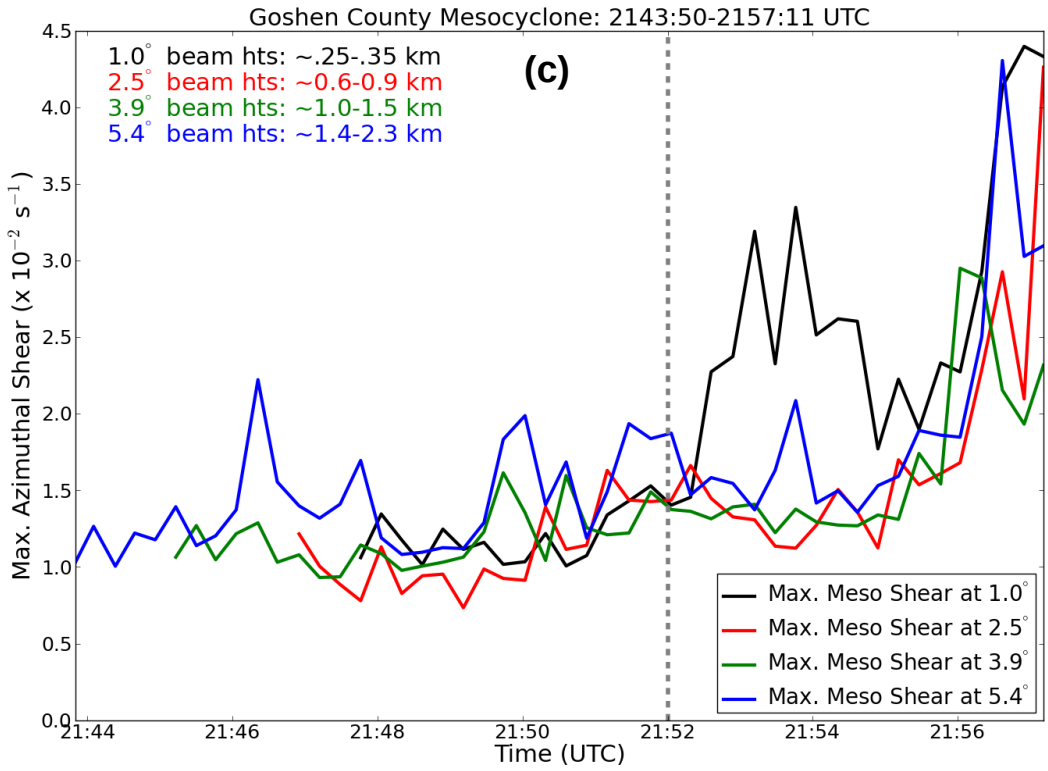

Figure 5.41. Time series of (a) maximum ΔV (m s^{-1}), (b) Δx (km), and (c) maximum shear (s^{-1}) in the mesocyclone of the Goshen County supercell at 1.0°, 2.5°, 3.9°, and 5.4° elevation angle from 2143:50-2157:11 UTC. The gray dashed line marks the approximate time of tornadogenesis. Approximate center beam heights are provided in the upper left of each figure.

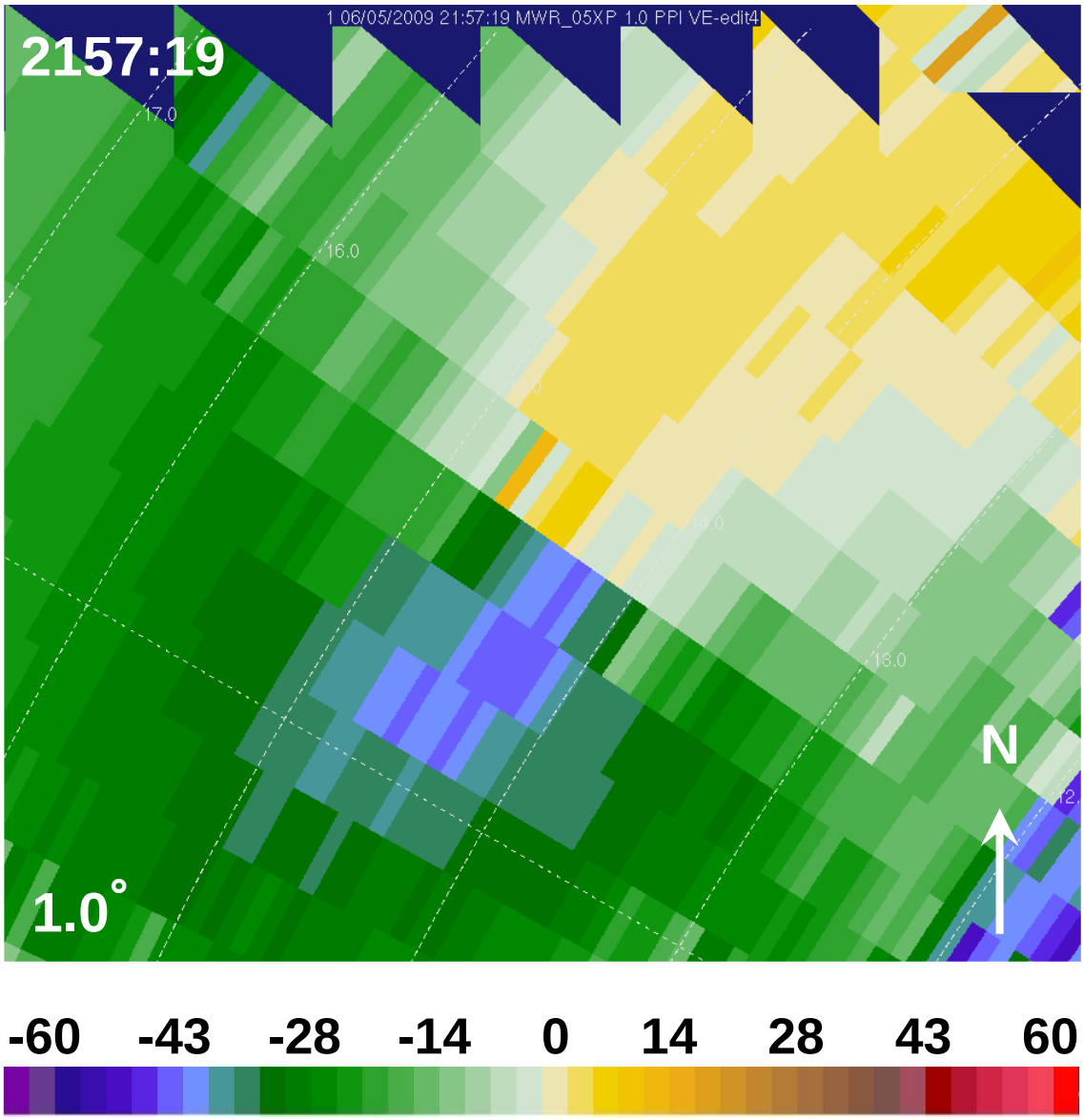

Figure 5.42. PPI of radial velocity (m s^{-1}) at 1.0° elevation angle at 2157:19 UTC after tornadogenesis. Range rings are every 1 km. Approximate height at the center of the domain range is 250 m. The radial velocity colorbar appears beneath the figure.

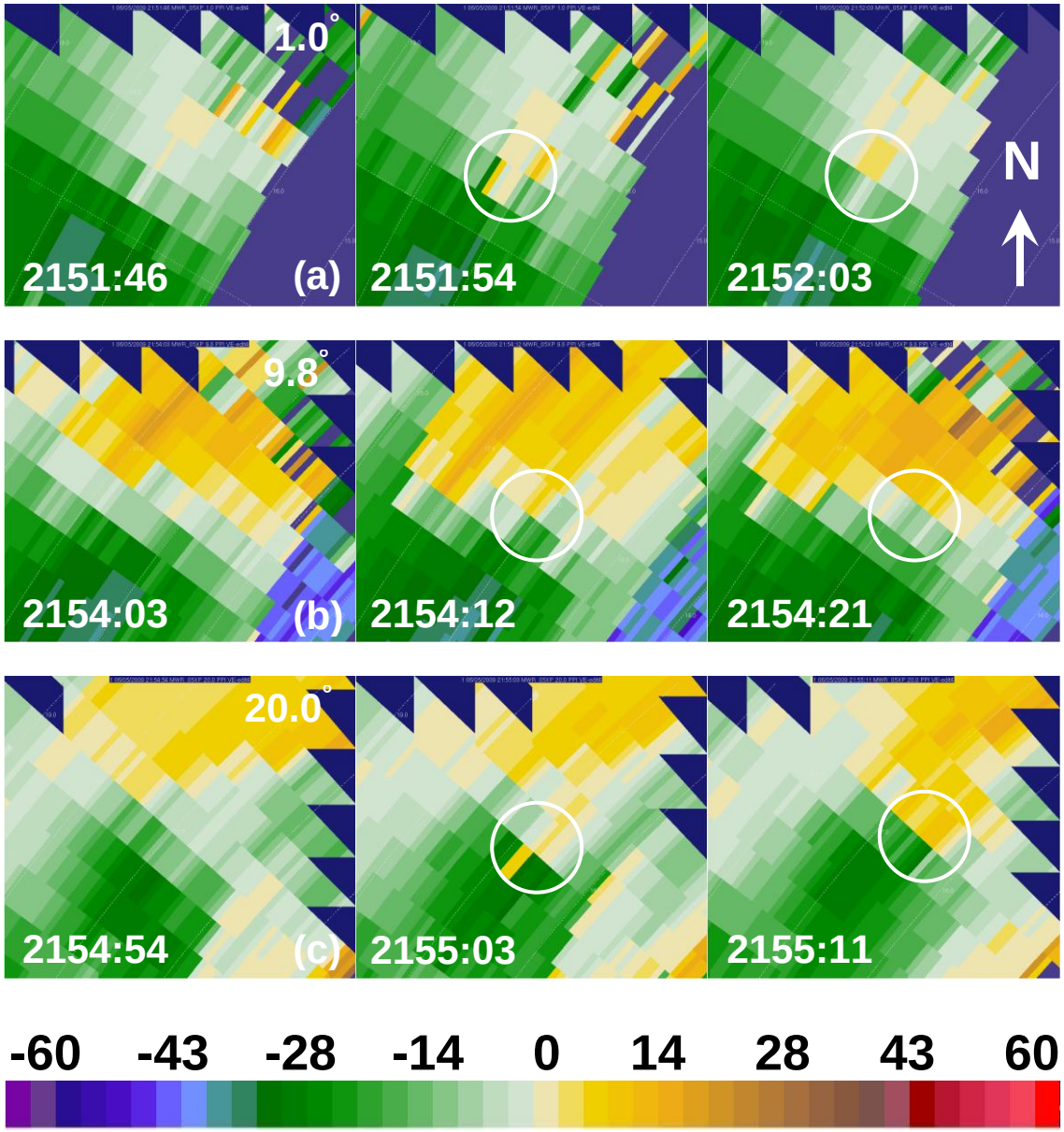

Figure 5.43. PPIs of radial velocity (m s^{-1}) at (a) 1.0°, (b) 9.8°, and (c) 20.0° elevation angle at the time the TVS was first identified (center) and the scans immediately before (left) and after (right). The TVS associated with the Goshen County tornado is enclosed by white circles. Range rings are every 1 km. The radial velocity colorbar appears beneath the figure.

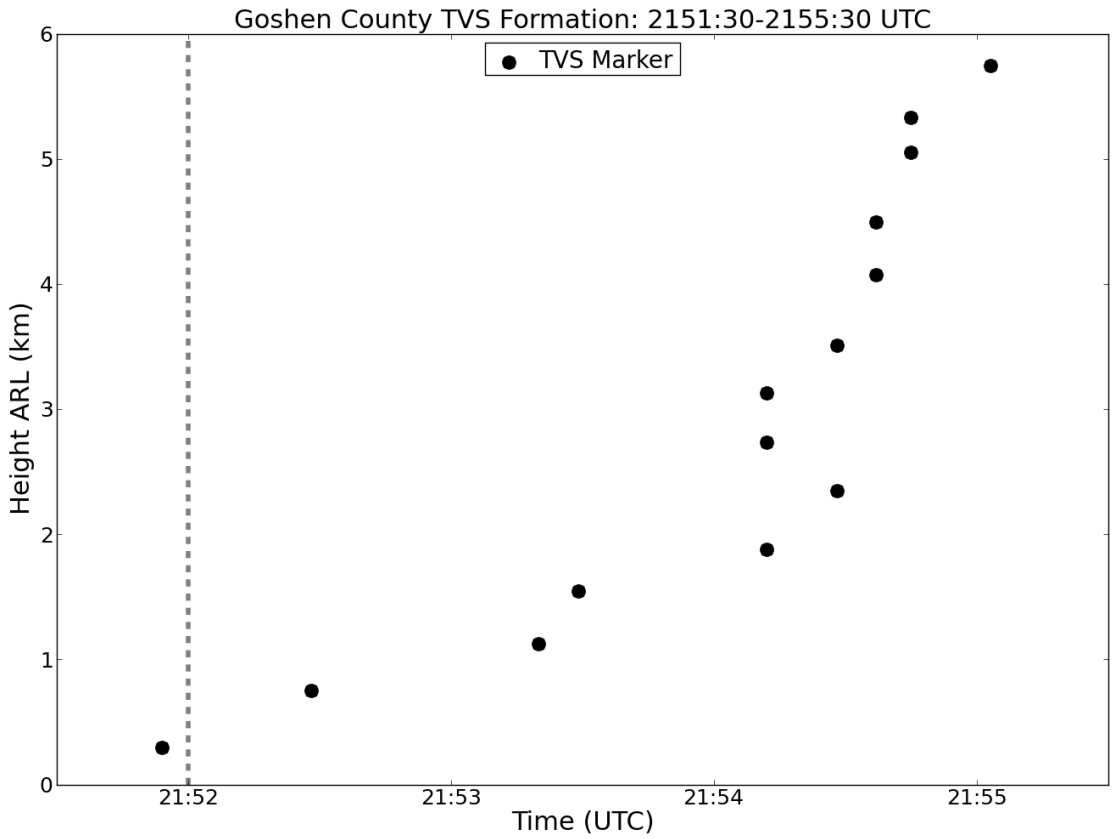

Figure 5.44. Time-height series of the formation of the TVS associated with the Goshen County tornado. The black markers indicate the time and approximate height that the TVS was first identified at each of the 14 elevation angles used in MWR-05XP data collection. The dotted gray line shows the approximate time of tornadogenesis according to other mobile Doppler radars and the results of a damage survey.

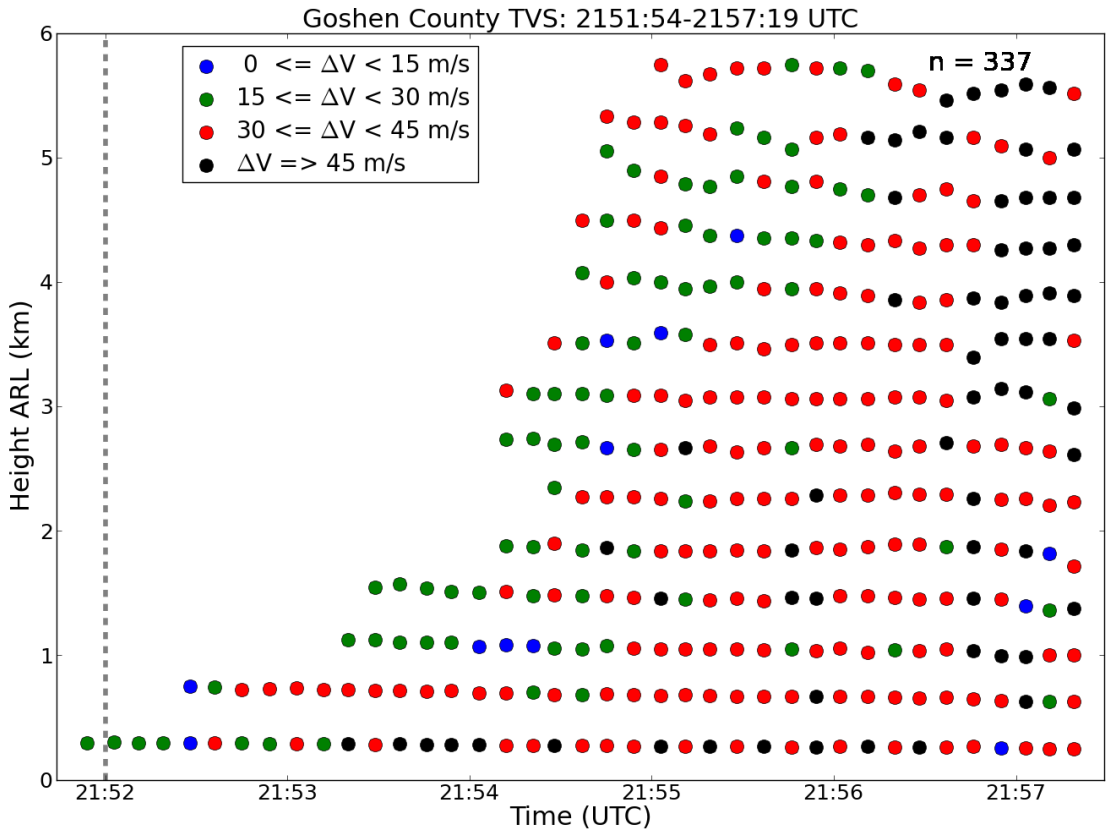

Figure 5.45. Time-height series of the Goshen County TVS ΔV in the ~5 min. after tornadogenesis. The markers indicate the time and approximate height of the TVS at each of the 14 elevation angles used in MWR-05XP data collection. The markers are color coded according to the ΔV value. The dotted gray line shows the approximate time of tornadogenesis according to other mobile radars and the results of a damage survey.

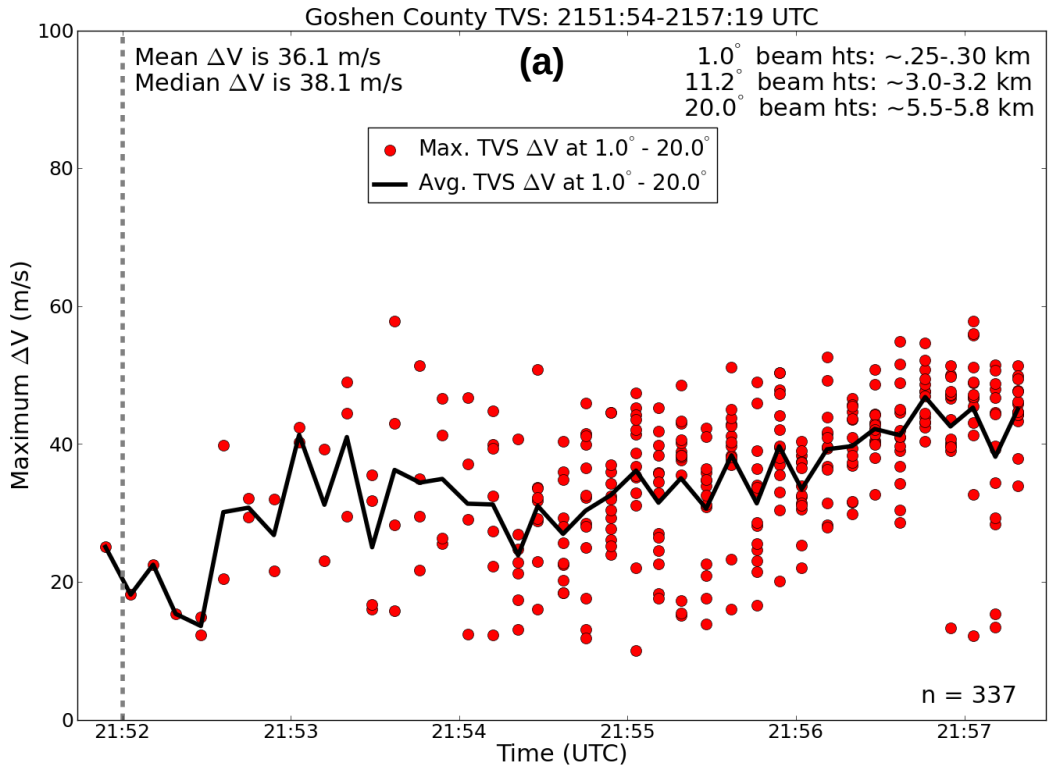
Goshen County TVS: 2151:54-2157:19 UTC
Mean ΔV is 36.1 m/s
Median ΔV is 38.1 m/s
(a)
1.0° beam hts: ~.25-.30 km
11.2° beam hts: ~3.0-3.2 km
20.0° beam hts: ~5.5-5.8 km
Max. TVS ΔV at 1.0° - 20.0°
Avg. TVS ΔV at 1.0° - 20.0°
n = 337
Maximum ΔV (m/s)
Time (UTC)
0
20
40
60
80
100
21:52
21:53
21:54
21:55
21:56
21:57

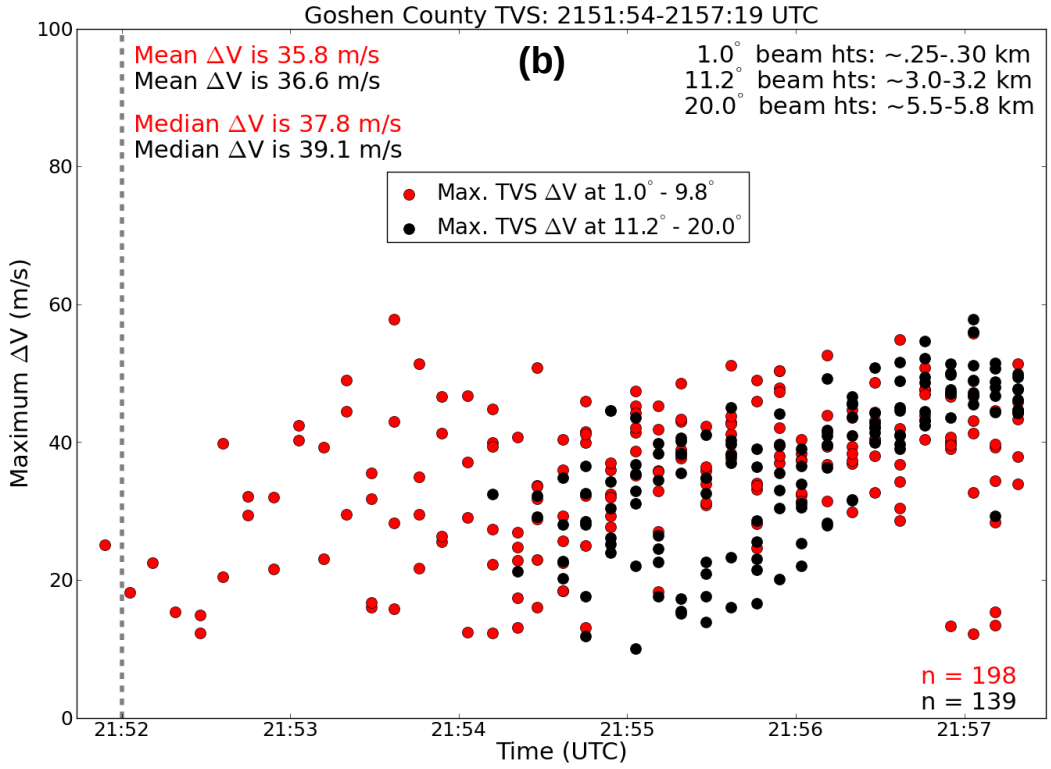
Goshen County TVS: 2151:54-2157:19 UTC
Mean ΔV is 35.8 m/s
Mean ΔV is 36.6 m/s
Median ΔV is 37.8 m/s
Median ΔV is 39.1 m/s
(b)
1.0° beam hts: ~.25-.30 km
11.2° beam hts: ~3.0-3.2 km
20.0° beam hts: ~5.5-5.8 km
Max. TVS ΔV at 1.0° - 9.8°
Max. TVS ΔV at 11.2° - 20.0°
n = 198
n = 139
Maximum ΔV (m/s)
Time (UTC)
0
20
40
60
80
100
21:52
21:53
21:54
21:55
21:56
21:57

Figure 5.46. Time series of Goshen County TVS ΔV in the ~5 min. after tornadogenesis (a) at all observed levels and (b) color coded for above and below ~3 km. In (a) the black line is a time series of the average ΔV at each time. The dotted gray line shows the approximate time of tornadogenesis according to other mobile Doppler radars and the results of a damage survey. The number of data points, mean and median ΔV values, and approximate radar center beam heights also are provided.

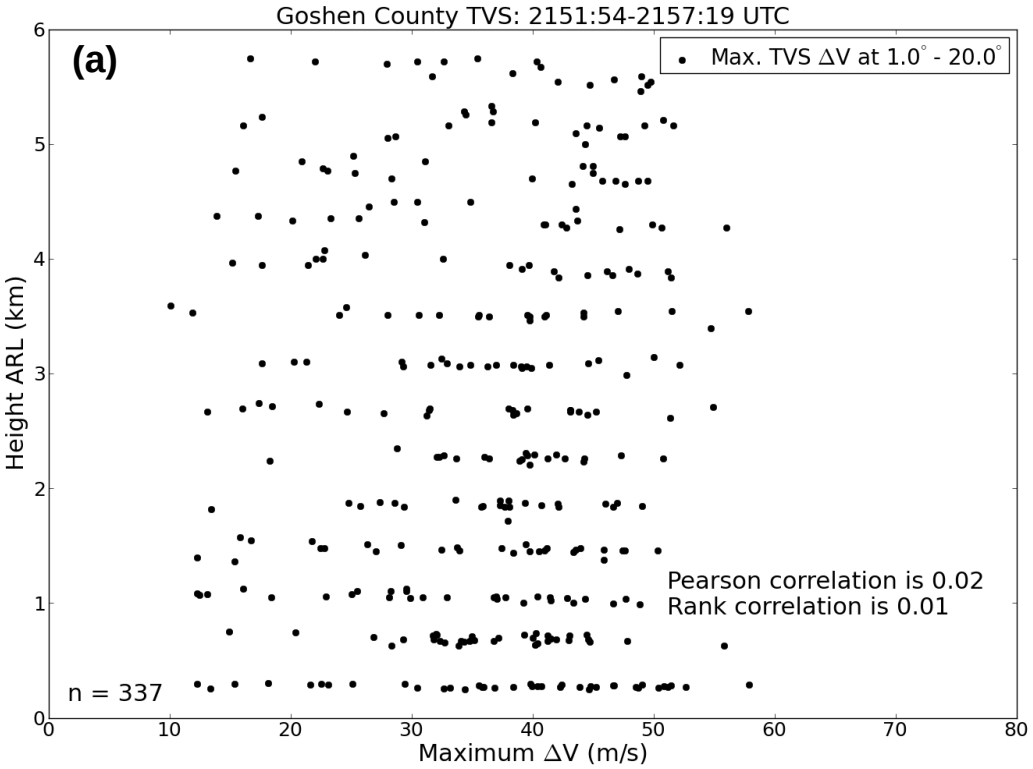
Goshen County TVS: 2151:54-2157:19 UTC
(a)
Max. TVS ΔV at 1.0° - 20.0°
Pearson correlation is 0.02
Rank correlation is 0.01
n = 337
Height ARL (km)
Maximum ΔV (m/s)
0
1
2
3
4
5
6
0
10
20
30
40
50
60
70
80

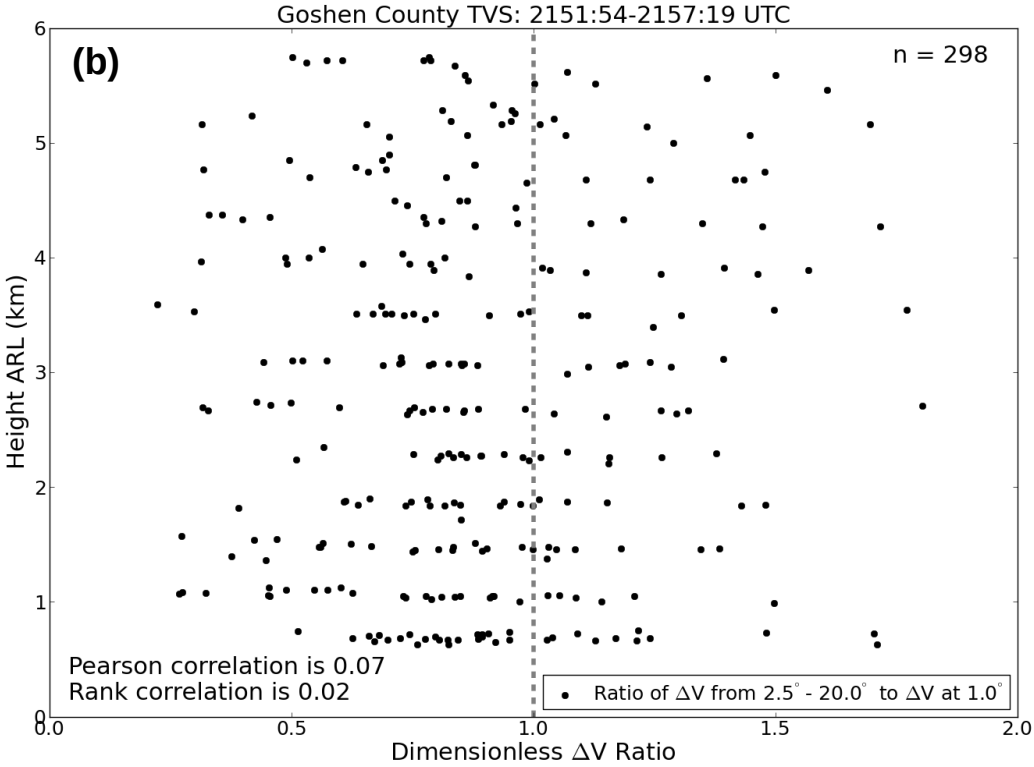
Goshen County TVS: 2151:54-2157:19 UTC
(b)
n = 298
Pearson correlation is 0.07
Rank correlation is 0.02
Ratio of ΔV from 2.5° - 20.0° to ΔV at 1.0°
Height ARL (km)
Dimensionless ΔV Ratio
0
1
2
3
4
5
6
0.0
0.5
1.0
1.5
2.0

Figure 5.47. Vertical profiles of (a) ΔV from every TVS data point and (b) the ratio of TVS ΔV from 2.5-20.0° elevation angle to the TVS ΔV at 1.0° elevation angle for each data point from the first ~5 min. of the Goshen County tornado. The gray line in (b) marks a ratio of 1. The number of data points and the Pearson and Rank correlations also are provided.

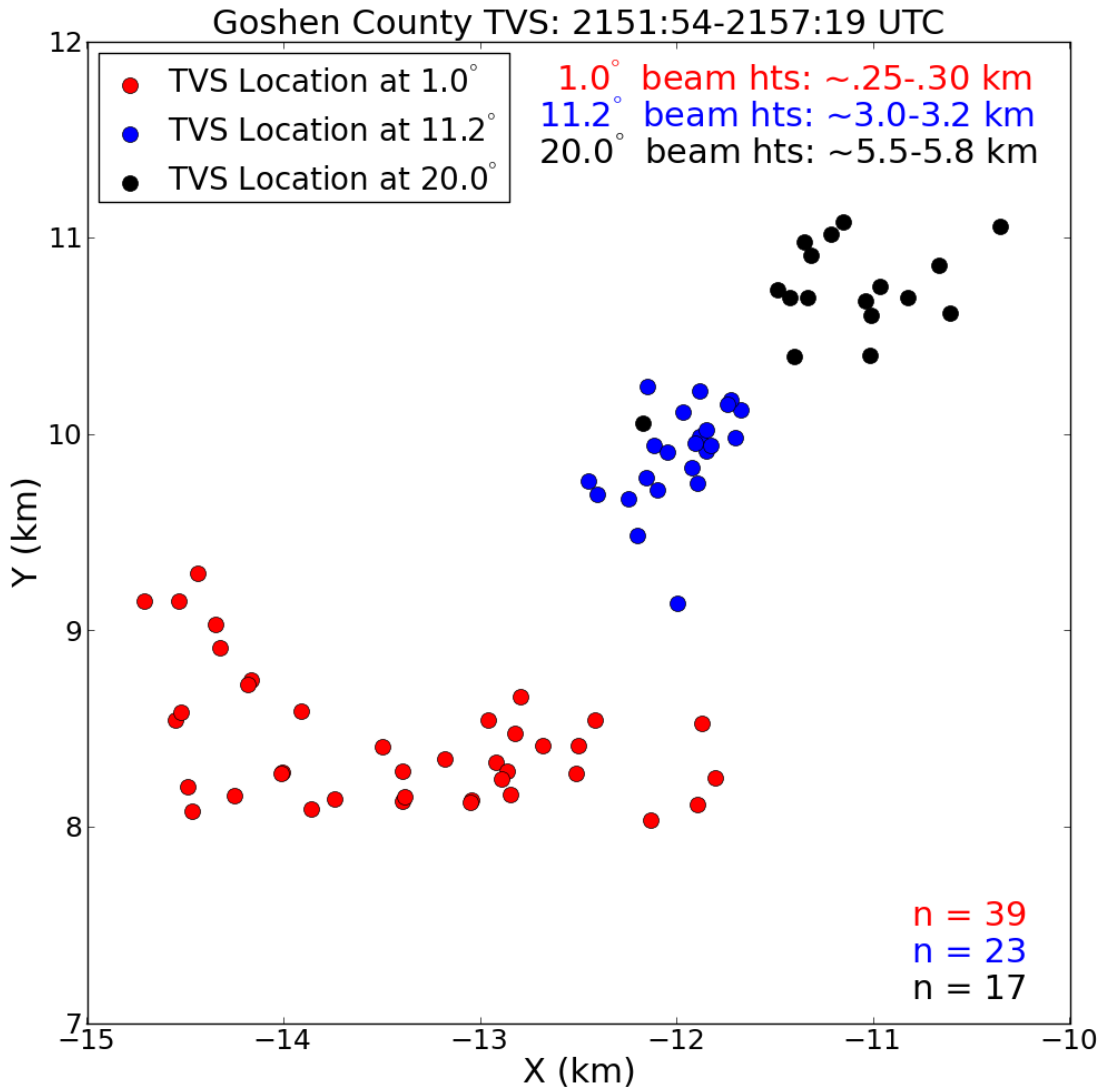

Figure 5.48. Plan view of the TVS location at 1.0°, 11.2°, and 20.0° elevation angle in the 5 min. after formation of the Goshen County tornado. The number of data points and approximate radar center beam heights also are provided.

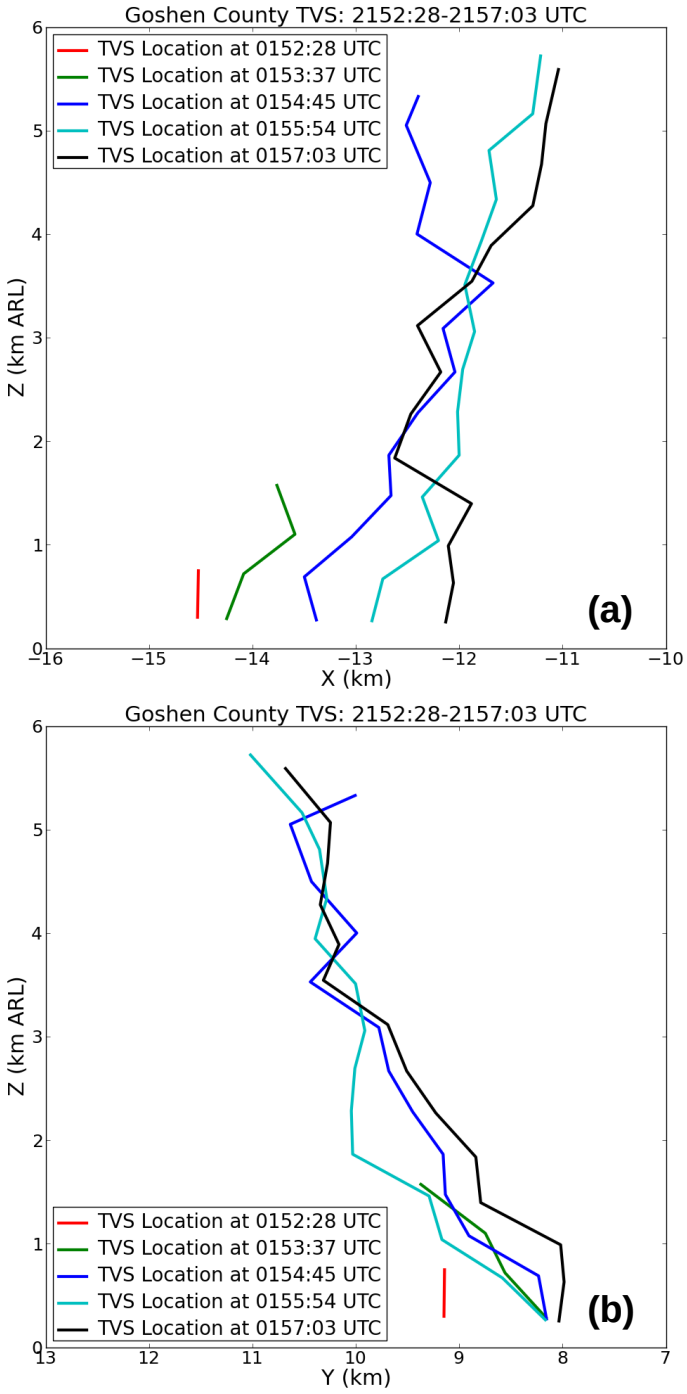

Figure 5.49. Vertical cross sections of the Goshen County tornado TVS position in an (a) x-z and (b) y-z reference frame every ~65 sec. in the ~5 min. after its formation. The MWR-05XP is located at the origin (not shown) and the grids are not stretched. The times shown for (a) and (b) are the same.

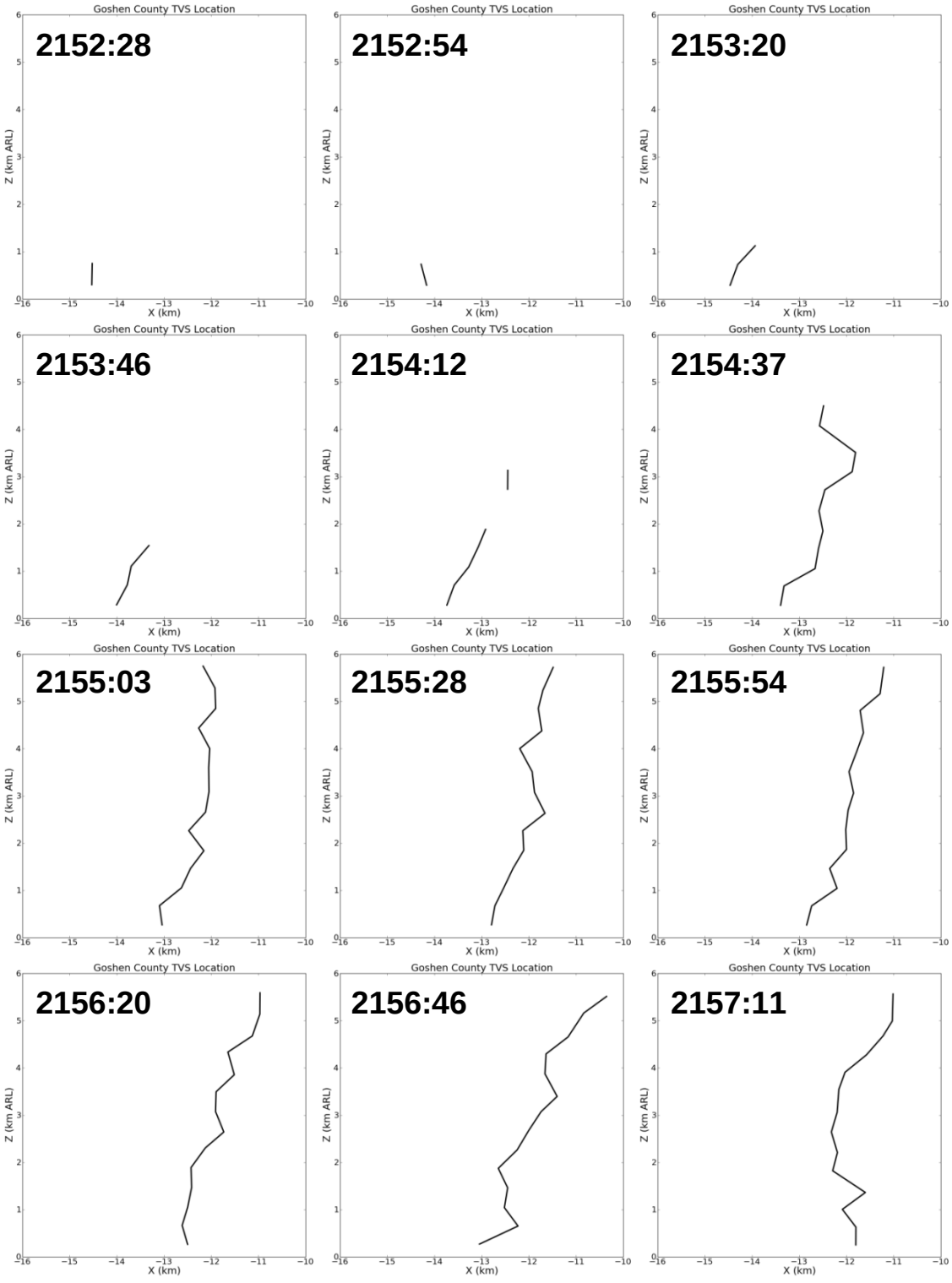
Goshen County TVS Location
2152:28
2152:54
2153:20
2153:46
2154:12
2154:37
2155:03
2155:28
2155:54
2156:20
2156:46
2157:11
Z (km ARL)
X (km)

Figure 5.50. Vertical cross sections of the Goshen County tornado TVS position in an x-z reference frame every ~25 sec. in the ~5 min. after its formation. The MWR-05XP is located at the origin (not shown). The grid is not stretched and from left to right (bottom to top) extends 6 km to the east (upward) in the x (z) direction.

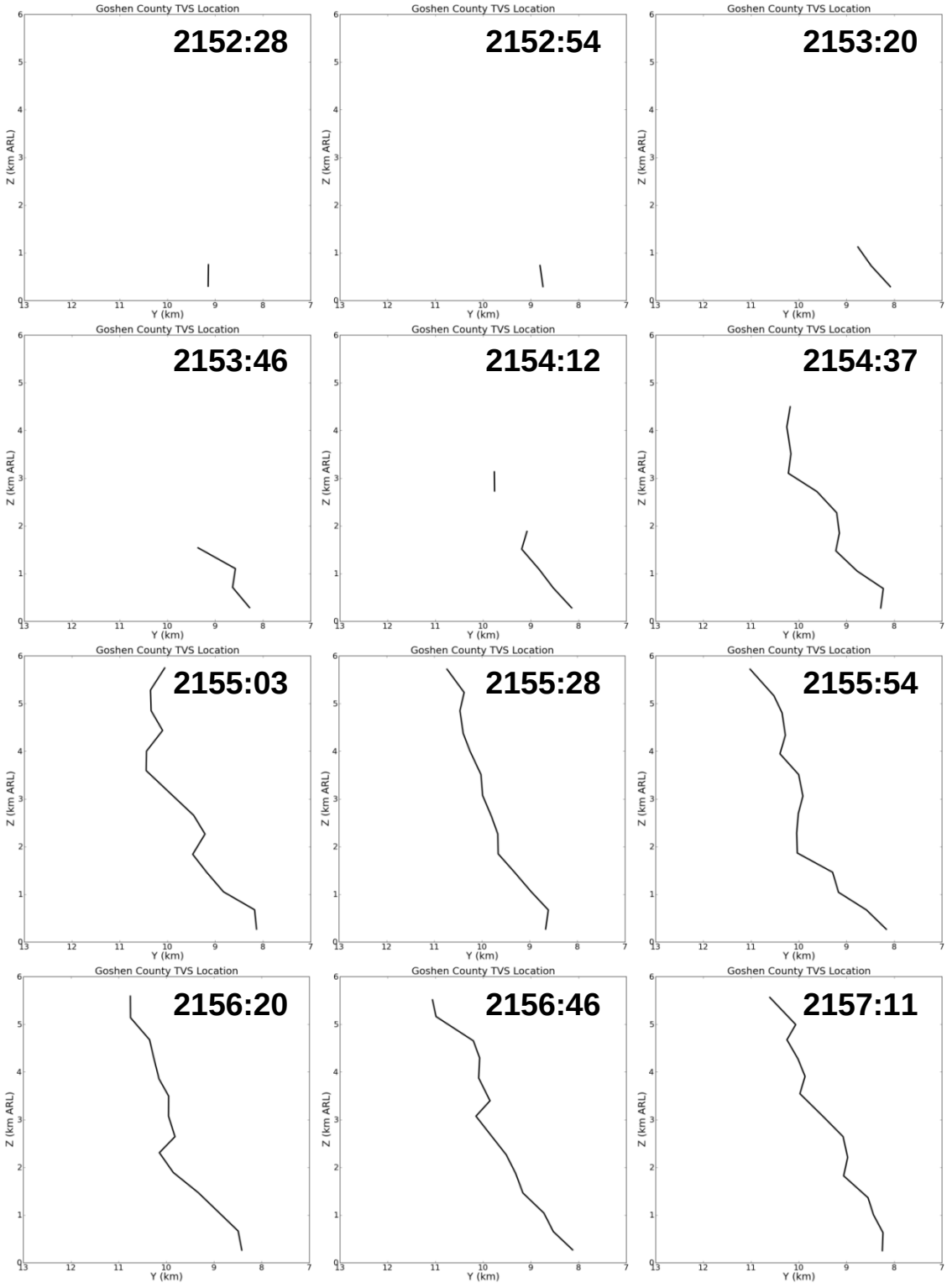
Goshen County TVS Location
2152:28
2152:54
2153:20
2153:46
2154:12
2154:37
2155:03
2155:28
2155:54
2156:20
2156:46
2157:11
Z (km ARL)
Y (km)

Figure 5.51. Vertical cross sections of the Goshen County tornado TVS position in a y-z reference frame every ~25 sec. in the ~5 min. after its formation. The MWR-05XP is located at the origin (not shown). The grid is not stretched and from left to right (bottom to top) extends 6 km to the south (upward) in the y (z) direction.

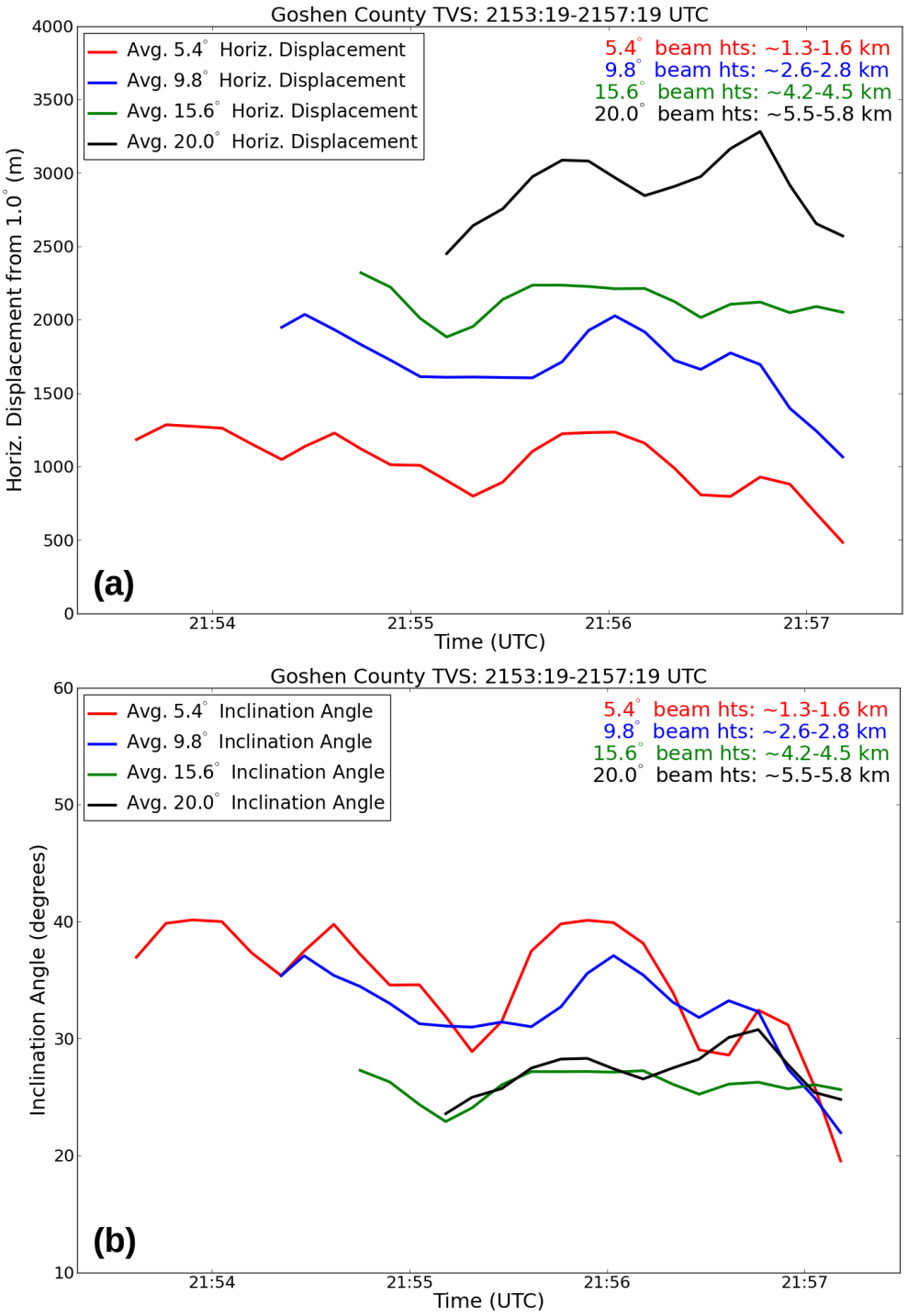

Figure 5.52. The Goshen County tornado TVS (a) horizontal displacement and (b) inclination angle at 5.4°, 9.8°, 15.6°, and 20.0° elevation angle in the ~4 min. after its formation. A simple 1-2-1 time filter was employed to smooth the time series. The approximate radar center beam heights also are provided.

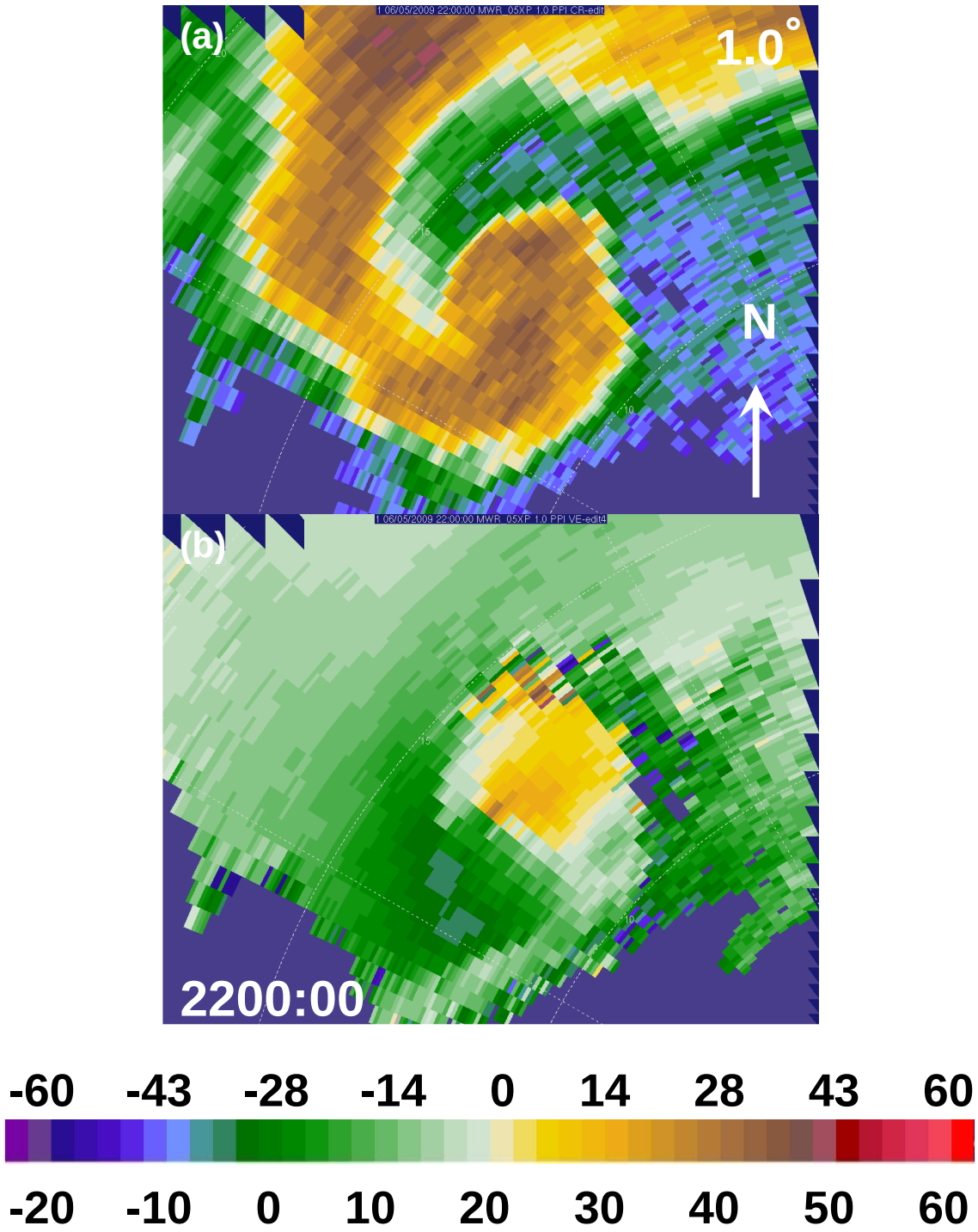

Figure 5.53. PPIs of (a) radial velocity (m s^{-1}) and (b) reflectivity (dBZ) at 1.0° elevation angle at 2200:00 UTC. Range rings are every 5 km. Approximate height at the center of the domain is 230 m. The scale for radial velocity (reflectivity) appears on the top (bottom) of the colorbar.

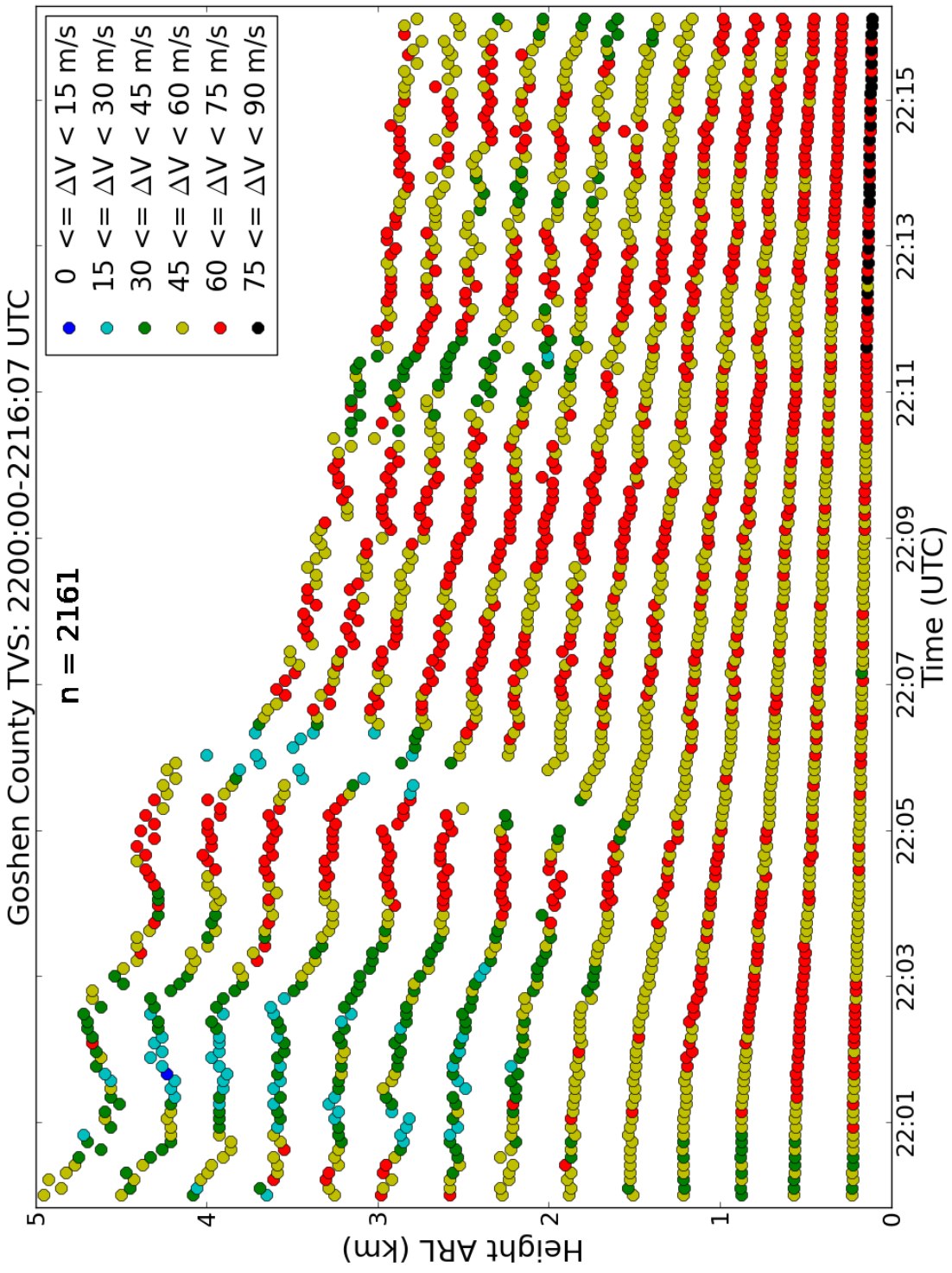

Figure 5.54. As in Fig. 5.45, but for the tornado mature stage. The lack of TVS markers at ~2205:30 UTC are not caused by poor or missing data, but rather from the TVS criteria not being meet.

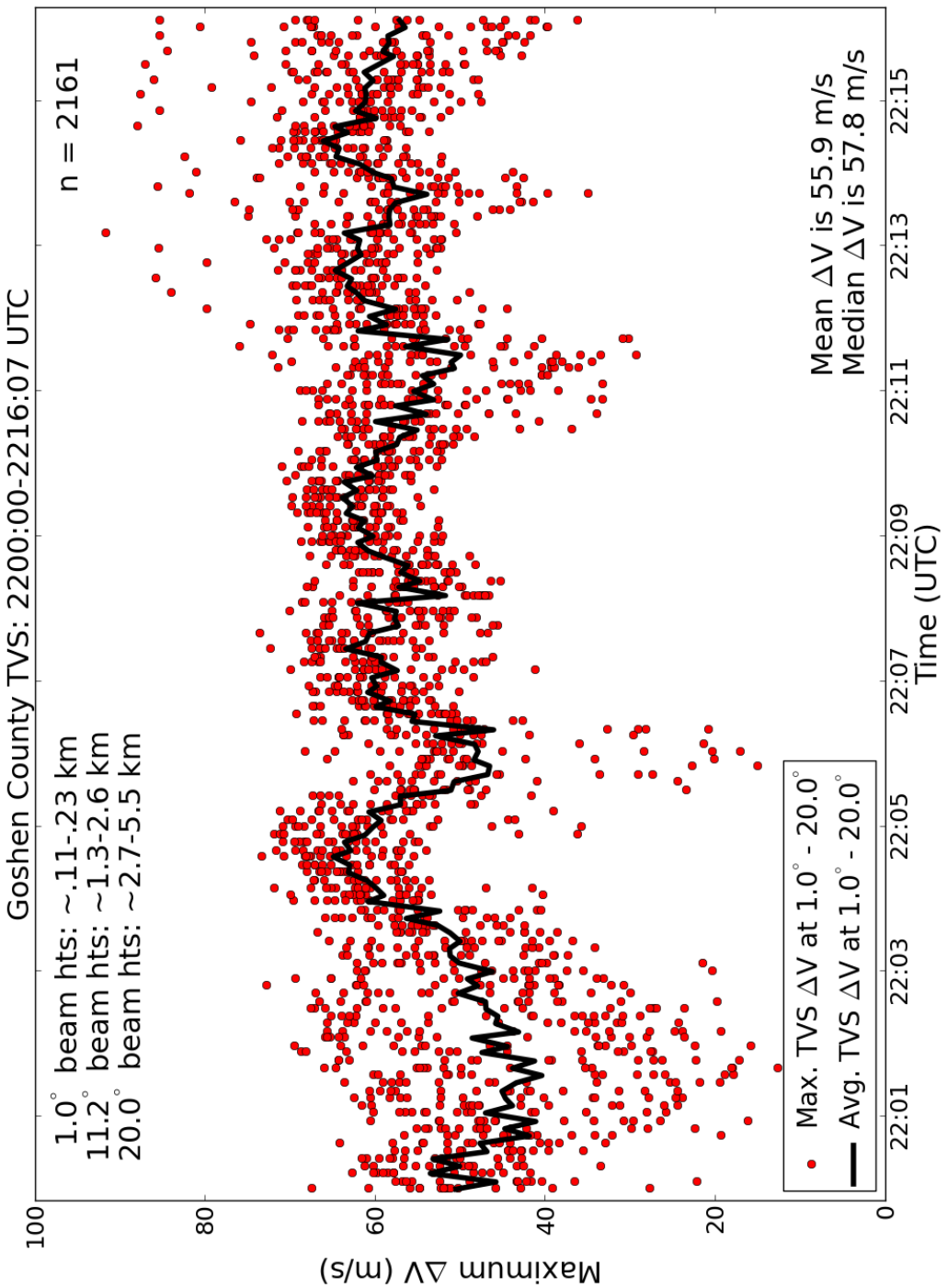

Figure 5.55. Time series of the Goshen County TVS ΔV during the mature stage of the tornado. The black line is a time series of the average ΔV at each time. The number of data points, mean and median ΔV values, and approximate radar center beam heights also are provided.

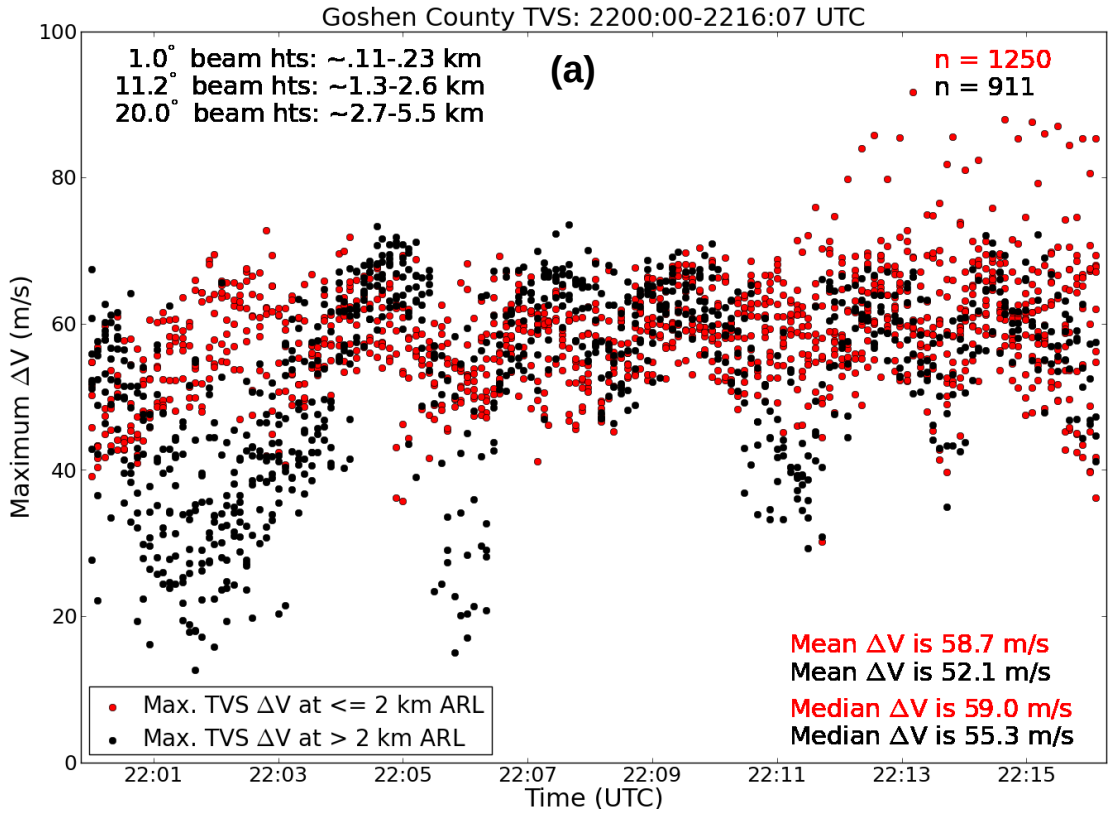
Goshen County TVS: 2200:00-2216:07 UTC
1.0° beam hts: ~.11-.23 km
11.2° beam hts: ~1.3-2.6 km
20.0° beam hts: ~2.7-5.5 km
(a)
n = 1250
n = 911
Maximum ΔV (m/s)
Time (UTC)
Max. TVS ΔV at <= 2 km ARL
Max. TVS ΔV at > 2 km ARL
Mean ΔV is 58.7 m/s
Mean ΔV is 52.1 m/s
Median ΔV is 59.0 m/s
Median ΔV is 55.3 m/s

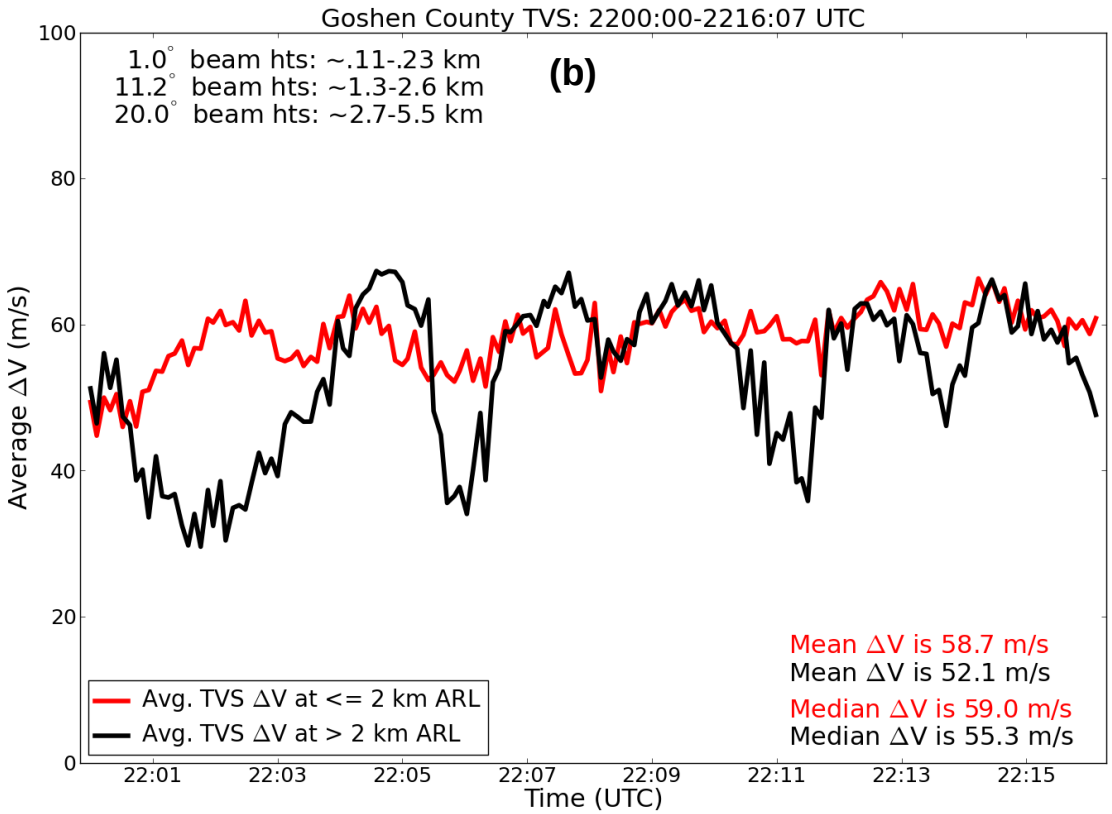
Goshen County TVS: 2200:00-2216:07 UTC
1.0° beam hts: ~.11-.23 km
11.2° beam hts: ~1.3-2.6 km
20.0° beam hts: ~2.7-5.5 km
(b)
Average ΔV (m/s)
Time (UTC)
Avg. TVS ΔV at <= 2 km ARL
Avg. TVS ΔV at > 2 km ARL
Mean ΔV is 58.7 m/s
Mean ΔV is 52.1 m/s
Median ΔV is 59.0 m/s
Median ΔV is 55.3 m/s

Fig. 5.56. Time series of the Goshen County TVS ΔV during the tornado mature stage above and below 2 km (a) for all data points and (b) averaged at each time. The number of data points, mean and median ΔV values, and approximate radar center beam heights also are provided.

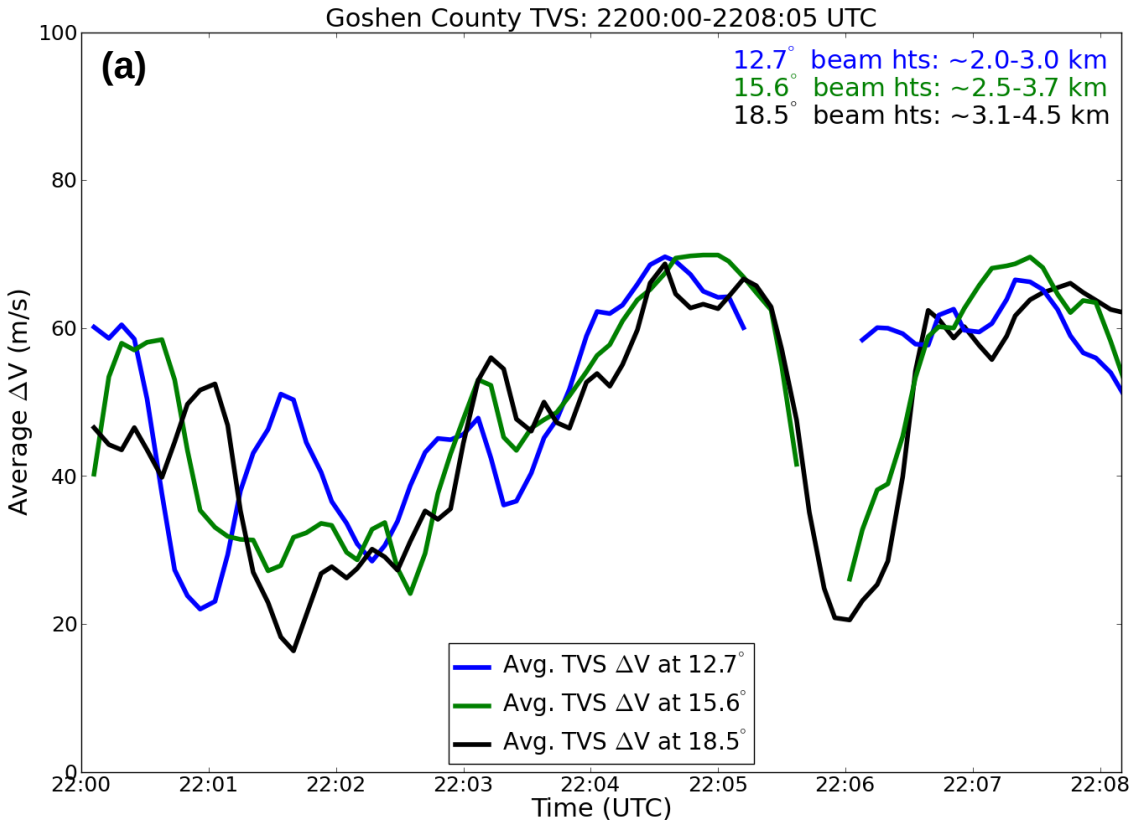
Goshen County TVS: 2200:00-2208:05 UTC
(a)
12.7° beam hts: ~2.0-3.0 km
15.6° beam hts: ~2.5-3.7 km
18.5° beam hts: ~3.1-4.5 km
Average ΔV (m/s)
Time (UTC)
Avg. TVS ΔV at 12.7°
Avg. TVS ΔV at 15.6°
Avg. TVS ΔV at 18.5°

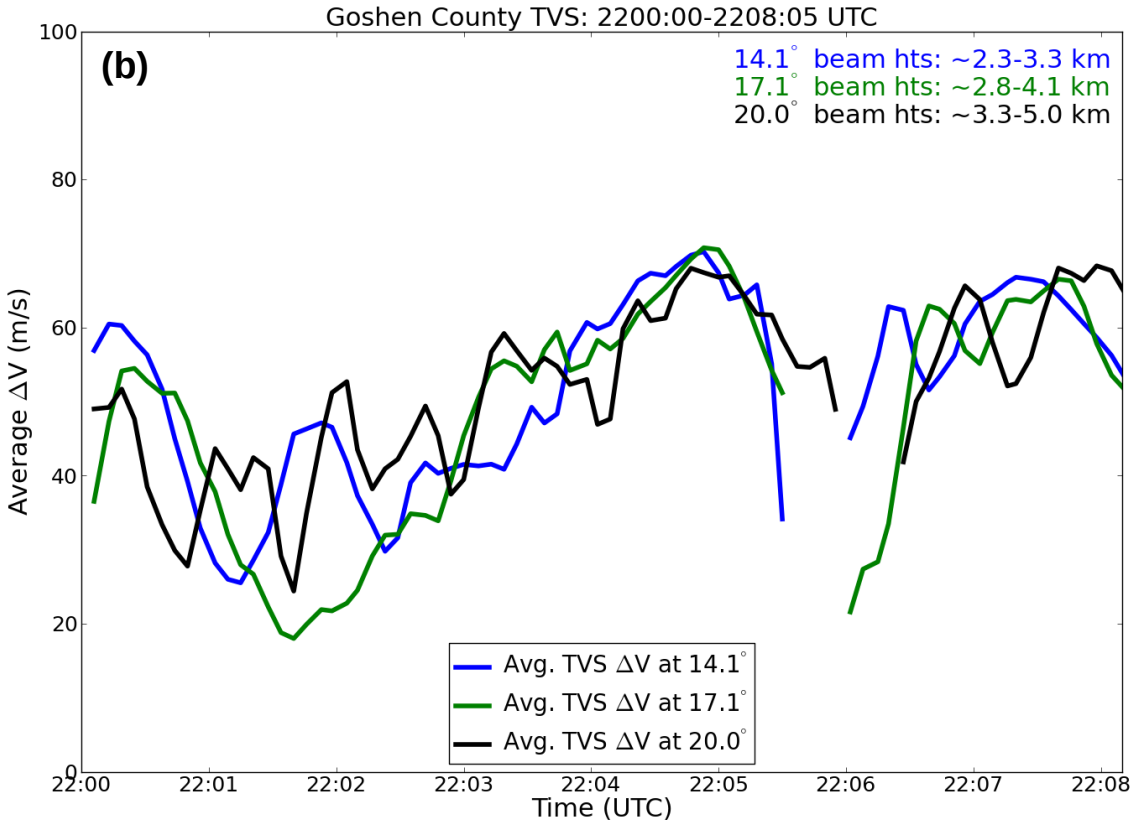
Goshen County TVS: 2200:00-2208:05 UTC
(b)
14.1° beam hts: ~2.3-3.3 km
17.1° beam hts: ~2.8-4.1 km
20.0° beam hts: ~3.3-5.0 km
Average ΔV (m/s)
Time (UTC)
Avg. TVS ΔV at 14.1°
Avg. TVS ΔV at 17.1°
Avg. TVS ΔV at 20.0°

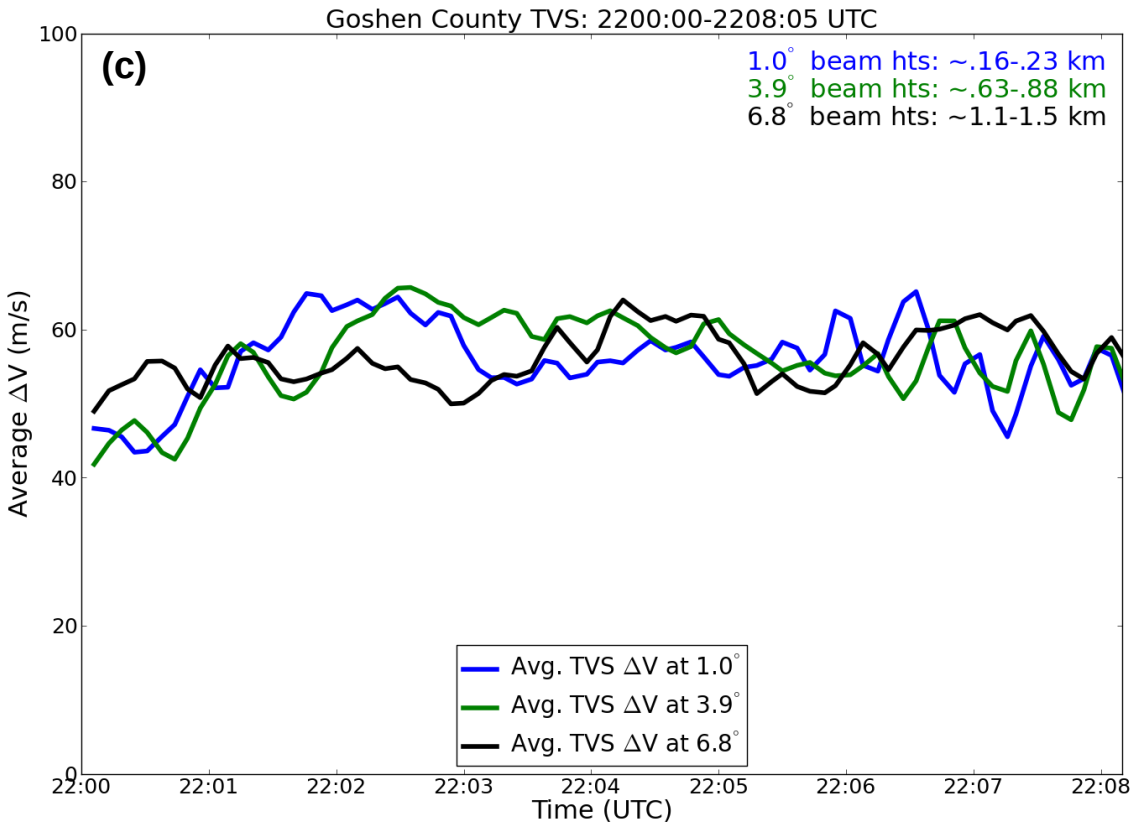

Fig. 5.57. Time series of the Goshen County TVS ΔV during the first two oscillations at (a) 12.7°, 15.6°, 18.5°, (b) 14.1°, 17.1°, 20.0°, and (c) 1.0°, 3.9°, and 6.8° elevation angle. A simple 1-2-1 filter in time was applied to smooth the curves. The approximate radar center beam heights also are provided.

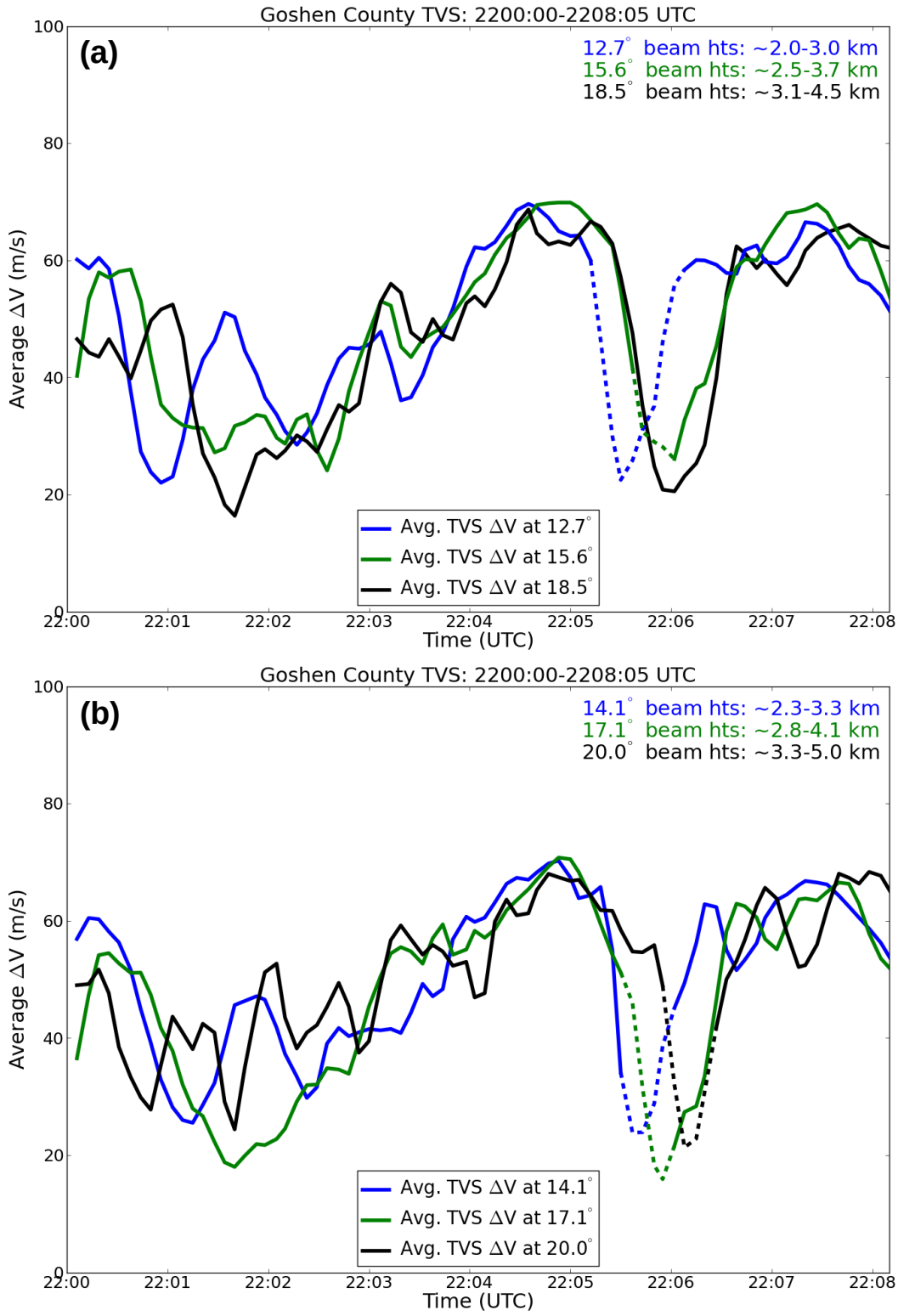

Fig. 5.58. As in Fig. 5.57, but including maximum GTG shear values (dotted lines) during times when the TVS criteria were not met.

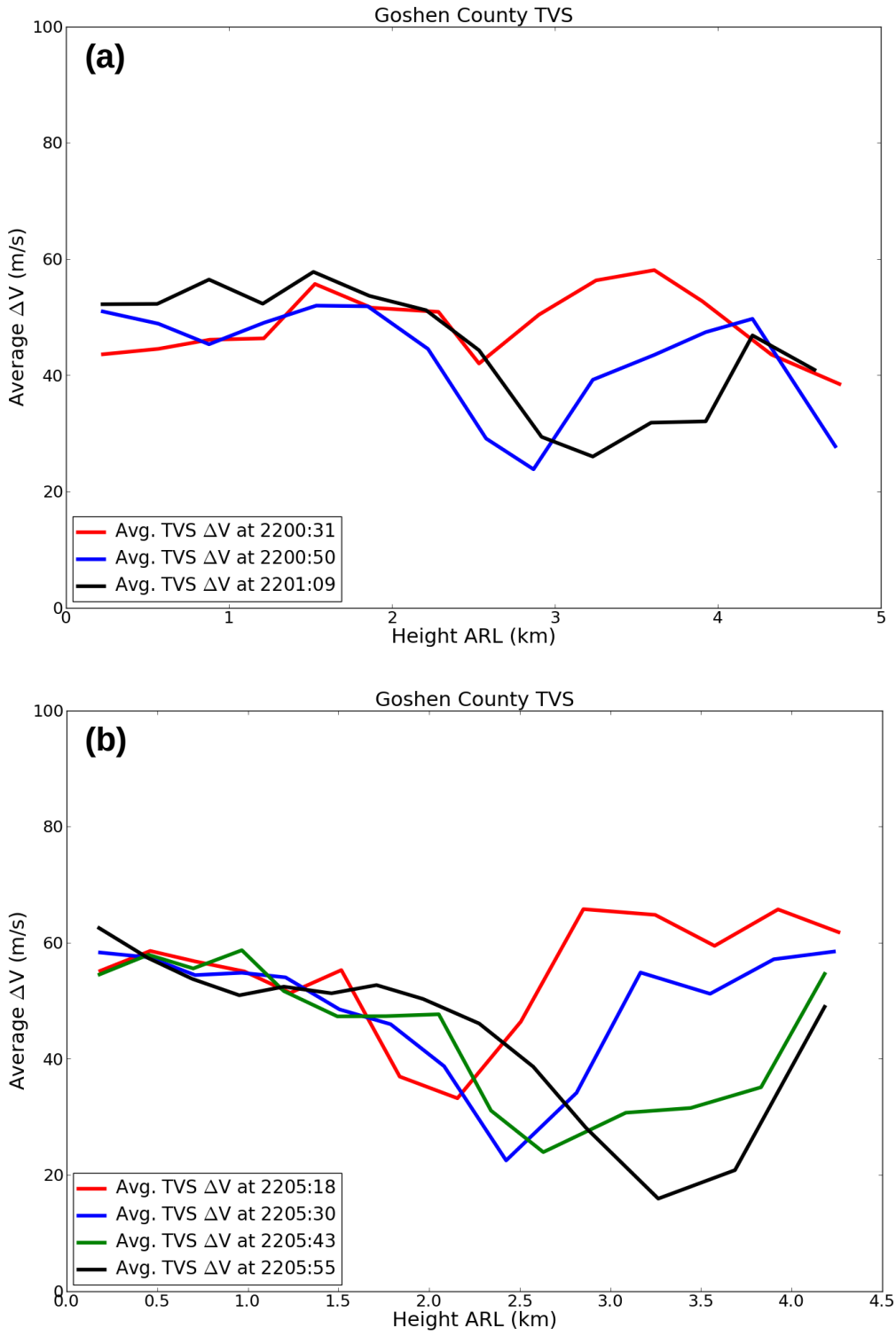

Fig. 5.59. Vertical profile of the Goshen County TVS ΔV during the (a) first and (b) second oscillation at various times. A simple 1-2-1 filter in time was applied to smooth the curves. The height scales in (a) and (b) are different.

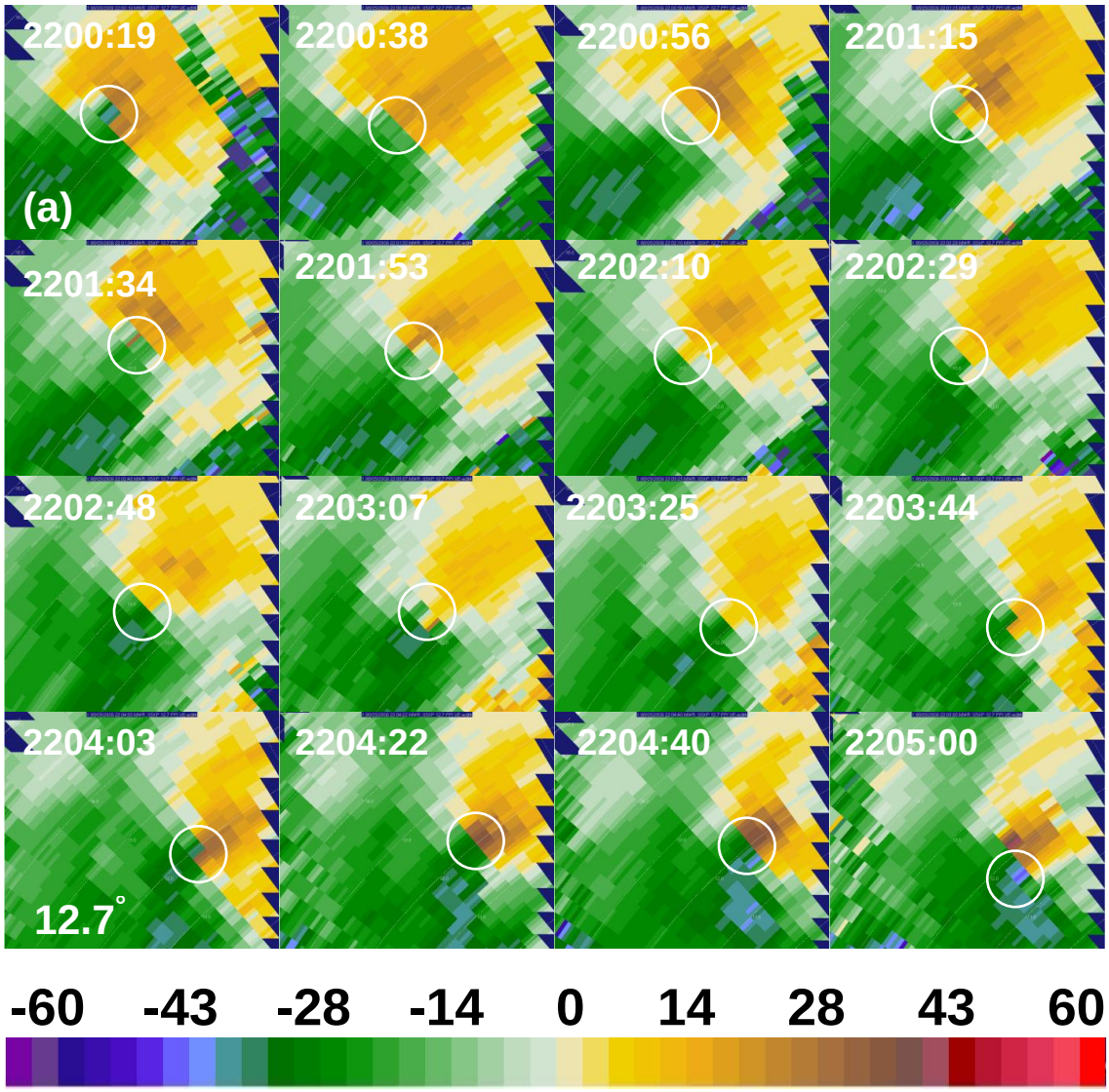

Figure 5.60. PPIs of radial velocity (m s^{-1}) every ~6.5 sec. at (a) 12.7° and (b) 20.0° elevation angle during the first ΔV oscillation in the TVS associated with the Goshen County tornado. Range rings are every 1 km. White circles enclose TVSs. Approximate heights at the center of the domain are 2900 m and 4600 m, respectively. The colorbar appears beneath the first set of images.

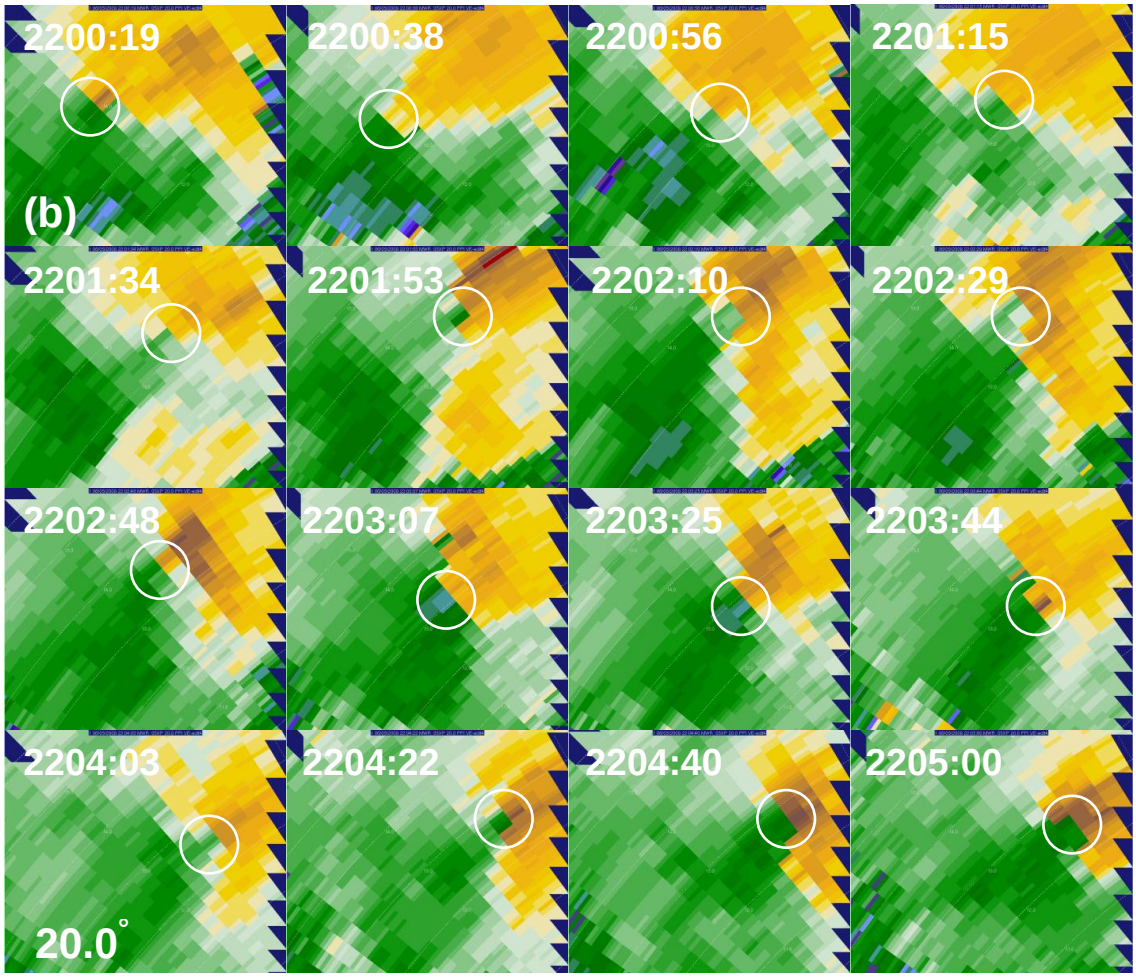
2200:19
2200:38
2200:56
2201:15
(b)
2201:34
2201:53
2202:10
2202:29
2202:48
2203:07
2203:25
2203:44
2204:03
2204:22
2204:40
2205:00
20.0°

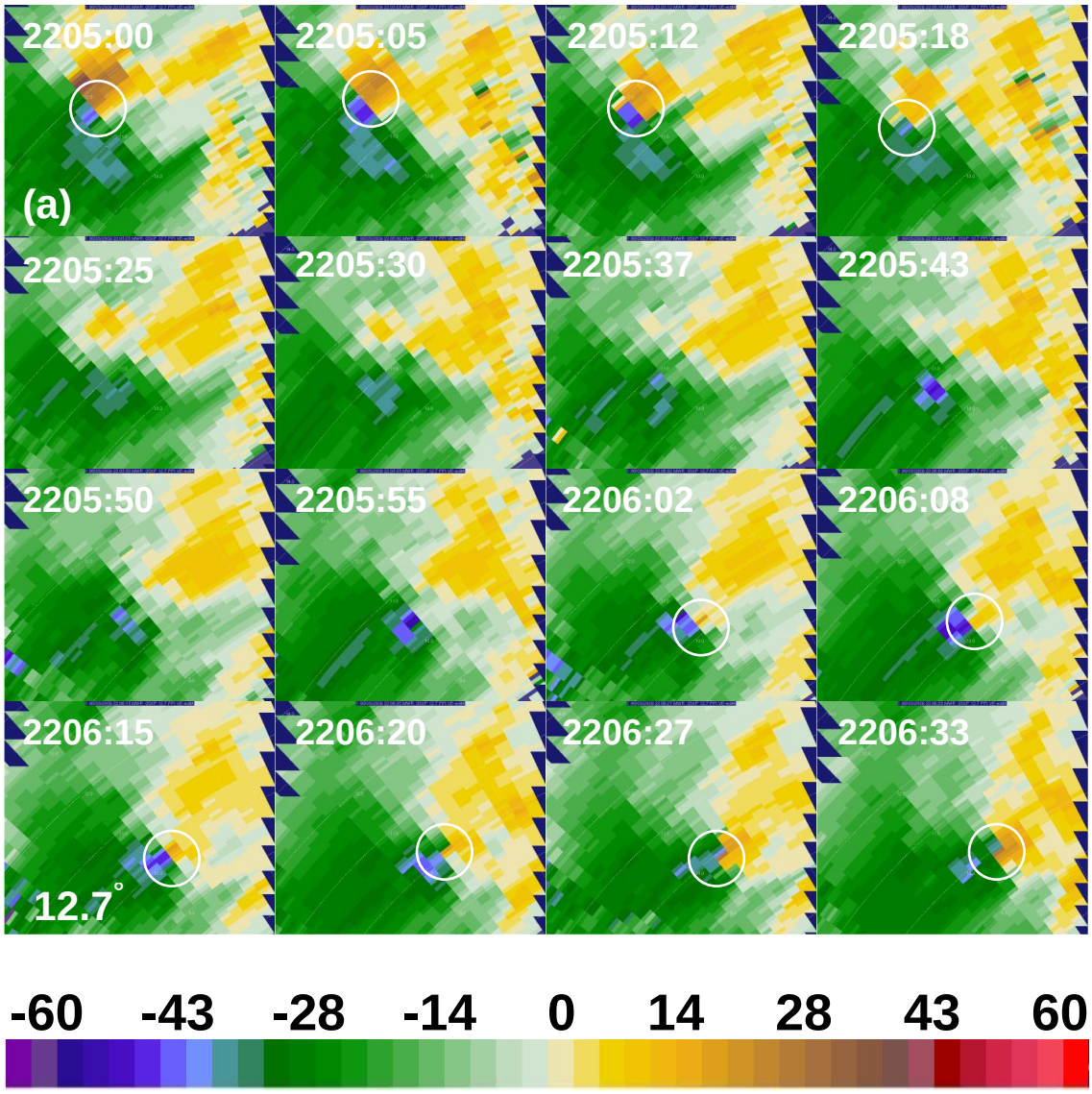

Figure 5.61. As in Fig. 5.60, but for the second ΔV oscillation of the TVS associated with the Goshen County tornado. Approximate heights at the center of the domain are 2300 m and 4000 m, respectively.

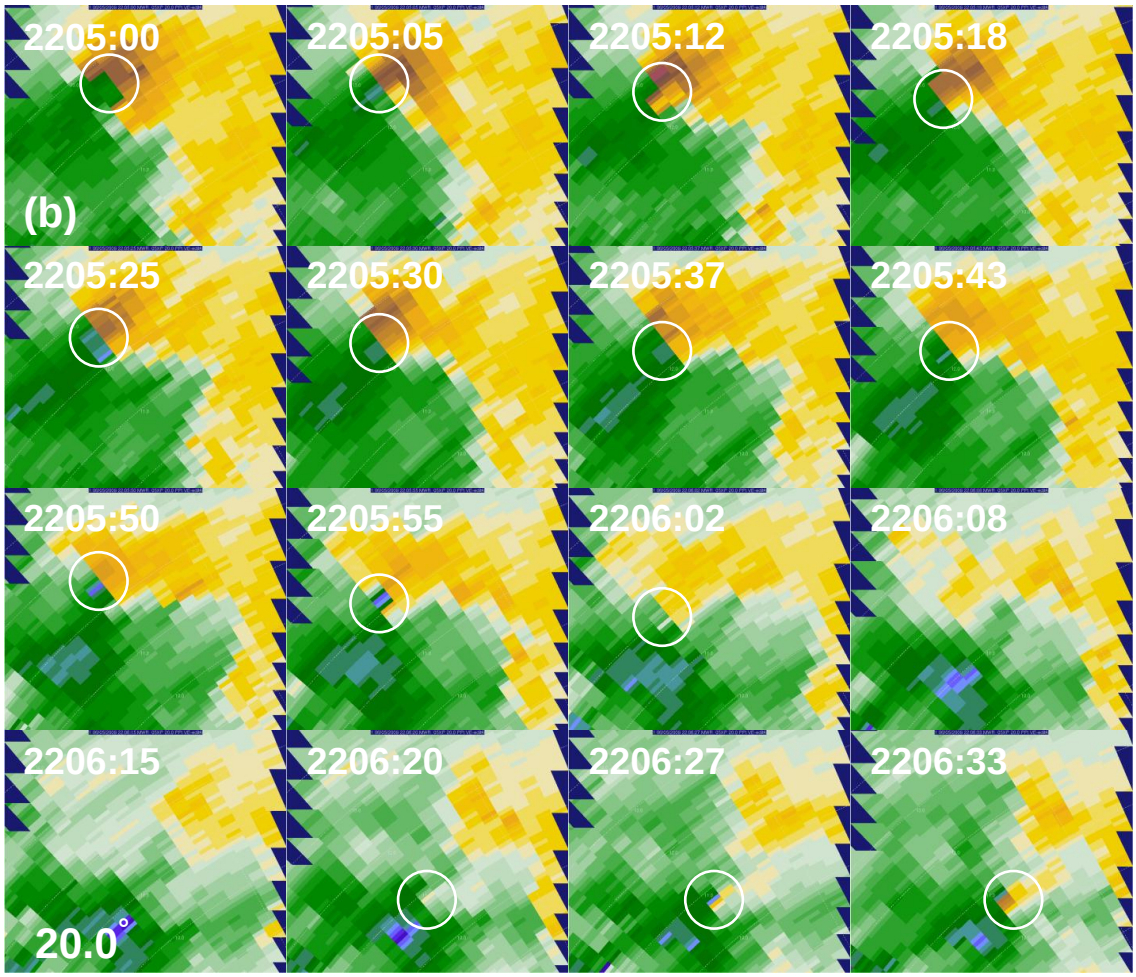
2205:00
2205:05
2205:12
2205:18
(b)
2205:25
2205:30
2205:37
2205:43
2205:50
2205:55
2206:02
2206:08
2206:15
2206:20
2206:27
2206:33
20.0°

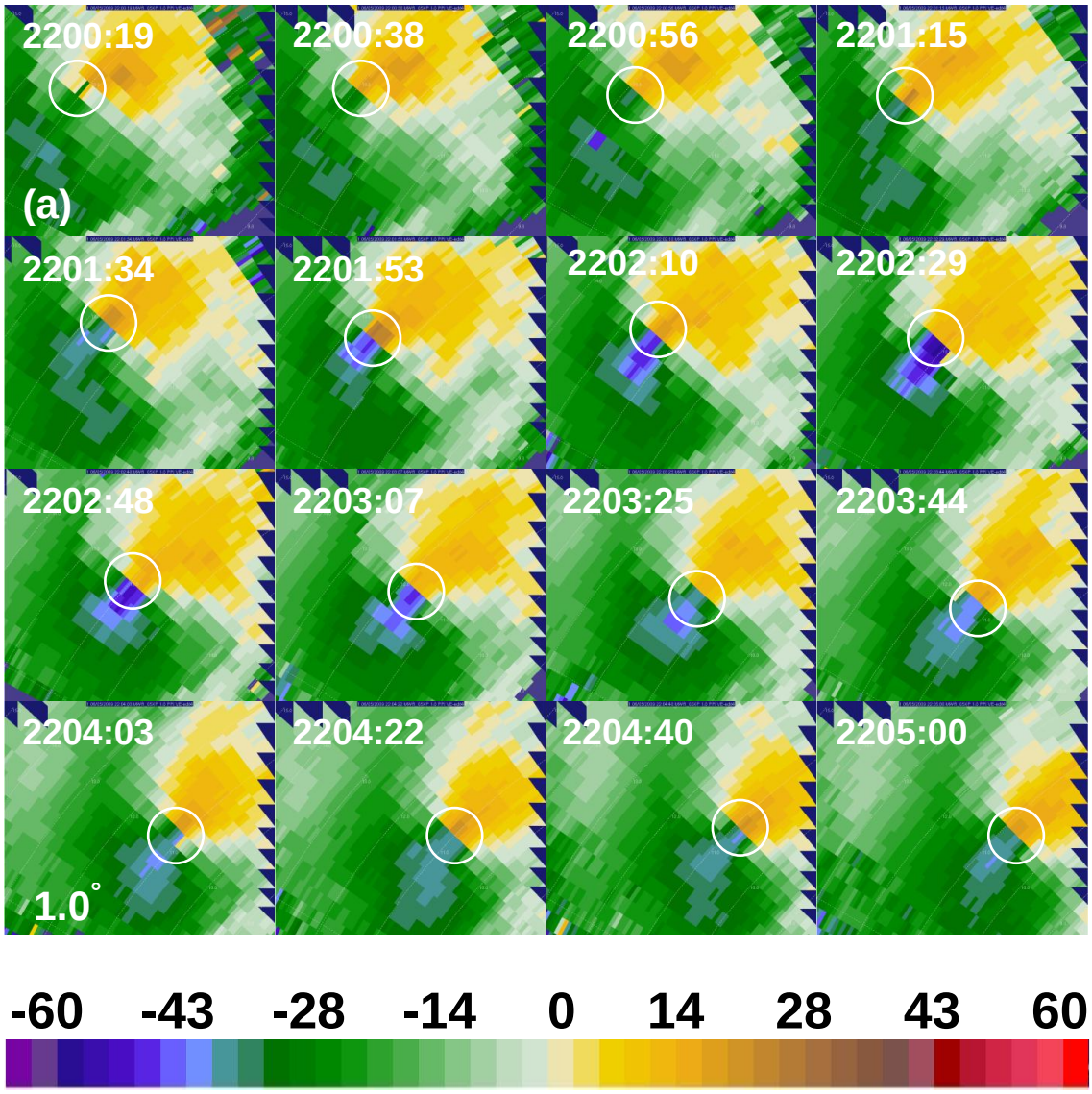

Figure 5.62. PPIs of radial velocity (m s^{-1}) every ~6.5 sec. at 1.0° elevation angle for the (a) first and (b) second ΔV oscillation of the TVS associated with the Goshen County tornado. Range rings are every 1 km. White circles enclose TVSs. Approximate heights at the center of the domain are 210 m and 175 m, respectively. The colorbar appears beneath the first set of images.

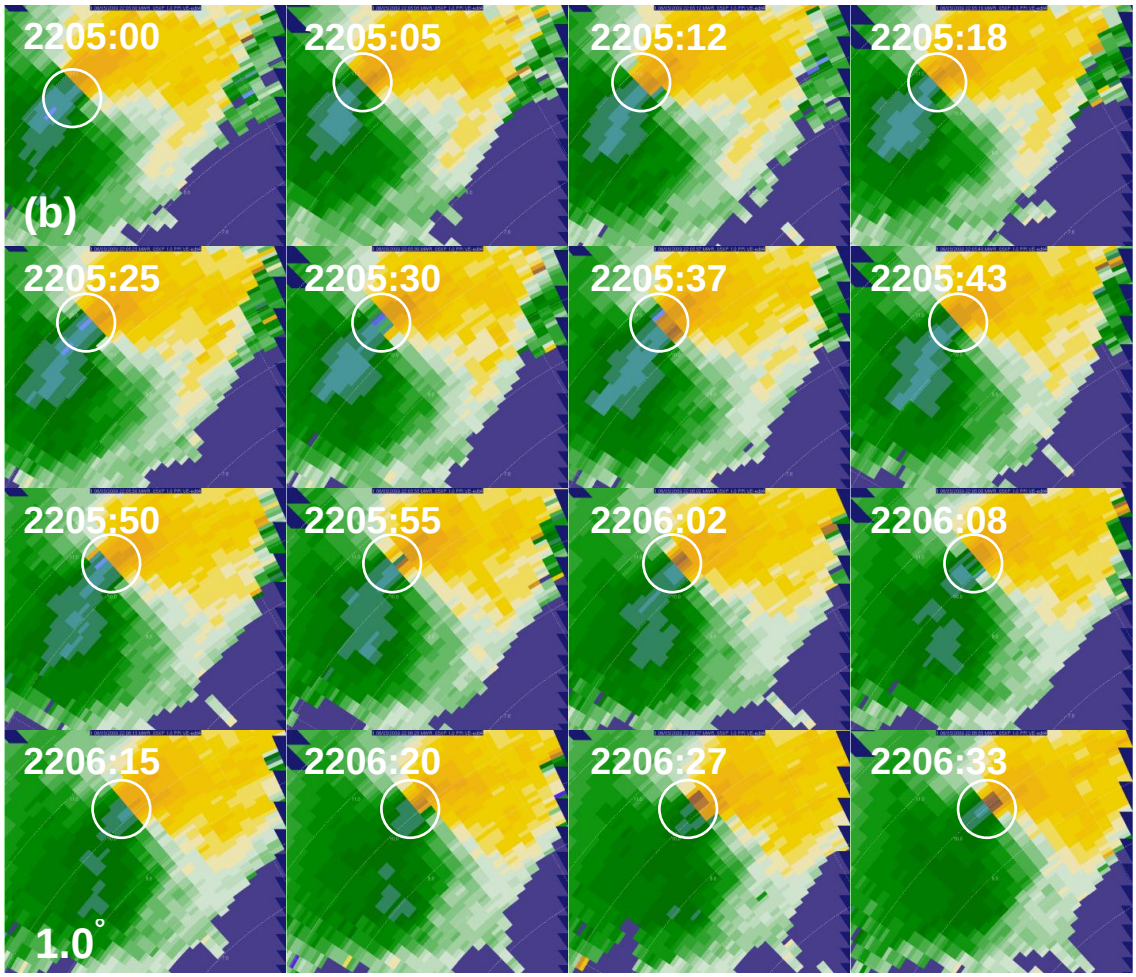
2205:00
2205:05
2205:12
2205:18
(b)
2205:25
2205:30
2205:37
2205:43
2205:50
2205:55
2206:02
2206:08
2206:15
2206:20
2206:27
2206:33
1.0°

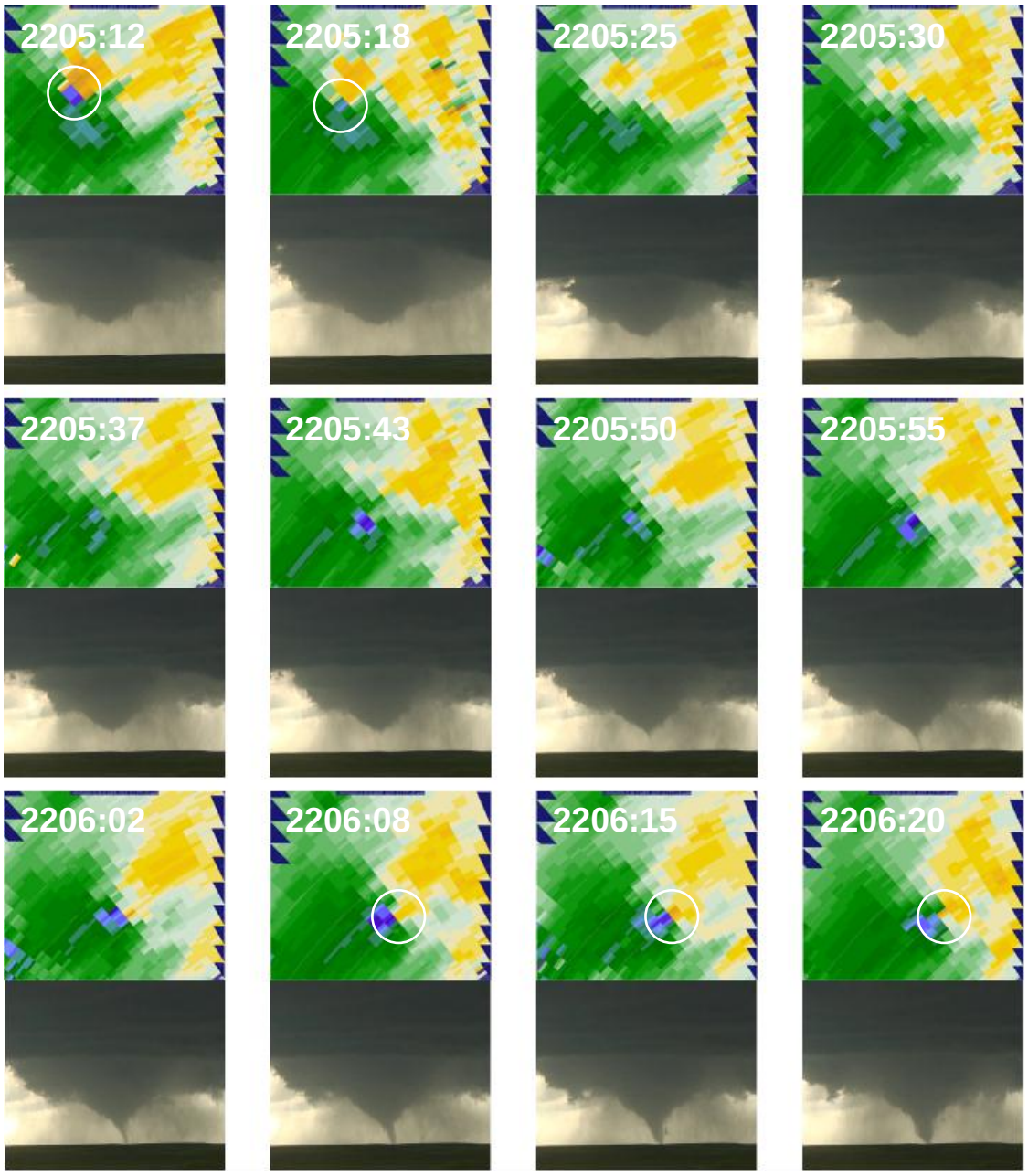

Figure 5.63. PPIs of radial velocity (m s^{-1}) at 12.7° elevation angle (top) and coincident video stills of the formation of the second and final condensation funnel in the Goshen County tornado (bottom) every ~6.5 sec. during the second ΔV oscillation. Video stills are from the Lyndon State College photogrammetry team A in VORTEX2. Range rings are every 1 km. White circles enclose TVSs. Approximate heights at the center of the domain are ~2300 m. The colorbar matches that used in Fig. 5.62.

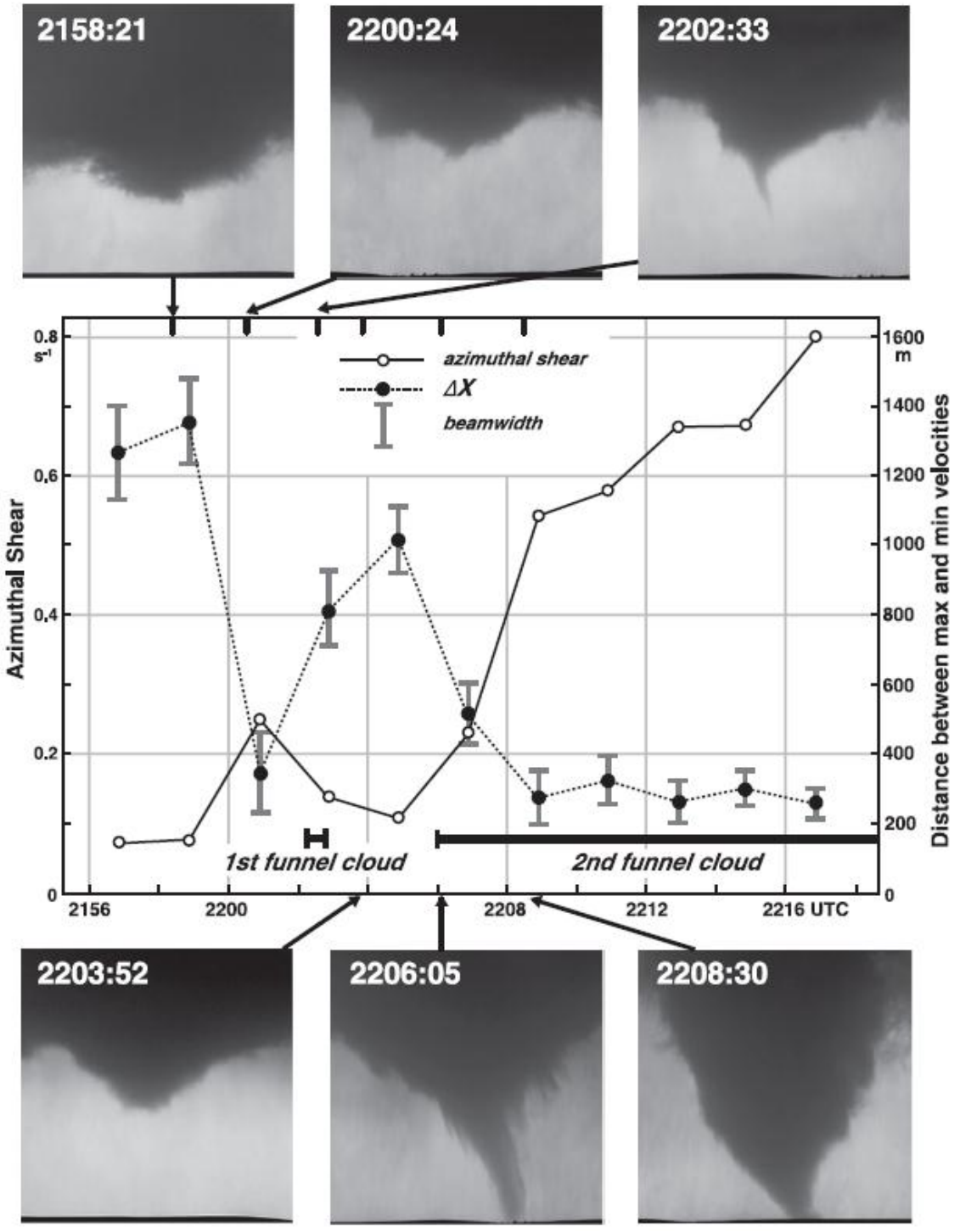
2158:21
2200:24
2202:33
azimuthal shear
ΔX
beamwidth
Azimuthal Shear
s-1
Distance between max and min velocities
m
0.8
0.6
0.4
0.2
0
1600
1400
1200
1000
800
600
400
200
0
2156
2200
2208
2212
2216 UTC
1st funnel cloud
2nd funnel cloud
2203:52
2206:05
2208:30

Figure 5.64. Time plot of azimuthal shear (black line) and distance between the maximum and minimum radial velocities (dashed line) associated with the tornado based on measurements from DOW7. The beamwidth (m) at the location of the tornado is also plotted. Photos taken from the DOW7 site are shown at 2158:21, 2200:24, 2202:33, 2203:52, 2206:05, and 2208:30 UTC. This is based on the scan at 0.5°. Times when two funnel clouds were observed are indicated. Photos were photogrammetrically enlarged or reduced so that the relative dimensions of the tornado can be estimated. From Wakimoto et al. (2011).

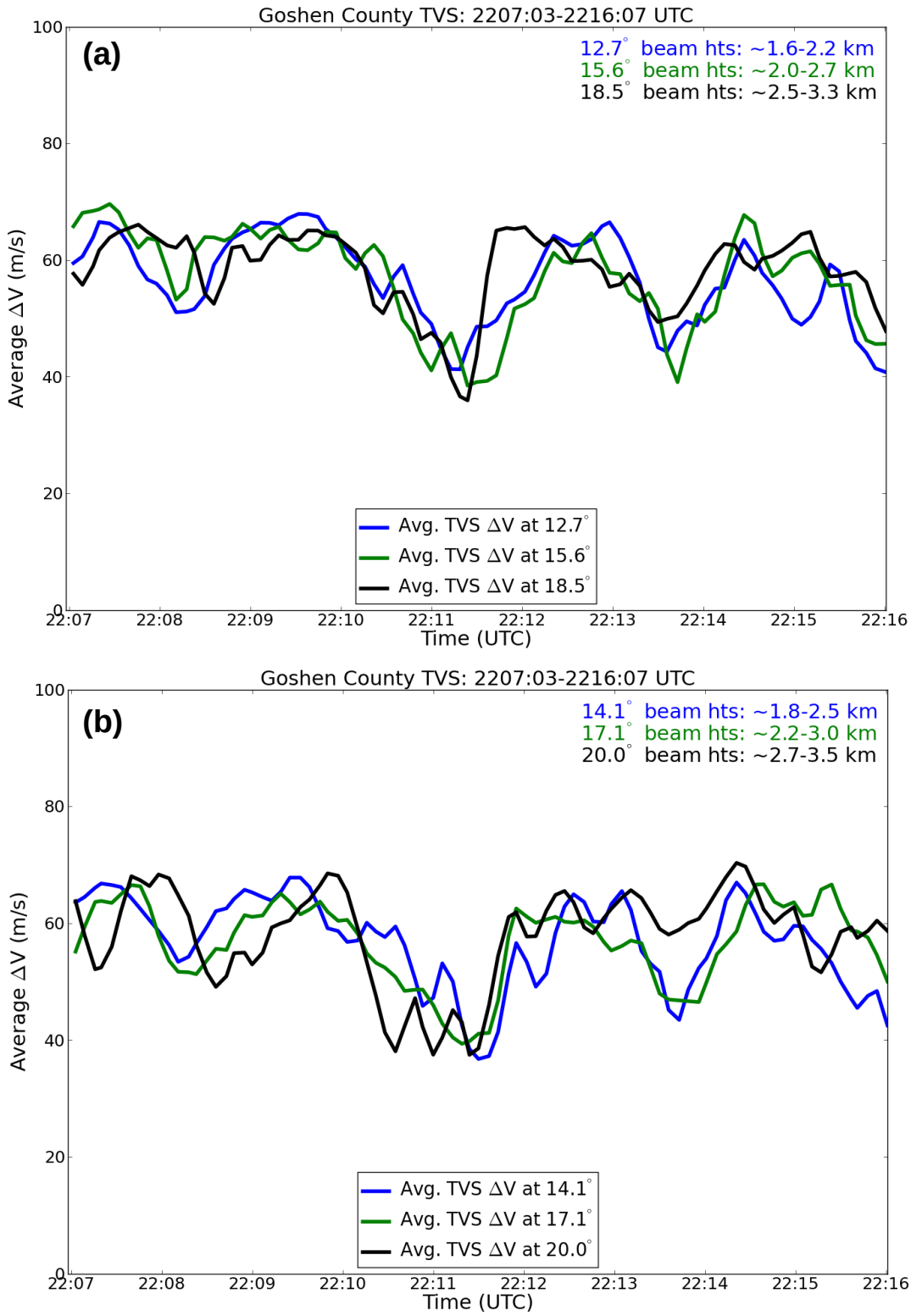

Fig. 5.65. As in Fig. 5.57, but for ΔV oscillations 3-5 in the Goshen County tornado. The low-level ΔV time series is not included for brevity.

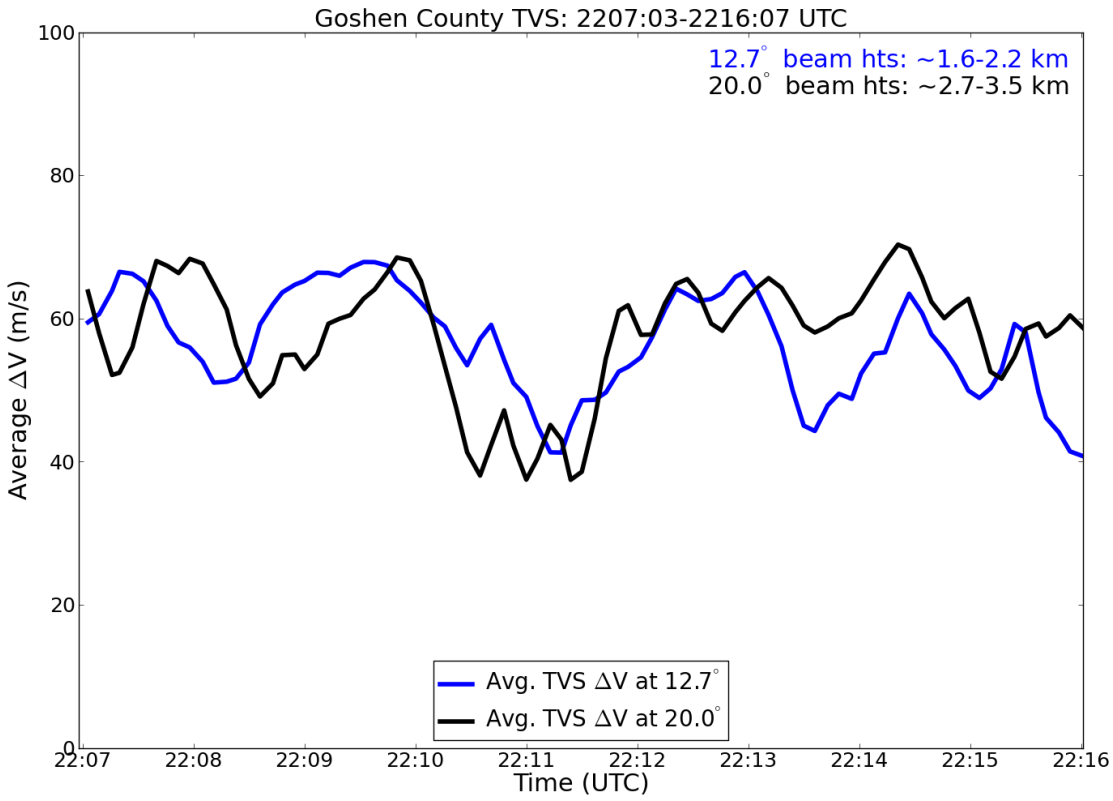

Fig. 5.66. As in Fig. 5.65, but for ΔV at 12.7° and 20.0° elevation angle.

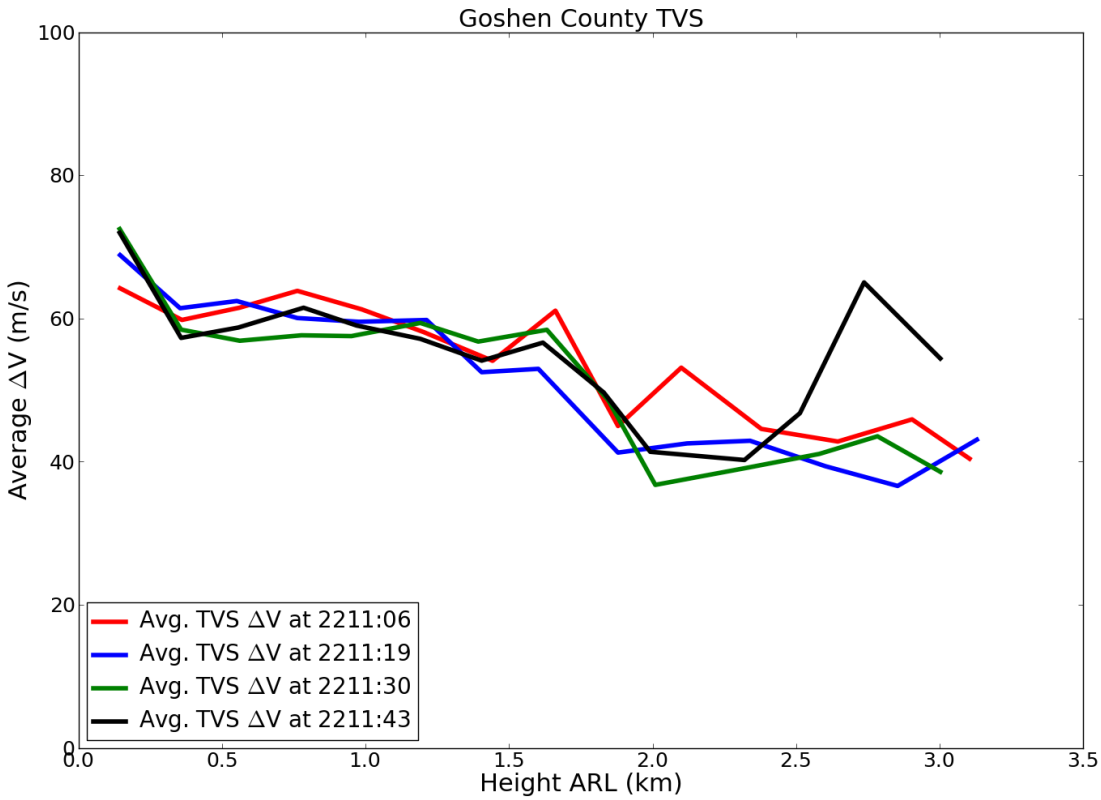

Fig. 5.67. As in Fig. 5.59, but for the fourth ΔV oscillation observed in the Goshen County tornado.

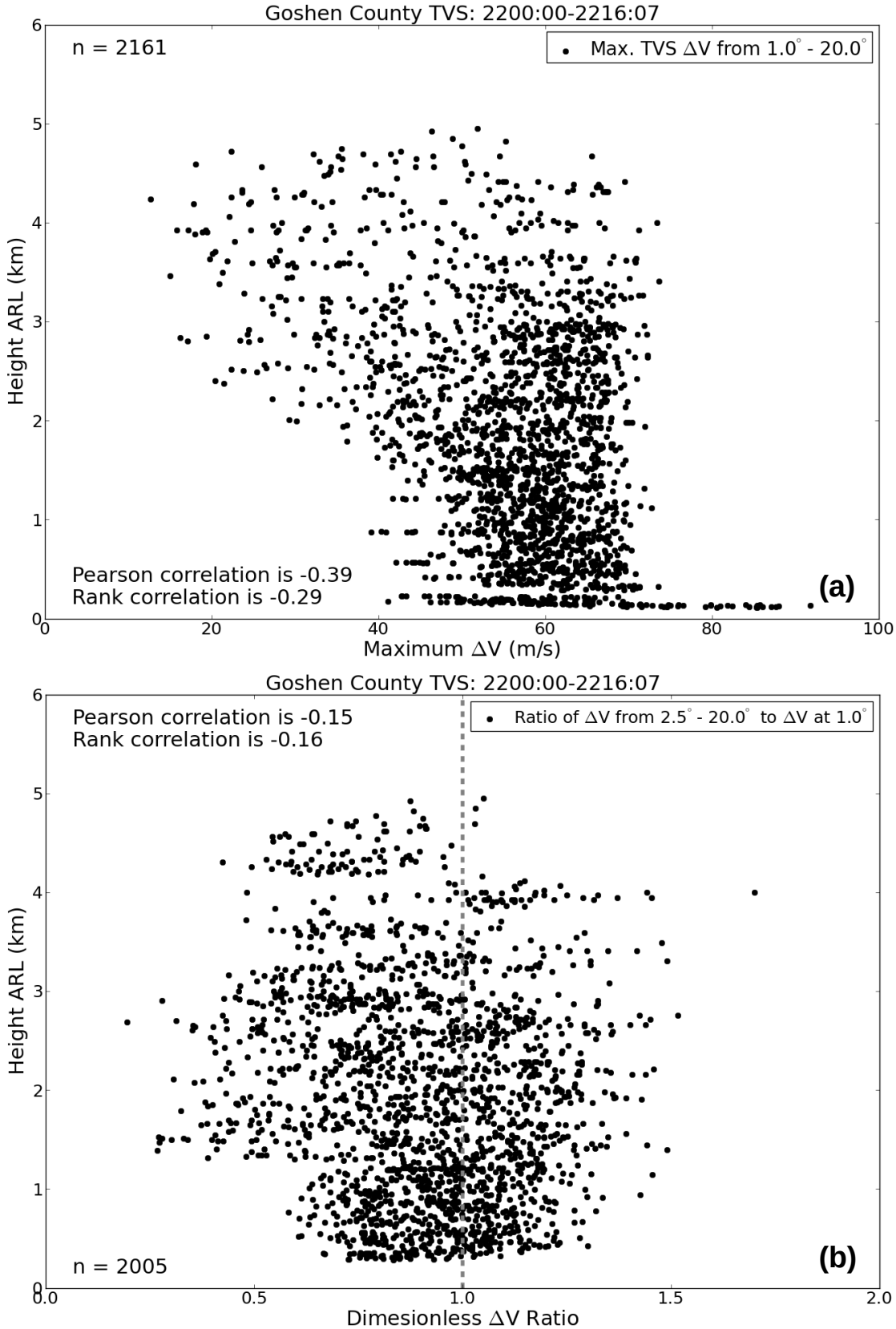

Figure 5.68. As in Fig. 5.47 but for the mature phase of the Goshen County tornado.

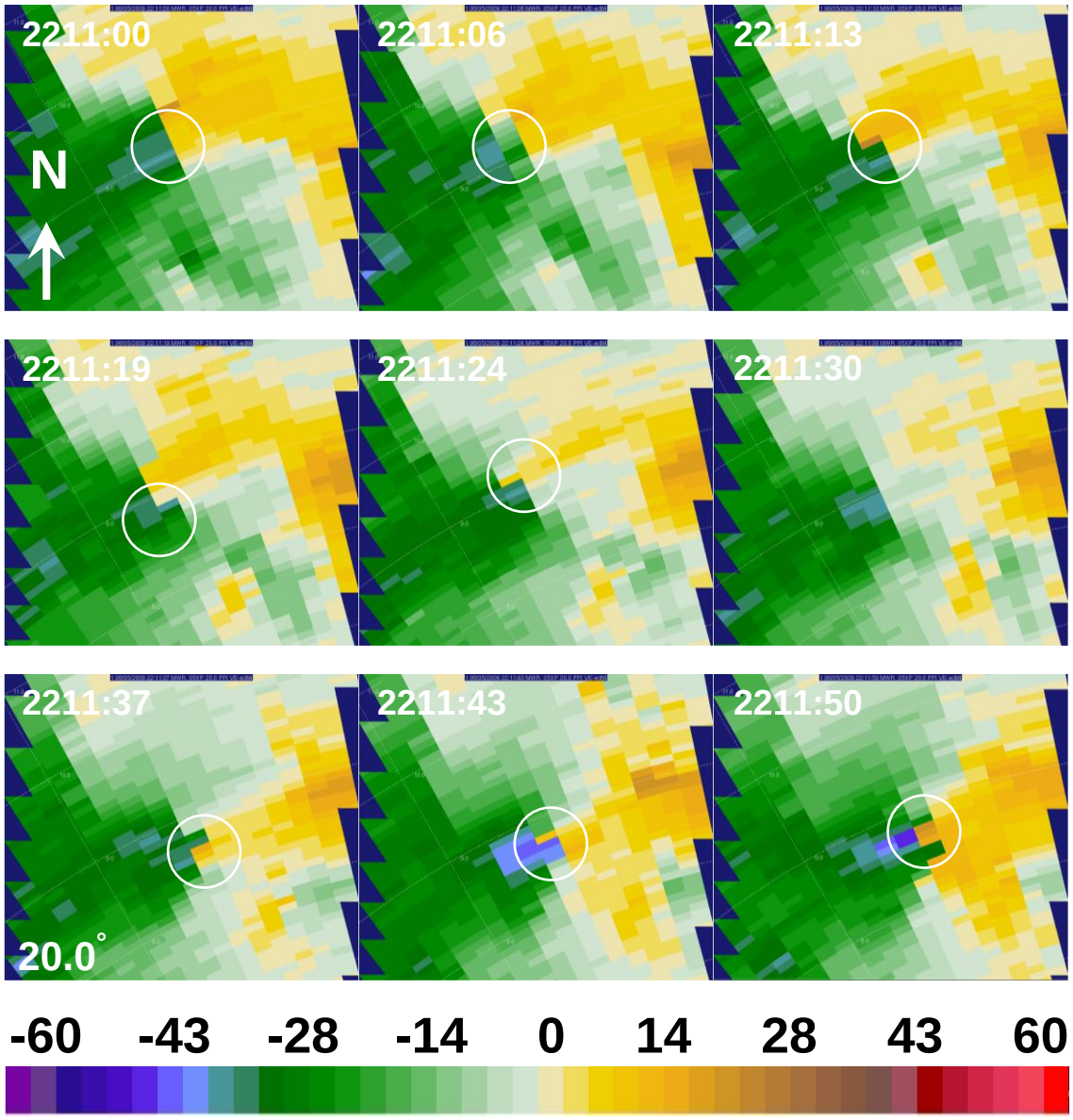

Figure 5.69. PPIs of radial velocity (m s^{-1}) every ~6.5 sec. at 20.0° elevation angle during the fourth ΔV oscillation in the TVS associated with the Goshen County tornado. Range rings are every 1 km. White circles enclose TVSs. The approximate height at the center of the domain is 3100 m. The radial velocity colorbar appears beneath the figure.

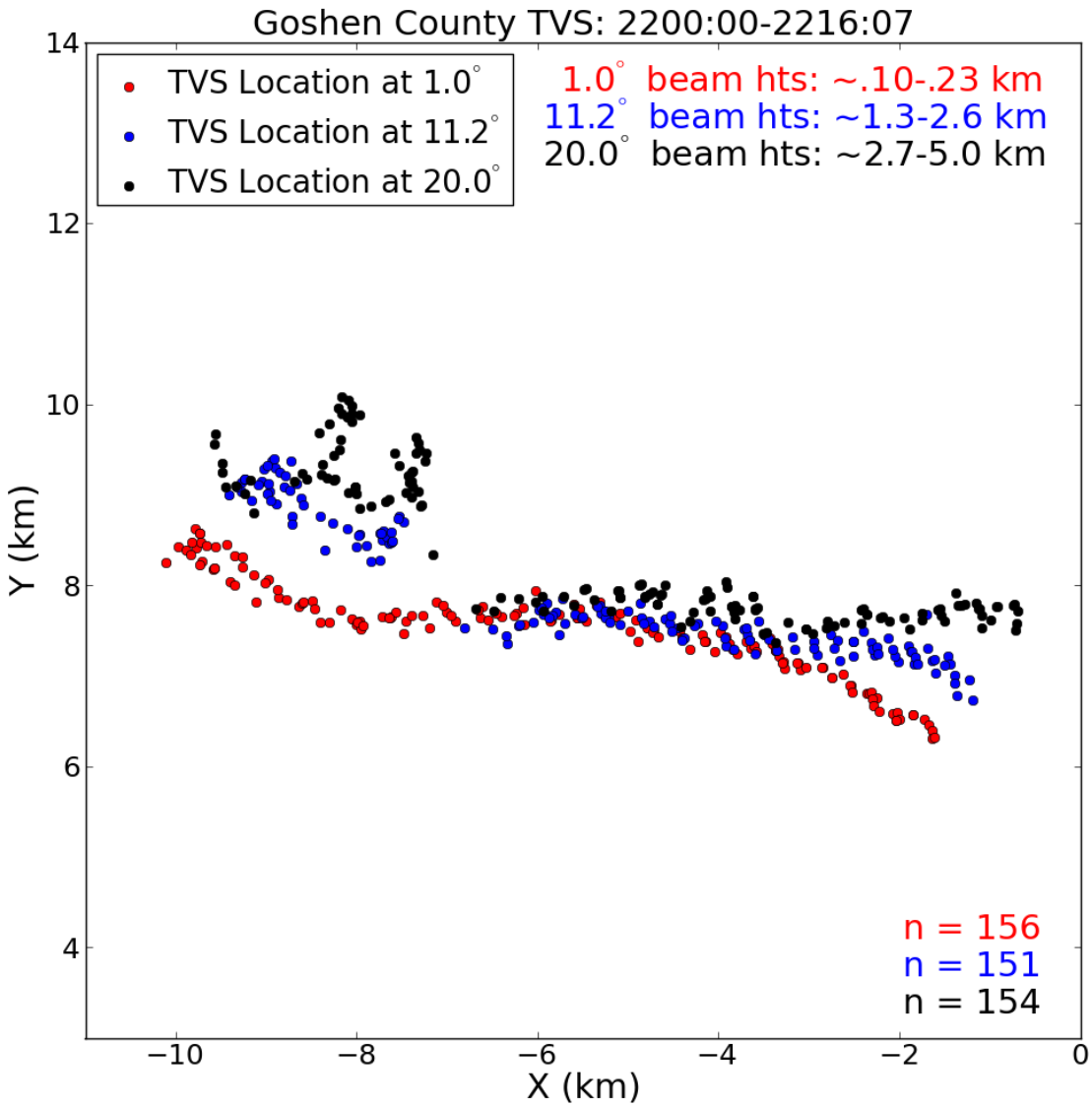

Figure 5.70. As in Fig. 5.48, but for the mature phase of the Goshen County tornado.

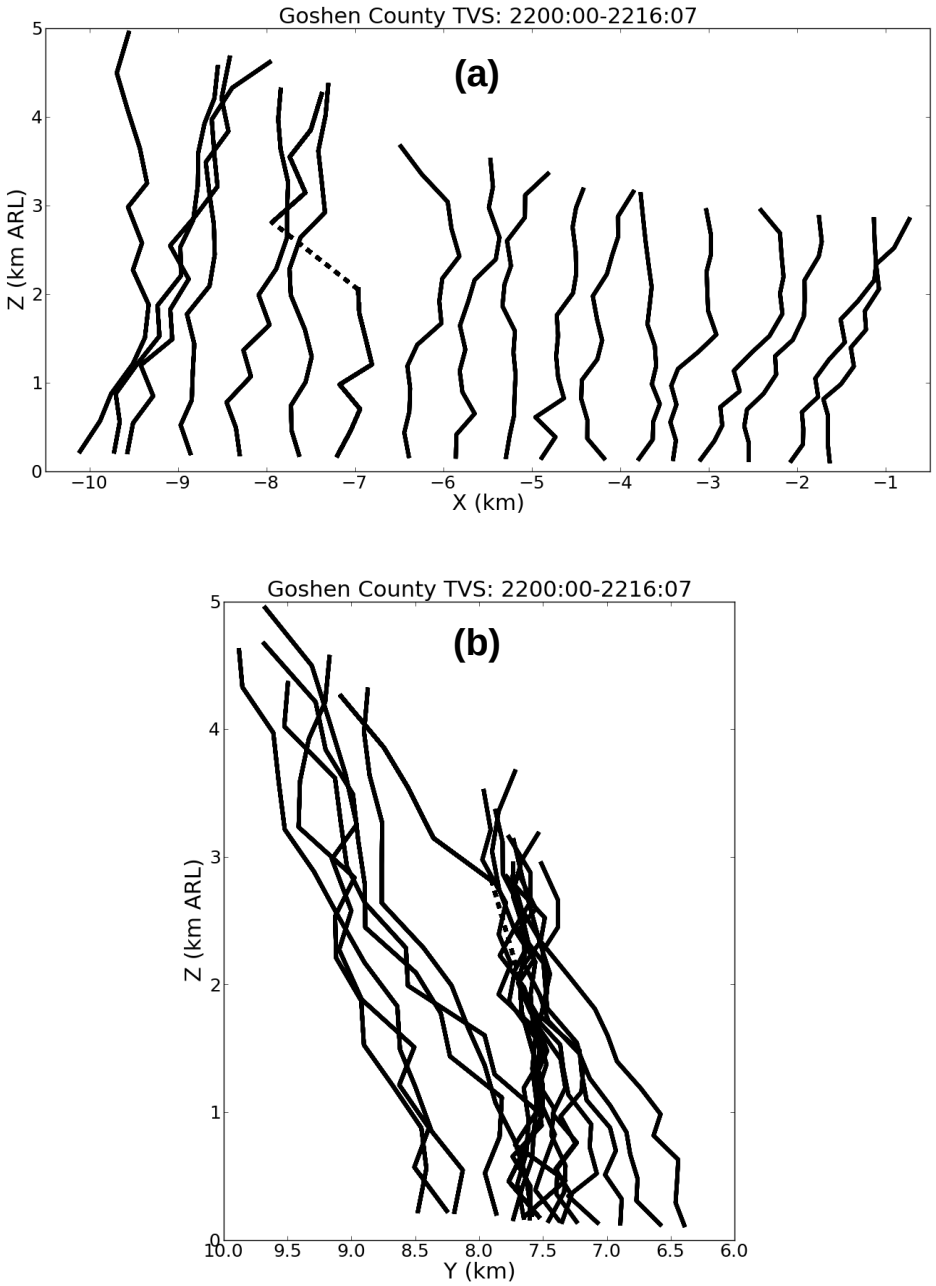

Fig. 5.71. Vertical cross sections of the Goshen County TVS position in an (a) x-z and (b) y-z reference frame every ~55 sec. during its mature phase. In both (a) and (b), the tornado generally is moving from left to right (west to east and north to south). The dotted line indicates locations where the TVS was not identified. The MWR-05XP is located at the origin (not shown) and the grid is not stretched. The times shown for (a) and (b) are the same.

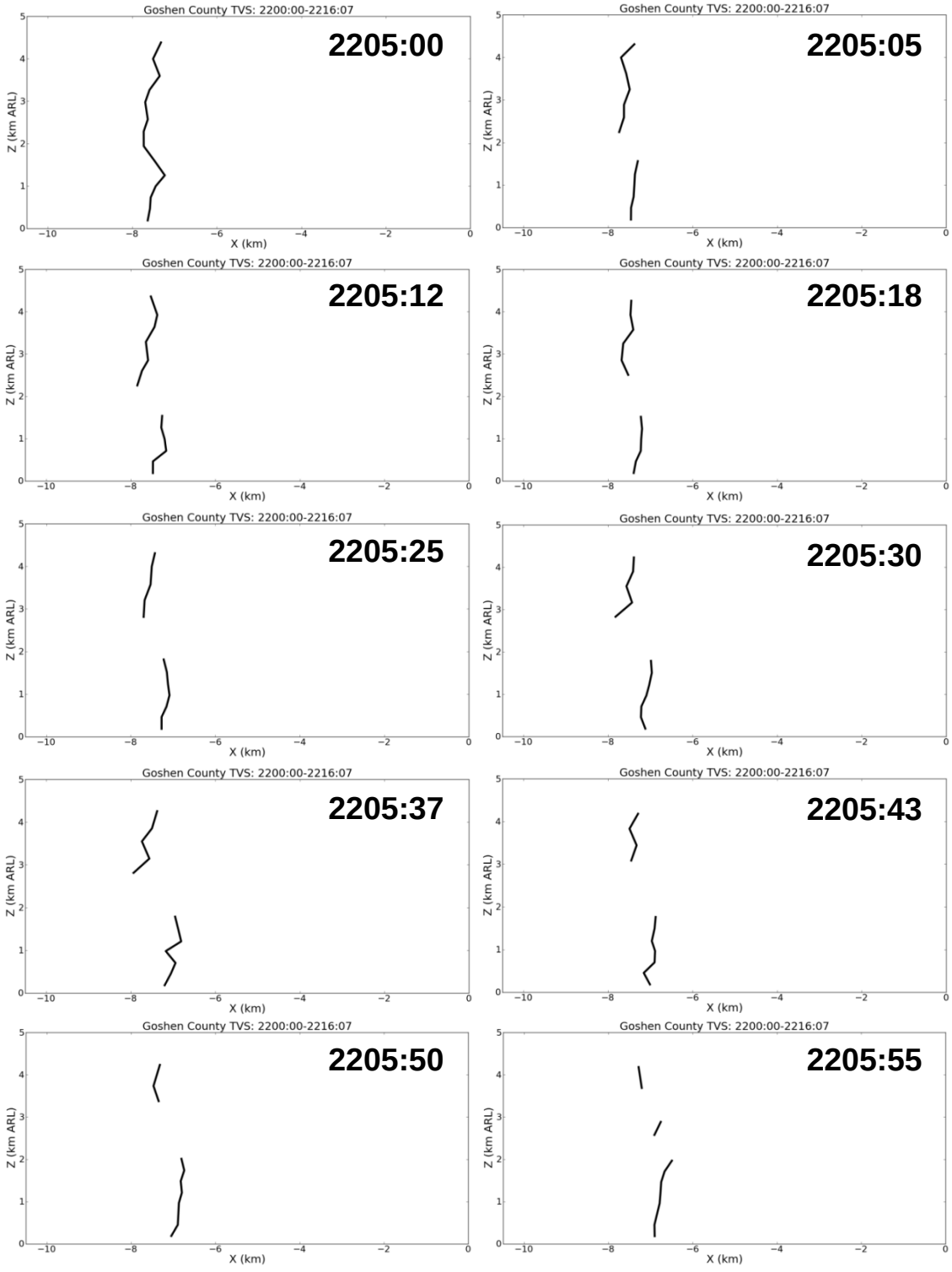
Goshen County TVS: 2200:00-2216:07
2205:00
2205:05
2205:12
2205:18
2205:25
2205:30
2205:37
2205:43
2205:50
2205:55
Z (km ARL)
X (km)

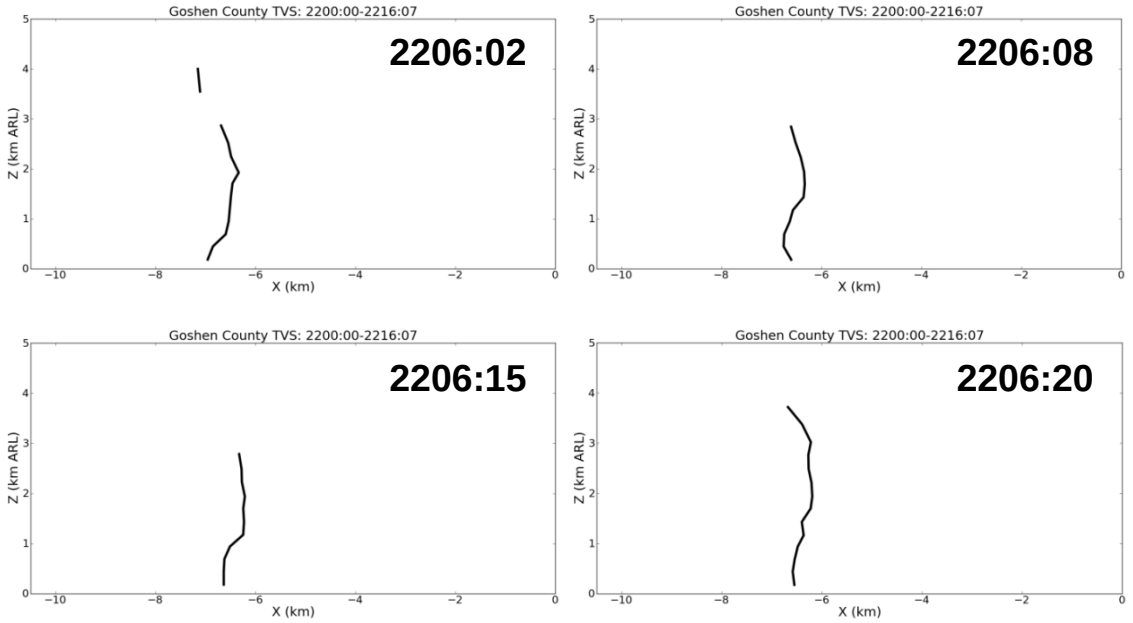

Figure 5.72. Vertical cross sections of the Goshen County TVS position in an x-z reference frame every ~6.5 sec. during the mature phase dissipation. The MWR-05XP is located at the origin (not shown). The grid is not stretched and from left to right (bottom to top) extends 10.5 (5) km to the east (upward) in the x (z) direction.

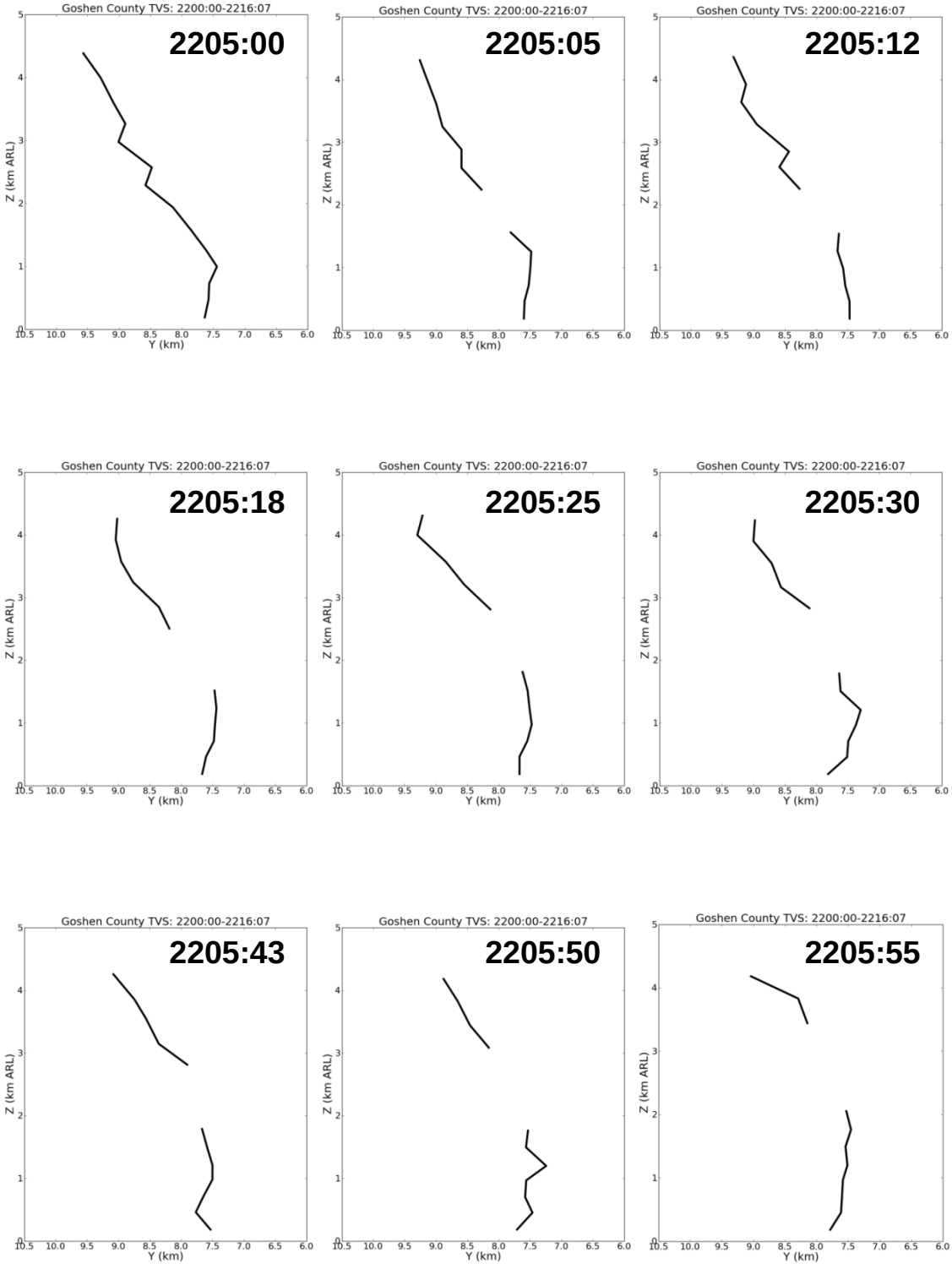
Goshen County TVS: 2200:00-2216:07
2205:00
2205:05
2205:12
2205:18
2205:25
2205:30
2205:43
2205:50
2205:55
Z (km ARL)
Y (km)

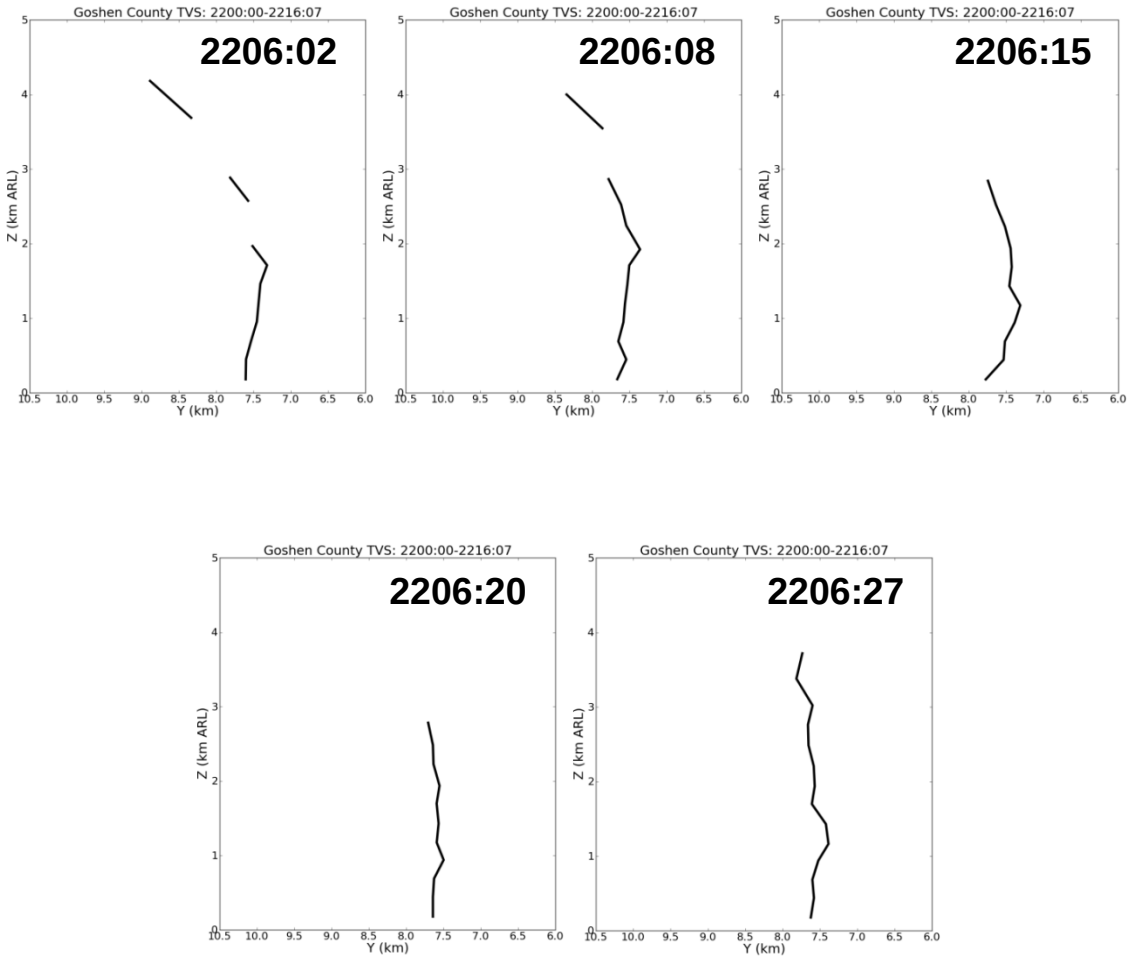

Figure 5.73. Vertical cross sections of the Goshen County TVS position in a y-z reference frame every ~6.5 sec. during the mature phase dissipation. The MWR-05XP is located at the origin (not shown). The grid is not stretched and from left to right (bottom to top) extends 4.5 (5) km to the south (upward) in the y (z) direction.

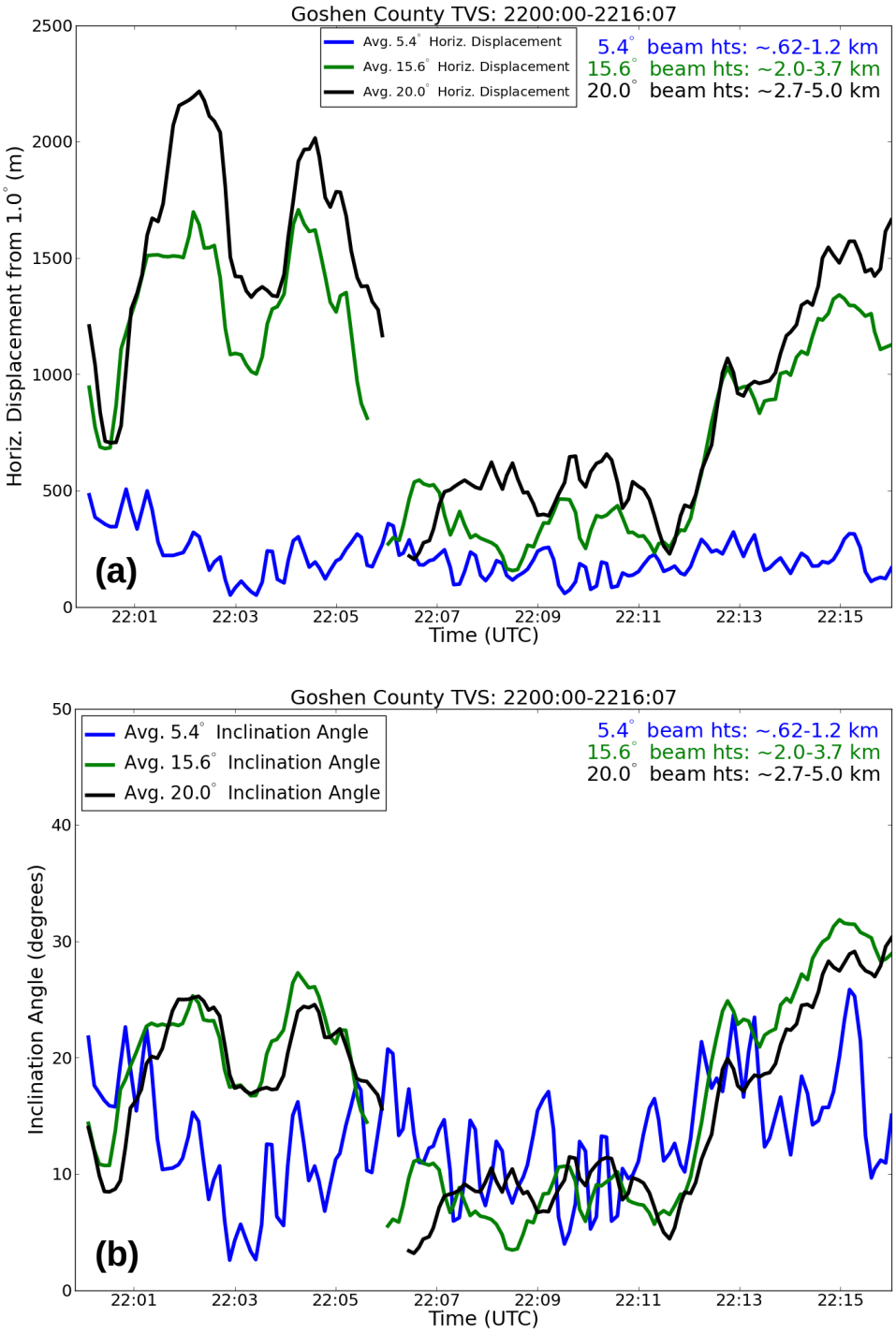

Figure 5.74. The Goshen County TVS (a) horizontal displacement (b) inclination angle at 5.4°, 15.6°, and 20.0° elevation angle during the mature phase of the tornado. A simple 1-2-1 time filter was employed to smooth the time series. The approximate radar center beam heights also are provided.

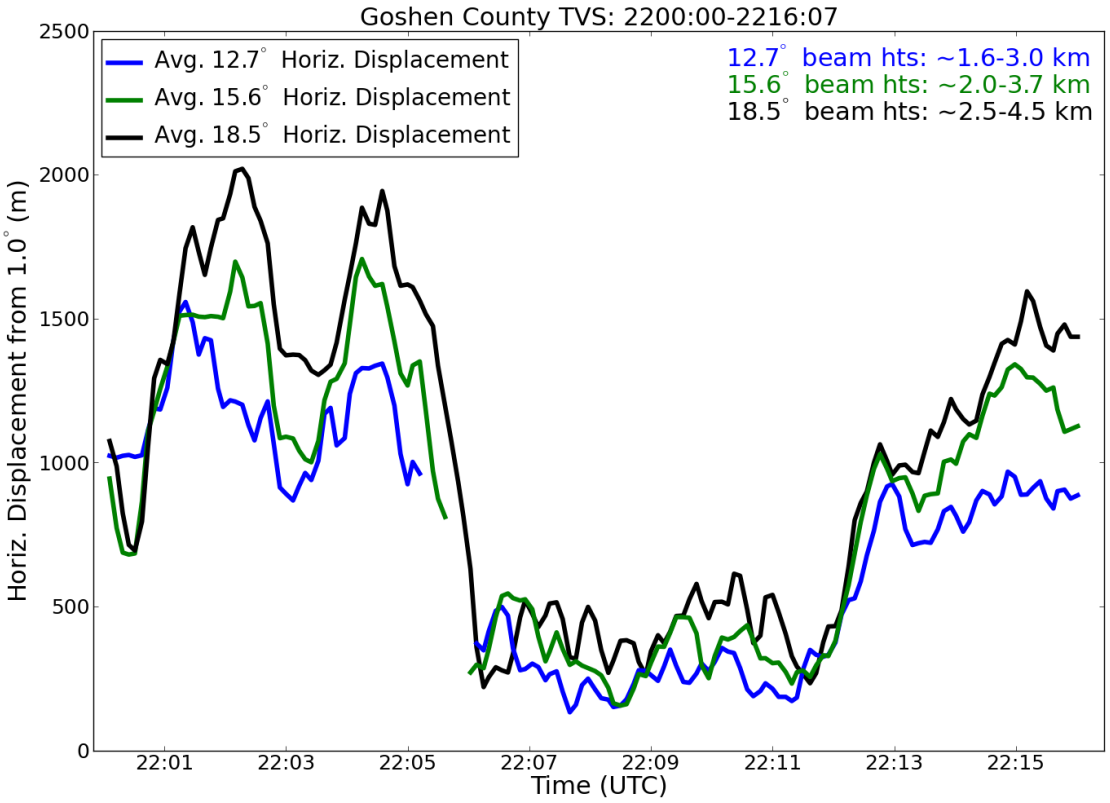

Figure 5.75. The Goshen County TVS horizontal displacement at 12.7°, 15.6°, and 18.5° elevation angle during the mature phase of the tornado. A simple 1-2-1 time filter was employed to smooth the time series. The approximate radar center beam heights also are provided.

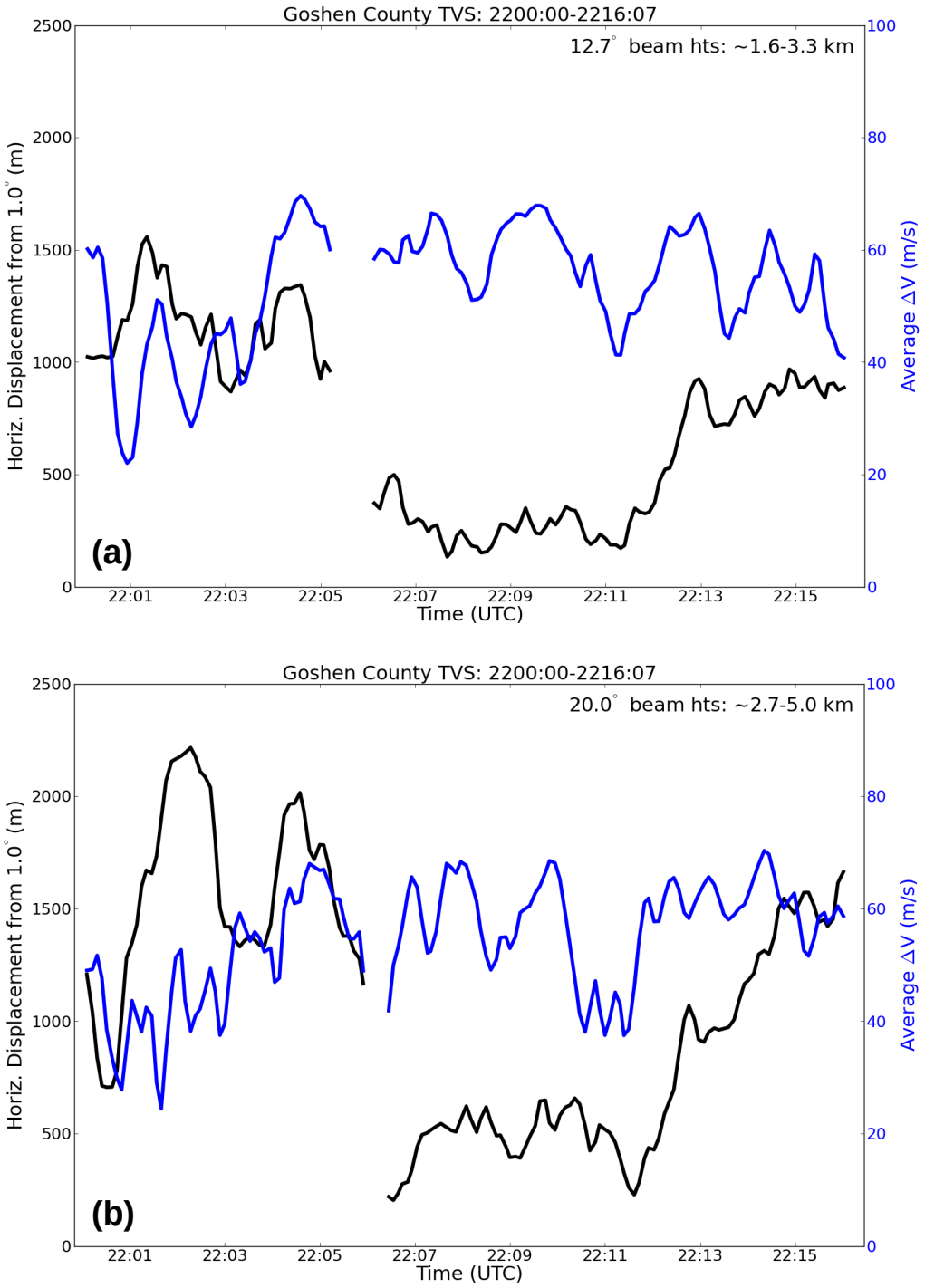

Figure 5.76. The Goshen County TVS horizontal displacement and average ΔV at (a) 12.7°, and (b) 20.0° elevation angle during the mature phase of the tornado. A simple 1-2-1 time filter was employed to smooth both time series. The approximate radar center beam heights also are provided.

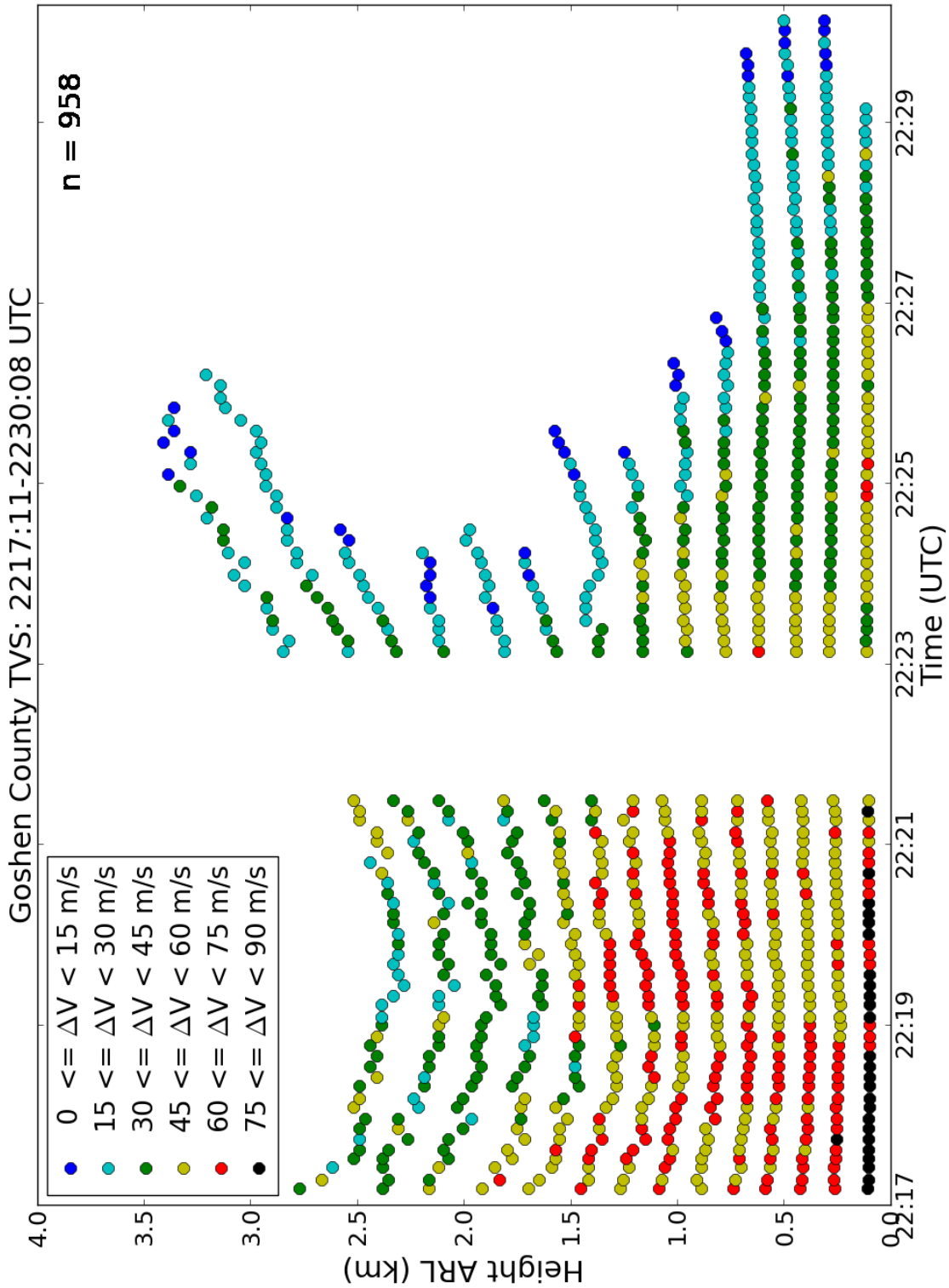

Fig. 5.77. As in Fig. 5.45, but for the tornado dissipation phase. Missing TVS markers at ~2222 UTC are from a gap in MWR-05XP data collection.

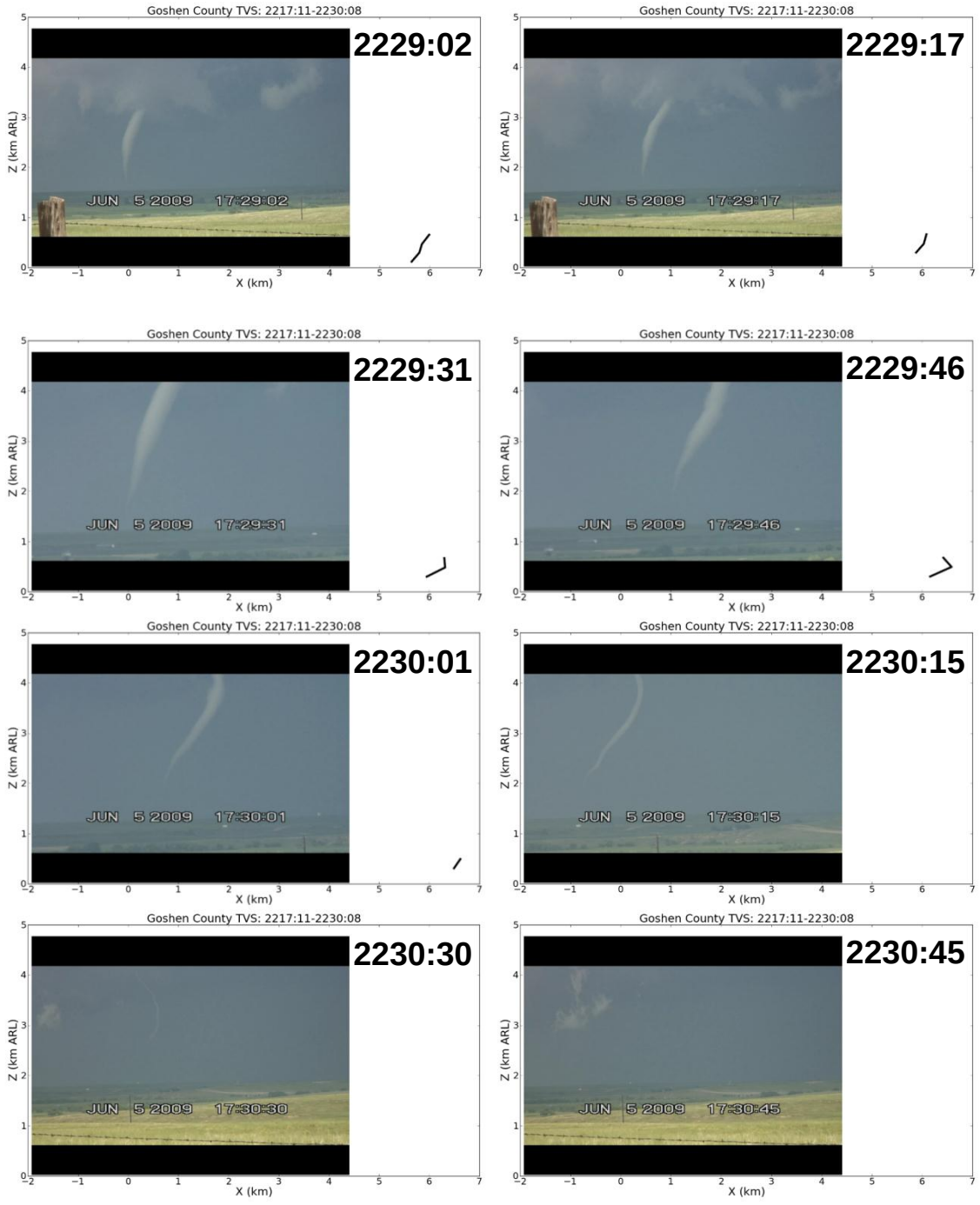

Figure 5.78. East-west vertical cross section of TVS position overlaid with still images from photogrammetry video taken by Lyndon State College team B during the Goshen County tornado dissipation phase.

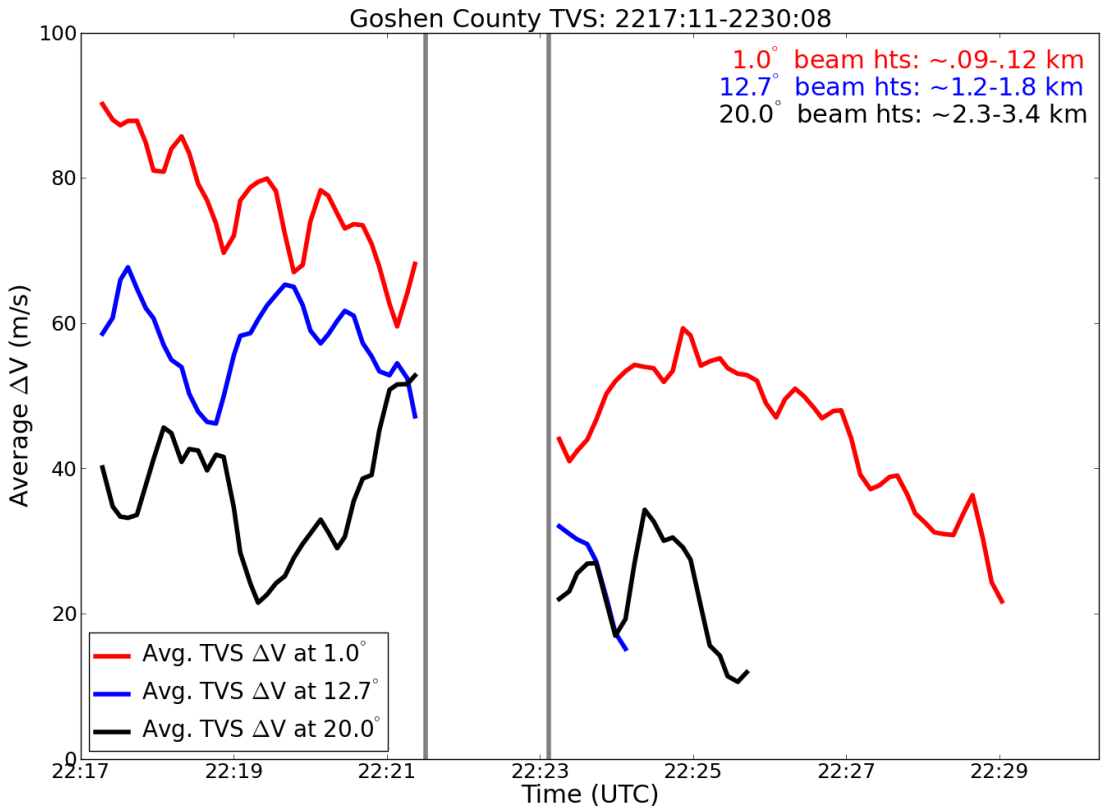

Figure 5.79. Time series of the Goshen County TVS ΔV during the dissipation phase at (a) 1.0°, 12.7°, and 20.0° elevation angle. A simple 1-2-1 filter in time was applied to smooth the curves. The gray lines enclose the times of a MWR-05XP data gap. The approximate radar center beam heights also are provided.

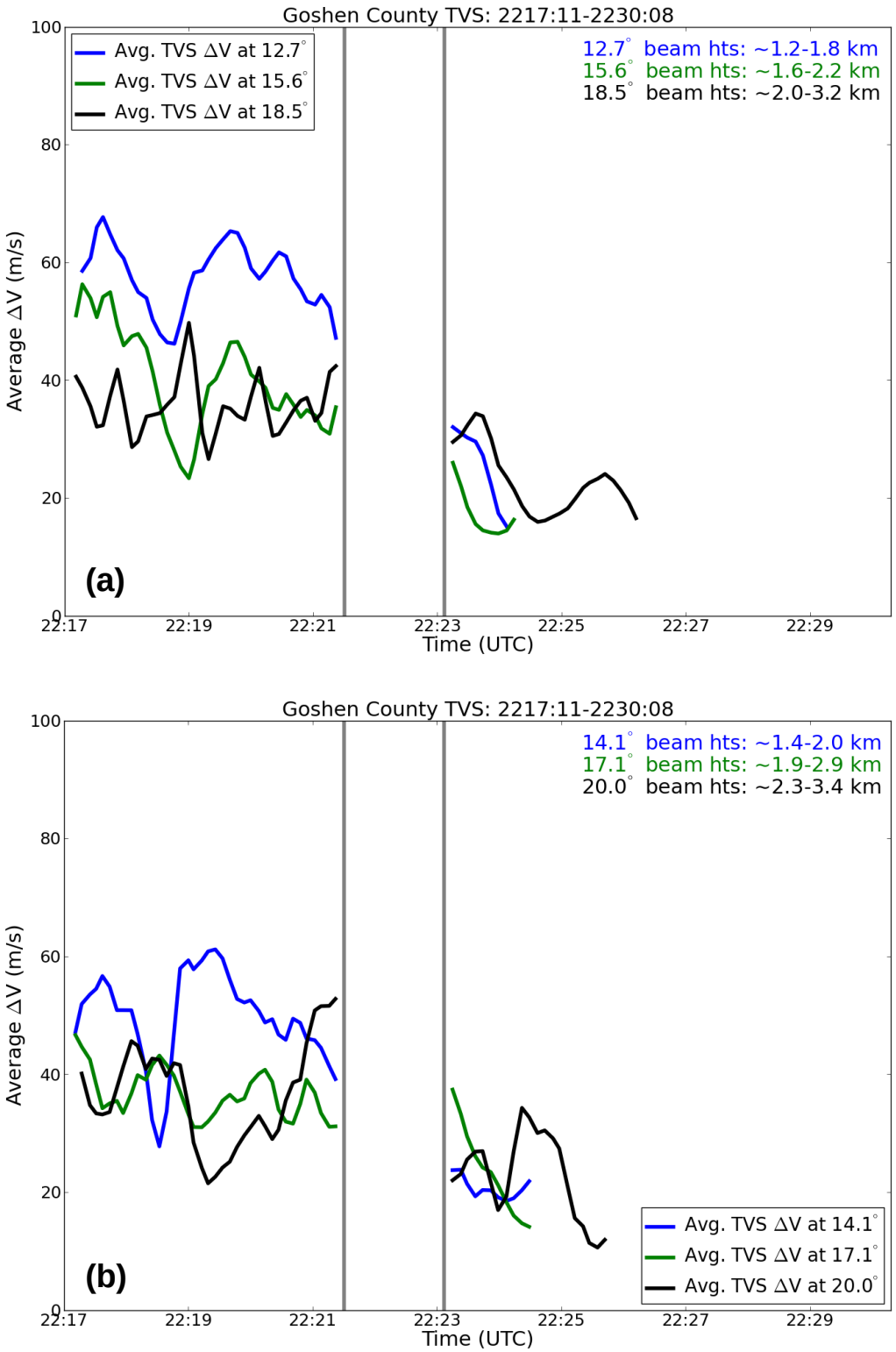

Figure 5.80. As in Fig. 5.79, but at (a) 12.7°, 15.6° and 18.5° and (b) 14.1°, 17.1°, and 20.0° elevation angle.

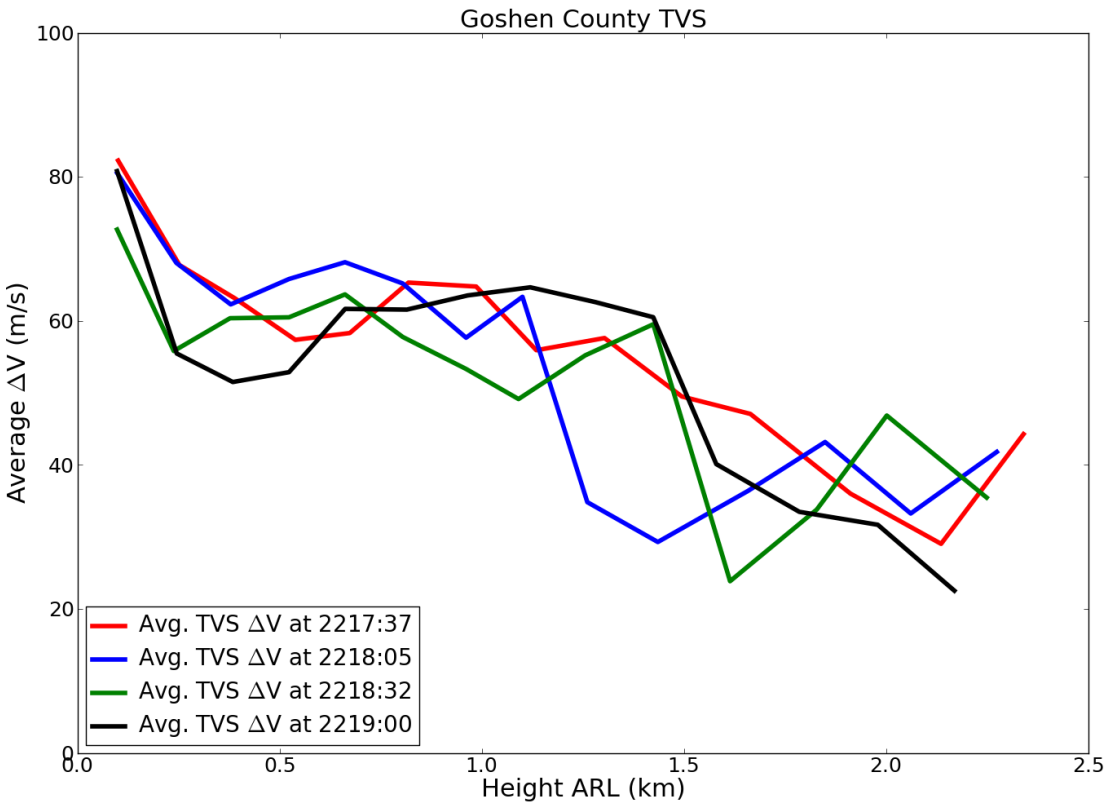

Figure 5.81. As in Fig. 5.59, but from 2217:37-2219:00 UTC during the dissipation phase of the tornado.

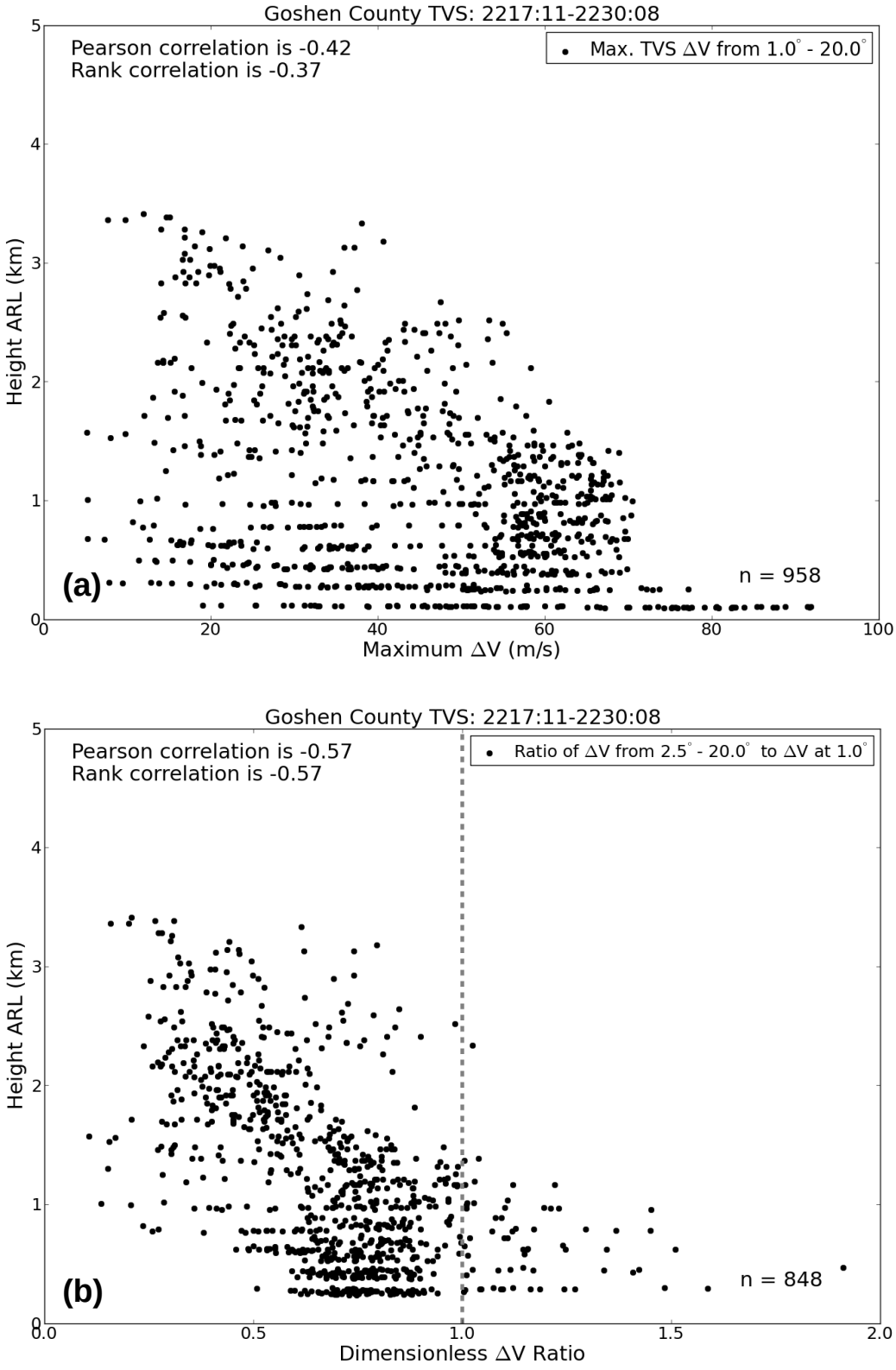

Figure 5.82. As in Fig. 5.47, but for the Goshen County tornado dissipation phase.

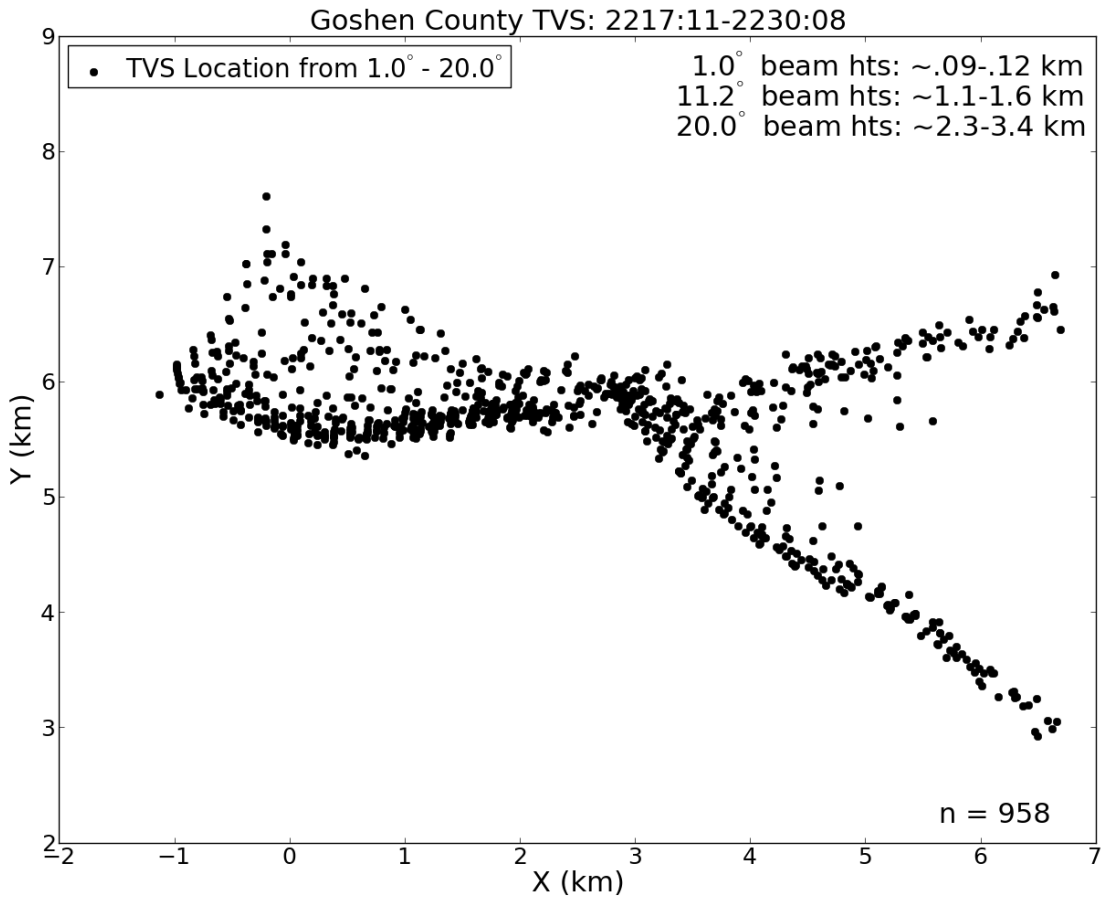

Figure 5.83. Plan view of the TVS location at all elevation angles in the dissipation phase of the Goshen County tornado. The number of data points also is provided.

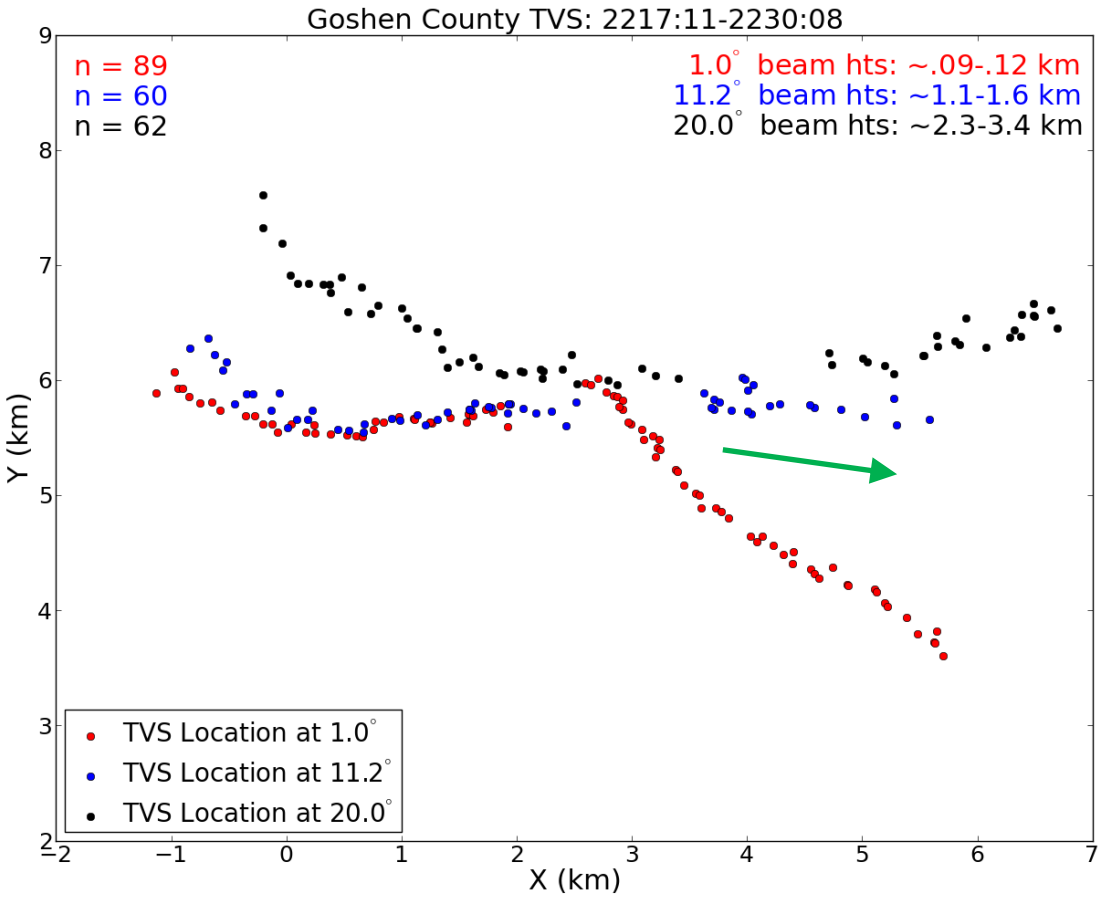

Figure 5.84. Plan view of TVS location at 1.0°, 11.2°, and 20.0° elevation angle in the dissipation phase of the Goshen County tornado. The green arrow represents the translational direction of the storm as determined in Markowski et al. (2012a). The approximate radar center beam heights also are provided.

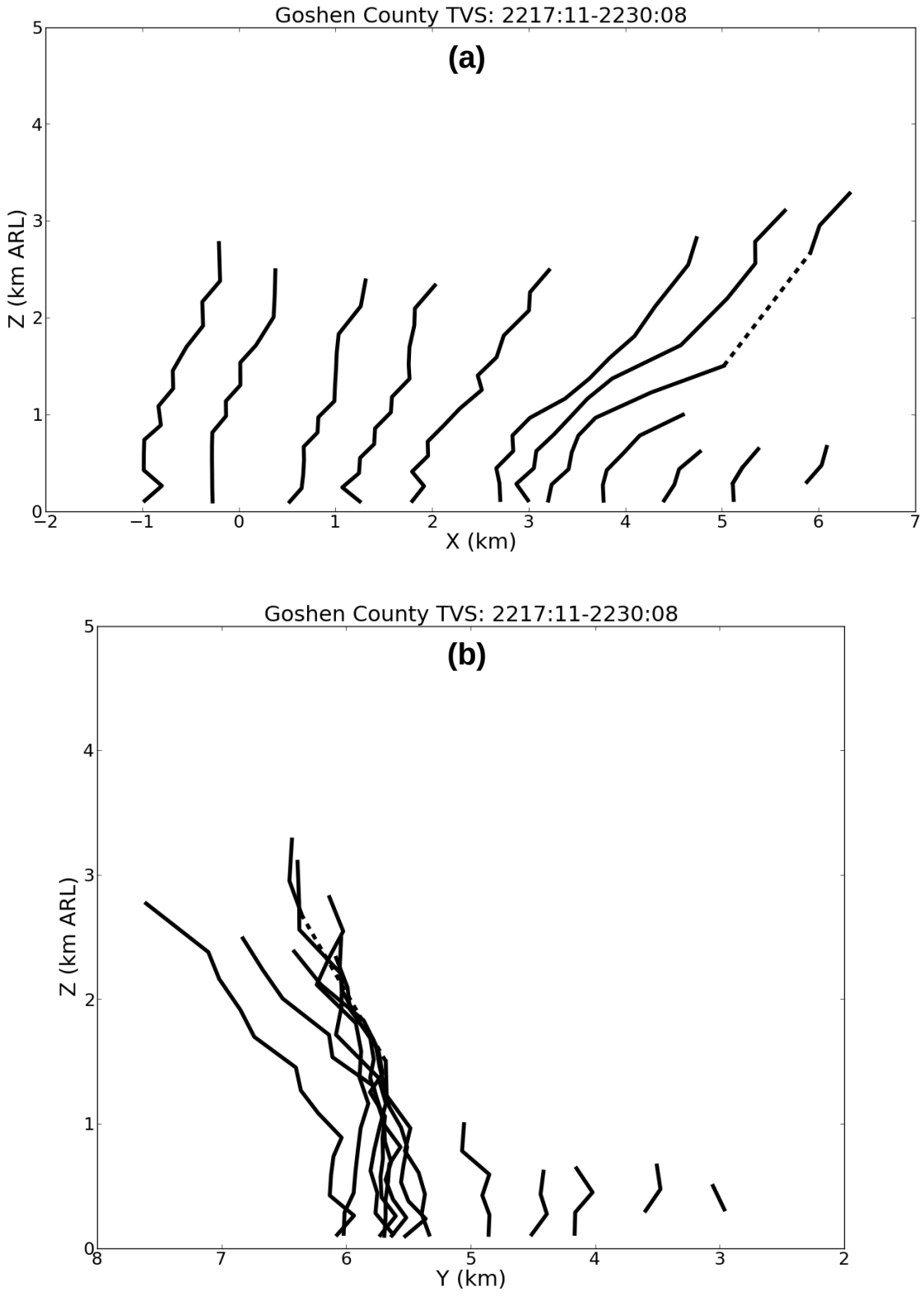

Fig. 5.85. As in Fig. 5.71, but from 2217:11-2230:08 during the tornado dissipation phase.

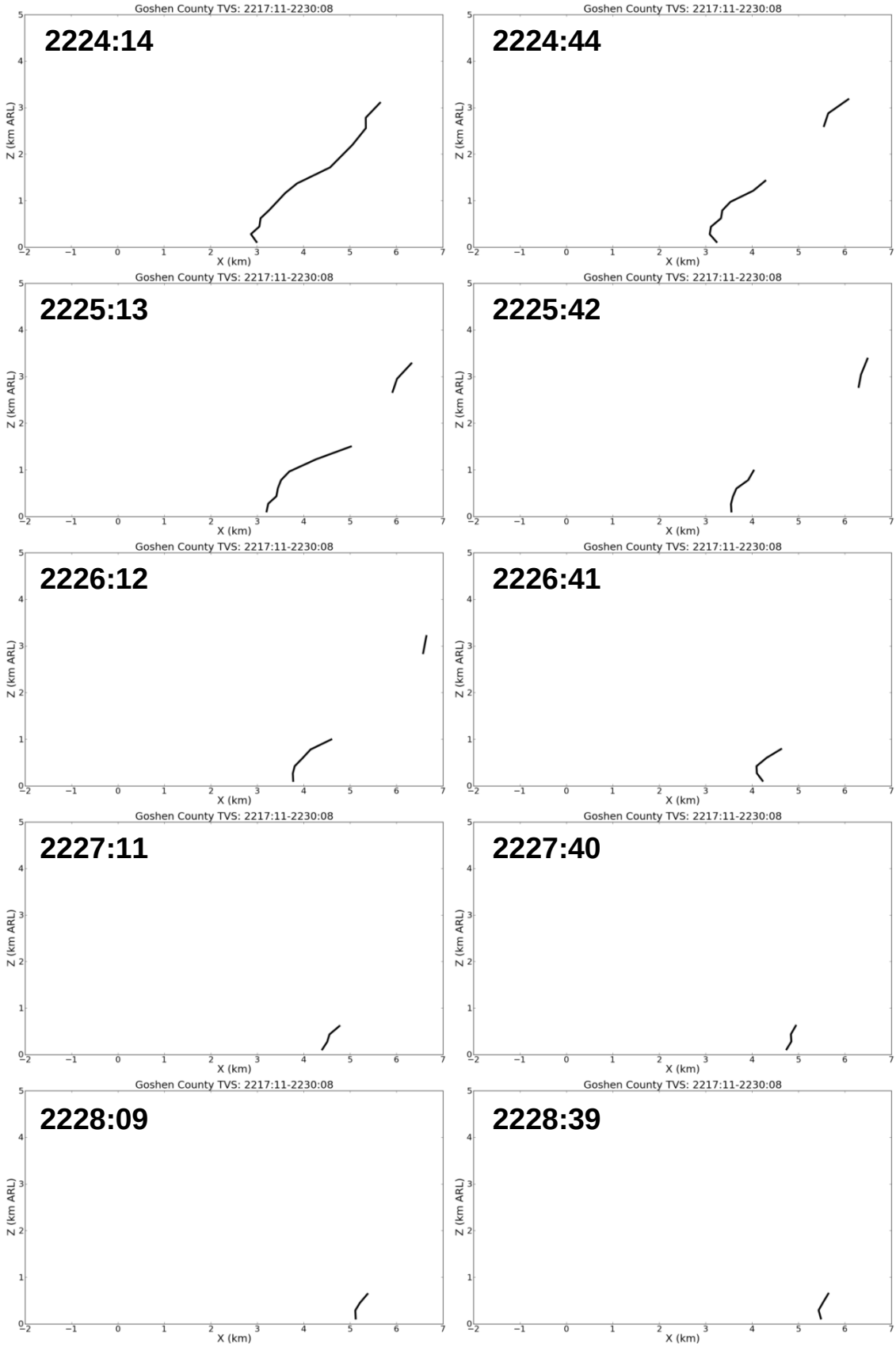
Goshen County TVS: 2217:11-2230:08
2224:14
2224:44
2225:13
2225:42
2226:12
2226:41
2227:11
2227:40
2228:09
2228:39
Z (km ARL)
X (km)

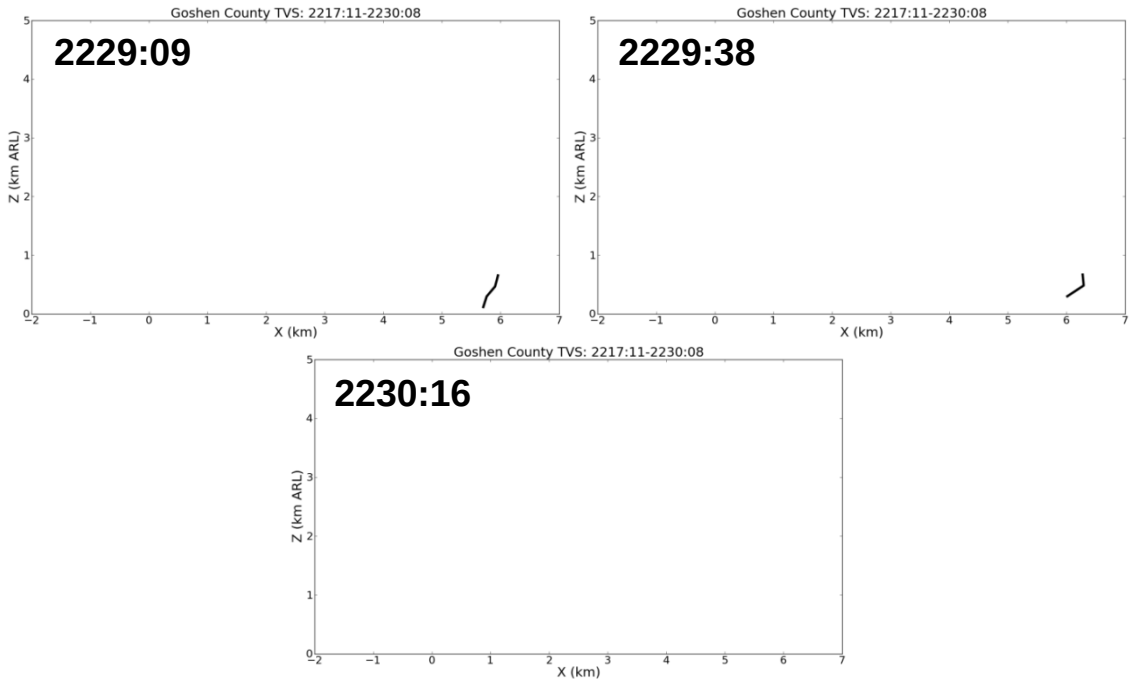

Figure 5.86. As in Fig. 5.72, but for the TVS dissipation process. The grid is not stretched and from left to right (bottom to top) extends 9 (5) km to the east (upward) in the x (z) direction.

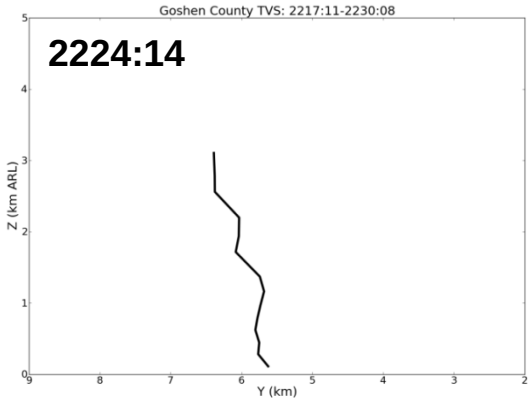
Goshen County TVS: 2217:11-2230:08
2224:14
Z (km ARL)
Y (km)

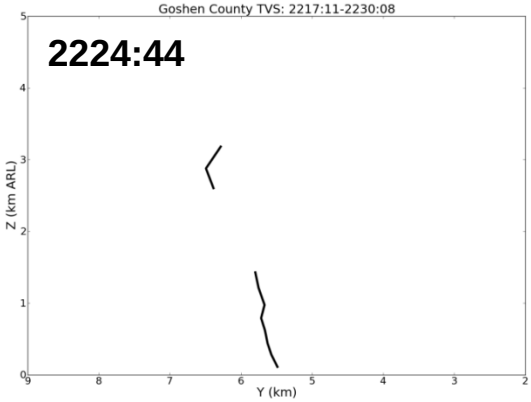
Goshen County TVS: 2217:11-2230:08
2224:44
Z (km ARL)
Y (km)

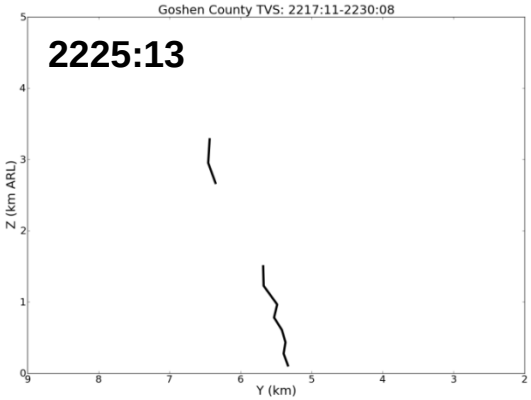
Goshen County TVS: 2217:11-2230:08
2225:13
Z (km ARL)
Y (km)

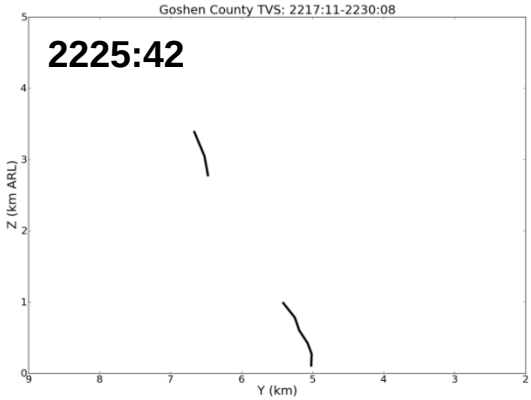
Goshen County TVS: 2217:11-2230:08
2225:42
Z (km ARL)
Y (km)

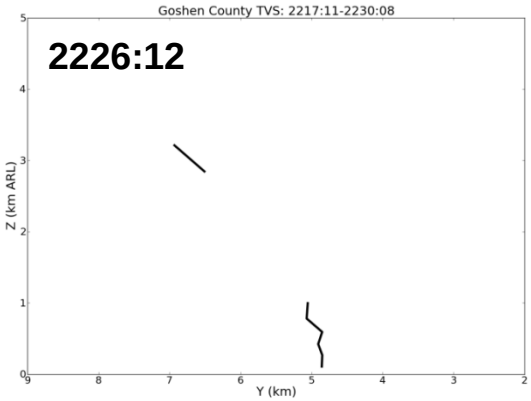
Goshen County TVS: 2217:11-2230:08
2226:12
Z (km ARL)
Y (km)

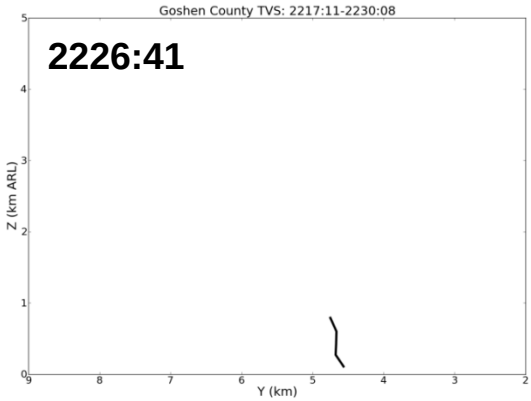
Goshen County TVS: 2217:11-2230:08
2226:41
Z (km ARL)
Y (km)

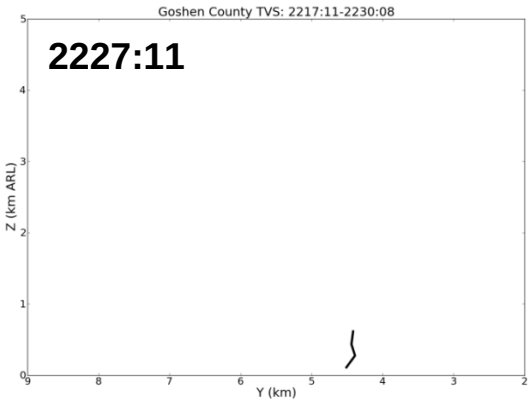
Goshen County TVS: 2217:11-2230:08
2227:11
Z (km ARL)
Y (km)

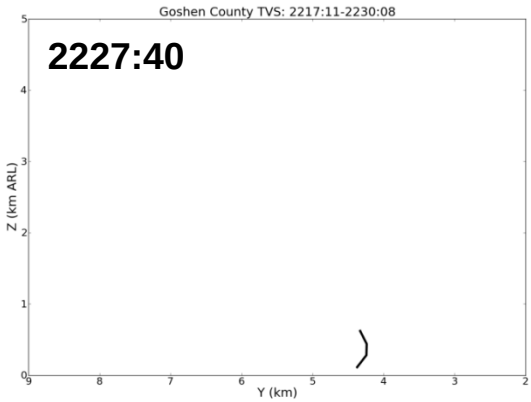
Goshen County TVS: 2217:11-2230:08
2227:40
Z (km ARL)
Y (km)

Figure 5.87. As in Fig. 5.73, but for the TVS dissipation process. The grid is not stretched and from left to right (bottom to top) extends 7 (5) km to the south (upward) in the y (z) direction.

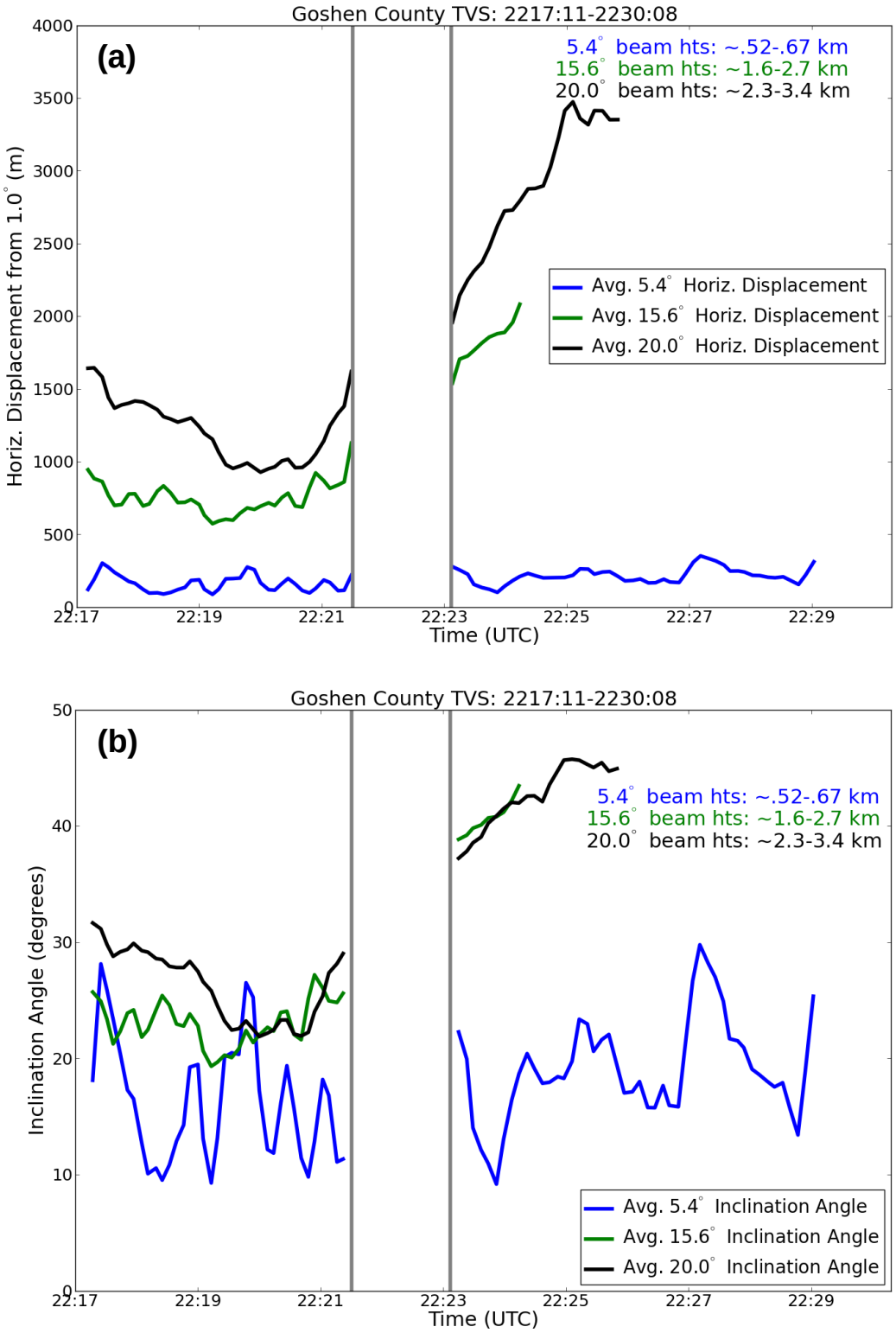

Figure 5.88. As in Fig. 5.74 but for the tornado dissipation phase. Note the higher upper bound in (a) compared to that shown in Fig. 5.74.

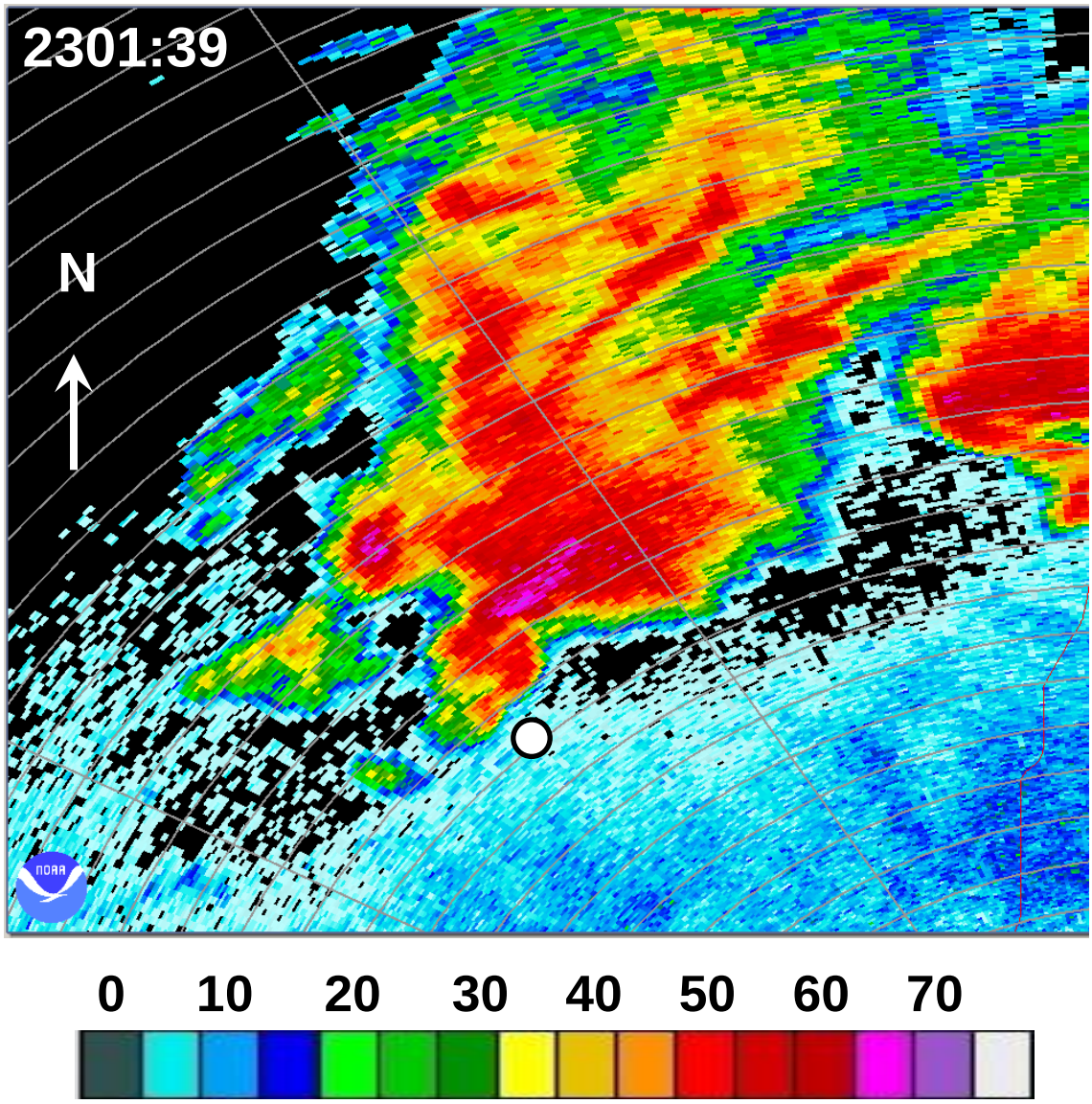

Figure 5.89. As in Fig. 5.1, but from the WSR-88D in Twin Lakes, Oklahoma at 2301:39 UTC on 19 May 2010 during the Kingfisher tornado. Range rings are every 5 km.

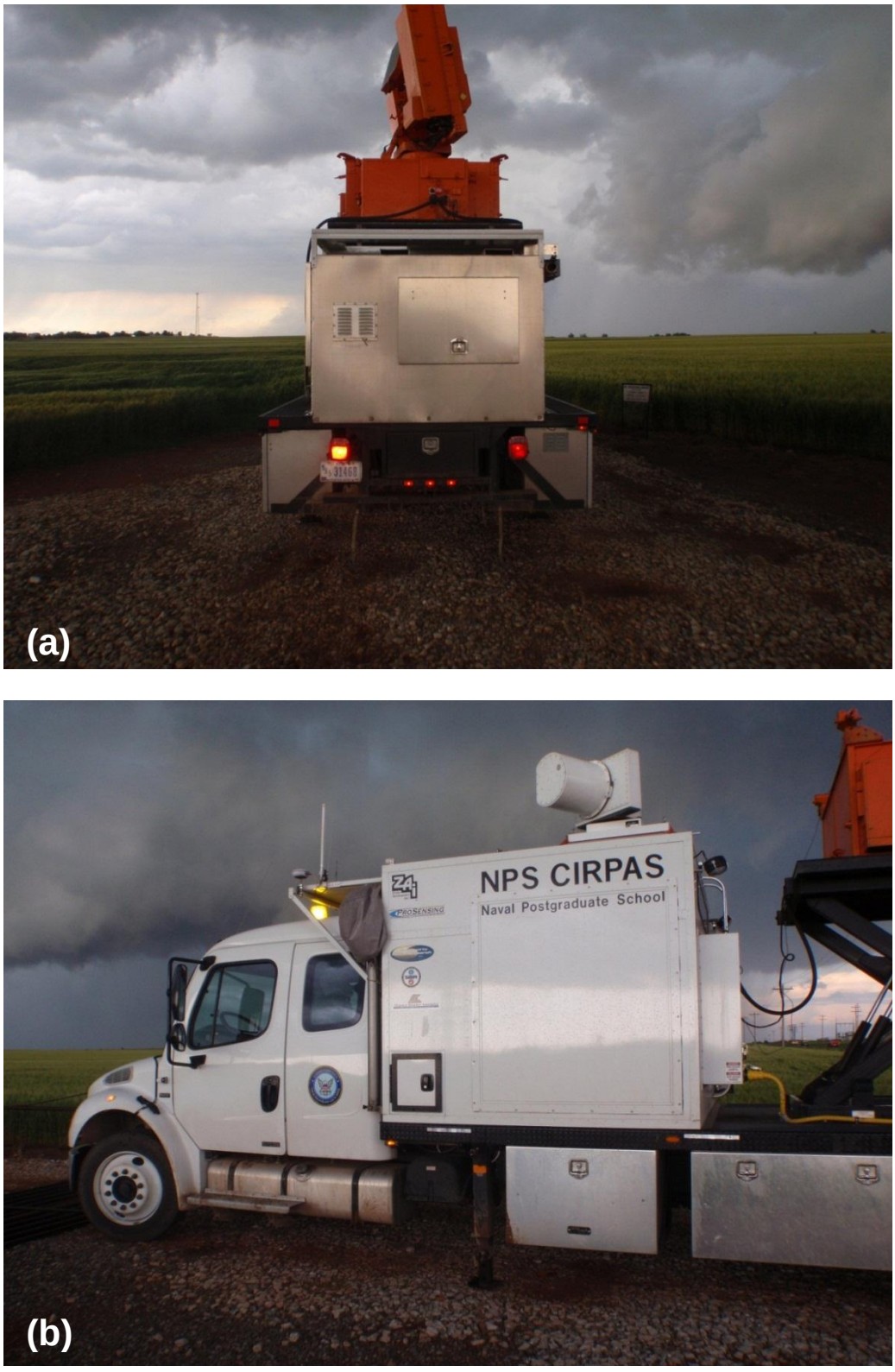

Figure 5.90. The MWR-05XP scanning the Kingfisher, Oklahoma tornado at 2307 UTC looking (a) north and (b) northeast. Photographs © Michael French.

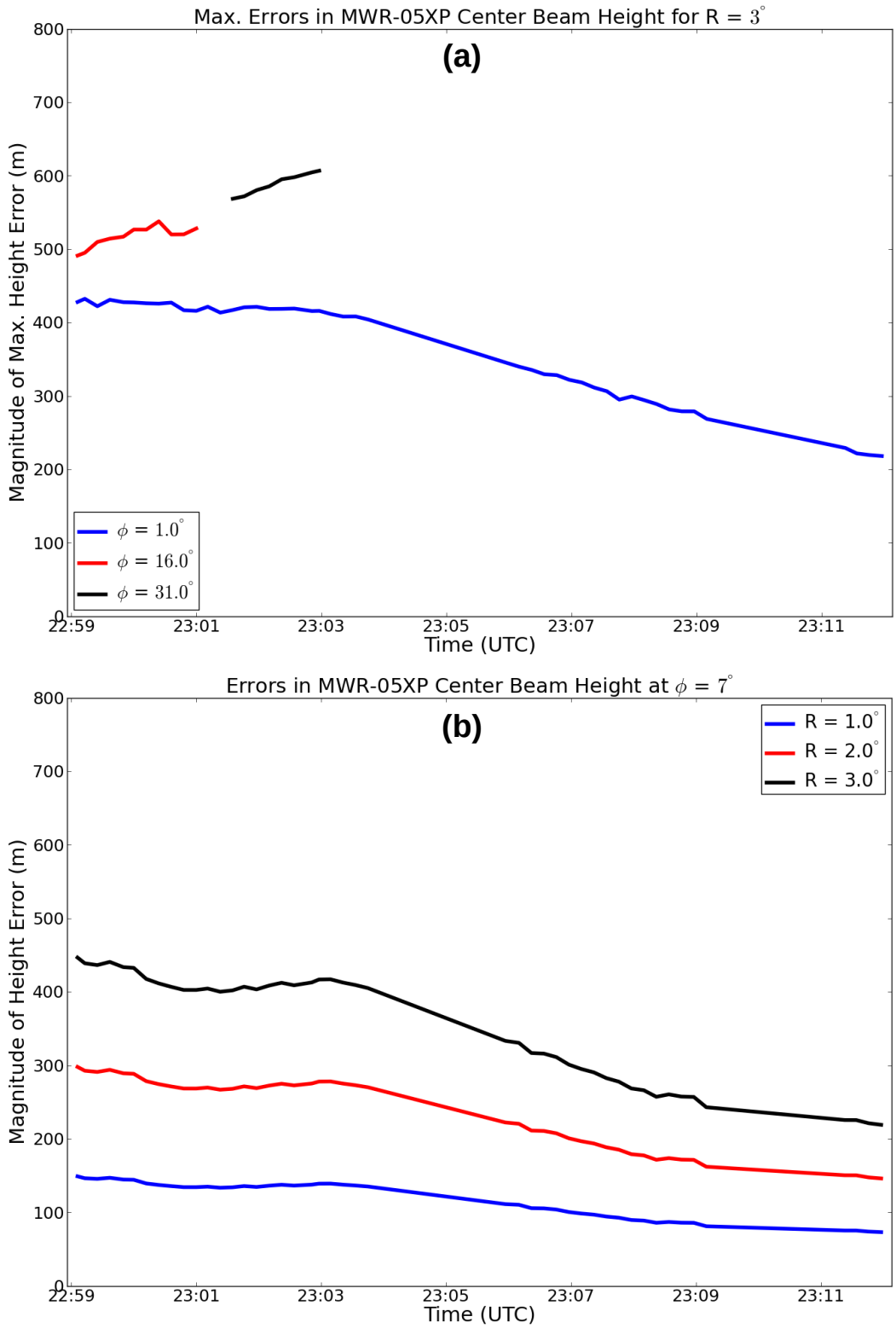

Figure 5.91. As in Fig. 5.33 but for the Kingfisher tornado. In (b) the elevation angle chosen is 7°.

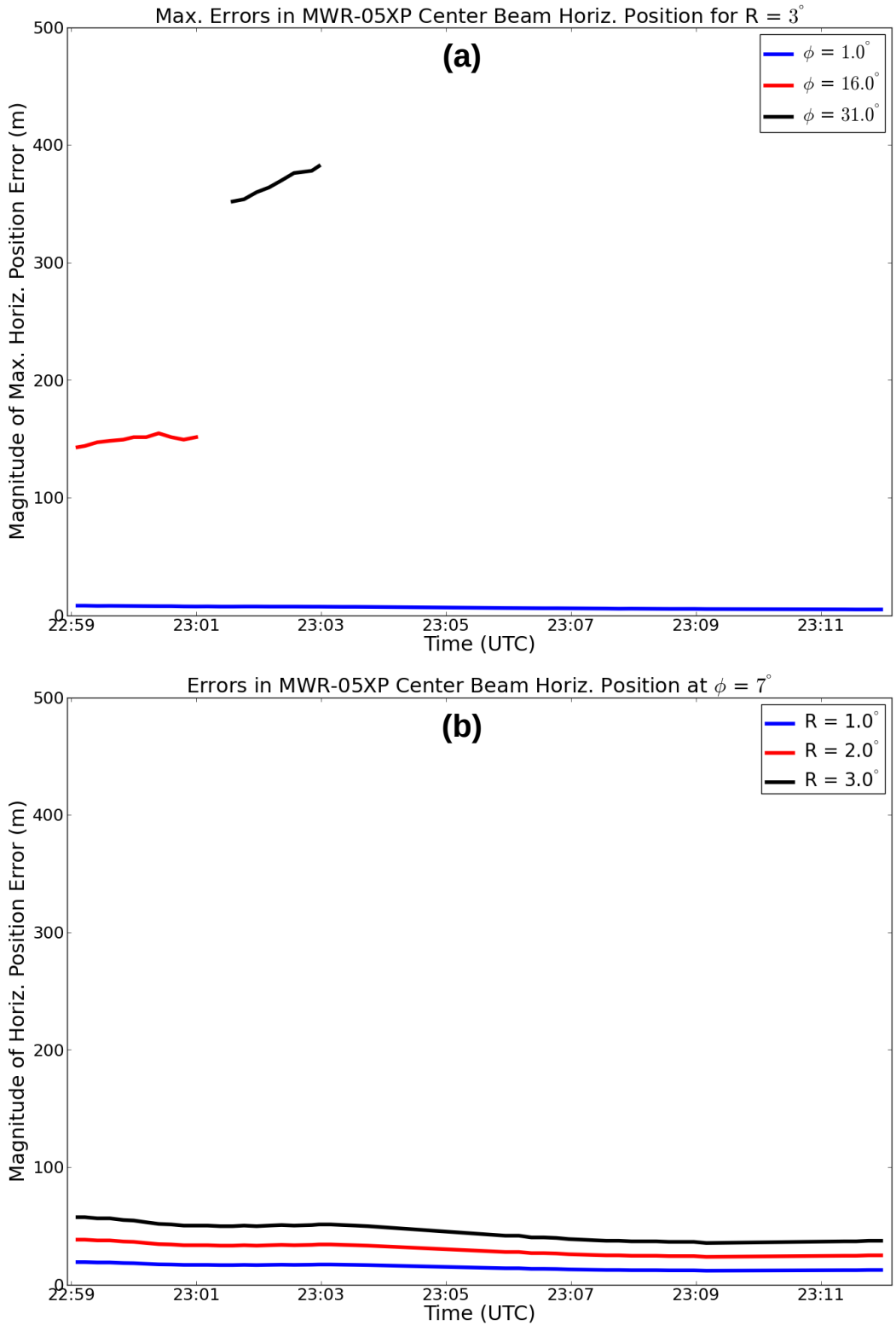

Figure 5.92. As in Fig. 5.34 but for the Kingfisher tornado. In (b) the elevation angle chosen is 7°.

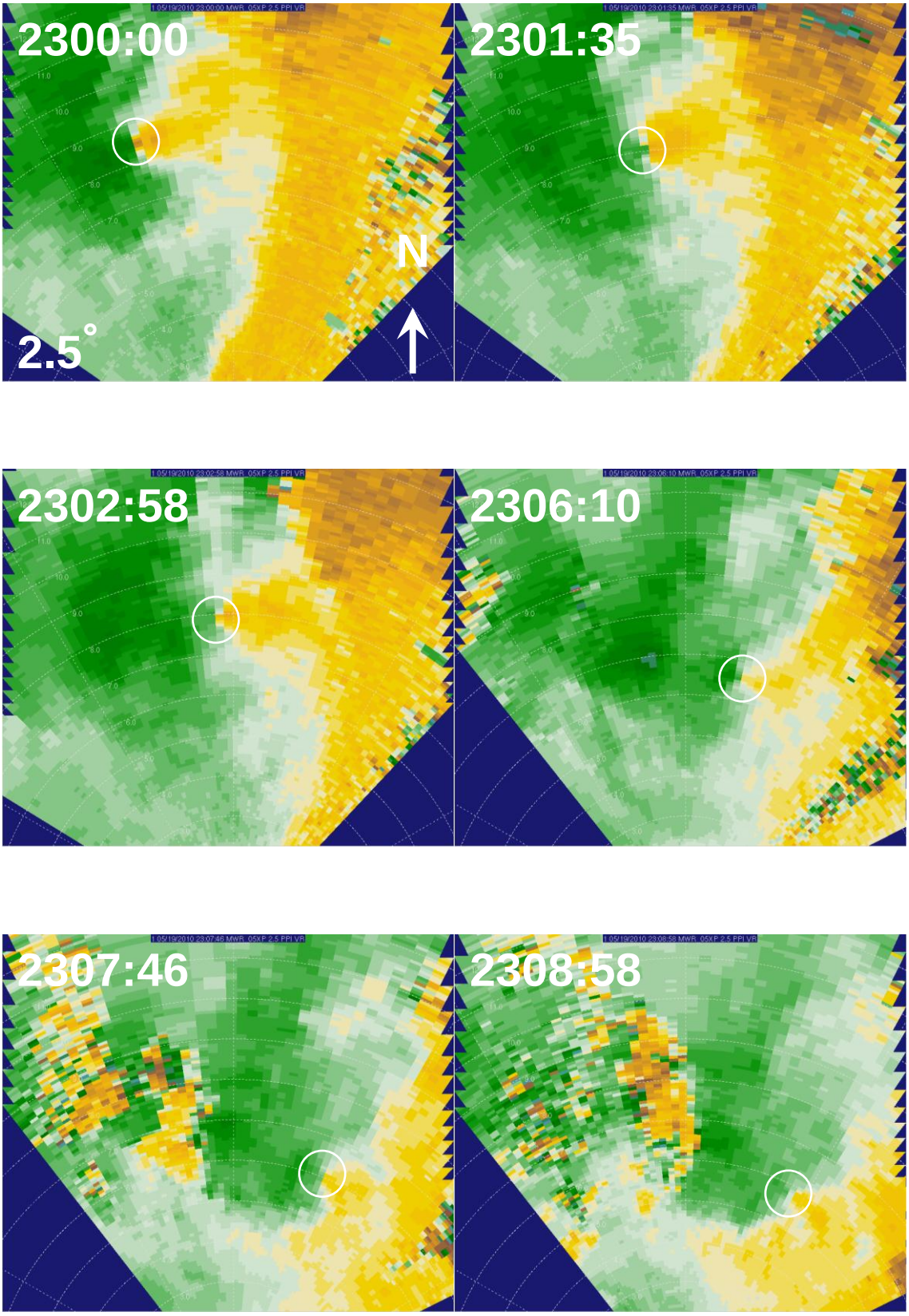
2300:00
N
2.5°
2301:35
2302:58
2306:10
2307:46
2308:58

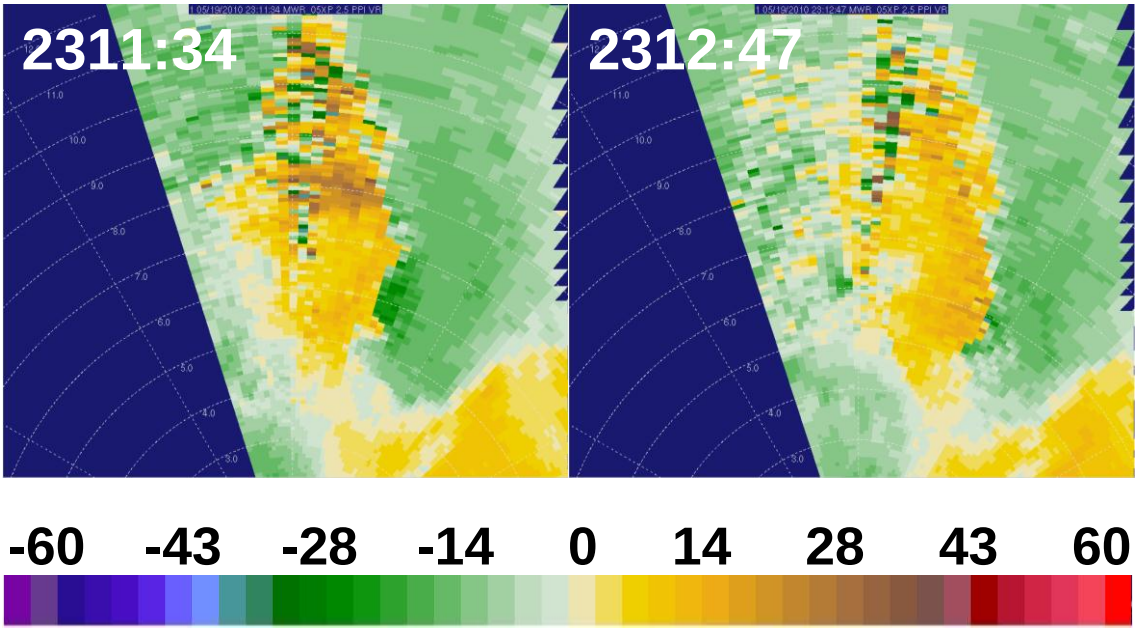

Figure 5.93. PPIs of radial velocity (m s^{-1}) at 2.5° elevation angle every ~90 sec. during the dissipation phase of the Kingfisher tornado. Areas of enhanced GTG cyclonic shear that meet the criteria for a TVS are enclosed by white circles. Range rings are every 1 km. Approximate heights at the location of the TVS range from 250-380 m. The colorbar appears beneath the figure.

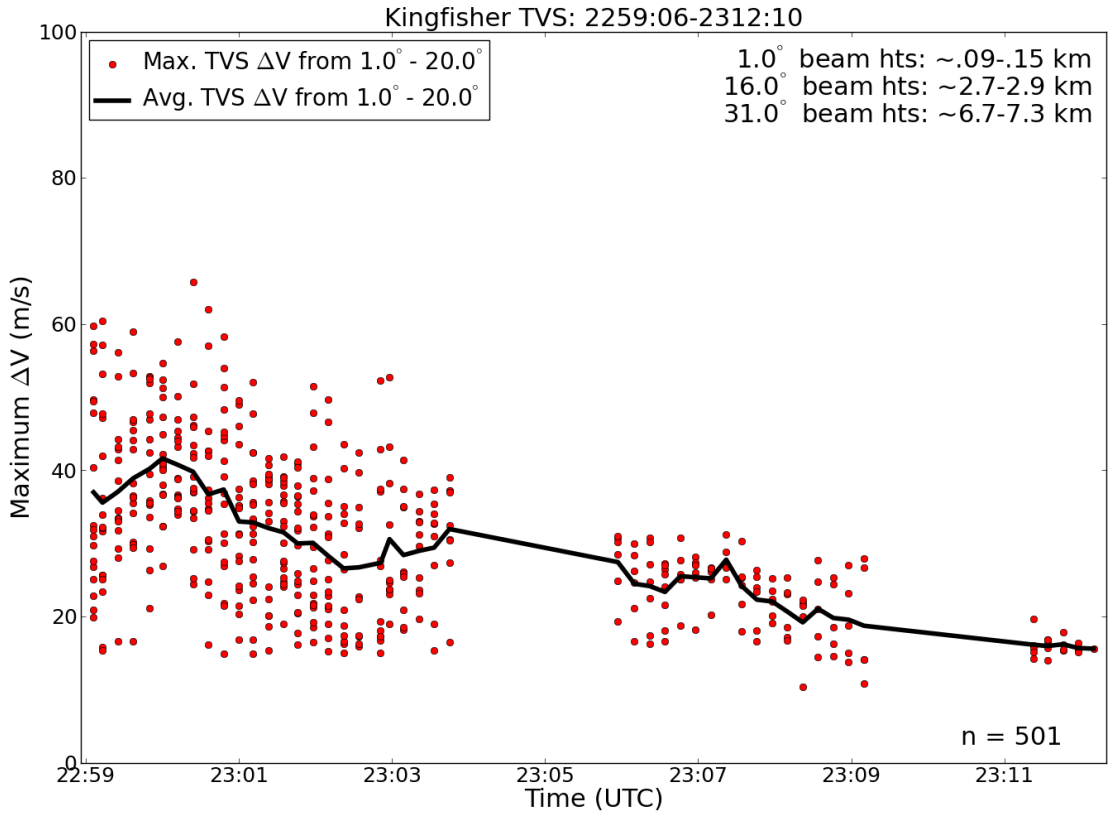

Figure 5.94. Time series of Kingfisher TVS ΔV at all observed levels. The black line is a time series of the average ΔV at each time. The number of data points, mean and median ΔV values, and approximate radar center beam heights also are provided.

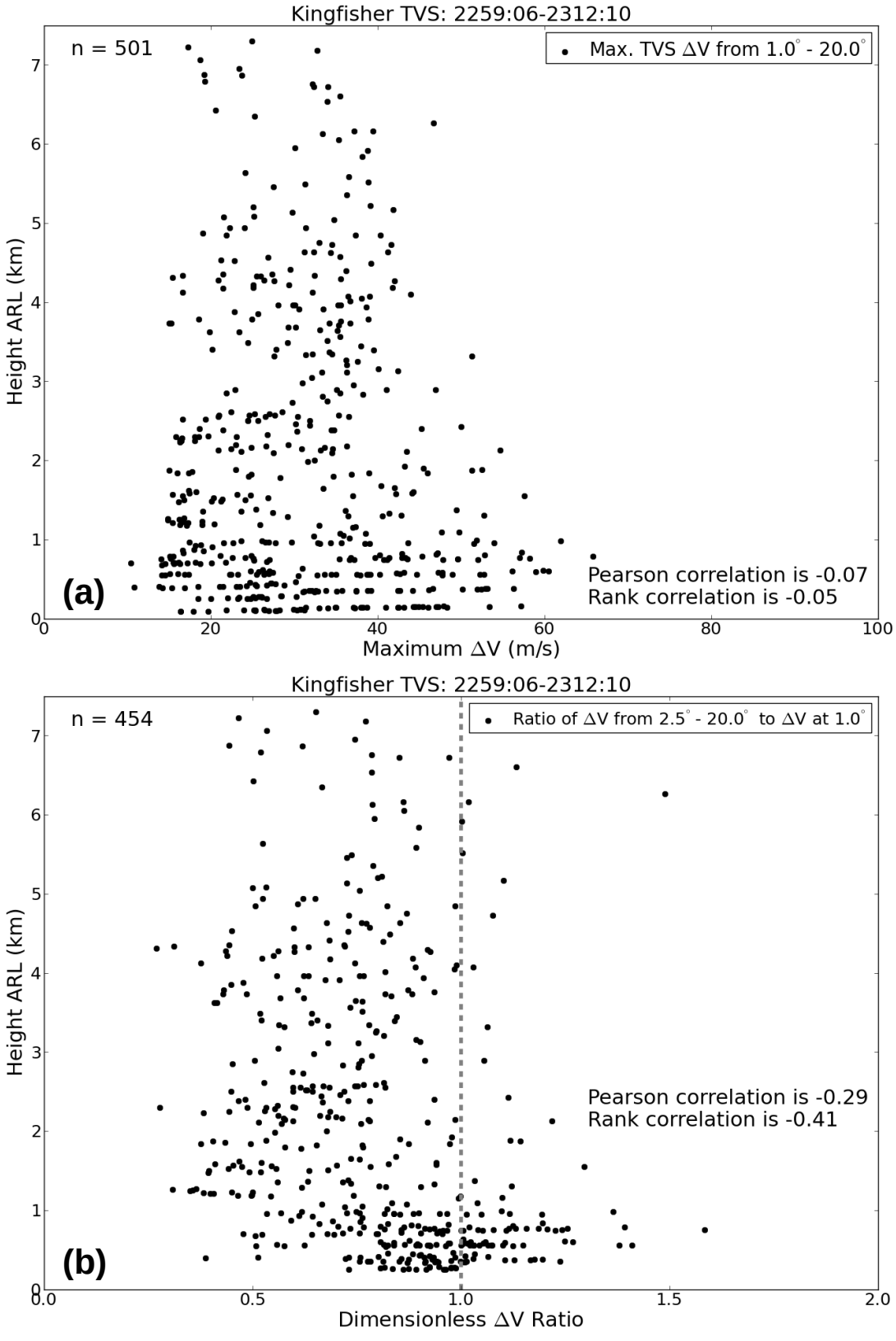

Figure 5.95. As in Fig. 5.47, but for the Kingfisher tornado dissipation phase.

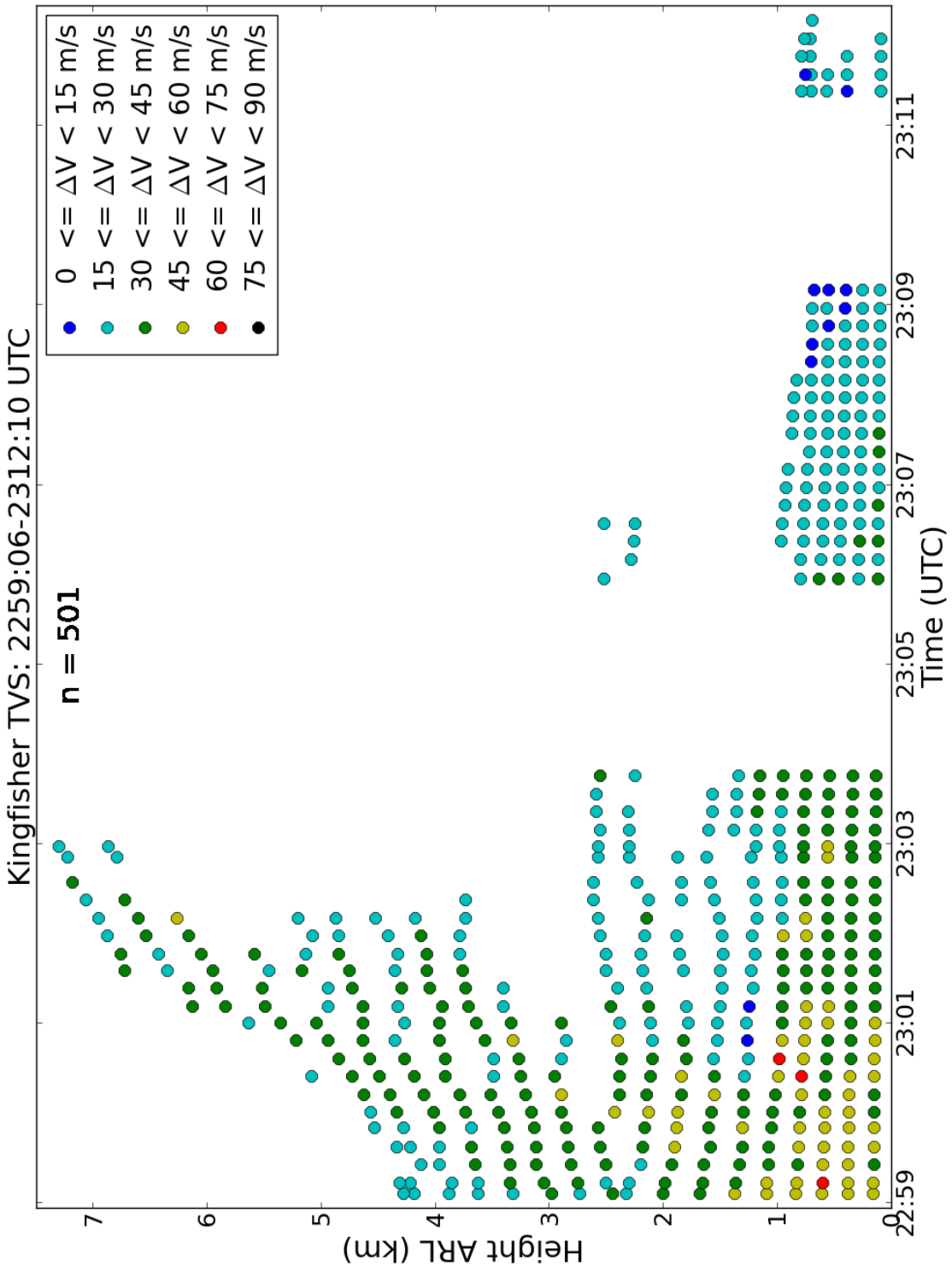

Fig. 5.96. As in Fig. 5.45, but for the Kingfisher tornado dissipation stage. The missing TVS markers at ~2305 and ~2310 UTC are from a gap in MWR-05XP data collection.

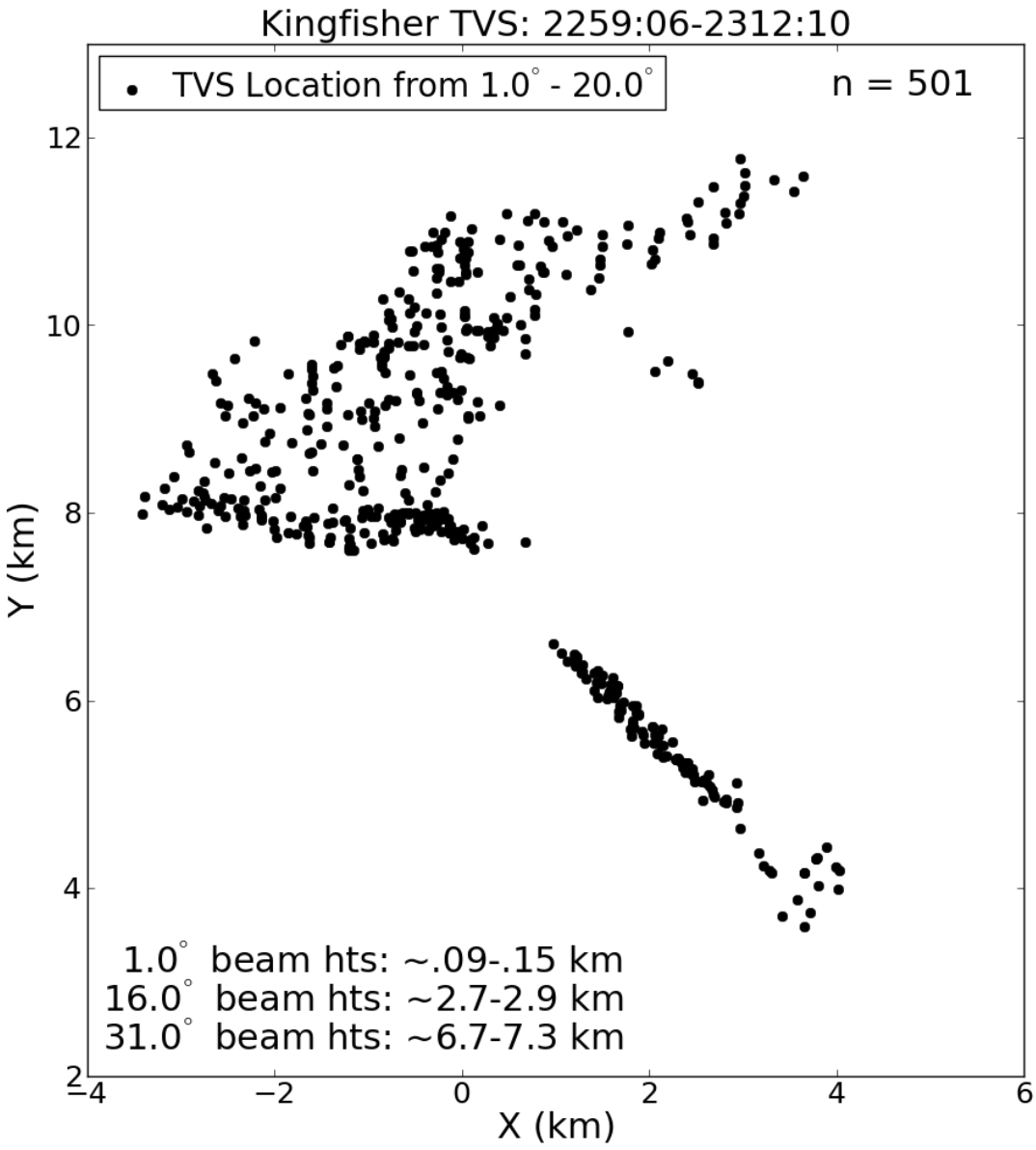

Figure 5.97. As in Fig. 5.83, but for the dissipation phase of the Kingfisher tornado.

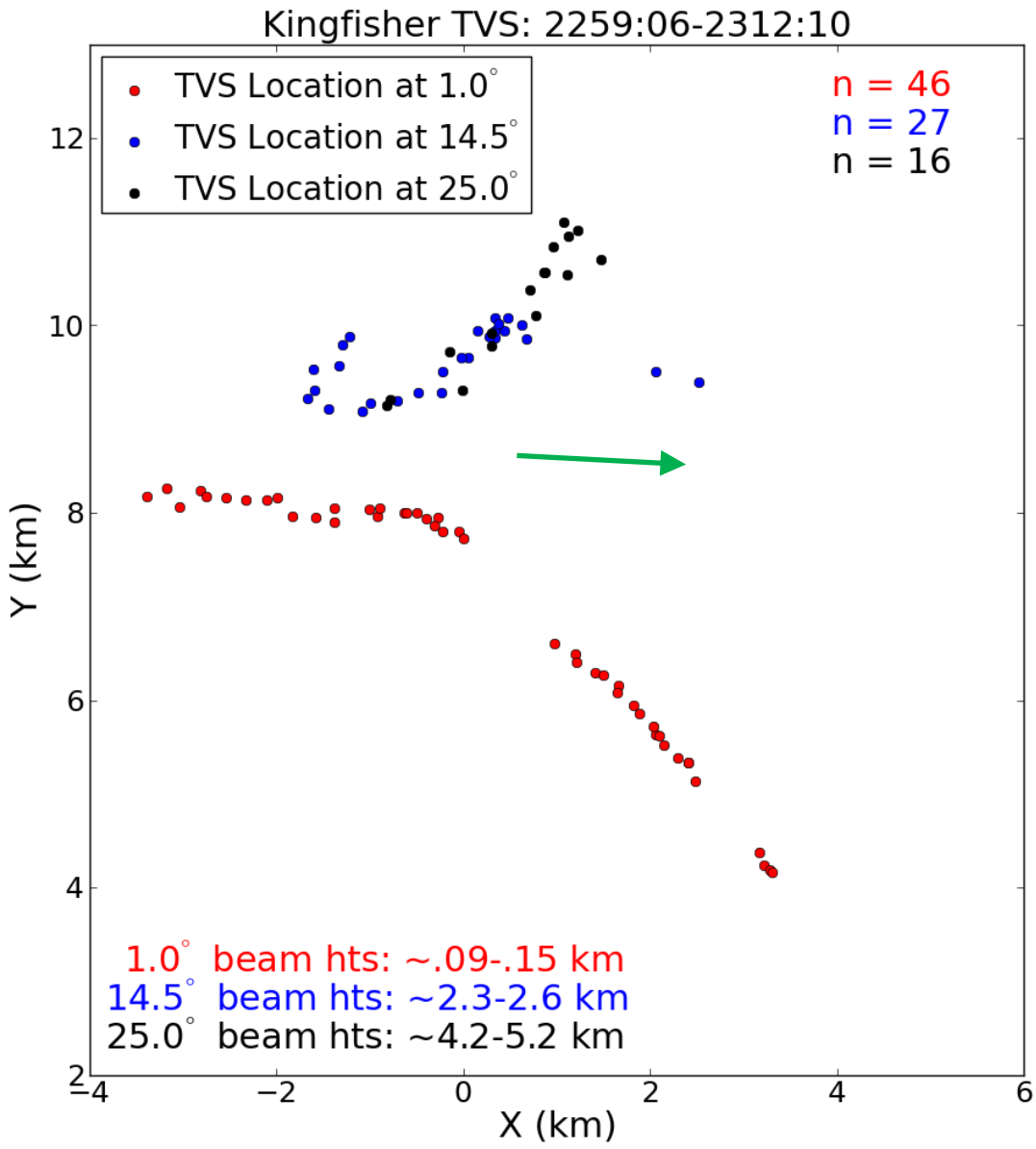

Figure 5.98. As in Fig. 5.84, but for the dissipation phase of the Kingfisher tornado.

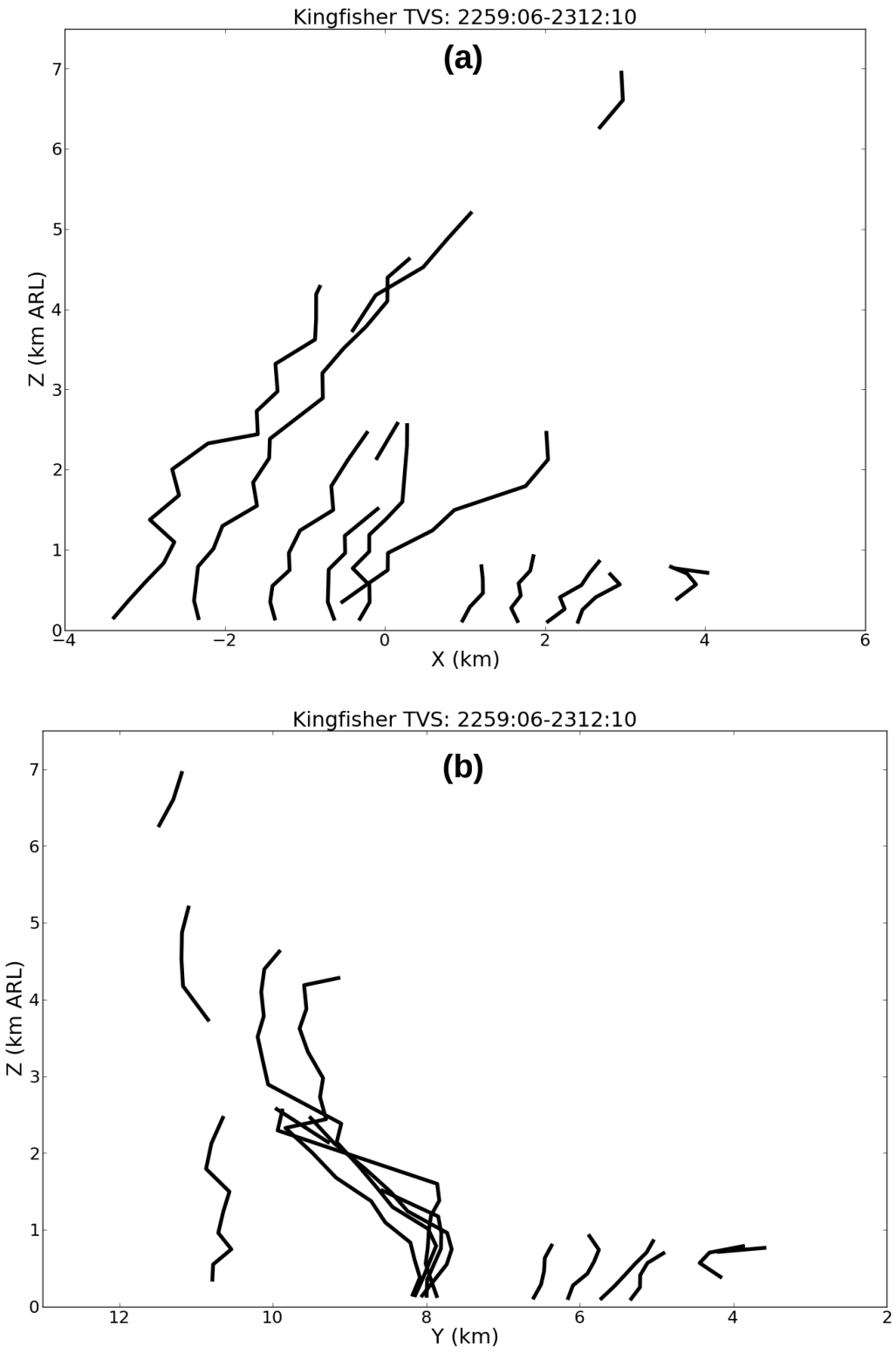

Fig. 5.99. As in Fig. 5.71, but for the Kingfisher tornado dissipation phase. In both (a) and (b), the tornado is moving from left to right (west to east and north to south).

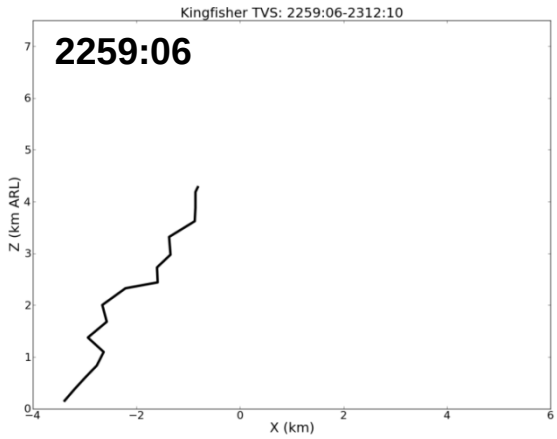
Kingfisher TVS: 2259:06-2312:10
2259:06
Z (km ARL)
X (km)

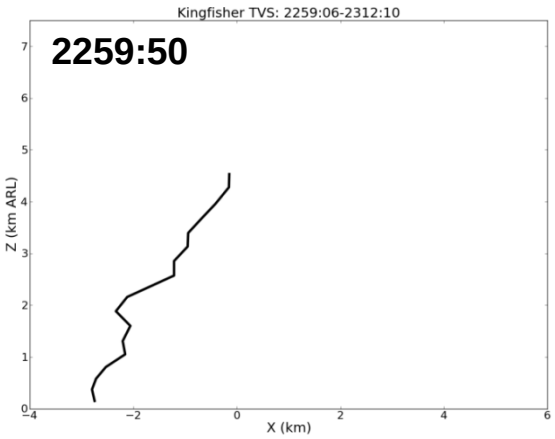
Kingfisher TVS: 2259:06-2312:10
2259:50
Z (km ARL)
X (km)

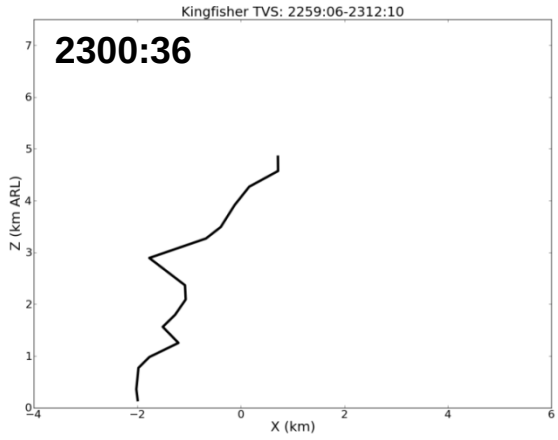
Kingfisher TVS: 2259:06-2312:10
2300:36
Z (km ARL)
X (km)


Kingfisher TVS: 2259:06-2312:10
2301:23
Z (km ARL)
X (km)

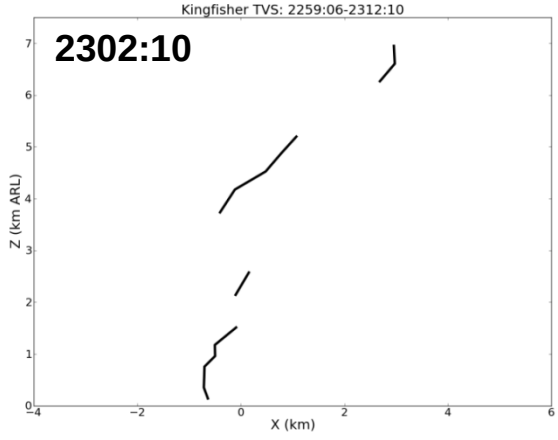
Kingfisher TVS: 2259:06-2312:10
2302:10
Z (km ARL)
X (km)

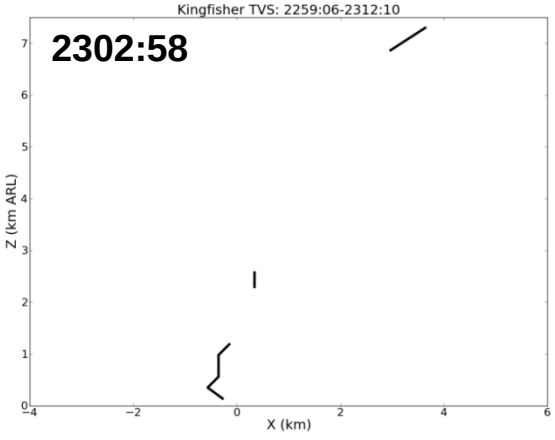
Kingfisher TVS: 2259:06-2312:10
2302:58
Z (km ARL)
X (km)

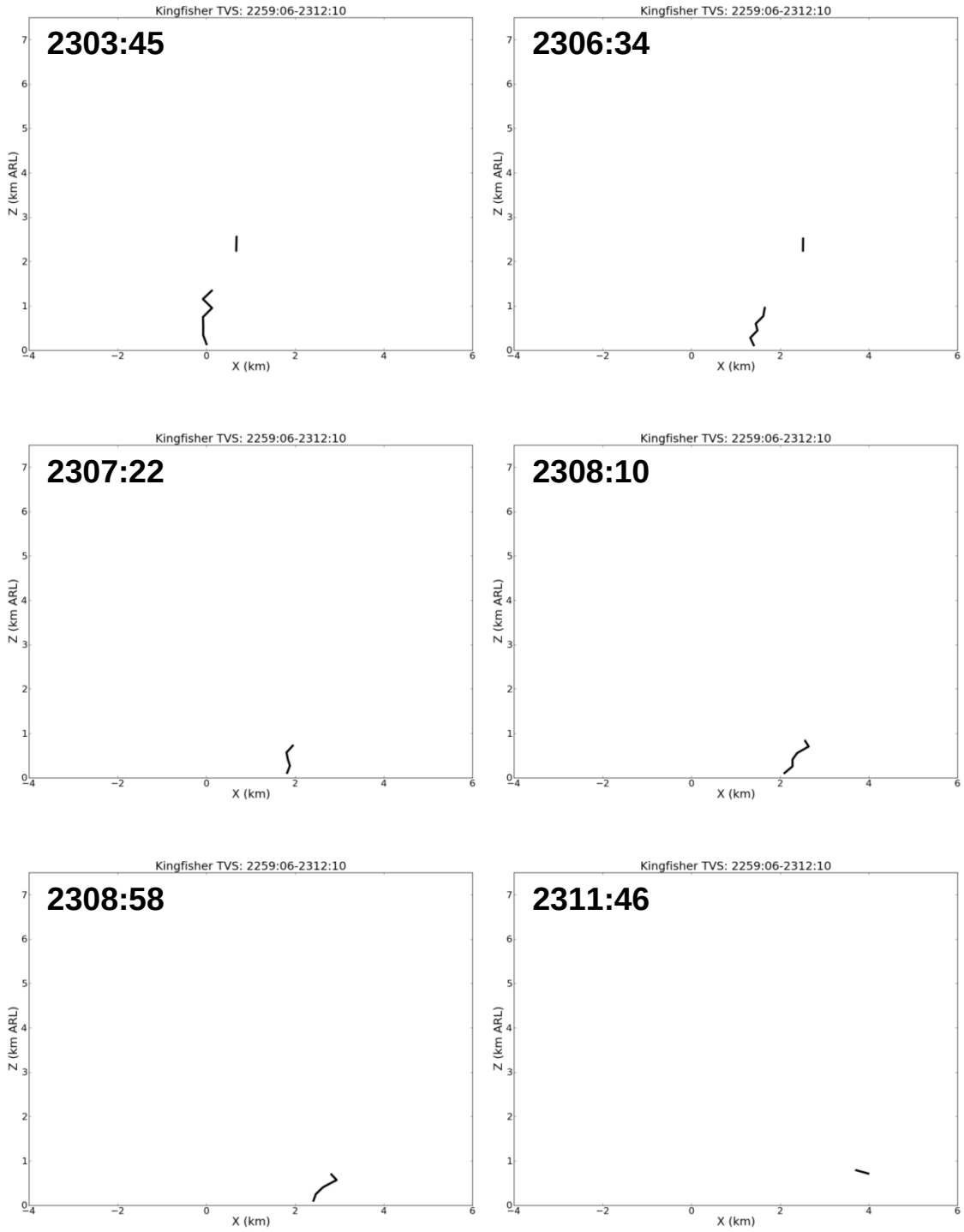

Figure 5.100. As in Fig. 5.86, but for the dissipation phase of the Kingfisher tornado. Note the variable time difference between plots caused by MWR-05XP data gaps.

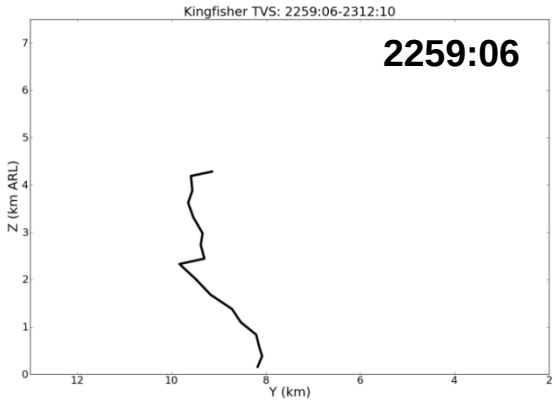
Kingfisher TVS: 2259:06-2312:10
2259:06
Z (km ARL)
Y (km)

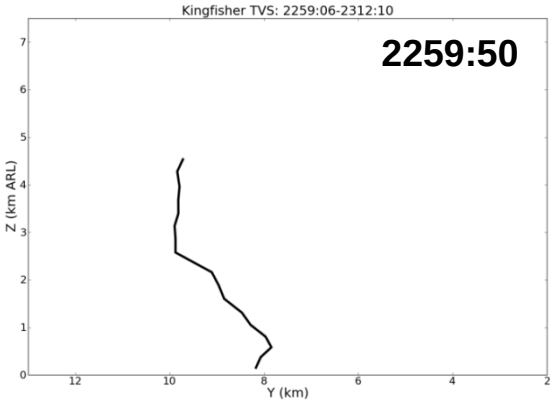
Kingfisher TVS: 2259:06-2312:10
2259:50
Z (km ARL)
Y (km)

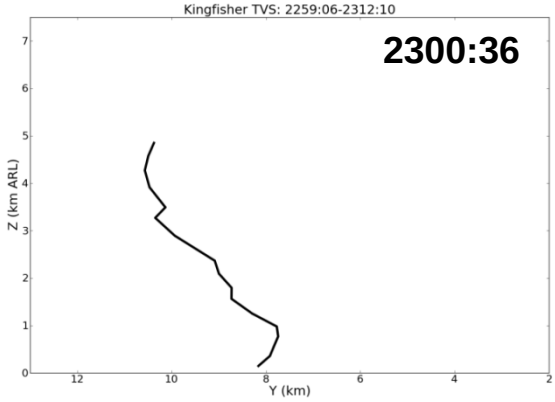
Kingfisher TVS: 2259:06-2312:10
2300:36
Z (km ARL)
Y (km)

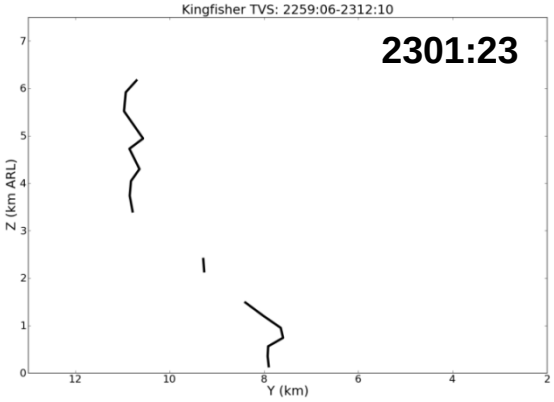
Kingfisher TVS: 2259:06-2312:10
2301:23
Z (km ARL)
Y (km)

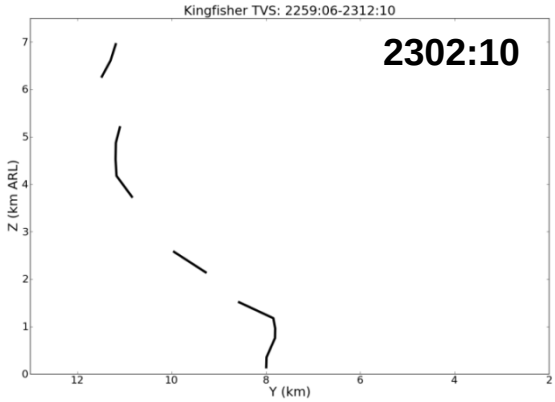
Kingfisher TVS: 2259:06-2312:10
2302:10
Z (km ARL)
Y (km)

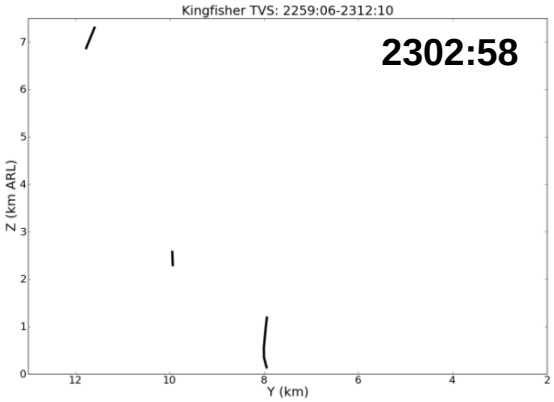
Kingfisher TVS: 2259:06-2312:10
2302:58
Z (km ARL)
Y (km)

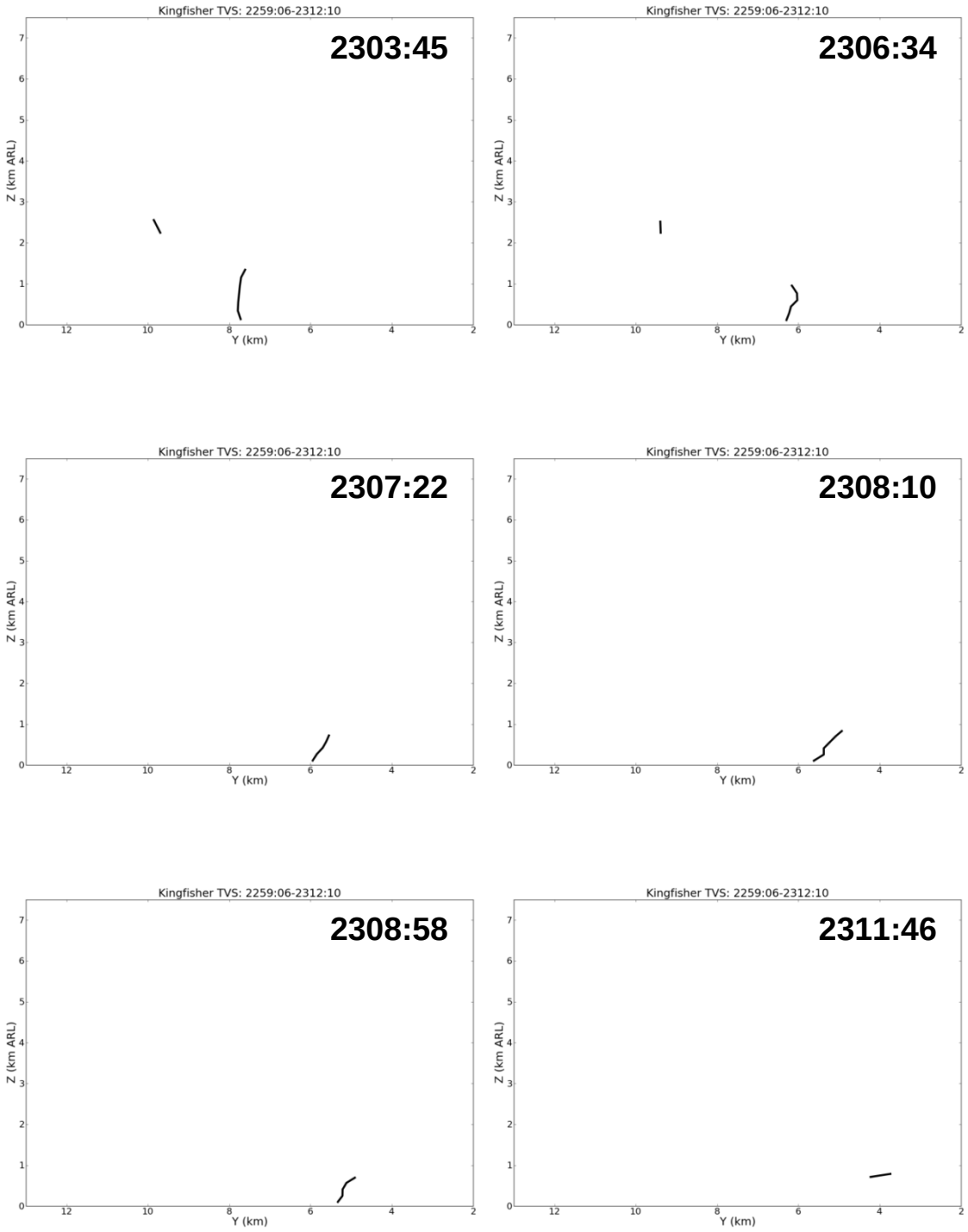

Figure 5.101. As in Fig. 5.87, but for the dissipation phase of the Kingfisher tornado. Note the variable time difference between plots caused by MWR-05XP data gaps.

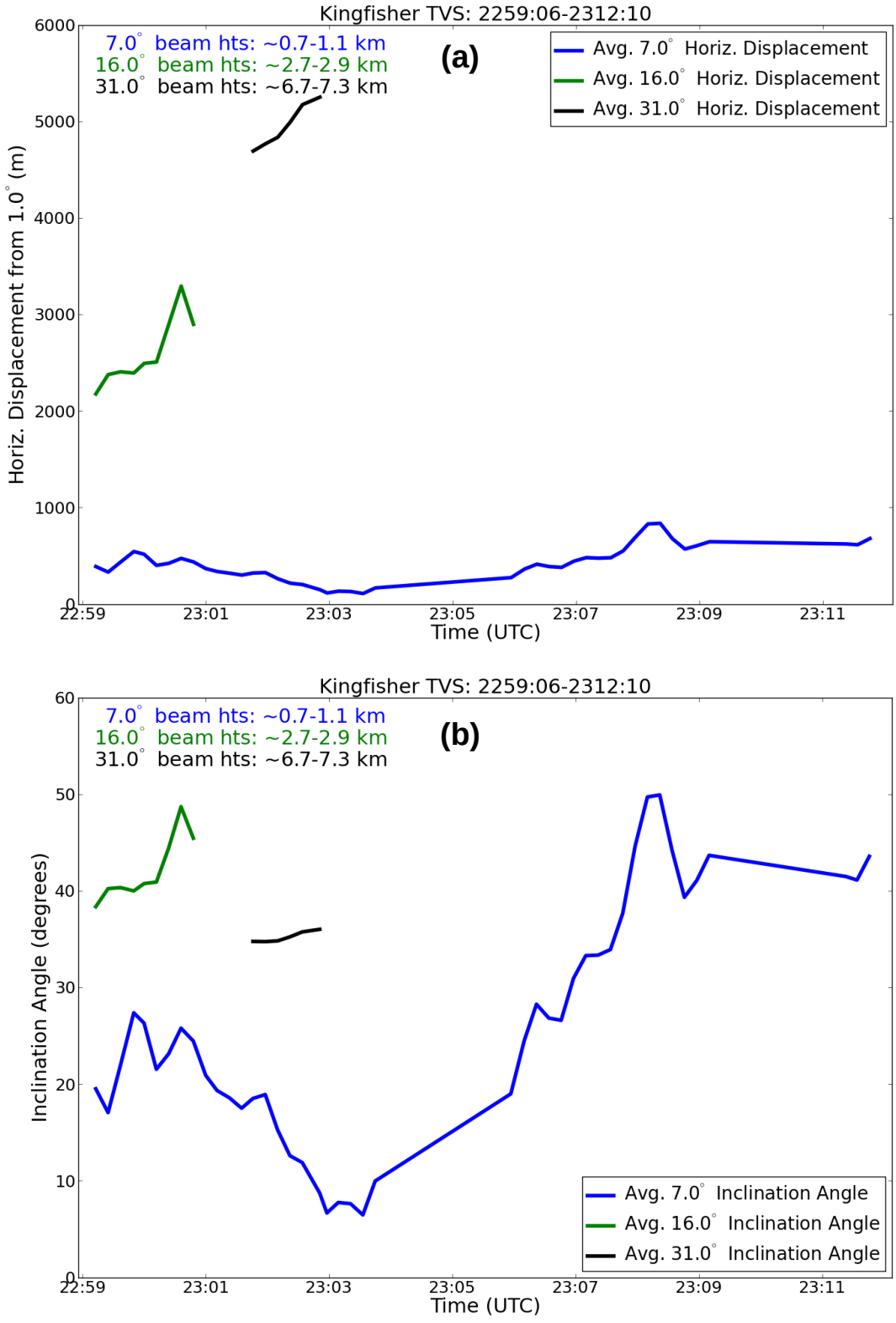

Figure 5.102. As in Fig. 5.74, but for the dissipation phase of the Kingfisher tornado. Note the higher upper bounds in (a) and (b) compared to that shown in Fig. 5.74.

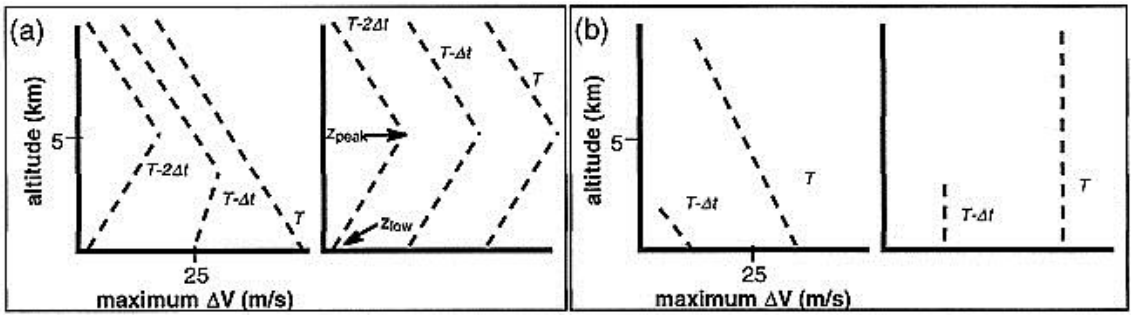

Figure 6.1. Vertical profiles of the maximum, GTG differential velocity, ΔV (m s^{-1}), at a few times (corresponding to radar volume scan times) during tornado development, for the idealized, empirically determined models on which the (a) descending and (b) nondescending classification is based. The altitude z_{peak} of the peak differential velocity ΔV_{peak} within a volume scan, and altitude z_{low} of the differential velocity ΔV_{low} at the lowest elevation angle, within the same volume scan, are indicated in (a). From Trapp et al. (1999).

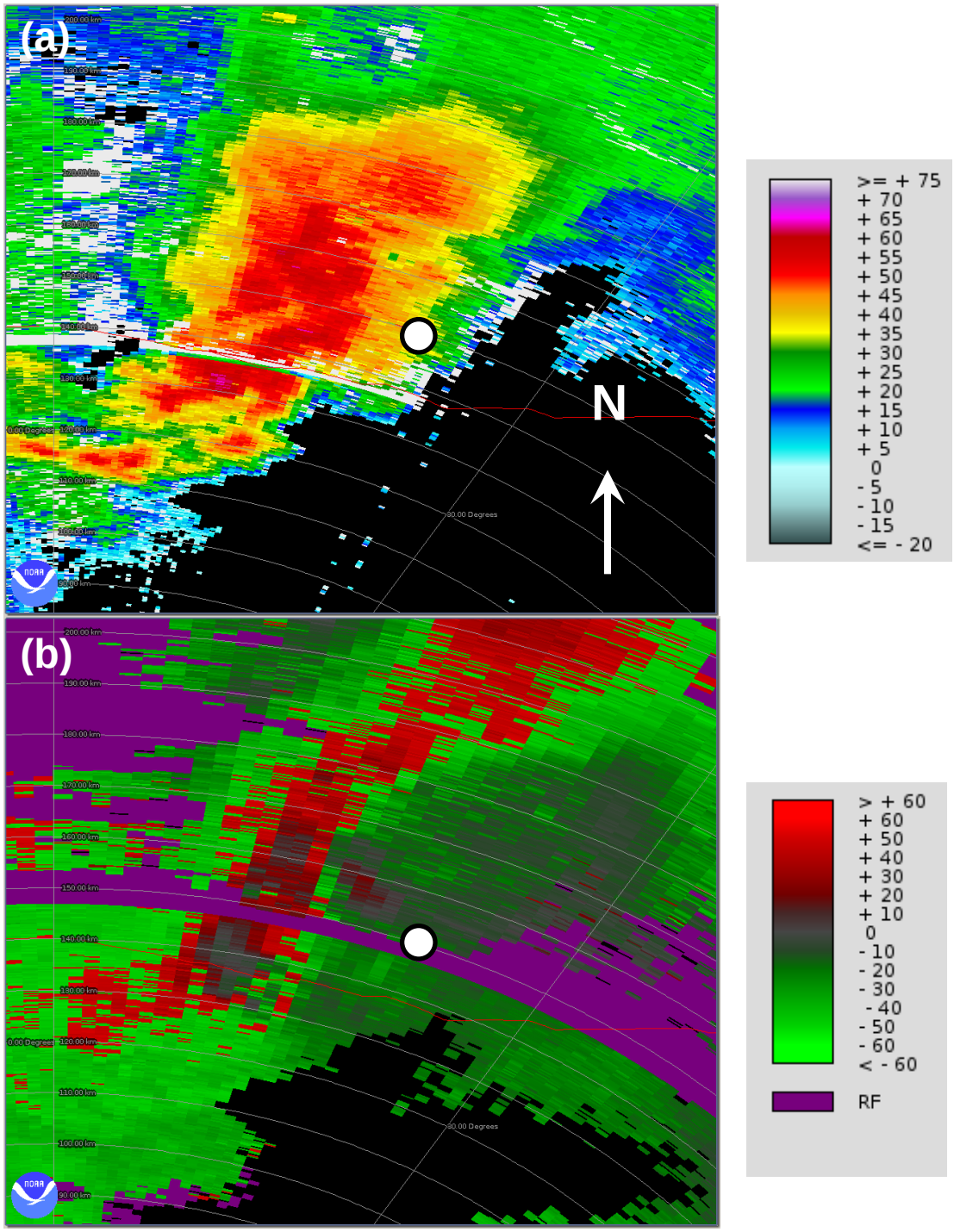

Figure 6.2. PPIs of (a) reflectivity (dBZ) and (b) radial velocity (kts) from the WSR-88D at 0.94° elevation angle in Dodge City, Kansas at 0158 UTC on 24 May 2008. The location of the MWR-05XP during its deployment is approximated by a white circle. Range rings are every 10 km. The scales appear to the right of the images.

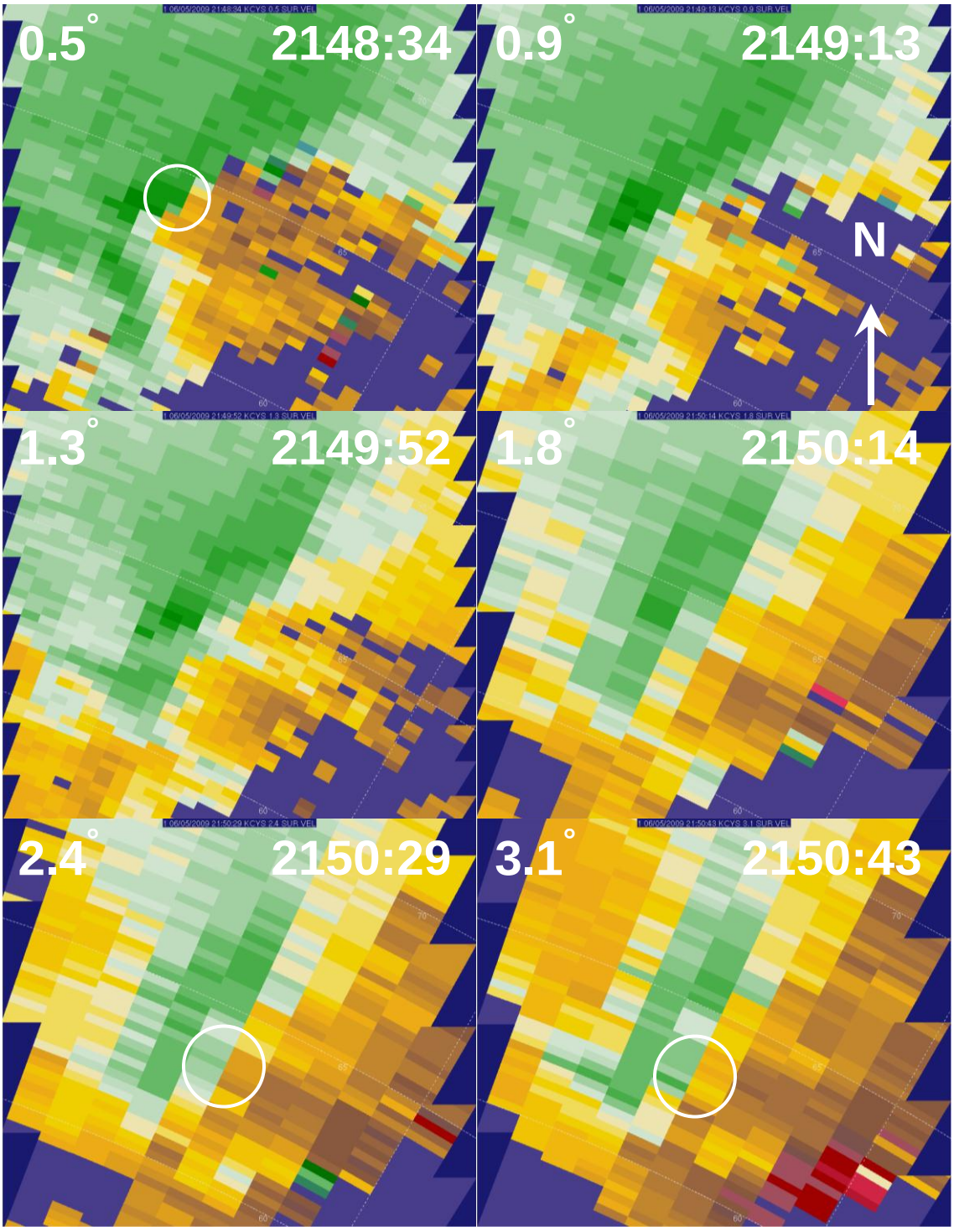
0.5°
2148:34
0.9°
2149:13
N
1.3°
2149:52
1.8°
2150:14
2.4°
2150:29
3.1°
2150:43

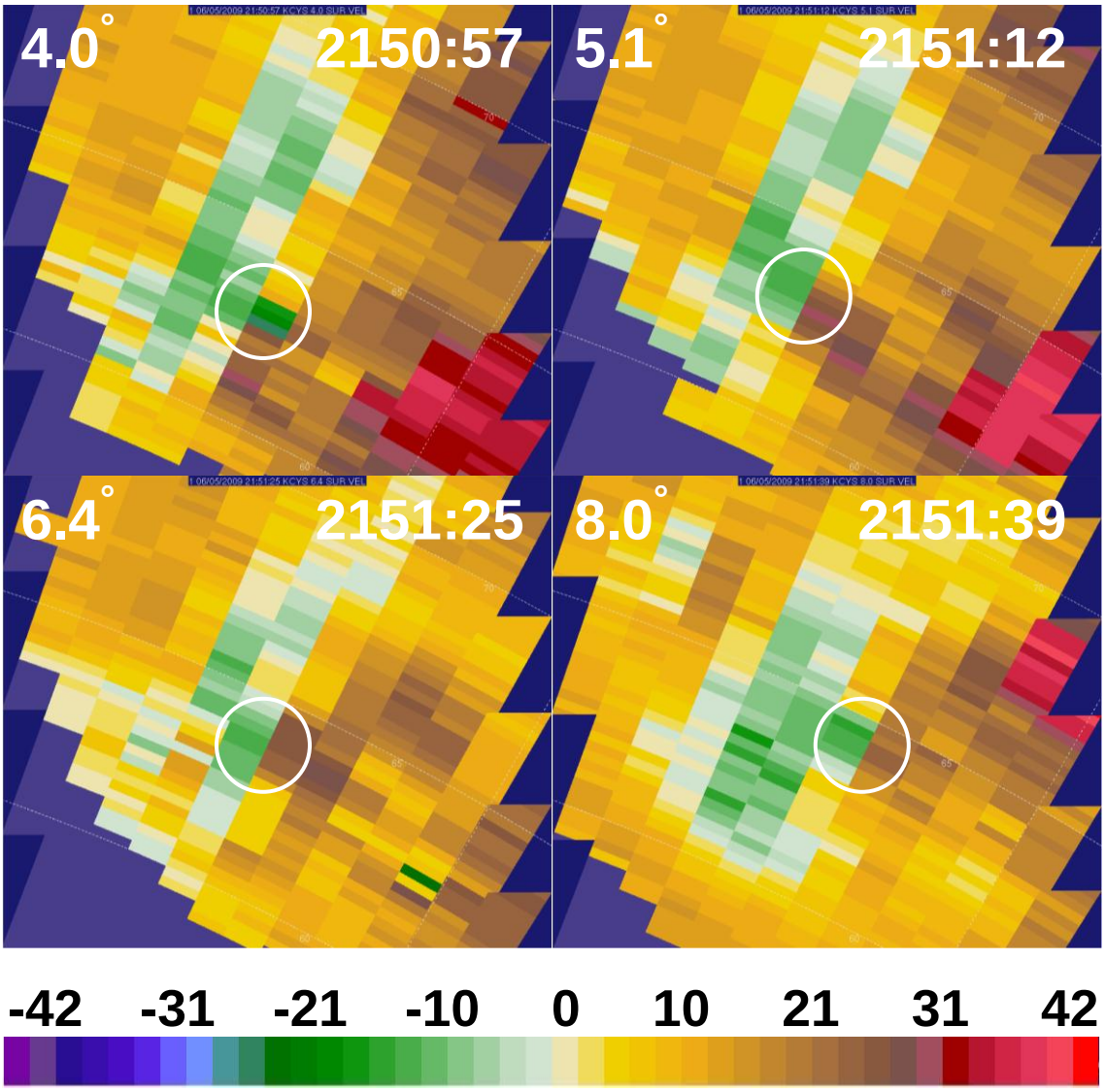

Figure 6.3. PPIs of radial velocity (m s^{-1}) from the KCYS WSR-88D at the ten lowest elevation angles at ~0150 UTC on 5 June 2009. TVSs are enclosed by white circles. Range rings are every 5 km. The scale appears below the figure.

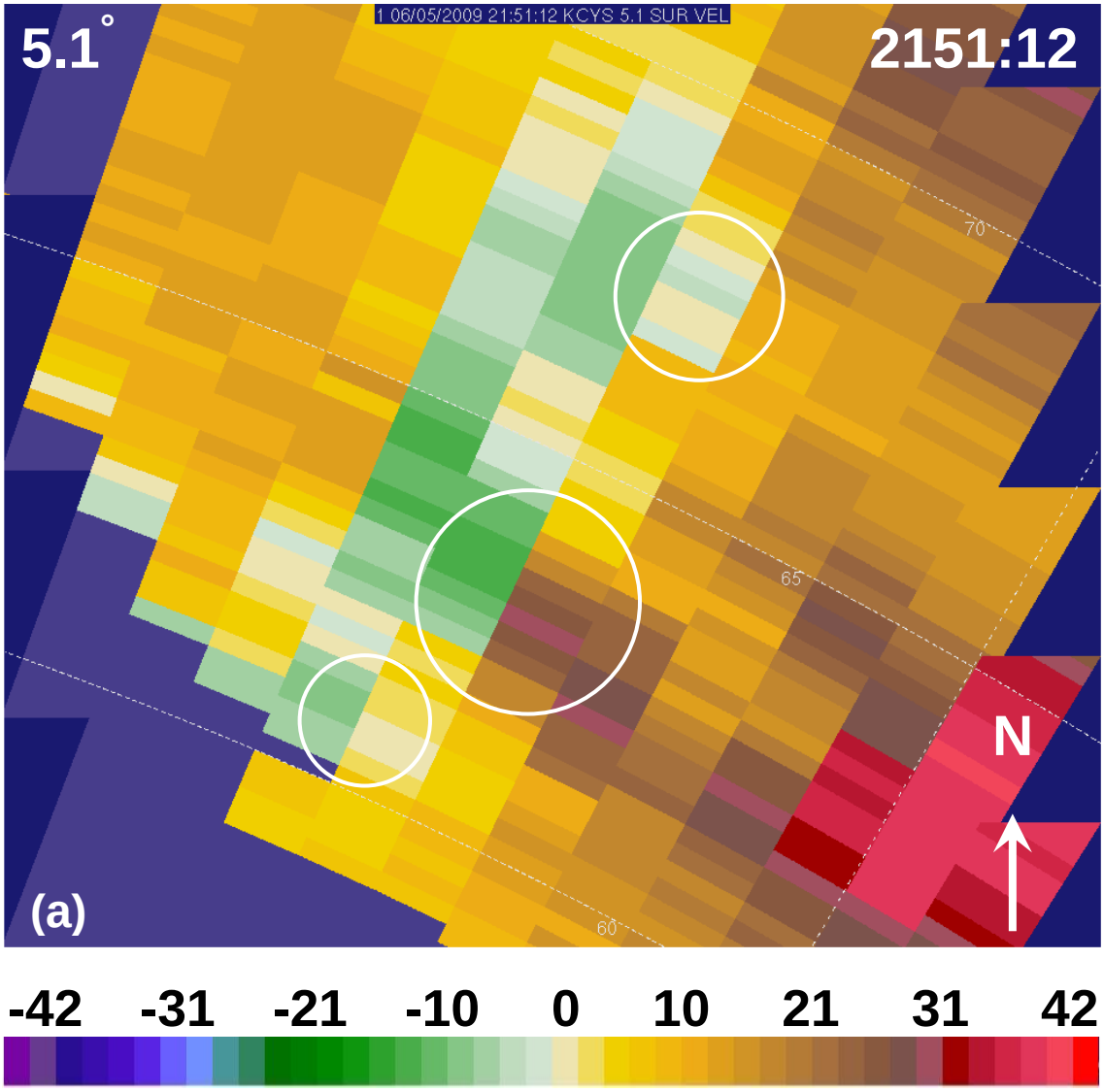

Figure 6.4. PPIs of radial velocity (m s^{-1}) from the (a) KCYS WSR-88D at 5.1° elevation angle and (b) MWR-05XP at 18.5° elevation angle at 2151:10 UTC on 5 June 2009. TVSs are enclosed by white circles. Range rings are every 5 km in (a) and 1 km in (b). The approximate center beam height at the location of the TVS is ~5.5 km in (a) and 6.0 km in (b). The radial velocity scales differ and appear below the respective images.

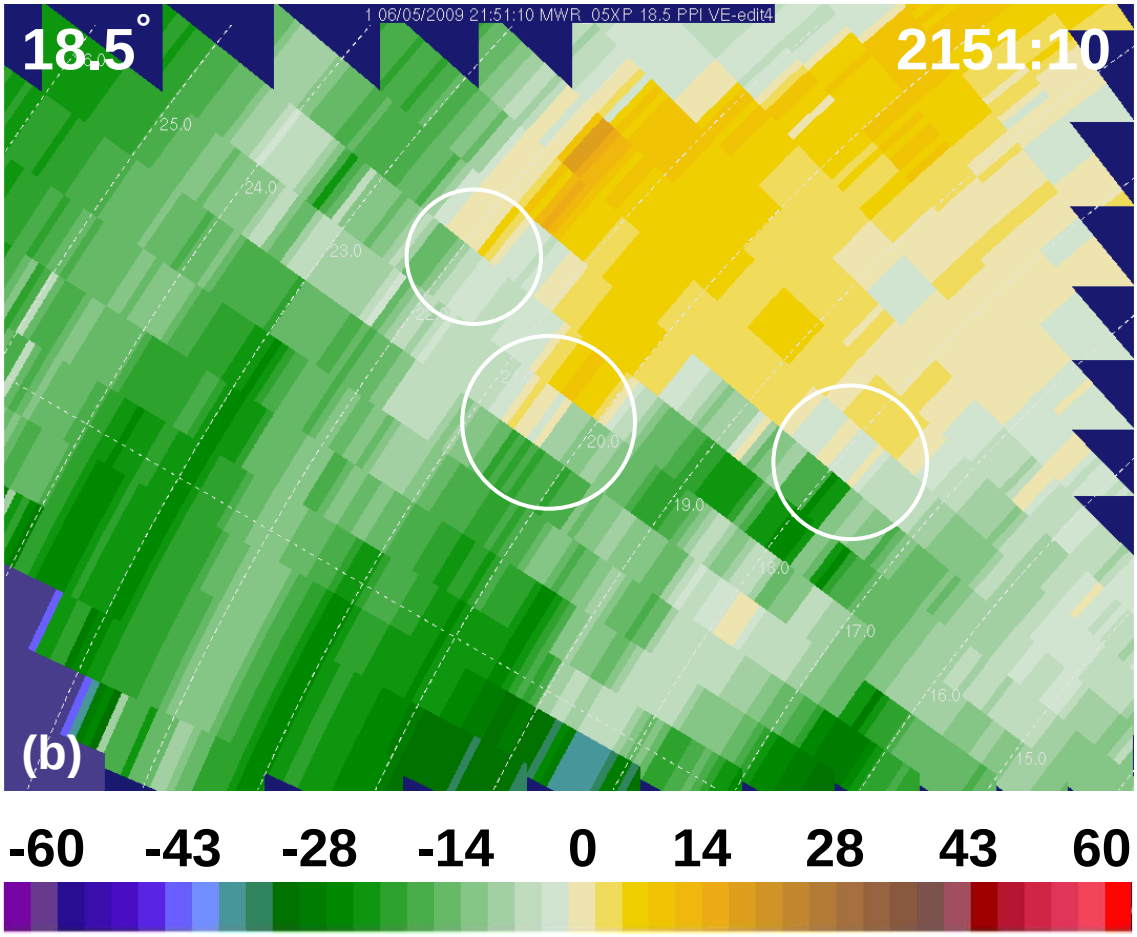
1 06/05/2009 21:51:10 MWR_05XP 18.5 PPI VE-edit4
18.5°
2151:10
25.0
24.0
23.0
20.0
19.0
18.0
17.0
16.0
15.0
(b)
-60 -43 -28 -14 0 14 28 43 60

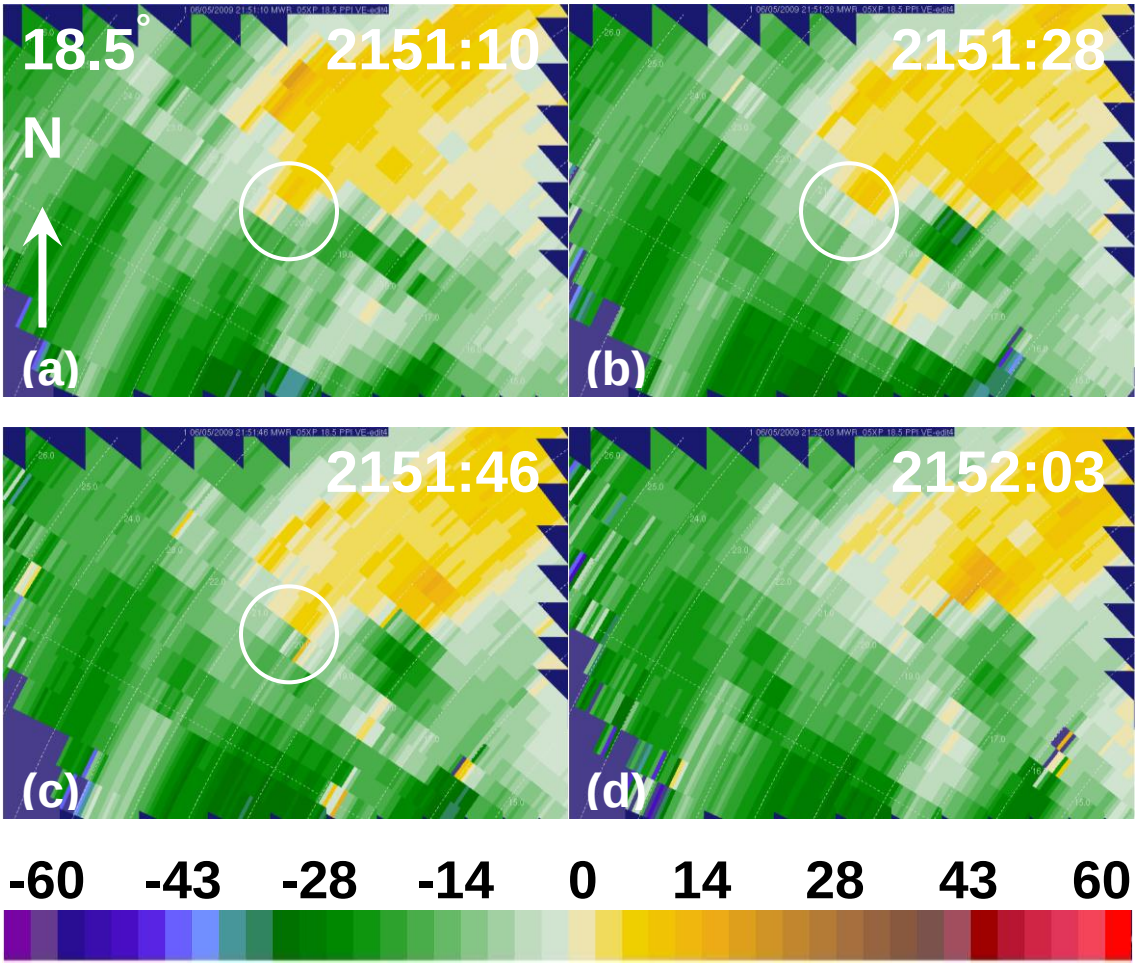

Figure 6.5. PPIs of radial velocity (m s^{-1}) from the MWR-05XP at 18.5° elevation angle at (a) 2151:10, (b) 2151:28, (c) 2151:46, and (d) 2152:03 UTC on 5 June 2009. The main TVS discussed in the text is enclosed by white circles. Range rings are every 1 km. The approximate center beam height at the location of the TVS is ~6.0 km. The radial velocity scale appears below the figure.

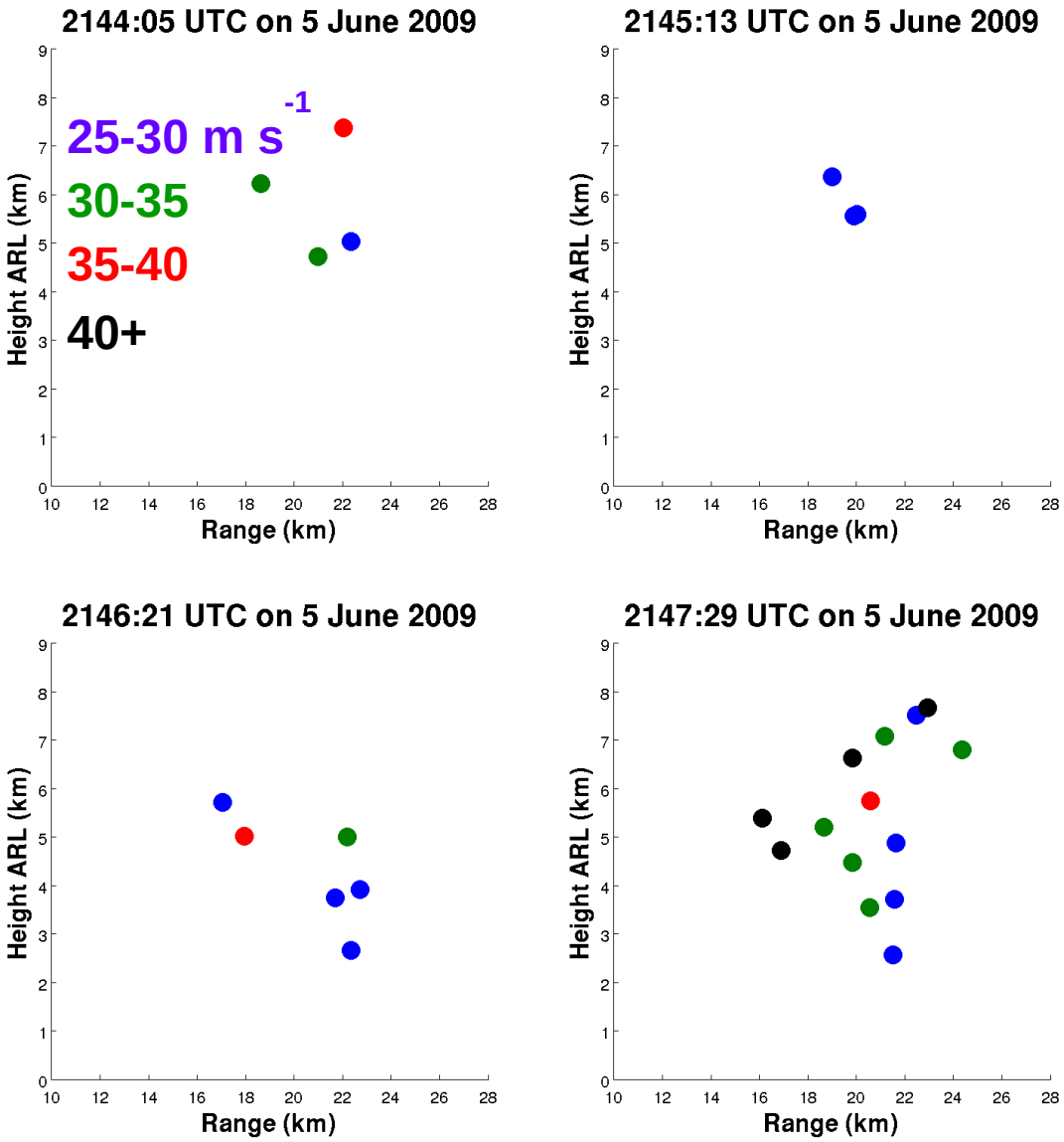

Figure 6.6. RHIs of TVS ΔV (m s^{-1}) every ~70 sec. during the pre-tornadogenesis and tornadogenesis phases of the Goshen County supercell. For the above plots, the ΔV time requirement was relaxed and the threshold increased to 25 m s^{-1}. The ΔV scale appears in the first image.

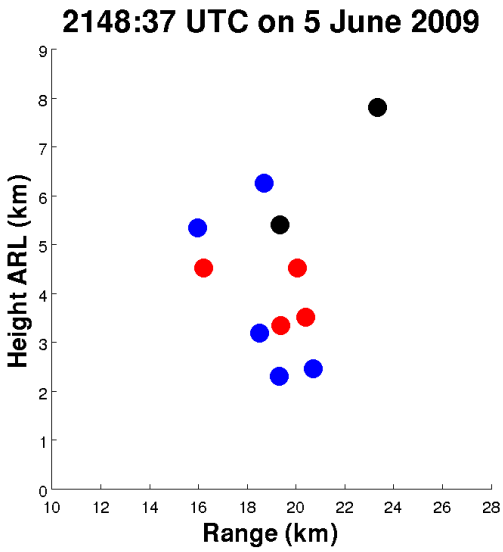
2148:37 UTC on 5 June 2009
Height ARL (km)
Range (km)

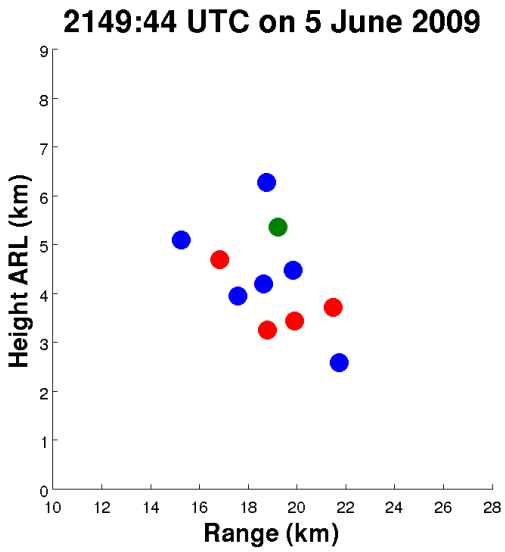
2149:44 UTC on 5 June 2009
Height ARL (km)
Range (km)

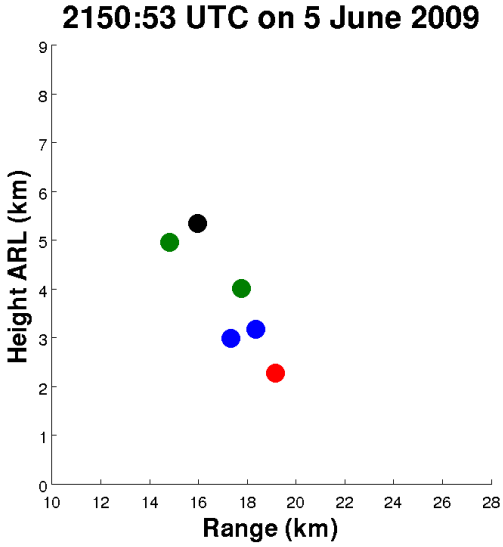
2150:53 UTC on 5 June 2009
Height ARL (km)
Range (km)

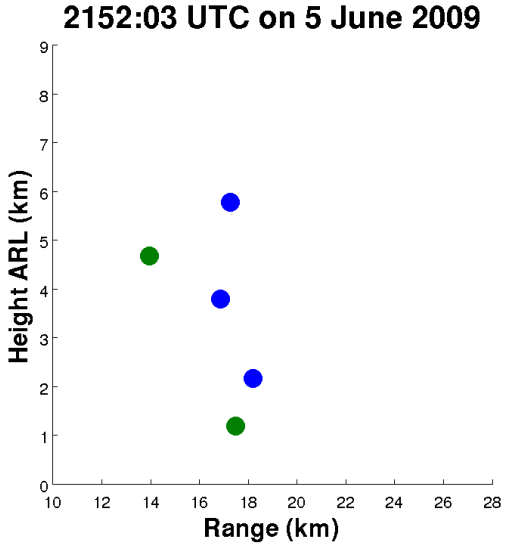
2152:03 UTC on 5 June 2009
Height ARL (km)
Range (km)

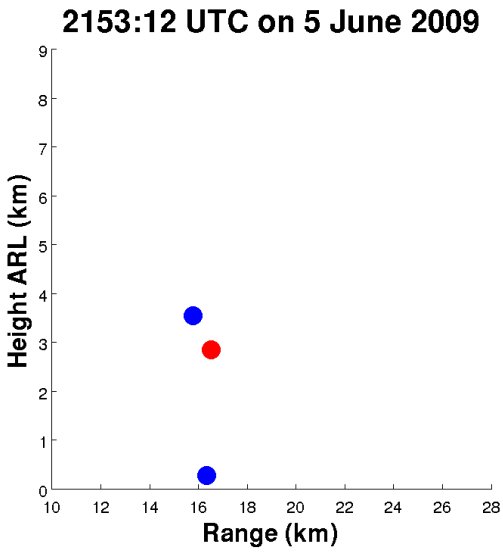
2153:12 UTC on 5 June 2009
Height ARL (km)
Range (km)

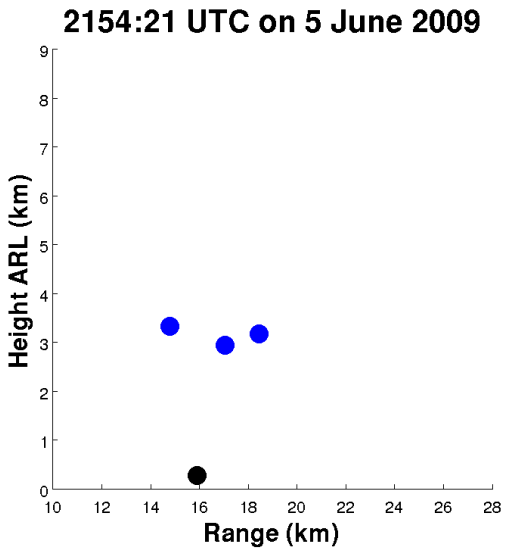
2154:21 UTC on 5 June 2009
Height ARL (km)
Range (km)

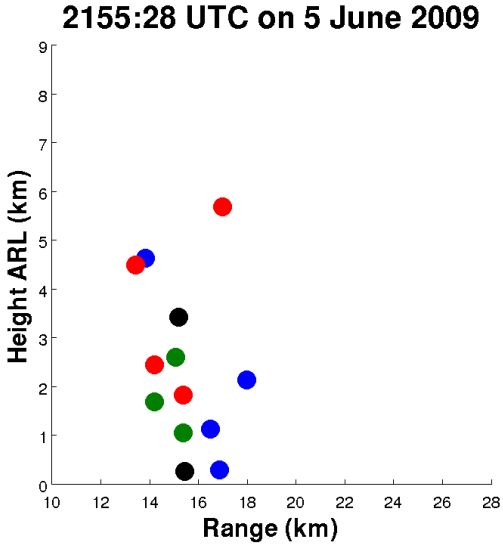
2155:28 UTC on 5 June 2009
Height ARL (km)
Range (km)

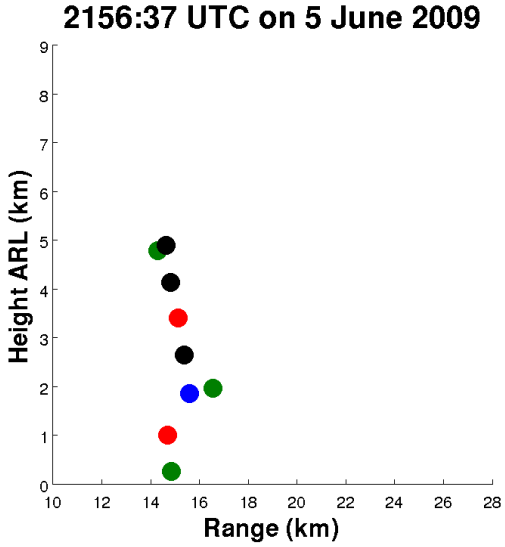
2156:37 UTC on 5 June 2009
Height ARL (km)
Range (km)

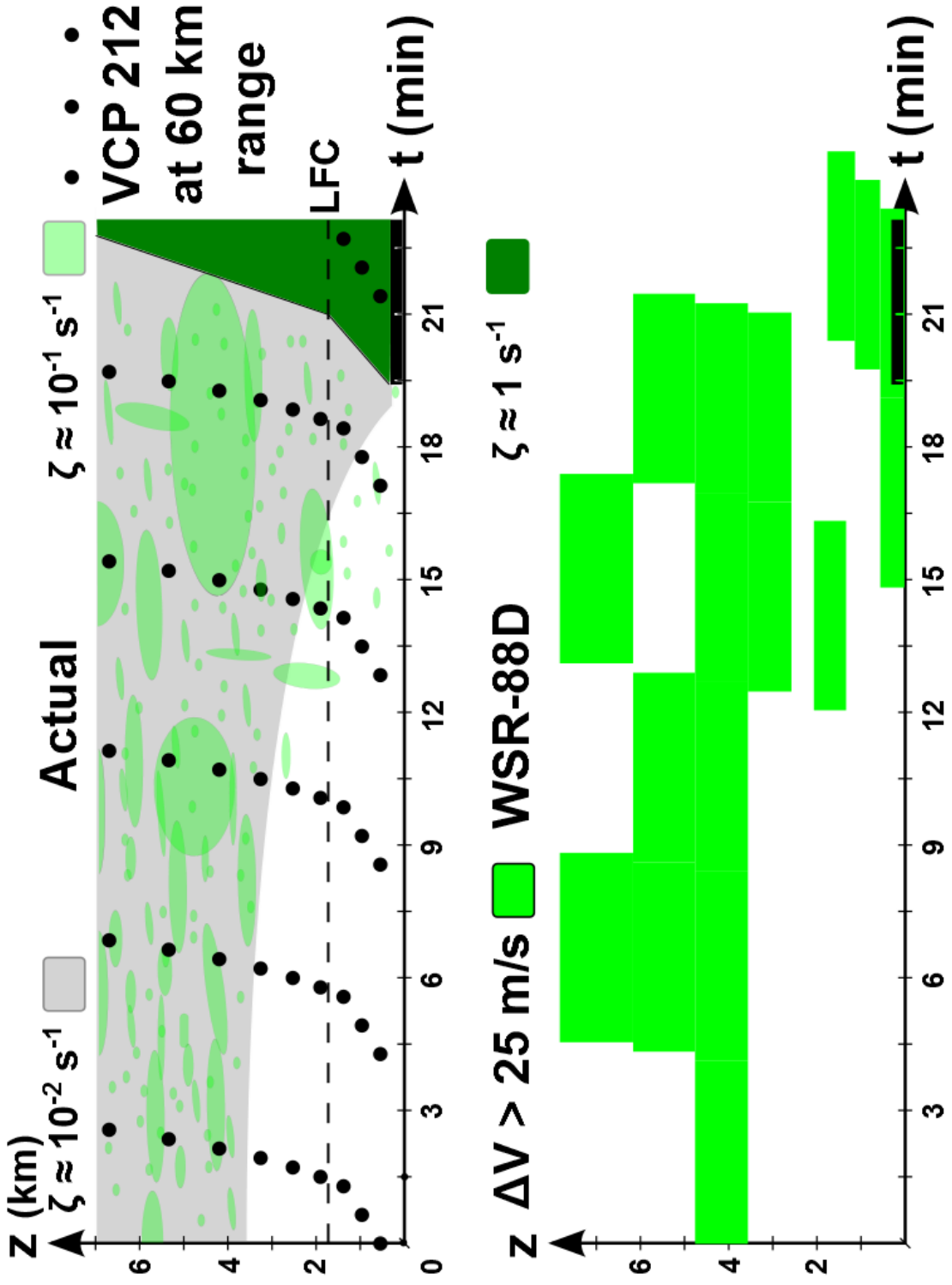

Fig. 6.7. Conceptual model illustrating how enhanced levels of vertical vorticity within a mesocyclone that builds down to the surface might appear as a descending incipient tornado in WSR-88D data.

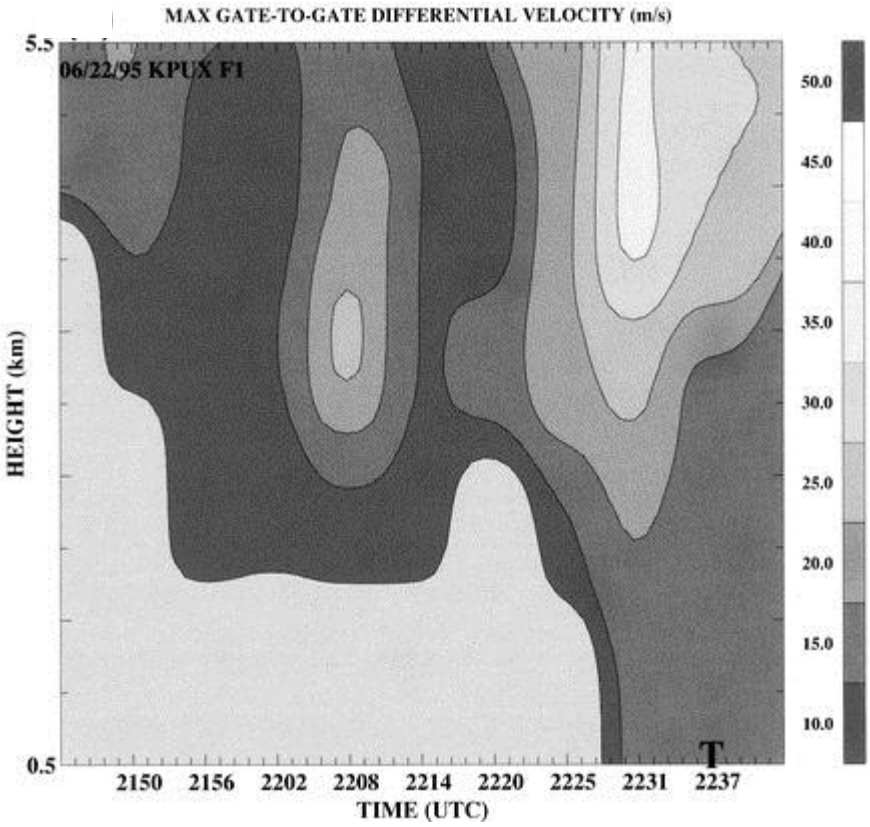

Figure 6.8. Time-height diagram of maximum, GTG differential velocity, ΔV (m s^{-1}) from the 22 June 1995 tornadic storm near Falcon, CO (descending TVS). Bold T denotes tornado time. From Trapp et al. (1999).

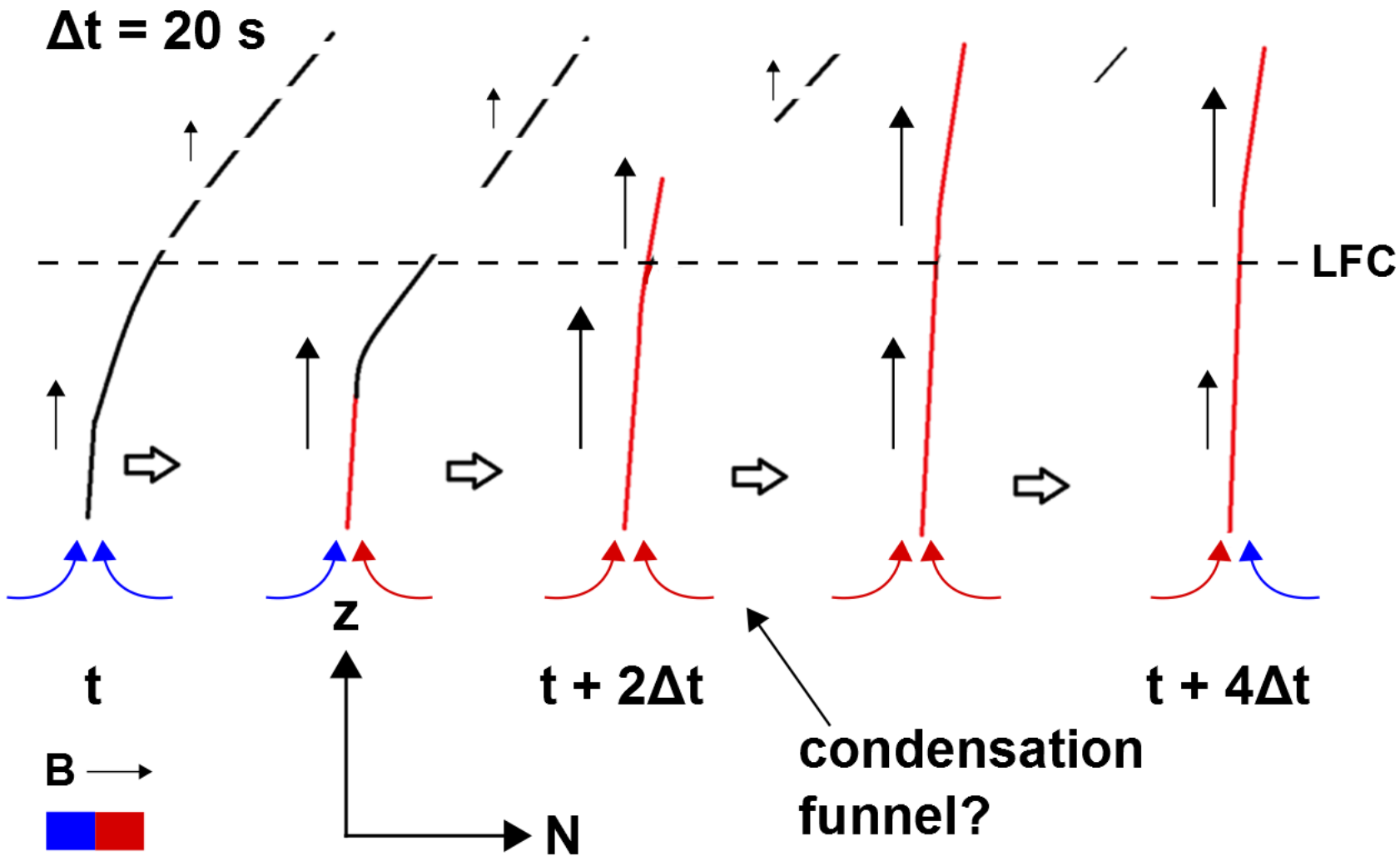
Δt = 20 s
LFC
z
t
t + 2Δt
t + 4Δt
B
N
condensation
funnel?

Fig. 6.9. Conceptual model illustrating how updraft pulses caused by changes in the buoyancy of tornado inflow can modulate the intensity of the tornado aloft. The colored arrows represent tornado inflow and the black arrows are qualitative indicators of the strength of the central tornado updraft. Weak (strong) buoyant inflow is shown in blue (red).

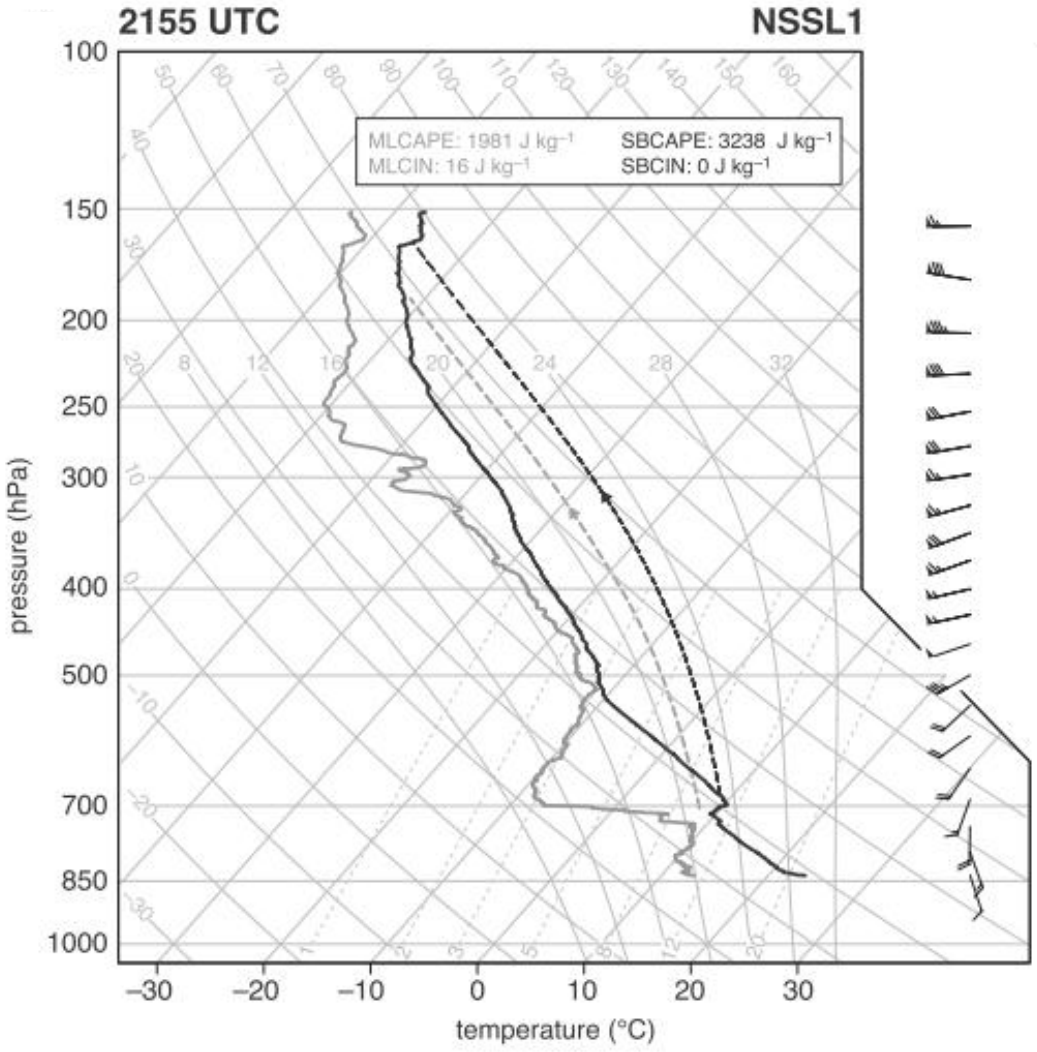

Figure 6.10. Skew T –log p diagram of the 2155 UTC NSSL1 sounding launched southeast of the Goshen County storm. The wind barbs are ground-relative (half-barb = 2.5 m s^{-1}; full-barb = 5 m s^{-1}; flag = 25 m s^{-1}). Surface-based CAPE and CIN (SBCAPE and SBCIN, respectively) and mixed-layer CAPE and CIN (MLCAPE and MLCIN, respectively) are indicated for the black and gray parcel process curves, respectively. The CAPE and CIN calculations include the effects of moisture on buoyancy and are based on the pseudoadiabatic ascent of a parcel lifted from the surface (black), or a lifted parcel having the mean potential temperature and water vapor concentration of the lowest 125 mb (gray). From Markowski et al. (2012a).

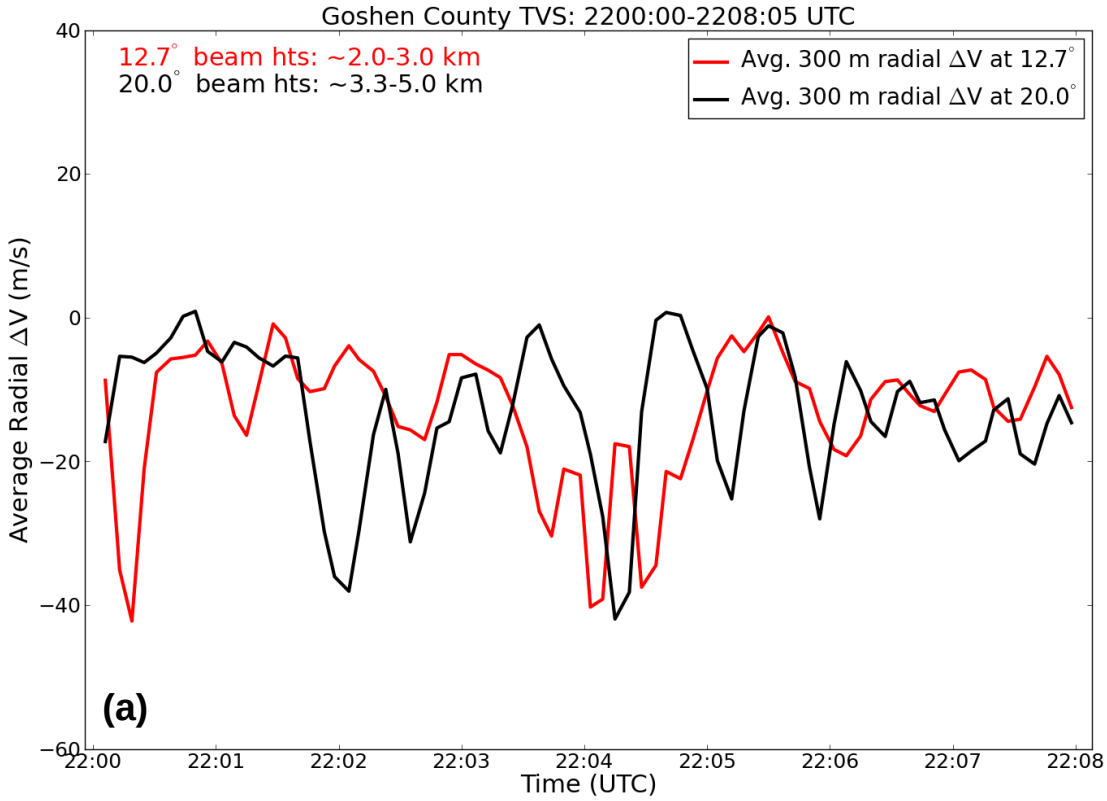
Goshen County TVS: 2200:00-2208:05 UTC
12.7° beam hts: ~2.0-3.0 km
20.0° beam hts: ~3.3-5.0 km
Avg. 300 m radial ΔV at 12.7°
Avg. 300 m radial ΔV at 20.0°
Average Radial ΔV (m/s)
Time (UTC)
(a)

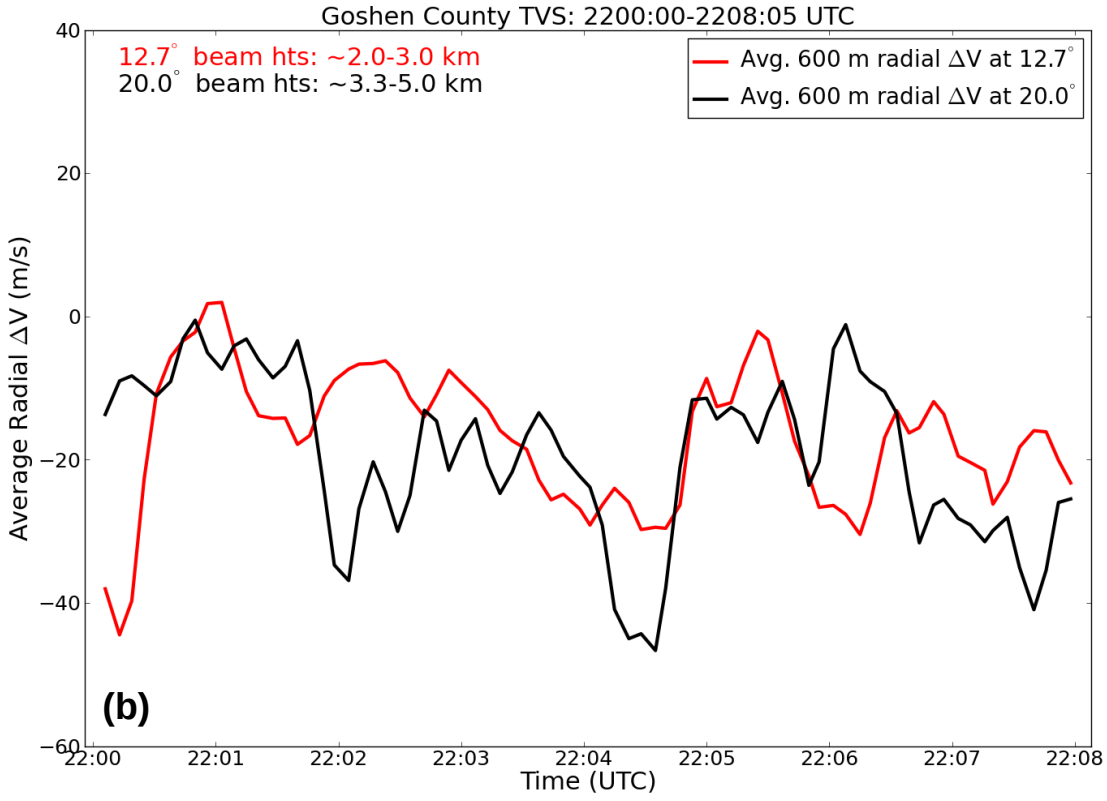
Goshen County TVS: 2200:00-2208:05 UTC
12.7° beam hts: ~2.0-3.0 km
20.0° beam hts: ~3.3-5.0 km
Avg. 600 m radial ΔV at 12.7°
Avg. 600 m radial ΔV at 20.0°
Average Radial ΔV (m/s)
Time (UTC)
(b)

Figure 6.11. Time series of radial ΔV calculated (a) 300 m and (b) 600 m from the maximum inbound radial velocity at 12.7° and 20.0° elevation angle in the Goshen County TVS. As the ordinate values increase, the flow away from the TVS is more divergent. A simple 1-2-1 filter was used to smooth the data. Approximate center beam heights also are provided.

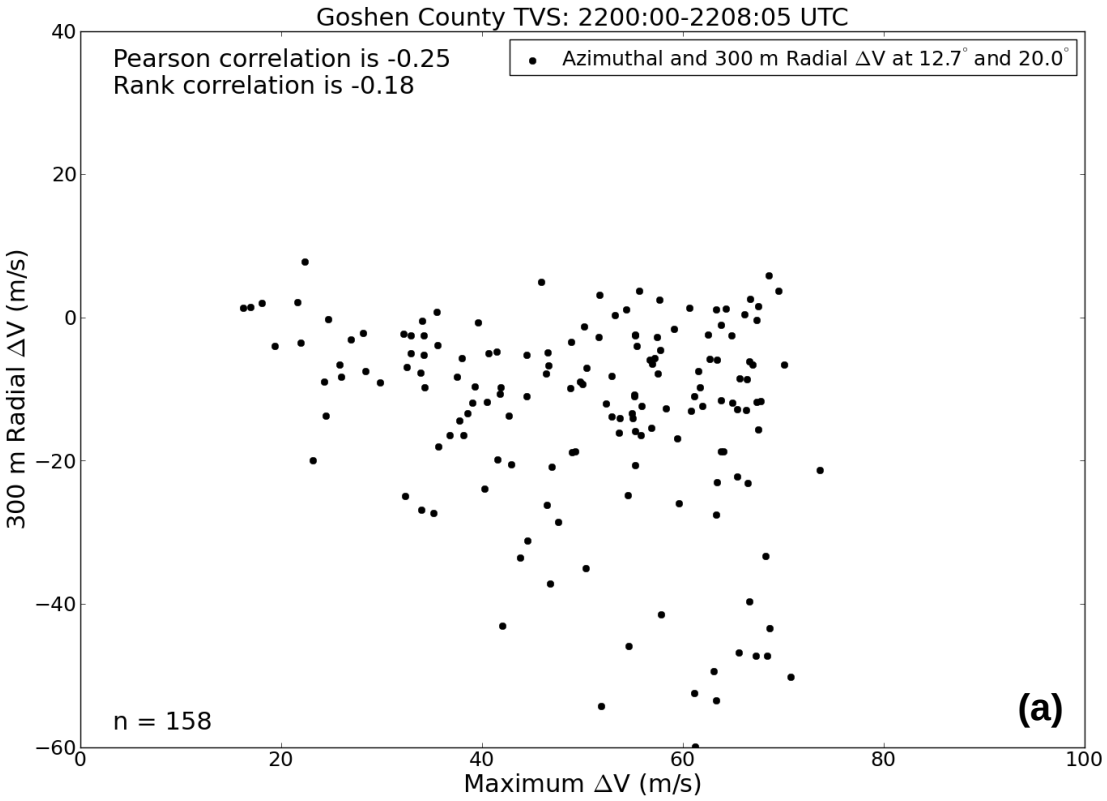
Goshen County TVS: 2200:00-2208:05 UTC
Pearson correlation is -0.25
Rank correlation is -0.18
Azimuthal and 300 m Radial ΔV at 12.7° and 20.0°
300 m Radial ΔV (m/s)
Maximum ΔV (m/s)
n = 158
(a)

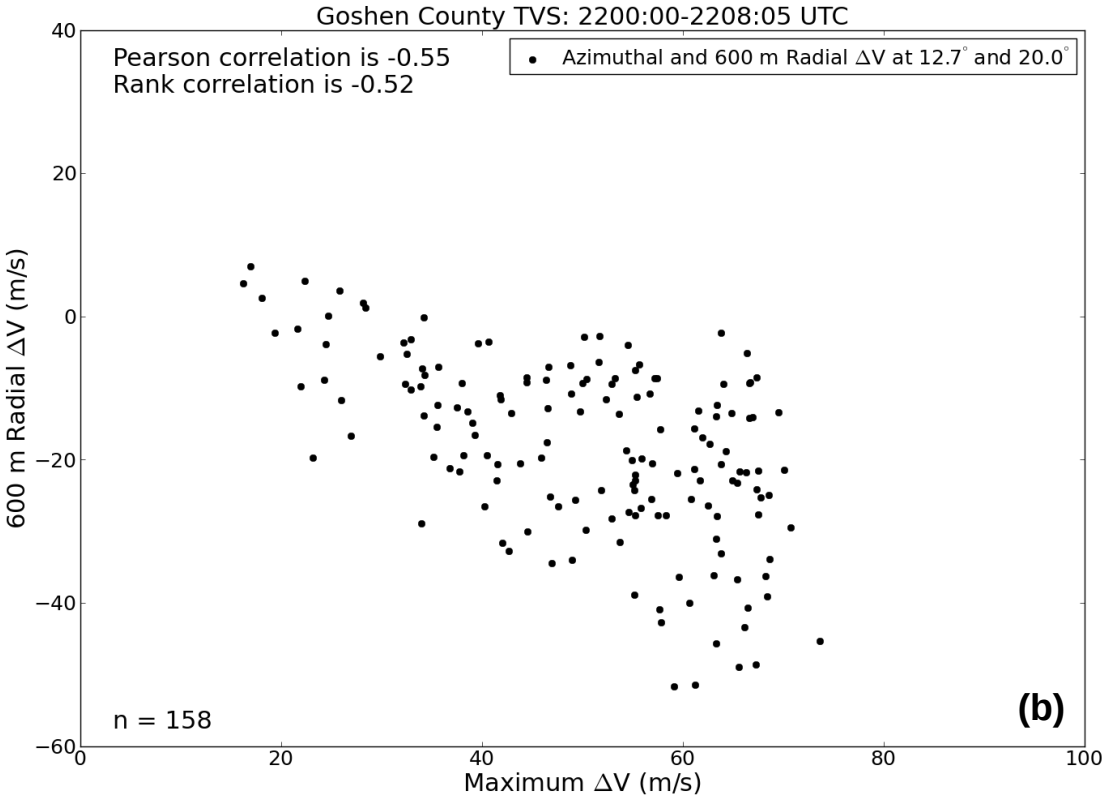
Goshen County TVS: 2200:00-2208:05 UTC
Pearson correlation is -0.55
Rank correlation is -0.52
Azimuthal and 600 m Radial ΔV at 12.7° and 20.0°
600 m Radial ΔV (m/s)
Maximum ΔV (m/s)
n = 158
(b)

Figure 6.12. Scatterplots of TVS ΔV and radial ΔV calculated (a) 300 m and (b) 600 m from the maximum inbound radial velocity at 12.7° and 20.0° elevation angle in the Goshen County TVS. As the ordinate values increase, the flow away from the TVS is more divergent. The number of data points and the Pearson and Rank correlations between the two variables also are provided.

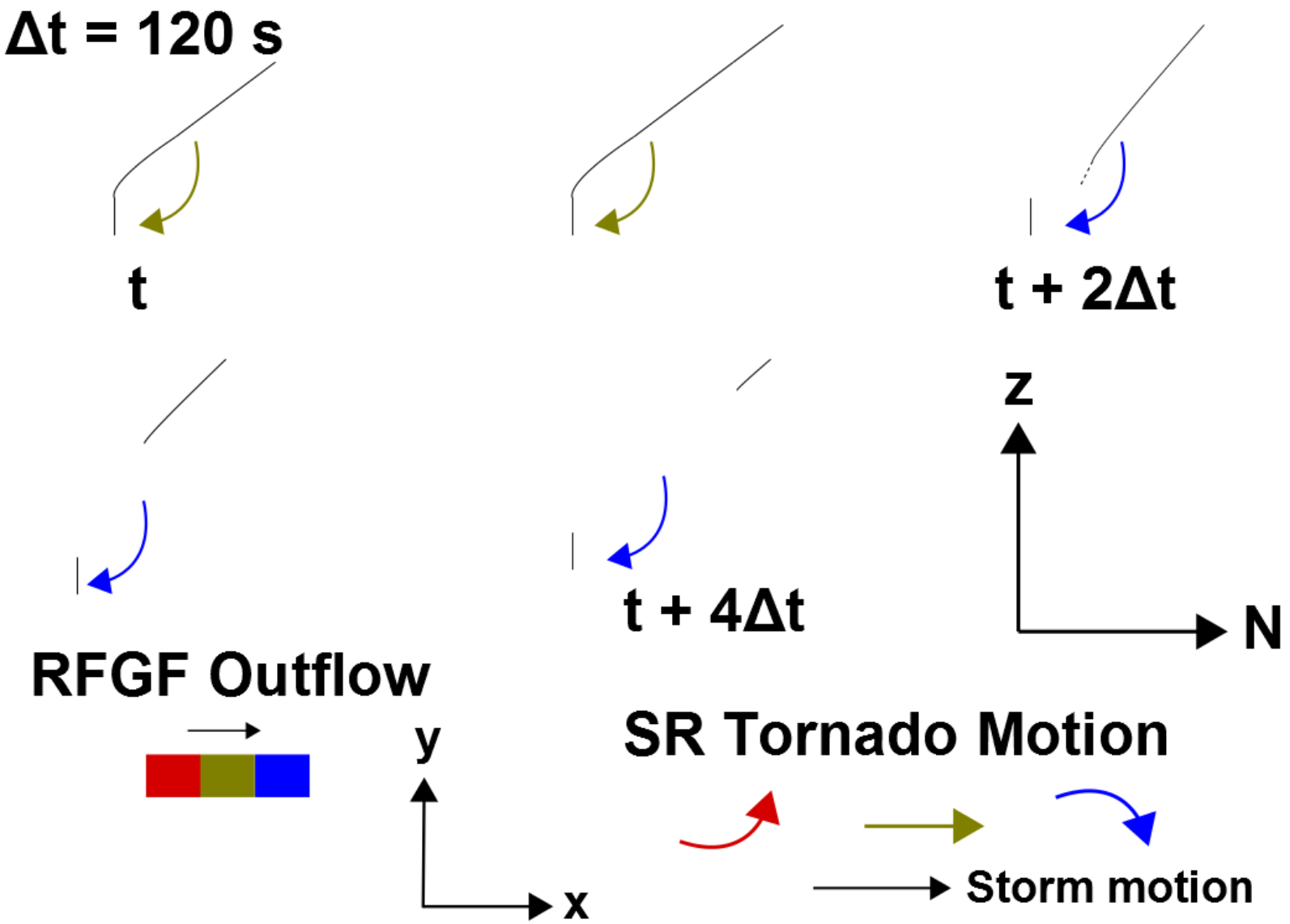
Δt = 120 s
t
t + 2Δt
t + 4Δt
z
N
RFGF Outflow
y
x
SR Tornado Motion
Storm motion

Fig. 6.13. Conceptual model illustrating how a vertically-disconnected tornado caused by changes in rear-flank gust front outflow can lead to tornado dissipation. The colored arrows represent the qualitative strength of rear-flank gust front outflow. In the bottom right, the proposed relationship between storm-relative tornado motion and outflow strength also is shown.

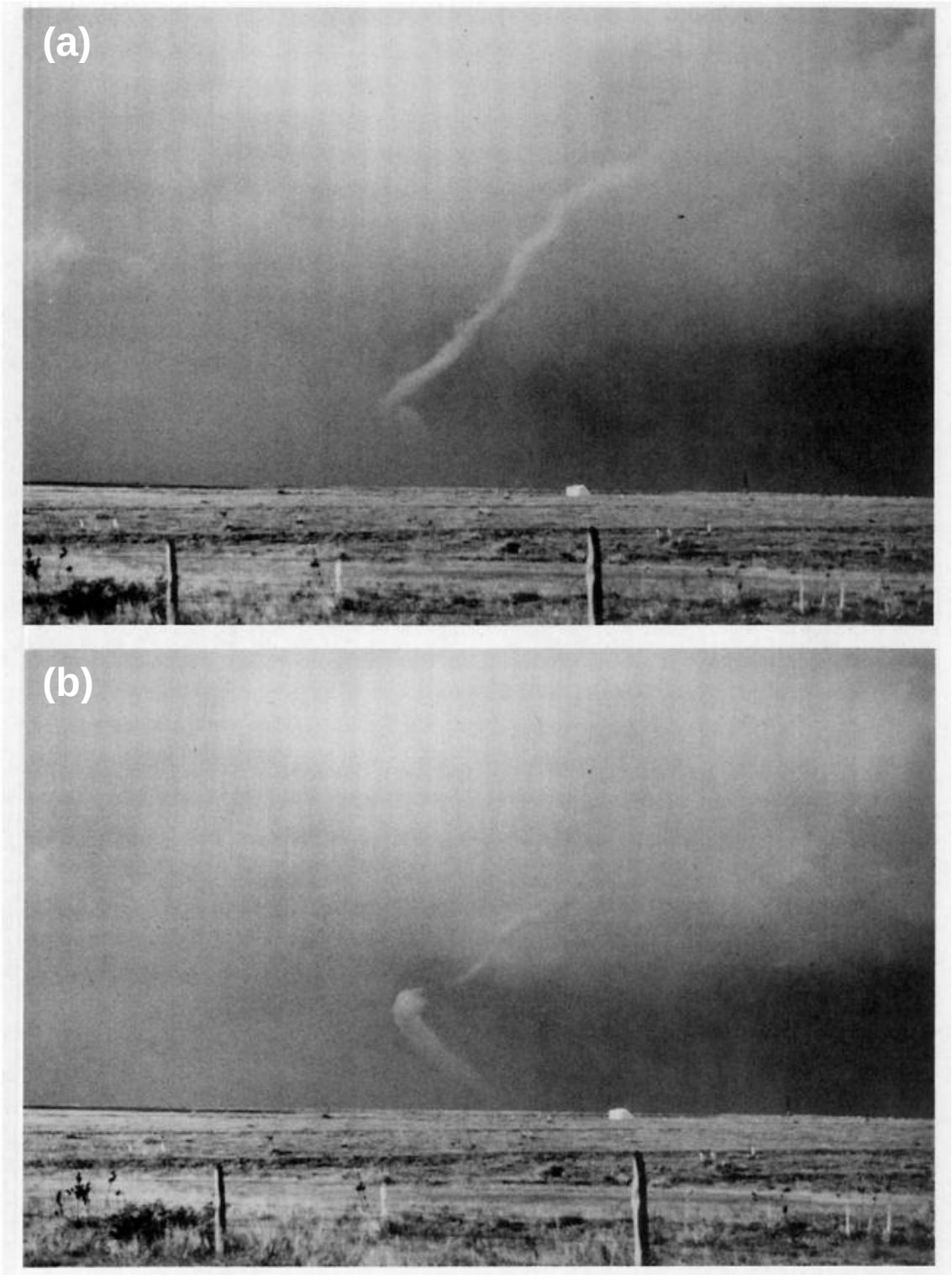
(a)
(b)

Figure 6.14. A tornado about 30 km north-northwest of Canadian, Texas, 8 May 1986 at (a) 0037 and (b),(c) 0038 UTC. View is to the northeast. From Bluestein et al. (1988).

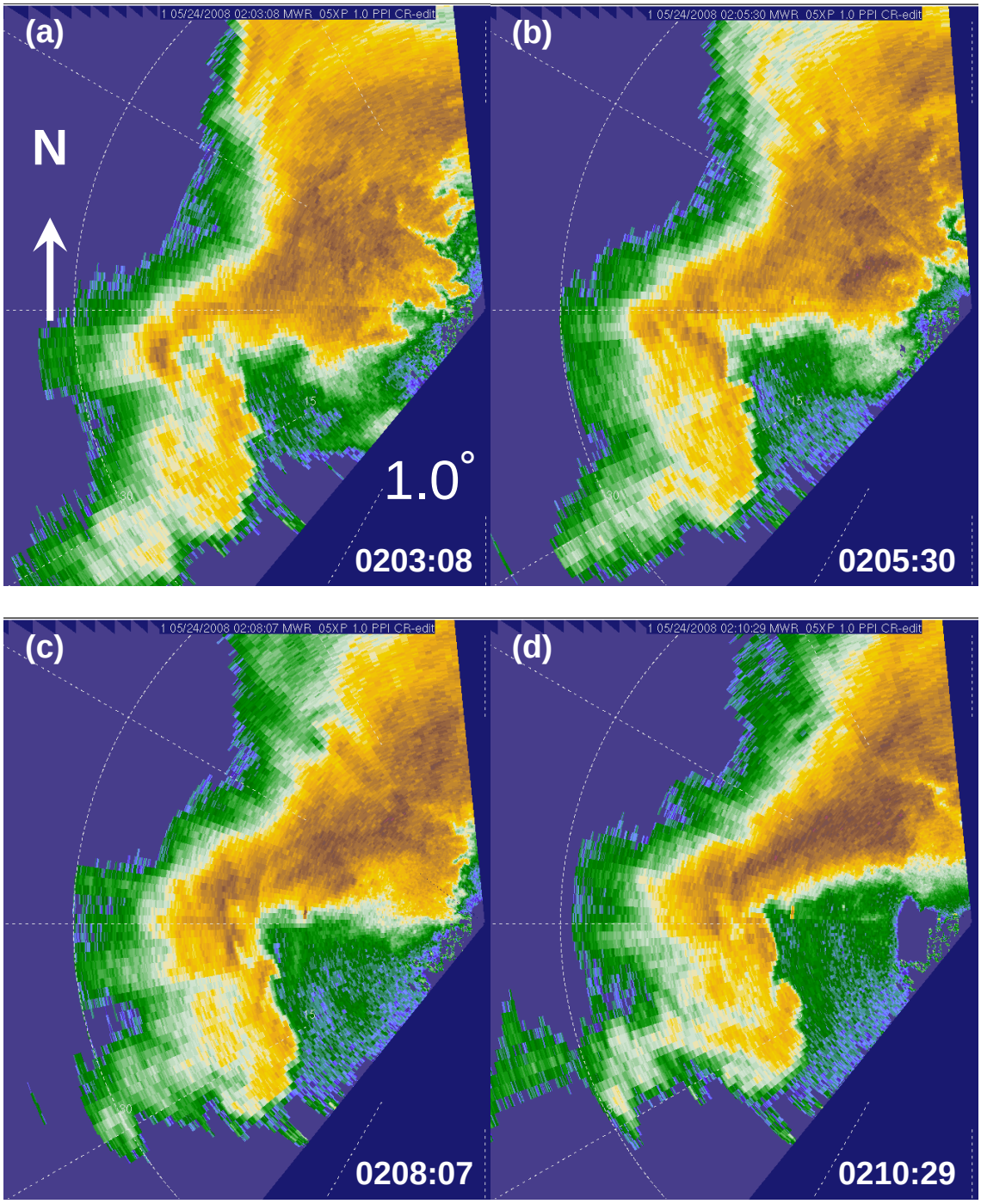
(a)
1 05/24/2008 02:03:08 MWR_05XP 1.0 PPI CR-edit
N
1.0°
0203:08
(b)
1 05/24/2008 02:05:30 MWR_05XP 1.0 PPI CR-edit
0205:30
(c)
1 05/24/2008 02:08:07 MWR_05XP 1.0 PPI CR-edit
0208:07
(d)
1 05/24/2008 02:10:29 MWR_05XP 1.0 PPI CR-edit
0210:29

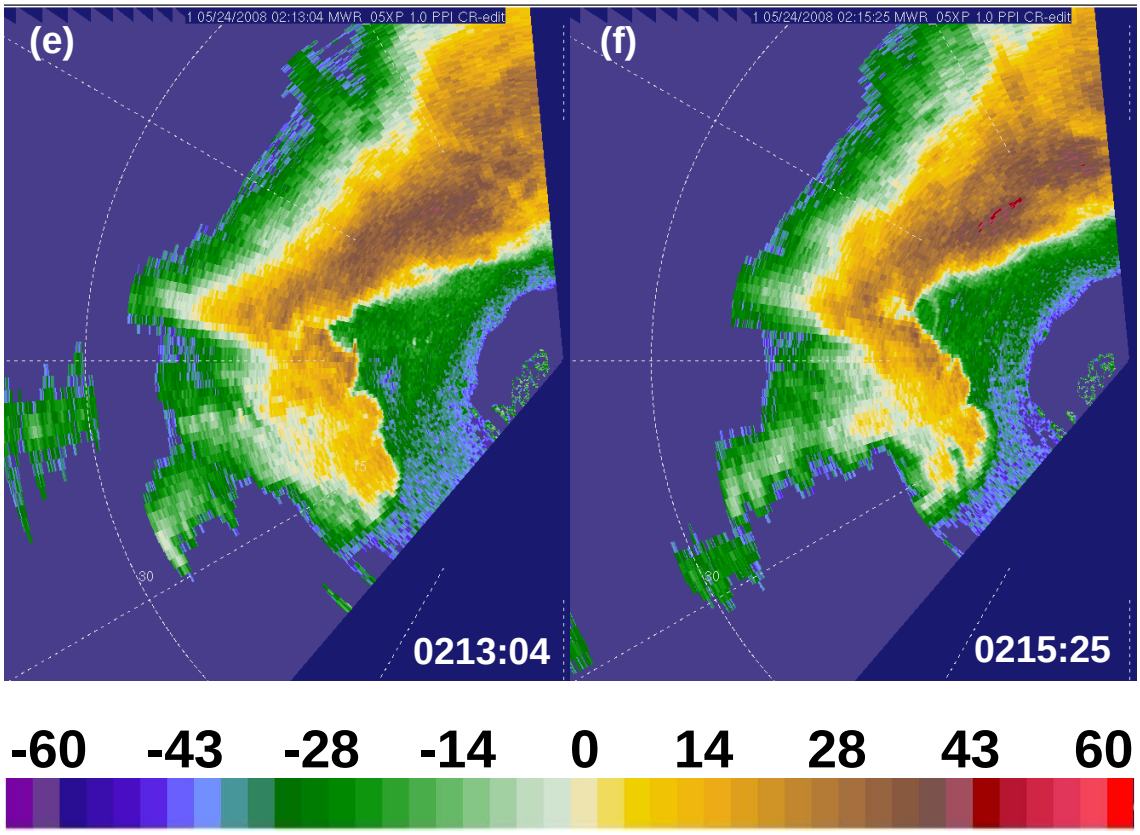

Figure 6.15. Reflectivity (dBZ) PPIs of the rear flank of the Ellis supercell from 1.0° elevation angle at (a) 0203:08, (b) 0205:30, (c) 0208:07, (d) 0210:29, (e) 0213:04, and (f) 0215:25 UTC on 24 May 2008. Range rings are every 15 km. The approximate center beam heights at the forward edge of the reflectivity gradient are ~0.25-0.35 km ARL. The colorbar for reflectivity appears beneath the figure.

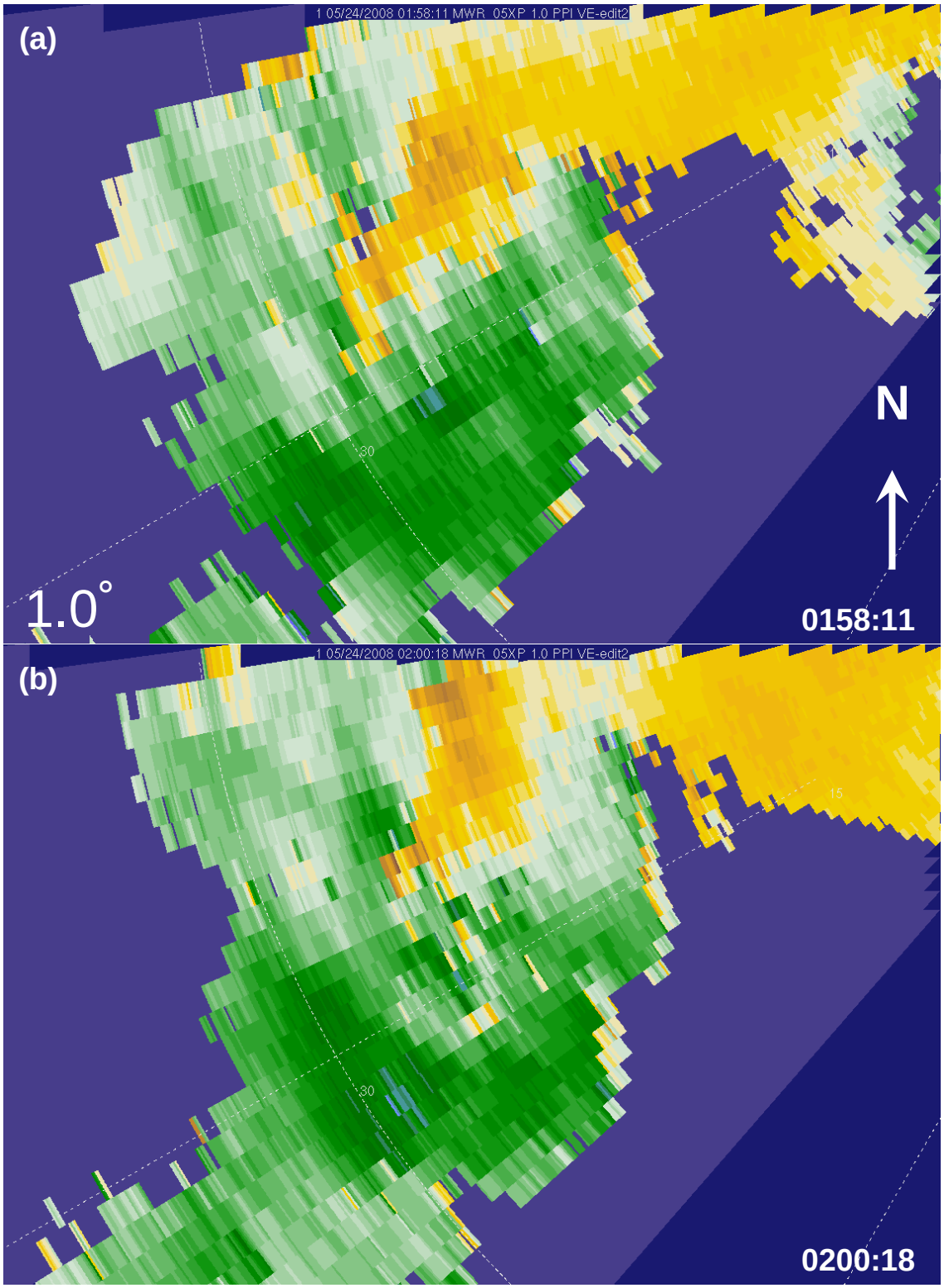
1 05/24/2008 01:58:11 MWR_05XP 1.0 PPI VE-edit2
(a)
N
30
1.0°
0158:11
1 05/24/2008 02:00:18 MWR_05XP 1.0 PPI VE-edit2
(b)
15
30
0200:18

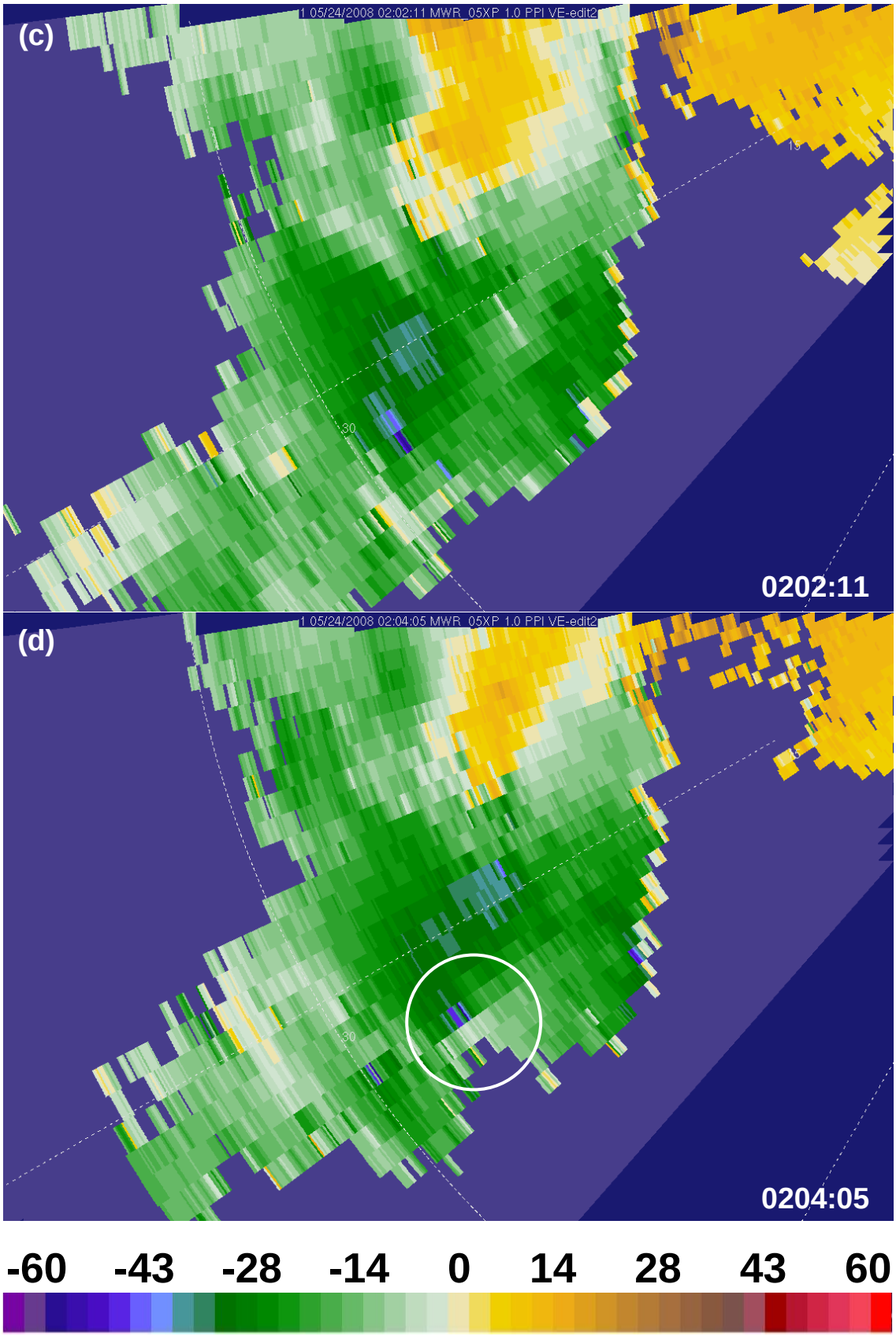
(c)
1 05/24/2008 02:02:11 MWR_05XP 1.0 PPI VE-edit2
30
0202:11
(d)
1 05/24/2008 02:04:05 MWR_05XP 1.0 PPI VE-edit2
30
0204:05
-60 -43 -28 -14 0 14 28 43 60

Figure 6.16. Radial velocity (m s^{-1}) PPIs at 1.0° elevation angle at (a) 0158:11, (b) 0200:18, (c) 0202:11, and (d) 0204:05 UTC preceding the EAC tornado on 24 May 2008. The region of anticyclonic shear where the EAC tornado TVS formed is enclosed by a white circle. Approximate center beam heights for the area in question are ~0.5 km ARL. Range rings are every 15 km. The colorbar for radial velocity appears beneath the figure.

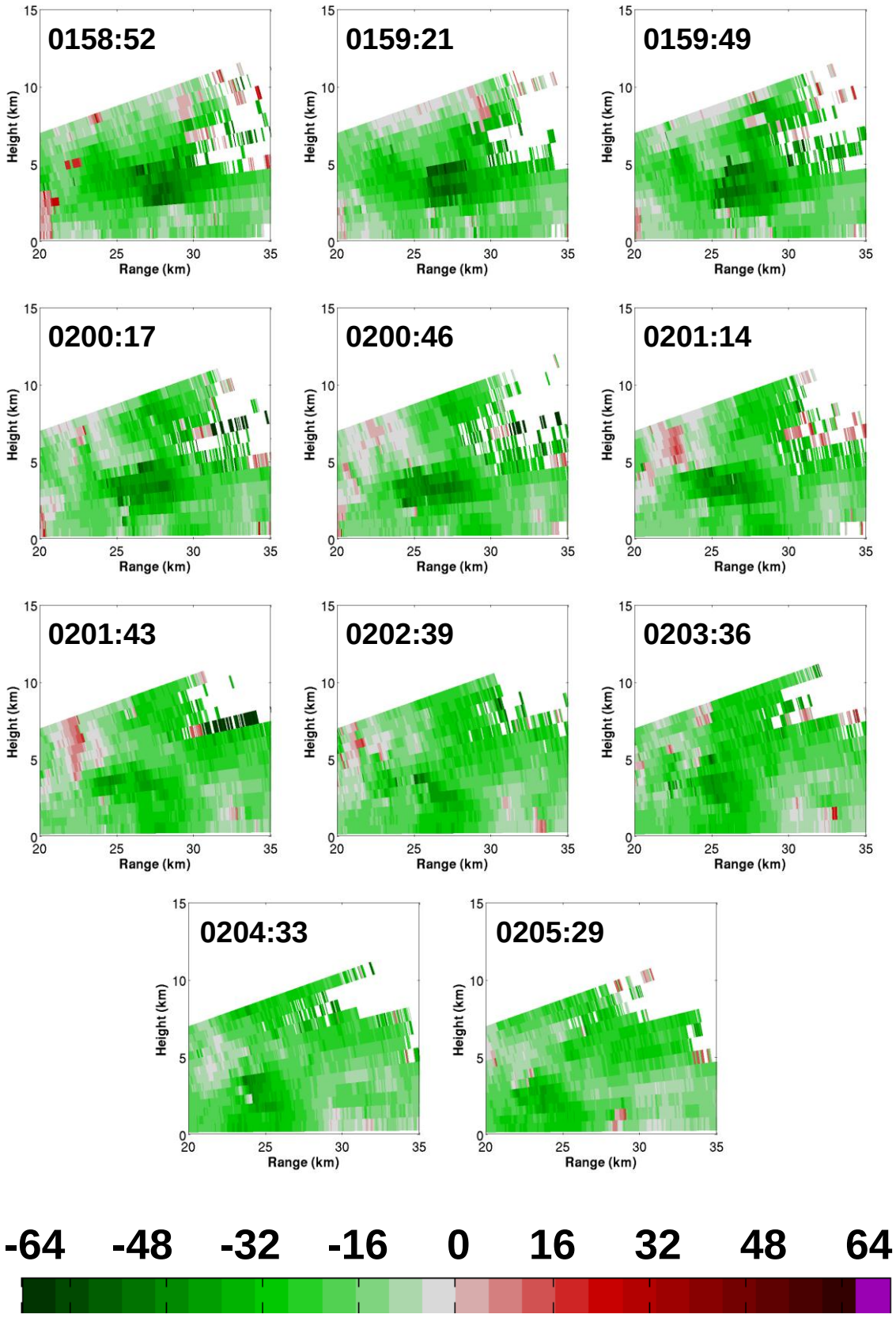
0158:52
0159:21
0159:49
0200:17
0200:46
0201:14
0201:43
0202:39
0203:36
0204:33
0205:29
Height (km)
Range (km)
0
5
10
15
20
25
30
35
-64
-48
-32
-16
0
16
32
48
64

Figure 6.17. Range height indicator (RHI) displays of radial velocity (m s^{-1}) at 240° azimuth prior to EAC tornadogenesis. RHIs are every 30-60 sec. from 0158:52-0205:29 UTC on 24 May 2008. The absolute location is unchanged for all plots. The vertical reference frame is not stretched. Colorbar appears beneath the figure.

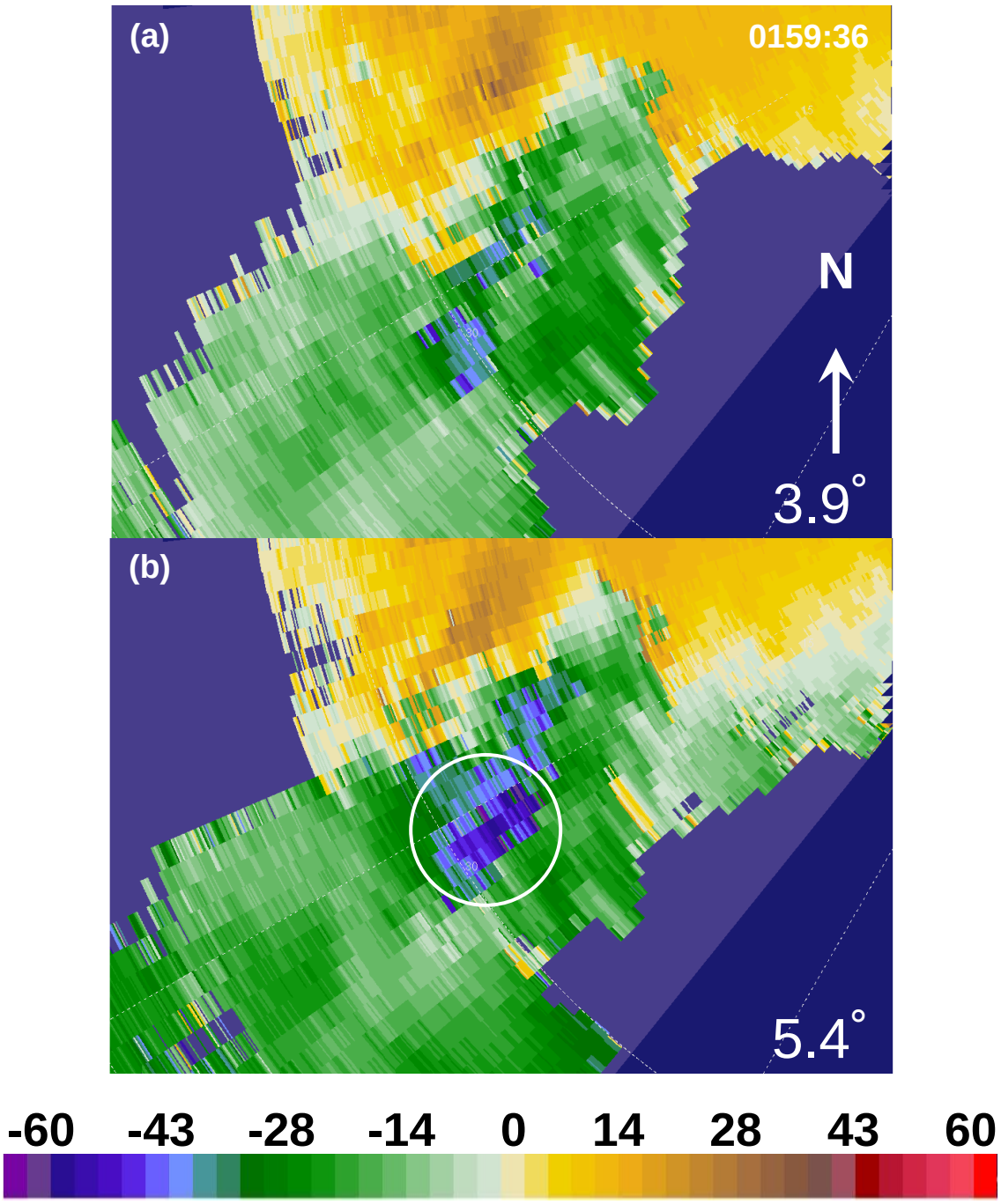

Figure 6.18. Radial velocity (m s^{-1}) PPIs from 0159:36 UTC at (a) 3.9° and (b) 5.4° elevation angle preceding the EAC tornado on 24 May 2008. The jet of inbound velocities present in (b) is enclosed by a white circle. Range rings are every 15 km. Approximate center beam heights for the area in question are ~1.75 (2.4) km ARL for 3.9° (5.4°) elevation angle. The colorbar for radial velocity appears beneath the figure.

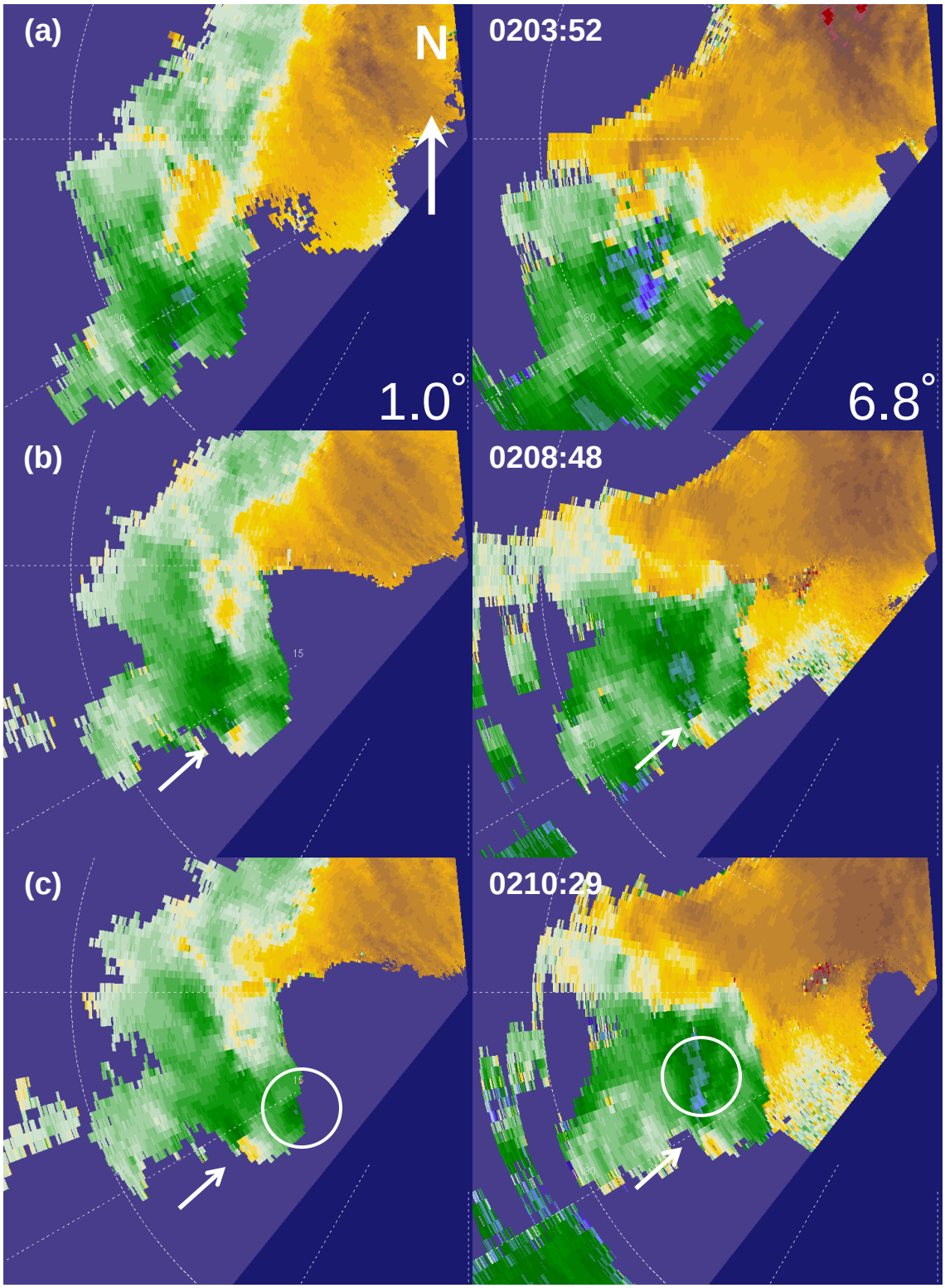
(a)
N
1.0°
0203:52
6.8°
(b)
0208:48
(c)
0210:29

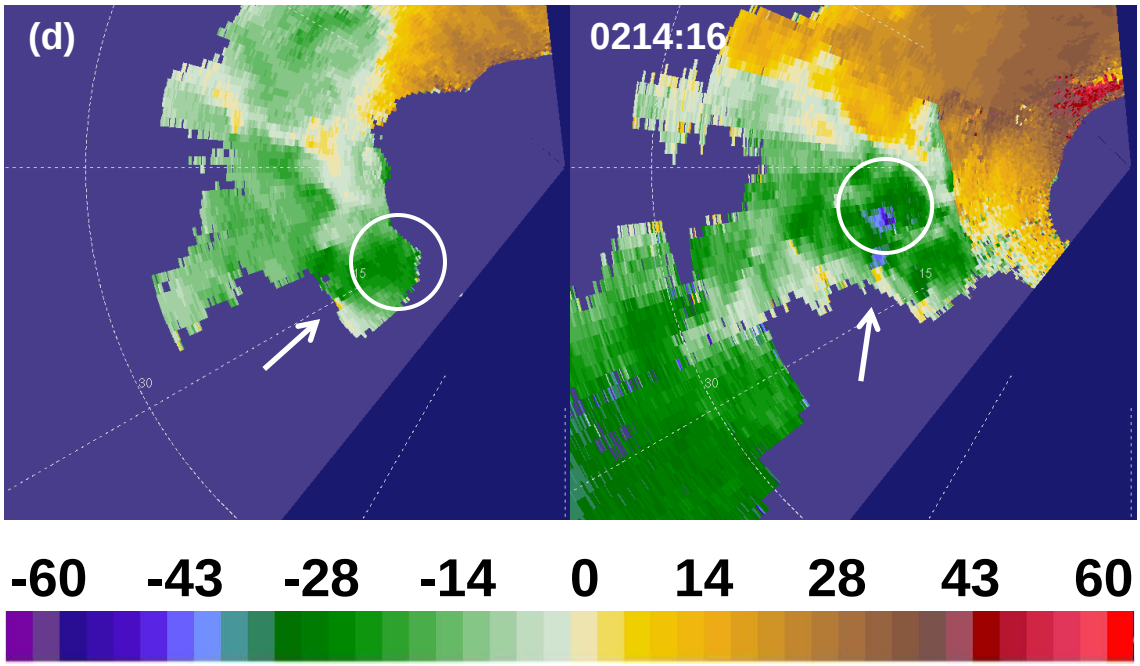

Figure 6.19. Radial velocity (m s^{-1}) PPIs at 1.0° elevation angle (left) and 6.8° elevation angle (right) at (a) 0203:52, (b) 0208:48, (c) 0210:29, and (d) 0214:16 UTC for the EAC tornado on 24 May 2008. The EAC TVS can be identified by a white arrow. The region of strongest inbound radial velocities outside of the EAC TVS is enclosed by a white circle. Approximate center beam heights for the EAS TVS are ~0.3-0.5 (1.75-3.0) km ARL at 1.0° (6.8°) elevation angle. Range rings are every 15 km. The colorbar for radial velocity appears beneath the figure.

References

Adler, R.F., and D.D. Fenn, 1981: Satellite-observed cloud-top height changes in tornadic thunderstorms. *J. Appl. Meteor.*, **20**, 1369–1375.

Agee, E.M., J.T. Snow, and P.R. Clare, 1976: Multiple vortex families in the tornado cyclone and the occurrence of tornado families. Mon. Wea. Rev., 104, 552-563.

Agee, E., C. Church, C. Morris, and J. Snow, 1975: Some synoptic aspects and dynamic features of vortices associated with the tornado outbreak of 3 April 1974. *Mon. Wea. Rev.*, **103**, 318–333.

Alexander, C.R., 2010: A mobile radar based climatology of supercell tornado structure and dynamics. Ph.D. Dissertation, University of Oklahoma, 229 pp.

Alexander, C.R., and J. Wurman, 2008: Updated mobile radar climatology of supercell tornado structure and dynamics. Preprints, *24th Conf. on Severe Local Storms*, Savannah, GA, Amer. Meteor. Soc., 19.4.

Alexander, C.R., and J. Wurman, 2005: The 30 May 1998 Spencer, South Dakota, storm. Part I: The structural evolution and environment of the tornadoes. *Mon. Wea. Rev.*, **133**, 72–97.

Benjamin, T.B., 1962: Theory of vortex breakdown phenomena. *J. Fluid Mech.*, **14**, 593-629.

Bluestein, H.B., M.M. French, I. PopStefanija, R.T. Bluth, and J.B. Knorr, 2010: A mobile, phased-array Doppler radar for the study of severe convective storms. *Bull. Amer. Meteor. Soc.*, **91**, 579–600.

Bluestein, H.B., 2009: The formation and early evolution of the Greensburg, Kansas, tornadic supercell on 4 May 2007. *Wea. Forecasting*, **24**, 899-920.

Bluestein, H.B., C.C. Weiss, M.M. French, E.M. Holthaus, R.L. Tanamachi, S. Frasier, and A.L. Pazmany, 2007a: The structure of tornadoes near Attica, Kansas, on 12 May 2004: High-resolution, mobile, Doppler radar observations. *Mon. Wea. Rev.*, **135**, 475–506.

Bluestein, H.B., M.M. French, R.L. Tanamachi, S. Frasier, K. Hardwick, F. Junyent, and A.L. Pazmany, 2007b: Close-range observations of tornadoes in supercells made with a dual-polarization, X-band, mobile Doppler radar. *Mon. Wea. Rev.*, **135**, 1522–1543.

Bluestein, H.B., C.C. Weiss, and A.L. Pazmany, 2004a: Doppler radar observations of dust devils in Texas. *Mon. Wea. Rev.*, **132**, 209–224.

Bluestein, H.B., C.C. Weiss, and A.L. Pazmany, 2004b: The vertical structure of a tornado near Happy, Texas, on 5 May 2002: High-resolution, mobile, W-band, Doppler radar observations. *Mon. Wea. Rev.*, **132**, 2325–2337.

Bluestein, H.B., C.C. Weiss, and A.L. Pazmany, 2003a: Mobile Doppler radar observations of a tornado in a supercell near Bassett, Nebraska, on 5 June 1999. Part I: Tornadogenesis. *Mon. Wea. Rev.*, **131**, 2954–2967.

Bluestein, H.B., W. Lee, M. Bell, C.C. Weiss, and A.L. Pazmany, 2003b: Mobile Doppler radar observations of a tornado in a supercell near Bassett, Nebraska, on 5 June 1999. Part II: Tornado-vortex structure. *Mon. Wea. Rev.*, **131**, 2968–2984.

Bluestein, H.B., and A.L. Pazmany, 2000: Observations of tornadoes and other convective phenomena with a mobile, 3–mm wavelength, Doppler radar: The spring 1999 field experiment. *Bull. Amer. Meteor. Soc.*, **81**, 2939–2951.

Bluestein, H.B., A.L. Pazmany, J.C. Galloway, and R.E. Mcintosh, 1995: Studies of the substructure of severe convective storms using a mobile 3-mm-wavelength Doppler radar. *Bull. Amer. Meteor. Soc.*, **76**, 2155–2169.

Bluestein, H.B., J.G. Ladue, H. Stein, D. Speheger, and W.F. Unruh, 1993: Doppler radar wind spectra of supercell tornadoes. *Mon. Wea. Rev.*, **121**, 2200–2222.

Bluestein, H.B., E.W. McCaul, G.P. Byrd, and G.R. Woodall, 1988: The unusual dissipation of a tornado funnel. *Mon. Wea. Rev.*, **116**, 950–952.

Brandes, E.A., 1984a: Vertical vorticity generation and mesocyclone sustenance in tornadic thunderstorms: The observational evidence. *Mon. Wea. Rev.*, **112**, 2253–2269.

Brandes, E.A., 1984b: Relationships between radar-derived thermodynamic variables and tornadogenesis. *Mon. Wea. Rev.*, **112**, 1033–1052.

Brandes, E.A., 1981: Finestructure of the Del City-Edmond tornadic mesocirculation. *Mon. Wea. Rev.*, **109**, 635–647.

Brandes, E.A., 1978: Mesocyclone evolution and tornadogenesis: Some observations. *Mon. Wea. Rev.*, **106**, 995–1011.

Brandes, E.A., 1977a: Flow in a severe thunderstorm observed by dual-Doppler radar. *Mon. Wea. Rev.*, **105**, 113–120.

Brandes, E.A., 1977b: Gust front evolution and tornado genesis as viewed by Doppler radar. *J. Appl. Meteor.*, **16**, 333–338.

Brown, R.A., L.R. Lemon, and D.W. Burgess, 1978: Tornado detection by pulsed Doppler radar. *Mon. Wea. Rev.*, **106,** 29–39.

Brown, R.A., and L.R. Lemon, 1976: Single-Doppler radar vortex recognition. Part II: Tornadic vortex signatures. Preprints, *The 17th Conference on Radar Meteorology*, Seattle, WA, Amer. Meteor. Soc., 104-109.

Browning, K., 1965a: Some inferences about the updraft within a severe local storm. *J. Atmos. Sci.*, **22**, 669–677.

Browning, K.A., 1965b: The evolution of tornadic storms. *J. Atmos. Sci.*, **22**, 664–668.

Browning, K.A., 1964: Airflow and precipitation trajectories within severe local storms which travel to the right of the winds. *J. Atmos. Sci.*, **21**, 634–639.

Browning, K.A., and R.J. Donaldson, 1963: Airflow and structure of a tornadic storm. *J. Atmos. Sci.*, **20**, 533–545.

Burgess, D.W., M.A. Magsig, J. Wurman, D.C. Dowell, and Y. Richardson, 2002: Radar observations of the 3 May 1999 Oklahoma City tornado. *Wea. Forecasting*, **17**, 456–471.

Burgess, D.W., R.J. Donaldson Jr., and P.R. Desrochers, 1993: Tornado detection and warning by radar. *The Tornado: Its Structure, Dynamics, Prediction, and Hazards, Geophys. Monogr.*, No. 79, Amer. Geophys. Union, 203–221.

Burgess, D.W., and L.R. Lemon, 1990: Severe thunderstorm detection by radar. *Radar in Meteorology*, D. Atlas, Ed., Amer. Meteor. Soc., 619-647.

Burgess, D.W., L.R. Lemon, and R.A. Brown, 1975: Tornado characteristics revealed by Doppler radar. *Geophys. Res. Lett*., **2**, 183-184.

Burgess, D.W., 1974: Study of a right-moving thunderstorm utilizing new single Doppler radar evidence. M.S. Thesis, Dept. Of Meteorology, University of Oklahoma, 77 pp.

Byko, Z., P. Markowski, Y. Richardson, J. Wurman, and E. Adlerman, 2009: Descending reflectivity cores in supercell thunderstorms observed by mobile radars and in a high-resolution numerical simulation. *Wea. Forecasting*, **24**, 155–186.

Carbone, R.E., M.J. Carpenter, and C.D. Burghart, 1985: Doppler radar sampling limitation in convective storms. *J. Atmos. Oceanic. Technol*., **2**, 357-361.

Chisholm, A.J., 1973: Alberta hailstorms. Part I: Radar case studies and airflow models. *Alberta Hailstorms, Meteor. Monogr.,* No. 36, Amer. Meteor. Soc., 1–36.

Church, C.R., J.T. Snow, G.L. Baker, and E.M. Agee, 1979: Characteristics of tornado-like vortices as a function of swirl ratio: A laboratory investigation. *J. Atmos. Sci.*, **36**, 1755–1776.

Davies-Jones, R.P., 2008: Can a descending rain curtain in a supercell instigate tornadogenesis barotropically? *J. Atmos. Sci.*, **65**, 2469–2497.

Davies-Jones, R.P., R.J. Trapp, and H.B. Bluestein, 2001: Tornadoes and tornadic storms, *Severe Convective Storms*, Meteorological Monogr., No. 50, Amer. Met. Soc., 167-221.

Davies-Jones, R.P., and H.E. Brooks, 1993: Mesocyclogenesis from a theoretical perspective. *The Tornado: Its Structure, Dynamics, Prediction, and Hazards, Geophys. Monogr.*, No. 79, Amer. Geophys. Union, 105–114.

Davies-Jones, R., 1984: Streamwise vorticity: The origin of updraft rotation in supercell storms. *J. Atmos. Sci.*, **41**, 2991–3006.

Davies-Jones, R.P., 1982: Observational and theoretical aspects of tornadogenesis. *Intense Atmospheric Vortices*, L. Bengtsson and J. Lighthill, Eds., Springer-Verlag, 175-189.

Dong, K., and C.J. Neuman, 1983: On the relative motion of binary tropical cyclones. *Mon. Wea. Rev.*, **111**, 945-953.

Doswell, C.A. III, and D.W. Burgess, 1993: Tornadoes and tornadic storms: A review of conceptual models. *The Tornado: Its Structure, Dynamics, Prediction, and Hazards*, Geophys. Monogr. No. 76, Amer. Geophys. Union, 161-172.

Dowell, D.C., C.R. Alexander, J.M. Wurman, and L.J. Wicker, 2005: Centrifuging of hydrometeors and debris in tornadoes: Radar-reflectivity patterns and wind-measurement errors. *Mon. Wea. Rev.*, **133**, 1501–1524.

Dowell, D.C., and H.B. Bluestein, 2002a: The 8 June 1995 McLean, Texas, storm. Part I: Observations of cyclic tornadogenesis. *Mon. Wea. Rev.*, **130**, 2626–2648.

Dowell, D.C., and H.B. Bluestein, 2002b: The 8 June 1995 McLean, Texas, storm. Part II: Cyclic tornado formation, maintenance, and dissipation. *Mon. Wea. Rev.*, **130**, 2649–2670.

Dowell, D.C., and H.B. Bluestein, 1997: The Arcadia, Oklahoma, storm of 17 May 1981: Analysis of a supercell during tornadogenesis. *Mon. Wea. Rev.*, **125**, 2562–2582.

Fiedler, B.H., 1998: Wind-speed limits in numerically simulated tornadoes with suction vortices. *Quart. J. Roy. Meteor. Soc.*, **124**, 2377–2392.

Dunn, L.B., and S.V. Vasiloff, 2001: Tornadogenesis and operational considerations of the 11 August 1999 Salt Lake City tornado as seen from two different Doppler radars. *Wea. Forecasting*, **16**, 377–398.

Dunn, L.B., 1990: Two examples of operational tornado warnings using Doppler radar data. *Bull. Amer. Meteor. Soc*., **71**, 145-153.

Fiedler, B.H., and R. Rotunno, 1986: A theory for the maximum windspeeds in tornado-like vortices. *J. Atmos. Sci.*, **43**, 2328–2340.

French, M.M., H.B. Bluestein, L.J. Wicker, D.C. Dowell, and M.R. Kramar, 2009: An example of the use of mobile, Doppler radar data for tornado verification. *Wea. Forecasting*, **24**, 884–891.

French, M.M., H.B. Bluestein, D.C. Dowell, L.J. Wicker, M.R. Kramar, and A.L. Pazmany, 2008: High-resolution, mobile Doppler radar observations of cyclic mesocyclogenesis in a supercell. *Mon. Wea. Rev.*, **136**, 4997–5016.

Fujita, T.T., 1981: Tornadoes and downbursts in the context of generalized planetary scales. *J. Atmos. Sci.*, **38**, 1511-1534.

Fujita, T.T., 1970: The Lubbock tornadoes: A study of suction spots. *Weatherwise*, **23**, 160–173.

Fujita, T.T., D.L. Bradbury, and P.G. Black, 1967: Estimation of tornado wind speed from characteristic ground marks. Preprints, *5th Conf. on Severe Local Storms*, St. Louis, Mo., Amer. Metor. Soc., 38-45.

Fujita, T.T., 1965: Formation and steering mechanisms of tornado cyclones and associated hook echoes. *Mon. Wea. Rev*., **93**, 67-78.

Fujita, T.T., 1958: Mesoanalysis of the Illinois tornadoes of 9 April 1953. *J. Meteor.*, **15**, 288-296.

Fujiwhara, S., 1931: Short note on the behavior of two vortices. *Proc. Phys. Math. Soc. Japan*, **13**, 106-110.

Gall, R.L., 1983: A linear analysis of the multiple vortex phenomenon in simulated tornadoes. *J. Atmos. Sci.*, **40**, 2010–2024.

Gaudet, B.J., and W.R. Cotton, 2006: Low-level mesocyclonic concentration by nonaxisymmetric transport. Part I: Supercell and mesocyclone evolution. *J. Atmos. Sci.*, **63**, 1113-1133.

Glickman, T.S., 2000: *Glossary of Meteorology*. 2nd ed. Amer. Meteor. Soc., 855 pp.

Golden, J.H., and D. Purcell, 1978: Life cycle of the Union City, Oklahoma tornado and comparison with waterspouts. *Mon. Wea. Rev.*, **106**, 3–11.

Golden, J.H., and D. Purcell, 1977: Photogrammetric velocities for the Great Bend, Kansas, tornado of 30 August 1974: Accelerations and asymmetries. *Mon. Wea. Rev.*, **105**, 485–492.

Grasso, L.D., and W.R. Cotton, 1995: Numerical simulation of a tornado vortex. *J. Atmos. Sci.*, **52**, 1192–1203.

Heymsfield, G.M., R.H. Blackmer, and S. Schotz, 1983: Upper-level structure of Oklahoma tornadic storms on 2 May 1979. I: Radar and satellite observations. *J. Atmos. Sci.*, **40**, 1740–1755.

Heymsfield, G.M., 1978: Kinematic and dynamic aspects of the Harrah tornadic storm analyzed from dual-Doppler radar data. *Mon. Wea. Rev.*, **106**, 233–254.

Hoecker, W.H., 1960: Wind speed and air flow patterns in the Dallas tornado of April 2, 1957. *Mon. Wea. Rev.*, **88**, 167-180.

Klemp, J.B., and R. Rotunno, 1983: A study of the tornadic region within a supercell thunderstorm. *J. Atmos. Sci.*, **40**, 359–377.

Klemp, J.B., R. Rotunno, and P.S. Ray, 1981: Observed and numerically simulated structure of a mature supercell thunderstorm. *J. Atmos. Sci.*, **38**, 1558–1580.

Kosiba, K., and J. Wurman, 2010: The three-dimensional axisymmetric wind field structure of the Spencer, South Dakota, 1998 tornado. *J. Atmos. Sci.*, **67**, 3074–3083.

Kramar, M.R., H.B. Bluestein, A.L. Pazmany, and J.D. Tuttle, 2005: The "Owl Horn" radar signature in developing Southern Plains supercells. *Mon. Wea. Rev.*, **133**, 2608–2634.

Kumjian, M.R., and A.V. Ryzhkov, 2008: Polarimetric signatures in supercell thunderstorms. *J. Appl. Meteor. Climatol.*, **47**, 1940–1961.

Lee, B.D., C.A. Finley, and T.M. Samaras, 2011: Surface analysis near and within the Tipton, Kansas, tornado on 29 May 2008.*Mon. Wea. Rev.*, **139**, 370–386.

Lee, W-C., and J. Wurman, 2005: Diagnosed three-dimensional axisymmetric structure of the Mulhall tornado on 3 May 1999. *J. Atmos. Sci.*, **62**, 2373–2393.

Lee, W-C., J-D. Jou, P-L. Chang, and S-M. Deng, 1999: Tropical cyclone kinematic structure retrieved from single Doppler radar observations. Part I: Interpretation of Doppler velocity patterns and the GBVTD technique. *Mon. Wea. Rev.*, **127**, 2419–2439.

Lemon, L.R., and C.A. Doswell, 1979: Severe thunderstorm evolution and mesocyclone structure as related to tornadogenesis. *Mon. Wea. Rev.*, **107**, 1184–1197.

Leslie, L.M., 1971: The development of concentrated vortices: A numerical study. *J. Fluid Mech.,* **48,** 1–21.

Lewellen, D.C., and W.S. Lewellen, 2007: Near-surface intensification of tornado vortices. *J. Atmos. Sci.*, **64**, 2176–2194.

Lewellen, D.C., and W.S. Lewellen, 2007b: Near-surface vortex intensification through corner flow collapse. *J. Atmos. Sci.*, **64**, 2195–2209.

Lewellen, W.S., D.C. Lewellen, and R.I. Sykes, 1997: Large-eddy simulation of a tornado's interaction with the surface. *J. Atmos. Sci.*, **54**, 581–605.

Markowski, P.M., Y. Richardson, J. Marquis, J. Wurman, K. Kosiba, P. Robinson, D. Dowell, and E. Rasmussen, 2012a: The pretornadic phase of the Goshen County, Wyoming, supercell of 5 June 2009 intercepted by VORTEX2. Part I: Evolution of kinematic and surface thermodynamic fields. *Mon. Wea. Rev.*, in press.

Markowski, P.M., Y. Richardson, J. Marquis, J. Wurman, K. Kosiba, P. Robinson, E. Rasmussen, and D. Dowell, 2012b: The pretornadic phase of the Goshen County, Wyoming, supercell of 5 June 2009 intercepted by VORTEX2. Part II: Intensification of low-level rotation. *Mon. Wea. Rev.*, in press.

Markowski, P.M., J.M. Straka, and E.N. Rasmussen, 2003: Tornadogenesis resulting from the transport of circulation by a downdraft: Idealized numerical simulations. *J. Atmos. Sci.*, **60**, 795–823.

Markowski, P.M., J.M. Straka, and E.N. Rasmussen, 2002: Direct surface thermodynamic observations within the rear-flank downdrafts of nontornadic and tornadic supercells. *Mon. Wea. Rev.*, **130**, 1692–1721.

Markowski, P.M., 2002: Hook echoes and rear-flank downdrafts: A review. *Mon. Wea. Rev.*, **130**, 852–876.

Marquis, J., Y. Richardson, P. Markowski, D. Dowell, and J. Wurman, 2012: Tornado maintenance investigated with high-resolution dual-Doppler and EnKF analysis. *Mon. Wea. Rev.,* **140**, 3-27.

Marquis, J., Y. Richardson, J. Wurman, and P. Markowski, 2008: Single- and dual-Doppler analysis of a tornadic vortex and surrounding storm-scale flow in the Crowell, Texas, supercell of 30 April 2000. *Mon. Wea. Rev.*, **136**, 5017–5043.

Marshall, T.P., 2004: The enhanced Fujita (EF) scale. Preprints, *22nd Conf. on Severe Local Storms,* Hyannis, MA, Amer. Meteor. Soc., 3B.2.

Marquis, J., Y. Richardson, J. Wurman, and P. Markowski, 2008: Single- and dual-Doppler analysis of a tornadic vortex and surrounding storm-scale flow in the Crowell, Texas, supercell of 30 April 2000. *Mon. Wea. Rev.*, **136**, 5017–5043.

Moller, A.R., 1978: The improved NWS storm spotters' training program at Ft. Worth, Tex. *Bull. Amer. Meteor. Soc.*, **59**, 1574–1582.

Oye, R., C. Mueller, and S. Smith, 1995: Software for radar translation, visualization, editing, and interpolation. Preprints, *29th Conf. on Radar Meteorology*, Vail, CO, Amer. Meteor. Soc., 359-361.

Pauley, R.L., and J.T. Snow, 1988: On the kinematics and dynamics of the 18 July 1986 Minneapolis tornado. *Mon. Wea. Rev.*, **116**, 2731–2736.

Pazmany, A.L., and H.B. Bluestein, 2011: A mobile, rapid–scanning, X-band, polarimetric (RaXPol) Doppler radar system. Preprints, *35th Conference on Radar Meteorology*, Pittsburgh, PA, Amer. Meteor. Soc., 16B.2.

PopStefanija, I., J. Knorr, P. Buczynski, and R. Bluth, 2005: Advanced weather surveillance algorithms and techniques using a rapid scanning X-band radar—First results. Preprints, *32nd Conf. on Radar Meteorology,* Albuquerque, NM, Amer. Meteor. Soc., P12R.3.

Rasmussen, E.N., J.M. Straka, M.S. Gilmore, and R. Davies-Jones, 2006: A preliminary survey of rear-flank descending reflectivity cores in supercell storms. *Wea. Forecasting*, **21**, 923–938.

Rasmussen, E.N., S. Richardson, J.M. Straka, P.M. Markowski, and D.O. Blanchard, 2000: The association of significant tornadoes with a baroclinic boundary on 2 June 1995. *Mon. Wea. Rev.*, **128**, 174–191.

Rasmussen, E.N., J.M. Straka, R. Davies-Jones, C.A. Doswell III, F.H. Carr, M.D. Eilts, and D.R. MacGorman, 1994: Verification of the origins of rotation in tornadoes experiment: VORTEX. *Bull. Amer. Meteor. Soc.,***75,** 995–1006.

Ray, P.S., B.C. Johnson, K.W. Johnson, J.S. Bradberry, J.J. Stephens, K.K. Wagner, R.B. Wilhelmson, and J.B. Klemp, 1981: The morphology of several tornadic storms on 20 May 1977. *J. Atmos. Sci.*, **38**, 1643–1663.

Ray, P.S., 1976: Vorticity and divergence fields within tornadic storms from dual-Doppler observations. *J. Appl. Meteor.*, **15**, 879–890.

Rotunno, R., 1993: Supercell thunderstorm modeling and theory. *The Tornado: Its Structure, Dynamics, Prediction, and Hazards, Geophys. Monogr.*, No. 79, Amer. Geophys. Union, 57–74.

Rotunno, R., 1986: Tornadoes and tornadogenesis. *Mesoscale Meteorology and Forecasting,* P. S. Ray, Ed., Amer. Meteor. Soc., 414–436.

Rotunno, R., and J.B. Klemp, 1985: On the rotation and propagation of simulated supercell thunderstorms. *J. Atmos. Sci.*, **42**, 271–292.

Rotunno, R., 1977: Numerical simulation of a laboratory vortex. *J. Atmos. Sci.*, **34**, 1942–1956.

Shapiro, A., 2001: A centrifugal wave solution of the Euler and Navier-Stokes equations. *Z. Angew. Math. Phys.*, **52**, 913-923.

Skinner, P.S., C.C. Weiss, J.L. Schroeder, L.J. Wicker, and M.I. Biggerstaff, 2011: Observations of the surface boundary structure within the 23 May 2007 Perryton, Texas, supercell. *Mon. Wea. Rev.*, **139**, 3730–3749.

Smith, R.K., and L.M. Leslie, 1978: Tornadogenesis. *Quart. J. Roy. Meteor. Soc.*, **104,** 189–199.

Trapp, R.J., E.D. Mitchell, G.A. Tipton, D.W. Effertz, A.I. Watson, D.L. Andra, and M.A. Magsig, 1999: Descending and nondescending Tornadic Vortex Signatures detected by WSR-88Ds. *Wea. Forecasting*, **14**, 625–639.

Snyder, J.C., H.B. Bluestein, G. Zhang, and S.J. Frasier, 2010: Attenuation correction and hydrometeor classification of high-resolution, X-band, dual-polarized mobile radar measurements in severe convective storms. *J. Atmos. Oceanic Technol.*, **27**, 1979–2001.

Straka, J.M., E.N. Rasmussen, R.P. Davies-Jones, and P.M. Markowski, 2007: An observational and idealized numerical examination of low-level counter-rotating vortices toward the rear flank of supercells. *Electron. J. Severe Storms Meteor.*, **2** (8).

Tanamachi, R.L., H.B. Bluestein, W-C. Lee, M. Bell, and A. Pazmany, 2007: Ground-based velocity track display (GBVTD) analysis of W-Band Doppler radar data in a tornado near Stockton, Kansas, on 15 May 1999. *Mon. Wea. Rev.*, **135**, 783–800.

Trapp, R.J., 2000: A clarification of vortex breakdown and tornadogenesis. *Mon. Wea. Rev.*, **128**, 888–895.

Trapp, R.J., and R. Davies-Jones, 1997: Tornadogenesis with and without a Dynamic Pipe Effect. *J. Atmos. Sci.*, **54**, 113–133.

Trapp, R.J., and B.F. Fiedler, 1995: Tornado-like vortexgenesis in a simplified numerical model. *J. Atmos. Sci.*,**52,** 3757–3778.

Vasiloff, S.V., 1993: Single-Doppler radar study of a variety of tornado types. *The Tornado: Its Structure, Dynamics, Prediction, and Hazards, Geophys. Monogr.*, No. 79, Amer. Geophys. Union, 223–231.

Wakimoto, R.M., N.T. Atkins, and J. Wurman, 2011: The LaGrange tornado during VORTEX2. Part I: Photogrammetry analysis of the tornado combined with single-Doppler radar data. *Mon. Wea. Rev.*, **139**, 2233-2258.

Wakimoto, R.M., H.V. Murphey, D.C. Dowell, and H.B. Bluestein, 2003: The Kellerville tornado during VORTEX: Damage survey and Doppler radar analyses. *Mon. Wea. Rev.*, **131**, 2197–2221.

Wakimoto, R.M. and C. Liu, 1998: The Garden City, Kansas, storm during VORTEX 95. Part II: The wall cloud and tornado. *Mon. Wea. Rev.*, **126**, 393–408.

Wakimoto, R.M., and N.T. Atkins, 1996: Observations on the origins of rotation: The Newcastle tornado during VORTEX 94. *Mon. Wea. Rev.*, **124**, 384–407.

Wakimoto, R.M., W-C. Lee, H.B. Bluestein, C-H. Liu, and P.H. Hildebrand, 1996: ELDORA observations during VORTEX 95. *Bull. Amer. Meteor. Soc.*, **77**, 1465–1481.

Walko, R.L., 1993: Tornado spin-up beneath a convective cell: Required basic structure of the near-field boundary layer winds. *The Tornado: Its Structure, Dynamics, Prediction, and Hazards, Geophys. Monogr.*, No. 79, Amer. Geophys. Union, 89–95.

Walko, R., and R. Gall, 1984: A two-dimensional linear stability analysis of the multiple vortex phenomenon. *J. Atmos. Sci.*, **41**, 3456–3471.

Ward, N.B., 1972: The exploration of certain features of tornado dynamics using a laboratory model. *J. Atmos. Sci.*, **29**, 1194–1204.

Wicker, L.J., and R.B. Wilhelmson, 1995: Simulation and analysis of tornado development and decay within a three-dimensional supercell thunderstorm. *J. Atmos. Sci.*, **52**, 2675–2703.

Wilson, J., R. Carbone, H. Baynton, and R. Serafin, 1980: Operational application of meteorological Doppler radar. *Bull. Amer. Meteor. Soc.*, **61**, 1154-1168.

Wood, V.T., R.A. Brown, and D. Sirmans, 2001: Technique for improving detection of WSR-88D mesocyclone signatures by increasing angular sampling. *Wea. Forecasting*, **16**, 177–184.

Wood, V.T., and R.A. Brown, 1997: Effects of radar sampling on single-Doppler velocity signatures of mesocyclones and tornadoes. *Wea. Forecasting*, **12**, 928–938.

Wurman, J., L.J. Wicker, Y. Richardson, E.N. Rasmussen, P.M. Markowski, D.C. Dowell, D.W. Burgess, and H.B. Bluestein, 2011: The Verification of the Origins of Rotation in Tornadoes 2 (VORTEX2). Preprints, *35th Conference on Radar Meteorology*, Pittsburgh, PA, Amer. Meteor. Soc., 6.1.

Wurman, J., K. Kosiba, P. Markowski, Y. Richardson, D. Dowell, and P. Robinson, 2010: Finescale single- and dual-Doppler analysis of a tornado intensification, maintenance, and dissipation in the Orleans, Nebraska, supercell. *Mon. Wea. Rev*., **138**, 4439-4455.

Wurman, J., W.C. Lee, C.R. Alexander, and K.A. Kosiba, 2008: Rapid-scan mobile radar 3D GBVTD and traditional analysis of tornadogenesis. Preprints, *24th Conference on Severe Local Storms*, Savannah, GA, Amer. Meteor. Soc., P13.6.

Wurman, J., Y. Richardson, C. Alexander, S. Weygandt, and P. Zhang, 2007a: Dual-Doppler and single-Doppler analysis of a tornadic storm undergoing mergers and repeated tornadogenesis. *Mon. Wea. Rev.*, **135**, 736–758.

Wurman, J., Y. Richardson, C. Alexander, S. Weygandt, and P. Zhang, 2007b: Dual-Doppler analysis of winds and vorticity budget terms near a tornado. *Mon. Wea. Rev.*, **135**, 2392–2405.

Wurman, J., and C.R. Alexander, 2005: The 30 May 1998 Spencer, South Dakota, storm. Part II: Comparison of observed damage and radar-derived winds in the tornadoes. *Mon. Wea. Rev.*, **133**, 97–119.

Wurman, J., 2002: The multiple-vortex structure of a tornado. *Wea. Forecasting*, **17**, 473–505.

Wurman, J. and M. Randall, 2001: An inexpensive, mobile, rapid-scan radar. Preprints, *30th Conf. on Radar Meteorology*, Munich, Germany, Amer. Meteor. Soc., 98–100.

Wurman, J., J. Straka, E. Rasmussen, M. Randall, and A. Zahrai, 1997: Design and deployment of a portable, pencil-beam, pulsed, 3-cm Doppler radar. *J. Atmos. Oceanic Technol.*, **14**, 1502–1512.

Ziegler, C.L., E.N. Rasmussen, T.R. Shepherd, A.I. Watson, and J.M. Straka, 2001: The evolution of low-level rotation in the 29 May 1994 Newcastle–Graham, Texas, storm complex during VORTEX. *Mon. Wea. Rev.*, **129**, 1339–1368.

Zrnic, D.S., J.F. Kimpel, D.E. Forsyth, A. Shapiro, G. Crain, R. Ferek, J. Heimmer, W. Benner, T.J. McNellis, and R.J. Vogt, 2007: Agile-beam phased array radar for weather observations. *Bull. Amer. Meteor. Soc.*, **88**, 1753–1766.